



HAL
open science

Analysis of device properties of silicon nitride membrane nanoelectromechanical resonators for future optomechanical thermometry applications

Hao Xu

► **To cite this version:**

Hao Xu. Analysis of device properties of silicon nitride membrane nanoelectromechanical resonators for future optomechanical thermometry applications. Micro and nanotechnologies/Microelectronics. Université de Lille, 2023. English. NNT : 2023ULILN038 . tel-04684713

HAL Id: tel-04684713

<https://theses.hal.science/tel-04684713v1>

Submitted on 3 Sep 2024

HAL is a multi-disciplinary open access archive for the deposit and dissemination of scientific research documents, whether they are published or not. The documents may come from teaching and research institutions in France or abroad, or from public or private research centers.

L'archive ouverte pluridisciplinaire **HAL**, est destinée au dépôt et à la diffusion de documents scientifiques de niveau recherche, publiés ou non, émanant des établissements d'enseignement et de recherche français ou étrangers, des laboratoires publics ou privés.

THESE DE DOCTORAT

Présentée à L'UNIVERSITE DE LILLE

Ecole doctorale Sciences de l'Ingénierie et des Systèmes

Pour obtenir le grade de

DOCTEUR

Dans la spécialité:

Micro et Nano Technologies, Acoustique et Télécommunications

Par

Hao Xu

**Analysis of device properties of silicon nitride membrane
nanoelectromechanical resonators for future
optomechanical thermometry applications**

**Analyse des propriétés des résonateurs
nanoélectromécaniques à membrane en nitrure de silicium
pour les futures applications de thermométrie
optomécanique**

Soutenue le 29 Novembre 2023 devant le jury composé de :

| | |
|---|------------------------|
| Président du jury: Prof. Dr. Yan Pennec, Professeur à l'Université de Lille | Examineur |
| Dr. Bernard Legrand, Directeur de Recherche au CNRS-LAAS, Toulouse | Rapporteur |
| Prof. Dr. Gaëlle Lissorgues, Professeur à l'ESIEE, Laboratoire ESYCOM | Rapporteur |
| Dr. Eddy Collin, Directeur de Recherche au CNRS, Institut Néel | Examineur |
| Dr. Xin Zhou, Chargée de Recherche au CNRS-IEMN | Co-directrice de thèse |
| Dr. Didier Théron, Directeur de Recherche au CNRS-IEMN | Directeur de thèse |

Acknowledgement

All related research work, including nanofabrication, characterization and mission, was financially supported by research grants from X. Zhou.

I would like to express my sincere gratitude to Dr. Didier Theron and Dr. Xin Zhou, for supervising my thesis. Without their continuous and professional guidance, this thesis would not have been completed. When I was suffering, Dr. Didier Theron, provided me with insightful suggestions and said the warm words “little by little” that gave me great encouragement for preparing this thesis. I am also indebted to Dr. Xin Zhou, for helping and guiding me little by little in carrying out this thesis. Without her patience and support, this thesis is in the air.

I also would thank reviewers Dr. Bernard Legrand and Prof. Dr. Gaëlle Lissorgues for constructive suggestions and making further progress of the thesis work, and thank examiners Dr. Eddy Collin and Prof. Dr. Yan Pennec for examining the thesis work.

Besides, I would especially like to thank my IEMN group collaborators, Dr. Srisaran Venkatachalam, for helping me understand the nanofabrication process and nanodevice measurements, and Dr. Alok Pokharel for the help of making measurement of silicon nitride drum NEMS.

All my IEMN engineer colleagues, I would like to thank their help and technical support. In particular, I thank Mr. Pascal Tilmant for the help of spin coater training, Mr. Christophe Boyaval for the help of SEM training and taking SEM images used in this thesis, Dr. Francois Vaurette and Ms. Saliha Ouendi for the help of EBL training and preparing EB writing files, Dr. Timothy Bertrand for the help of RIE training, and Dr. Dmitri Yarekha for the help of XeF₂ etcher training, Mr. Marc Dewitte for the help of making all metallization process used in this thesis. Thank Dr. Flavie Braud for laser cutting samples. Very specially, thank Dr. Sophie Eliet for SMM measurement training and help of SMM techniques. I also would thank all our administrative staff, Ms. Nora Benbahlouli, Mr. Andy Ledent, for making many efforts for administration works.

Moreover, many thanks going to my other IEMN colleagues/friends for their helpful talks, jokes, and smiles. Especially, I would like to thank Dr. Zhixiong Gong, Dr. Wei Wei, Mr. Ronghua Zhou, Dr. Steve Arscott, Mr. Ali Reda, Ms. Yasmine Bousbaa, Mr. Fawzi Bouakkaz.

I would finally like to thank my parents for the endless love and support year by year.

Lille, 08/28/2023

Abstract

Micro-nano-electromechanical resonators play a more and more important role in various domains, such as sensing, high frequency communications, and even in fundamental research. They allow mechanical displacement to be coupled with electrical signals for both detection and manipulation. So far, researchers continue to develop new device designs in order to meet various requirements in applications. More recently, membrane nanoelectromechanical resonators have been developed, consisting of a silicon nitride membrane capacitively coupled to an aluminium suspended top-gate drum. This unique design not only provides large coupling capacitance to external electrical circuits but allows to study mechanical and electrical mode coupling.

In this thesis, we have focused on the study of this type of nanoelectromechanical resonator. In the theoretical analysis, we have modelled this silicon nitride membrane nanomechanical resonator as a parallel plate capacitor. The simple motion equations allow us to analyse parametric amplification in both non-degenerate and degenerate cases, in the linear response region. In addition, a double-tone driving scheme has also been investigated, through an analogy to optomechanical system. Besides, we also modelled both nanoelectromechanically induced transparency and amplification based on mode coupling between the two silicon nitride membrane and aluminium top-gate resonators. In the following part of nanofabrication, we have presented critical fabrication processes in achieving the device. Both reflow step and dry etching step have been discussed and analysed. In the measurement part, besides of basic characterization of mechanical properties through aluminium top gate, we exploit scanning microwave microscopy to investigate this silicon nitride membrane resonators, such as spatial mapping of mechanical modes. The interaction between the AFM tip and the membrane has been simulated based on a capacitive coupling. Besides, double-tone driving techniques have also been demonstrated through coupling the AFM tip mode to the membrane mode. In addition, we also discussed a microwave optomechanical system in which this membrane resonator is capacitively coupled to a microwave cavity, for developing microwave optomechanical thermometer in the future.

Keywords: nanofabrication, silicon nitride membrane, nanoelectromechanical resonator, nanoelectromechanical modelling, scanning microwave microscopy

Résumé

Les micro-nano-résonateurs électromécaniques jouent un rôle de plus en plus important dans divers domaines, tels que les capteurs, les communications à haute fréquence et même la recherche fondamentale. Ils permettent de coupler un déplacement mécanique à des signaux électriques à des fins de détection ou de manipulation. Jusqu'à présent, les chercheurs ont régulièrement développé des nouvelles formes de dispositifs afin de répondre aux diverses exigences des applications. Récemment, des résonateurs nanoélectromécaniques à membrane ont été mis au point. Ils se composent d'une membrane en nitrure de silicium couplée de manière capacitive à une grille en aluminium suspendue au-dessus de la membrane. Cette conception unique fournit une grande capacité de couplage aux circuits électriques externes, et permet également d'étudier le couplage des modes mécaniques et électriques.

Dans cette thèse, nous nous sommes concentrés sur l'étude de ce type de résonateur nano-électromécanique. Dans l'analyse théorique, nous avons modélisé ce résonateur nanomécanique à membrane en nitrure de silicium et grille en aluminium comme un condensateur à plaques parallèles. Les équations du mouvement nous permettent d'étudier l'amplification paramétrique de la membrane dans les cas dégénérés et non dégénérés, en régime de réponse linéaire. En outre, un schéma de commande à double signal (un sur la membrane et un sur la grille) a également été étudié, par analogie avec le système optomécanique. Nous avons modélisé la transparence et l'amplification induites par le couplage de mode entre les deux résonateurs à membrane SiN et à grille supérieure en Al. Dans la partie suivante, nous avons présenté les procédés de nanofabrication critiques pour la réalisation du dispositif. L'étape de fluage et l'étape de gravure plasma ont été discutées et analysées. Dans le chapitre dédié aux mesures, en plus de la caractérisation de base des propriétés mécaniques de la membrane actionnée capacitivement par la grille en Al, nous exploitons la microscopie à micro-ondes à balayage (SMM) pour étudier les résonateurs à membrane en nitrure de silicium, en réalisant une cartographie des modes mécaniques. L'interaction entre la pointe AFM et la membrane a été simulée sur la base d'un couplage capacitif. En outre, la technique de caractérisation à double signal a également été utilisée en couplant le mode de la pointe AFM au mode de la membrane. Par ailleurs, nous présentons un système optomécanique à micro-ondes dans lequel ce résonateur à membrane est couplé capacitivement à une cavité à micro-ondes, afin de développer à l'avenir un thermomètre optomécanique à micro-ondes.

Mots clés: nanofabrication, membrane en nitrure de silicium, résonateur nanoélectromécanique, modélisation nanoélectromécanique, microscopie micro-onde à balayage

Acronyms and abbreviations

| | |
|------------------|---|
| MEMS/NEMS | Micro/nano-electro-mechanical systems |
| IEMN | Institut d'Electronique, Microélectronique et Nanotechnologie |
| SiN | Silicon nitride (Si_3N_4) |
| OR | Optical readout |
| ER | Electrical readout |
| LA | Laser intensity measurement |
| MWV | Microwave voltage measurement |
| RT | Room temperature |
| R&D | Research & Development |
| TM | Thermometer |
| CMOS | Complementary metal oxide semiconductor |
| SMM | Scanning Microwave Microscopy |
| AFM | Atomic Force Microscopy |
| SEM | Scanning Electron Microscopy |
| PMMA | Poly-(methyl methacrylate) |
| MMA | Methyl methacrylate |
| CSAR62 | Chemical Semi-Amplified positive tone EB resist |
| EBL | Electron beam lithography |
| RIE | Reactive ion etching |
| XeF ₂ | Xenon difluoride |
| FEM | Finite element method |
| 2D | Two-dimensional |
| 3D | Three-dimensional |

vii

| | |
|-------------|-------------------------|
| AC | Alternating current |
| DC | Direct current |
| RF | Radio frequency |
| LO | Local oscillator |
| IF | Intermediate frequency |
| DUT | Device under test |
| VNA | Vector network analyser |
| PD | Photodetector |
| S-parameter | Scattering- parameter |
| PSD | Power spectrum density |
| PCB | Printed circuit board |

Symbols

| Symbol | Meaning |
|-----------------|---|
| r | Radial coordinate in cylindrical coordinate system |
| θ | Azimuthal coordinate in cylindrical coordinate system |
| m | The m_{th} order Bessel functions of the first kind |
| n | The n_{th} zero for the m_{th} order Bessel functions of the first kind |
| ω_{mn} | Angular frequency, mode (m,n) |
| α_{mn} | Factor corresponding to mode (m,n) |
| $m_{eff,mn}$ | Effective mass corresponding to mode (m,n) |
| f_{mn} | Resonance frequency, mode (m,n), in the unit of Hz |
| Q_{mn} | Quality factor, mode (m,n) |
| $C_g(x)$ | Coupling capacitance between the mechanical element and its gate |
| δk_{dc} | The modulation of spring constant by DC voltage |
| Ω_m | Mechanical resonance frequency |
| γ_m | Mechanical damping rate |
| δk | Modulation of mechanical spring constant |
| α | Duffing nonlinear parameter |
| ω_p | Pump signal frequency |
| ω_s | Drive signal frequency |
| ω_i | Idler signal generated from frequency mixing |
| φ | Phase difference between pump and drive signal |
| Δ | Pump tone detuning from Ω_m , $= \frac{\omega_p}{2} - \Omega_m$ |
| δ | Pump tone detuning from driving signal ω_s , $= \omega_s - \frac{\omega_p}{2}$ (parametric pump) |

| | |
|--------------------------|---|
| χ_s | Mechanical susceptibility of drive signal |
| χ_i | Mechanical susceptibility of idler signal |
| Ω_1 | Resonance frequency of mechanical resonator <1> |
| Ω_2 | Resonance frequency of mechanical resonator <2> |
| x_1 | Amplitude of mechanical resonator <1> |
| x_2 | Amplitude of mechanical resonator <2> |
| γ_1 | Damping rate of mechanical resonator <1> |
| γ_2 | Damping rate of mechanical resonator <2> |
| Δ | Pump tone detuning from sideband, namely $\Omega_p = \Omega_1 \pm \Omega_2 + \Delta$ |
| δ | Probe tone detuning from probe signal, namely $\Omega_d + \delta$ (double-tone) |
| $\chi_{1,2}^{red}$ | Mechanical susceptibility at red sideband, resonator <1> or <2> |
| $\chi_{1,2}^{blue}$ | Mechanical susceptibility at blue sideband, resonator <1> or <2> |
| $\gamma_{eff1,2}^{red}$ | Effective damping rate at red sideband while probing signal at the mechanical resonator <1> or <2> |
| $\gamma_{eff1,2}^{blue}$ | Effective damping rate at blue sideband while probing signal at the mechanical resonator <1> or <2> |
| G | Coupling strength between resonators <1> and <2> |
| g_0 | Single photon coupling rate, namely $g_0 = Gx_{ZPF}$ |
| x_{ZPF} | Zero-point fluctuations, namely $x_{ZPF} = \sqrt{\hbar/2m_{eff}\Omega_m}$ |
| n_p | Photon number generated by pump tone |
| n_m | Phonon number carried by NEMS |
| n_c | Photon number circulating in cavity |
| T_m | Physical temperature occupied by NEMS |
| S_x^\pm | Symmetrized spectral density |

| | |
|-------------------|-------------------------------|
| κ_{cavity} | Decay rate of cavity |
| γ_{cavity} | Phonon-cavity damping rate |
| Γ_{opt} | Optical damping effect |
| ω_c | Detection frequency of cavity |
| ω_d | Driving frequency |

In this list, frequency parameters are angular frequency, with SI unit of radians per second (rad/s).

Contents

| | |
|--|-------------|
| Acknowledgement | ii |
| Abstract | iii |
| Résumé | iv |
| Acronyms and abbreviations..... | vi |
| Symbols | viii |
| Chapter 1 Introduction | 1 |
| 1.1 SiN mechanical resonators | 3 |
| 1.2 SiN membrane nanoelectromechanical resonator | 6 |
| 1.3 Thermometer | 10 |
| 1.4 Objectives of this thesis..... | 11 |
| Chapter 2 Theory and measurement results of nano-electro-mechanics..... | 14 |
| 2.1 High prestressed SiN circular membrane | 14 |
| 2.1.1 Mechanical modes of circular membranes | 14 |
| 2.1.2 Resonance frequency of circular membranes | 21 |
| 2.1.3 Effective mass of circular membranes | 23 |
| 2.1.4 Summary | 27 |
| 2.2 Nanoelectromechanics in a capacitive driving scheme | 28 |
| 2.2.1 Motion equation of nanoelectromechanical resonator driving through a capacitively coupling scheme..... | 28 |
| 2.2.2 Mechanical parametric pumping..... | 34 |
| 2.2.2.1 Non-degenerate analytical calculation | 34 |
| 2.2.2.2 Degenerate analytical calculation | 37 |
| 2.2.2.3 Summary | 42 |
| 2.2.3 Duffing nonlinearity..... | 43 |
| 2.2.4 Double-tone driving scheme in nanoelectromechanics, an analogy to optomechanical system | 47 |
| 2.2.4.1 Analytical modelling of the double tone driving scheme | 47 |
| 2.2.4.2 Simulation results of the nanoelectromechanically induced transparency and amplification | 64 |
| 2.2.4.3 Motion behaviours between two parallel circular membranes in the nanoelectromechanical system..... | 75 |
| 2.2.4.4 Summary | 77 |
| 2.3 Experiment setup and basic related measurement results | 78 |
| 2.3.1 Experiment setup | 78 |
| 2.3.2 Mechanical response vs. frequency (in the linear region) | 82 |

| | |
|---|------------|
| 2.3.3 Resonance frequency vs. DC voltage (the modulation of spring constant)..... | 84 |
| 2.3.4 Duffing mechanical response vs. frequency (in the nonlinear region) | 86 |
| 2.3.5 Parametric pumping applications (gain amplification and de-amplification)..... | 89 |
| Chapter 3 Fabrication of SiN membrane nano-electro-mechanical resonator | 95 |
| 3.1 Introduction to fabrication tools | 95 |
| 3.1.1 Electron beam lithography (EBL)..... | 95 |
| 3.1.2 Reactive ion etching (RIE)..... | 99 |
| 3.1.3 Xenon difluoride etching (XeF ₂)..... | 100 |
| 3.2 Design of SiN circular membrane by finite element simulation | 102 |
| 3.3 Fabrication process of SiN membrane nano-electro-mechanical resonator | 105 |
| 3.3.1 Alignment marks, contact lines and pads | 107 |
| 3.3.2 Release of SiN membrane from silicon substrate | 109 |
| 3.3.3 Aluminium film deposition on the released SiN membrane..... | 119 |
| 3.3.4 Aluminium suspended top gate on the top of the SiN membrane | 122 |
| 3.3.4.1 Coating of EB resist sacrificial layer | 123 |
| 3.3.4.2 Formation of suspended Al top gate on the top of SiN membrane..... | 127 |
| 3.4 Summary..... | 132 |
| Chapter 4 Scanning microwave microscopy for detecting mechanical vibration of SiN membrane | 133 |
| 4.1 Scanning microwave microscopy | 133 |
| 4.1.1 The overview and the state-of-the-art of scanning microwave microscopy | 133 |
| 4.1.2 AFM-tip-sample interface and principle..... | 135 |
| 4.1.3 Vector network analyser measurement | 142 |
| 4.1.4 Measurement setup | 146 |
| 4.2 Characterization and results discussion of mechanical vibration of SiN membrane ... | 147 |
| 4.2.1 Finite element method simulation of the tip-membrane scheme | 147 |
| 4.2.2 Linear mechanical response of SiN membrane..... | 156 |
| 4.2.3 Resonance frequency modulation of SiN membrane..... | 157 |
| 4.2.4 Duffing nonlinear mechanical response of SiN membrane | 160 |
| 4.2.5 Mechanical modes detection of SiN membrane | 163 |
| 4.2.6 Capacitive coupling two mechanical modes in a two-tones driving scheme..... | 168 |
| 4.2.7 White noise drive of SiN membrane..... | 180 |
| 4.3 Summary..... | 185 |
| Chapter 5 Microwave optomechanical thermometry | 187 |
| 5.1 The thermometry principles..... | 187 |

| | |
|---|------------|
| 5.1.1 Cavity optomechanical scheme..... | 188 |
| 5.1.2 Cavity optomechanical readout of thermal Brownian motion..... | 192 |
| 5.2 Experiment expectations..... | 196 |
| 5.3 Summary..... | 197 |
| Chapter 6 Conclusion and outlook | 198 |
| 6.1 Conclusion | 198 |
| 6.2 Outlook | 199 |
| List of publications | 202 |
| Bibliography | 203 |

Chapter 1 Introduction

Microsystems, applied either in optical or electrical readout, have gained enormous attention in various applications, for biology with breath/blood pressure sensors in health monitoring [1], microfluidics in biological diagnosis [2], for inertial measurements with accelerators [3] and gyroscopes [4] in mobile systems, and RF communication components [5] in modern semiconductor industry. In the optical readout scheme, mechanical resonator has been widely studied that shows characterizing high resonance frequency, high quality factor and designing photonic crystals membrane through the dissipation engineering [6–8]. In the electrical readout scheme, micro/nano-electromechanical systems (MEMS/NEMS) resonators, due to having electrostatic transductions with low power operation, have been widely applied in high frequency electrical systems. MEMS/NEMS have a great promise for allowing for electrical integration. In recent years, MEMS/NEMS devices have been made by exploiting varieties of materials, such as aluminium [9,10], silicon [11,12], SiN [13,14], silicon carbide [15,16], graphene [17,18] and carbon nanotubes [19,20].

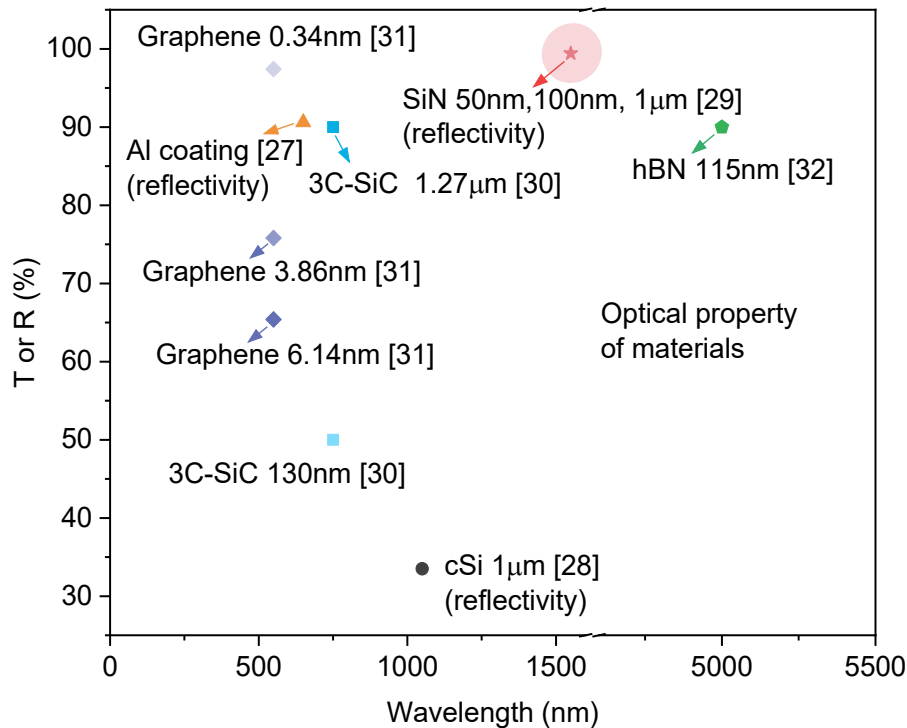


Figure 1.1.1. Optical properties of thin films, containing aluminium, crystalline silicon, SiN, cubic silicon carbide, graphene and hexagonal boron nitride. Data correspond to transmittance (T) except specific reflectivity (R) mention.

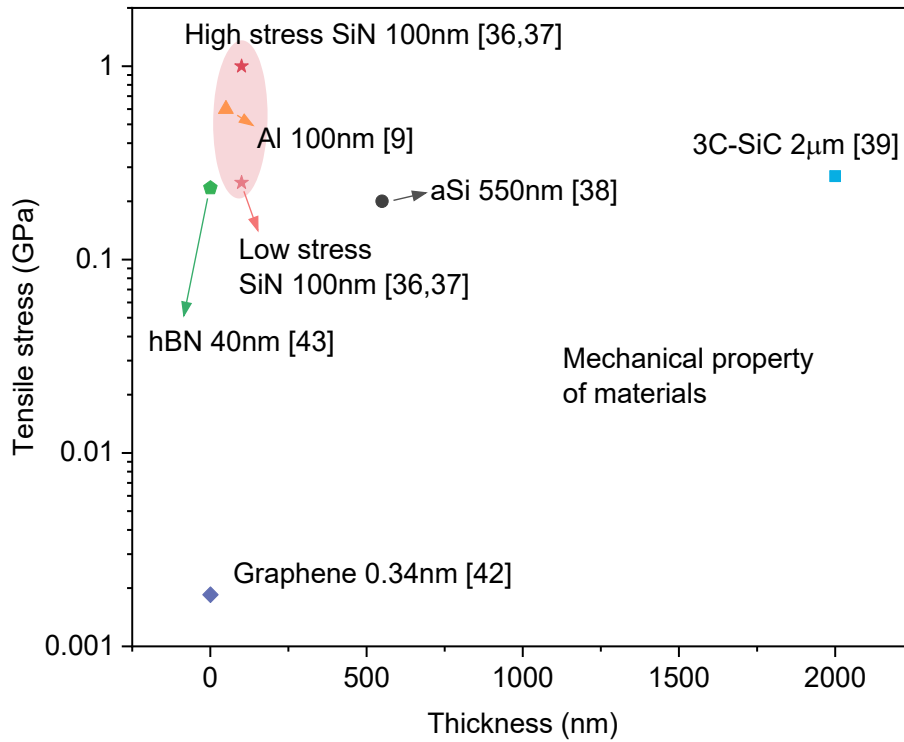


Figure 1.1.2. Mechanical properties of thin films for MEMS/NEMS or nanomechanical resonator, containing aluminium, amorphous silicon, SiN, cubic silicon carbide, graphene and hexagonal boron nitride.

Table 1.1.1. Mechanical properties of related materials

| Materials | Mass density (kg/m^3) | Young's modulus (GPa) |
|--------------------------|---|-----------------------|
| Graphene (0.34nm) | 2270 kg/m^3 or 0.77 mg/m^2 | 1000 [21] |
| hBN (0.33nm) | 2300 kg/m^3 or 0.76 mg/m^2 | 865 [22] |
| Aluminium bulk | 2700 | 70 [23] |
| SiN (800nm) | 3084 | 280 [24] |
| Silicon bulk | 2330 | 168 [25] |
| SiC (2-5 μm) | 3200 | 400 [26] |

When selecting materials for MEMS/NEMS fabrication, two properties are generally considered. (i) Optical properties, e.g., absorption, of these materials [27–33] determine the

driving power when MEMS/NEMS coupled with optical system, such as opto-electro-mechanical system. The material with high optical loss requires larger drive power, leading to the undesired heating effects. **Fig.1.1.1** shows optical properties of various thin films. SiN thin films have very high reflectivity (99.42%), comparing with all other materials, indicating it's the lowest optical loss. Although monolayer graphene with the transmittance (97.4%) is seen, however, high quality sample transfer [34,35], as it is suspended over substrate, still limits its high quality electrical integration. (ii) Mechanical properties, e.g., tensile stress and mass density, of materials [9,36–41][42][43] have also been another important issue. High tensile stress yields the potential of achieving high operating frequency [36]. **Fig. 1.1.2** and **Table 1.1.1** show tensile stress, Young's modulus and mass density of various materials. In spite of general monolayer graphene with tensile stress (~ 1.85 MPa) and multilayer hexagonal boron nitride (hBN) with tensile stress (~ 234 MPa), they are not suitable for the practical electrical integration, because they not only have uneasy transfer process but also the hBN is insulating, further increasing the difficulties. Comparing with graphene and hBN, SiN with tensile stress (1 GPa or 0.2 GPa) can be one of the ideal candidate materials for fabricating MEMS/NEMS. Based on the mature chemical vapour deposition (CVD) process, the controllable tensile stress of SiN deposited on a silicon substrate can be easily implemented. In order to apply SiN to electrical systems, a thin conductive coating is required for satisfying this electrical scheme. For instance, an aluminium film is chosen, because the mechanical properties of aluminium are comparable with SiN.

1.1 SiN mechanical resonators

In recent years, SiN have been a good candidate because it has low optical loss [29] and tunability of mechanical properties, enabling low operation power, high tensile stress [44,45] and high quality factors [36,46,47]. SiN thin films have been used for optical readout applications, such as squeezed light [48] and entangled optical and mechanical degrees of freedom [49]. For example, SiN membranes with high quality factors (10^7) have been used to efficiently couple with an optical cavity [37]. Moreover, SiN also have excellent mechanical properties for electrical readout applications, such as mass [50–52] and force sensing [53]. To apply SiN to proper applications, we are intended to consider a product of frequency and quality factor as a useful merit. [54] It is worth to mention that this product also plays a major role in investigating quantum effects if $f \cdot Q > k_B T / h$ is feasible [7,55], where k_B is the Boltzmann constant and h is the Planck constant.

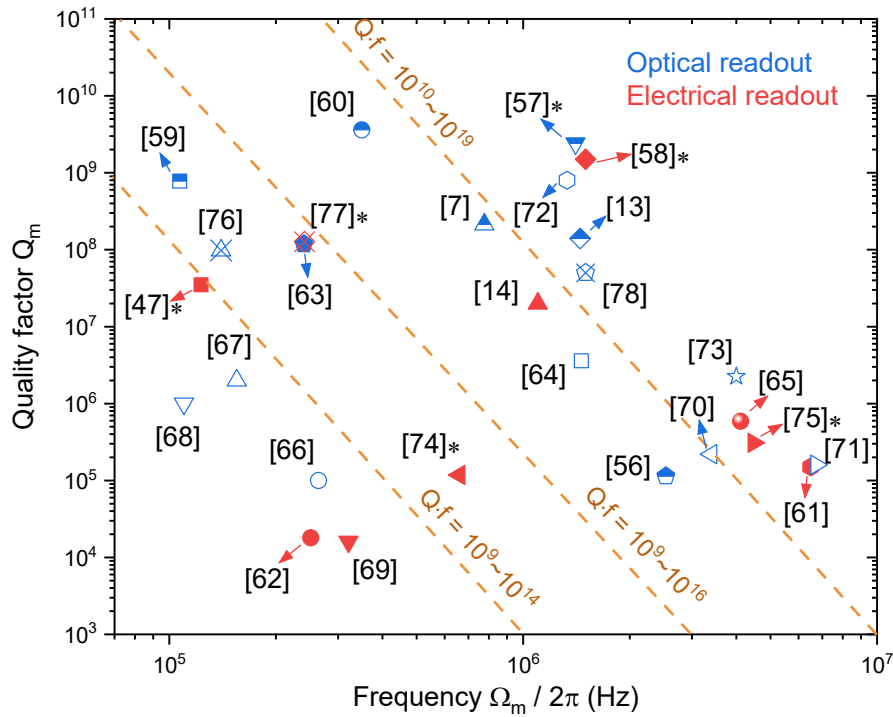


Figure 1.1.3. Quality factor of SiN mechanical resonators and MEMS/NEMS resonators versus frequency $\Omega_m/2\pi$. The blue and red symbols are optical and electrical readout, respectively. The orange dashed lines correspond to constant products of $Q \cdot f$. “*” is performed at cryogenics.

Fig. 1.1.3 shows a diagram of quality factor values of SiN mechanical resonators and MEMS/NEMS resonators [7,13,14,47,56–78]. In the figure, we see all quality factors beyond 10^4 . Additionally, they have high frequencies ranging from $10^5 \sim 10^7$ Hz. It indicates SiN MEMS/NEMS, thanks to miniaturization, have the great potential to be applied in high frequency electrical integrated systems, comparing with those applied in optical systems.

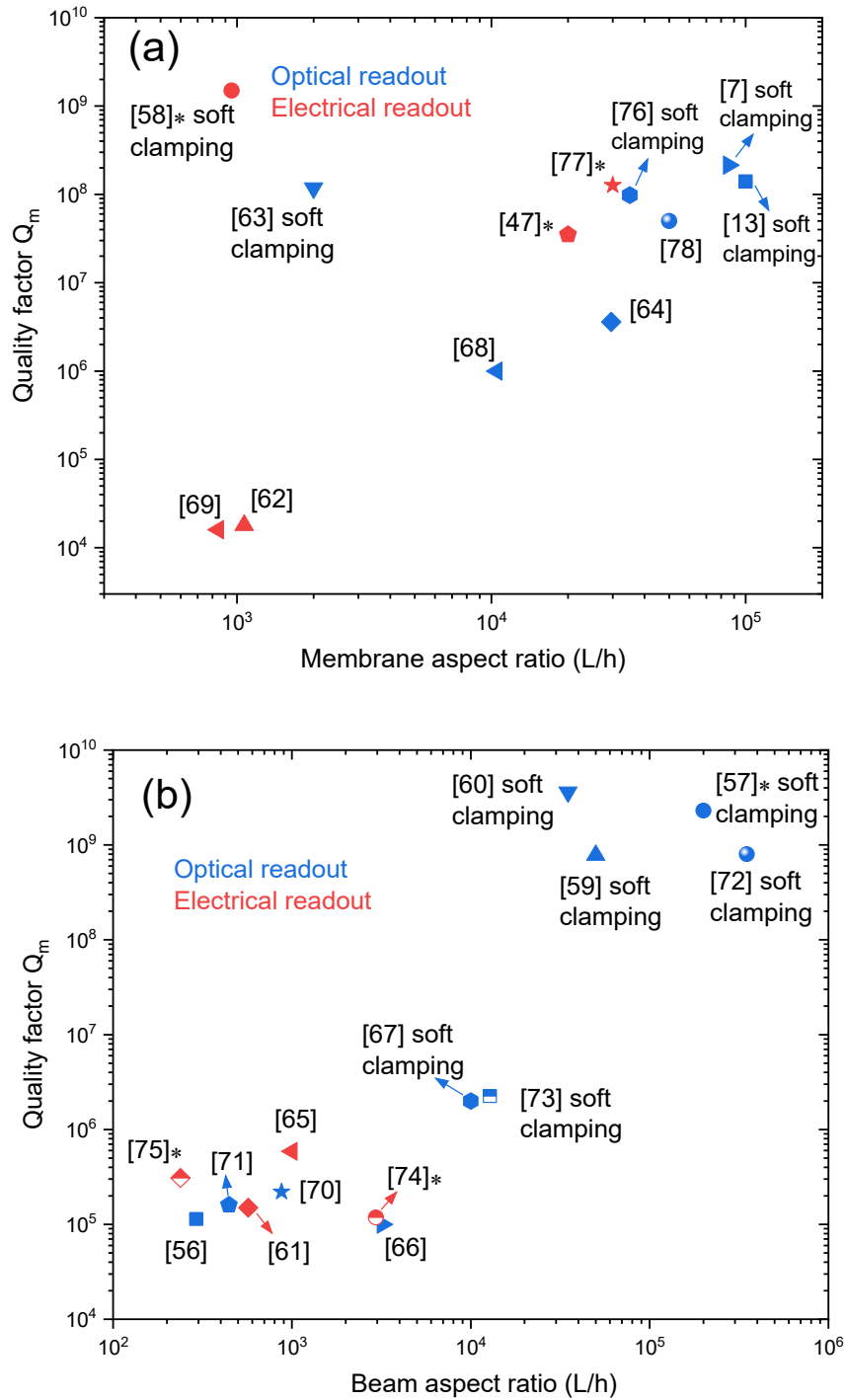


Figure 1.1.4. Quality factor of SiN membranes [7,13,47,58,62–64,68,69,76–78] (a) and beams [56,57,59–61,65–67,70–75](b) versus aspect ratio L/h , where L is the lateral length and h is the thickness. The red and blue symbols are optical and electrical readout, respectively. “*” is performed at cryogenics.

So far, two types of SiN MEMS/NEMS resonators, e.g., membrane and doubly-clamped beam, have been widely studied in the electrical readout. It is obvious that SiN membranes are simply symmetric and have larger surface areas than those of beams [61][79], enabling 10-times larger the coupling strength and allowing high efficient electrical operation in the integration circuits. We compare between SiN membranes and beams to show quality factor as function of the aspect ratio. **Fig. 1.1.4(a)** shows the quality factors of SiN membranes can exceed 10^9 in the electrical readout, rivalling with the optical readout. Besides, SiN membrane mechanical resonators have obtained with high quality factor (2.14×10^8 at RT) in the optical readout [7], because of the dissipation dilution engineering. In addition, soft clamping schemes have been exploited for further reducing damping effects, where most of SiN membrane edges are etched away to avoid full clamping [80]. Such SiN membrane resonators are suitable for optical readout applications. However, it is very challenging to achieve electrical integration, because this type of SiN membrane becomes so fragile to fabricate a suspended top gate. So as to apply SiN membrane to the electrical readout, in the nanofabrication process, our SiN membrane has been designed to be a fully clamped scheme [81]. It gives SiN membrane an access to achieve electrical integration.

1.2 SiN membrane nanoelectromechanical resonator

In recent years, capacitive transduction schemes become very successful and have been widely applied in MEMS applications, such as microphones [82,83] and pressure sensors [84]. Besides, resonance frequency tunability can be easily achieved by implementing electrostatic forces. In addition, such a capacitive coupling scheme brings flexibility in exploring coupled nanoelectromechanical resonators. With the recent development of nanotechnology, membrane-based MEMS/NEMS are becoming attractive because they offer large coupling, allowing mechanical degrees of freedom to be efficiently coupled with external circuits for electrical control and readout.

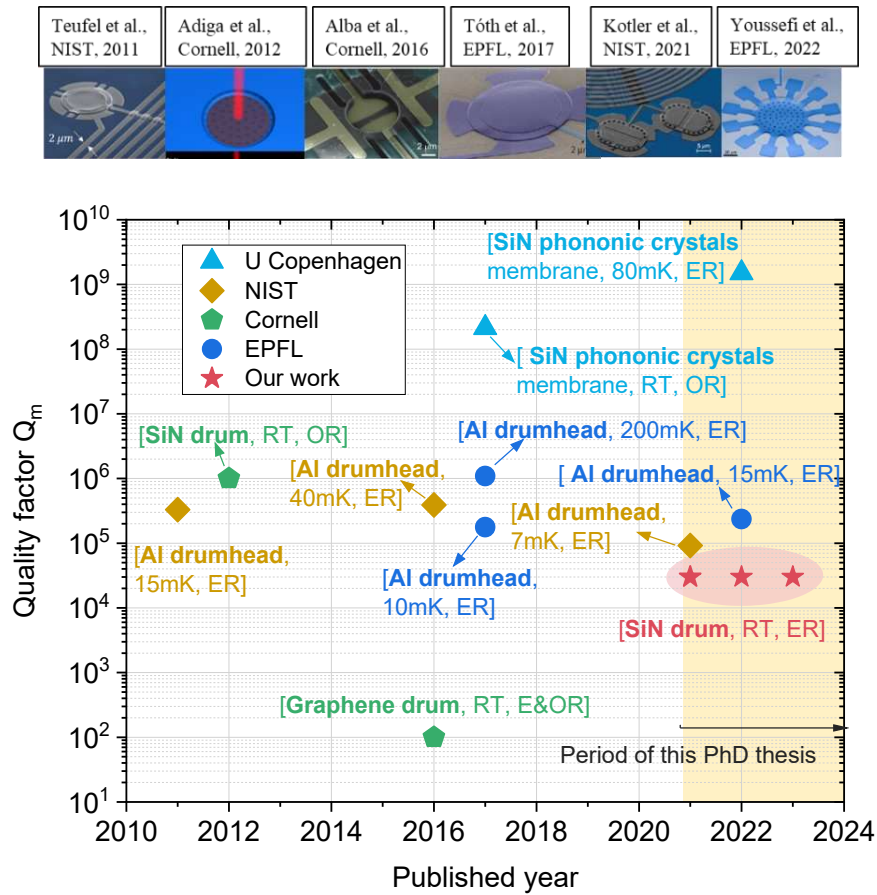


Figure 1.2.1. The electrical readout high-Q mechanical drum resonators made from aluminium, SiN, graphene, with prestigious and continuous research&development(R&D) contributions to the MEMS optomechanical community. In this community, several important works reported by University of Copenhagen, Denmark (group of A. Schliesser) [7,58], National institute of standards and technology (NIST), USA (group of John D. Teufel) [9,10,85,86], Cornell University, USA (groups/related groups of H. G. Craighead and J. M. Parpia) [42,87], Ecole Polytechnique Fédérale de Lausanne (EPFL), Switzerland (group of T. J. Kippenberg) [88–90] have been selected. Note that, optical readout (OR) and electrical readout (ER) are remarked respectively. Worth to mention that optical readout is laser intensity (LA) measurement and electrical readout is microwave voltage (MWV) measurement.

Thus far, membrane-based MEMS/NEMS resonators with capacitive transductions have been developed by using aluminium thin membrane [9], SiN drum membrane [46,77,91,92] and graphene drum [34,42]. SiN drum membrane, due to the low optical loss, high tensile stress and the feasibility of fabrication process, becomes promising. It offers good mechanical properties in a wide range of working temperatures and its tensile stress can be engineered in standard

Low Pressure Chemical Vapor Deposition (LPCVD). **Fig. 1.2.1** shows a review of the recent developed circular membrane MEMS resonators, regarding to one of the MEMS/NEMS parameters, quality factor, Q_m .

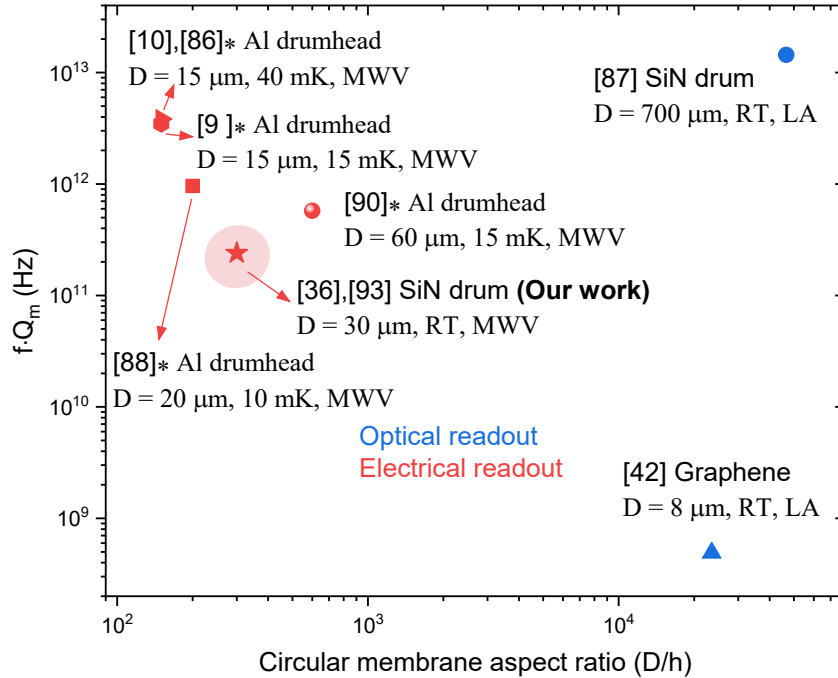


Figure 1.2.2. The product $f \cdot Q_m$ of circular membranes versus aspect ratio D/h , where D is the diameter and h is the thickness. The red and blue symbols are electrical and optical readout, respectively. “*” is performed at cryogenics. Optical readout is laser intensity (LA) measurement and electrical readout is microwave voltage (MWV) measurement.

For MEMS/NEMS, the other key parameter is resonance frequency, f . **Fig. 1.2.2** shows a diagram of the product $f \cdot Q_m$ values as function of the aspect ratio for various circular membrane MEMS/NEMS resonators, including aluminium drumhead [9,10,86,88,90], SiN drum [36,87,93] and graphene drum [42]. According to the figure, we see our SiN circular membrane based MEMS/NEMS have great potentials because of the product $f \cdot Q_m > 10^{11}$ at RT, competing with the previous results performed at low temperatures. Besides external laboratories, IEMN researchers also reported silicon ring-shaped MEMS resonators driven by microwave reflectometry method since the year of 2013, for resolution and frequency improvement applications of atomic force microscopy [94,95].

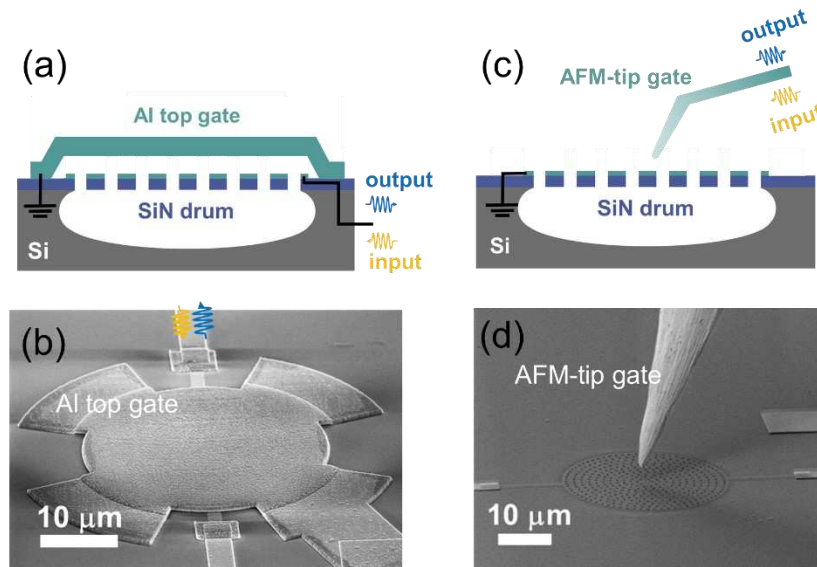


Figure 1.2.3. The studied device structures in this thesis. (a) shows side view and (b) shows the SEM image of SiN membrane nanoelectromechanical resonator capacitively coupled to a suspended aluminium top gate. (c) shows side view and (d) shows the SEM image of circular SiN membrane covered with a thin aluminium capacitively coupled to the metallic AFM-tip, which serves as the gate instead of the Al top gate.

In this thesis work, our studies are based on SiN circular membrane nanoelectromechanical resonators, which have been developed by Zhou et al [36] in 2021. As **Fig. 1.2.3(a,b)** shows, the device structure is based on two membrane-based resonators, in which a SiN membrane covered with a thin aluminium layer on its surface is capacitively coupled to a suspended aluminium top gate. Besides, **Fig. 1.2.3(c,d)** shows the SiN circular membrane covered with a thin aluminium, which will also be electrically detected by adding microwave ac signal onto the AFM-tip driving its motion, as it is thought of as flexible and movable gate.

1.3 Thermometer

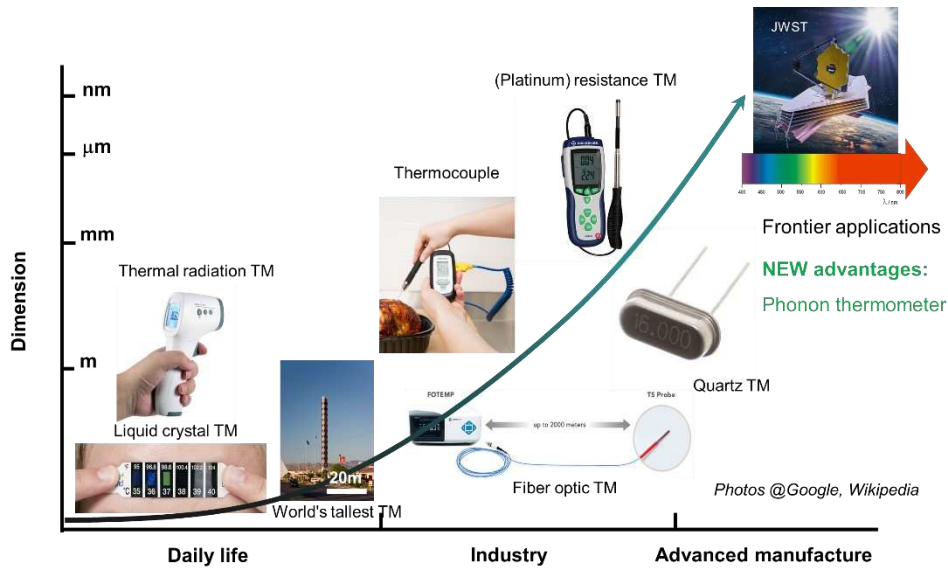


Figure 1.3.1. Gallery of different kinds of thermometer (TM)

Thermometer is a kind of temperature-recording device, which is used in daily life or industry as described in **Fig.1.3.1**. At present, different temperature readout mechanisms mainly involve thermoresistive [96,97], thermoelectric [98,99], and thermochromic effect [100][101,102]. These conventional thermometers, regarding temperature readout, are facing challenges (e.g., outer space or cryogenics), having the limits of Joule heating, localized thermal conductivity and extra calibration. There is still a lack of development of primary thermometers for both industry and research.

Nanomechanical resonators can be a type of phonon sensor. The thermal Brownian motions carry information of temperature. The basic principle is related to the formula $k_B T_m = n_m \hbar \Omega_m$, where T_m is the physical temperature carried by NEMS, \hbar is Planck's constant over 2π , Ω_m is resonance frequency of NEMS, and n_m is the phonon number occupied by the NEMS. By integrating the measured spectrum density of thermal Brownian motions, the value of n_m is given by $\frac{1}{2\pi} \int S_x^\pm d\omega = \frac{\hbar}{2m_{eff}\Omega_m} n_m$, relating n_m to the detected physical temperature T_m (see Chapter 5). In other words, NEMS can be used to detect the temperature in forms of phonon numbers. It is one kind of primary thermometer based on well-known expressions in physics and it does not need to extra calibration from other kind of thermometers. However, it needs an accurate determination of the parameter properties, which the present work contributes to

establishing. Optomechanical schemes offer a method to readout the thermal Brownian motion by using optical/microwave photons. In one part of this thesis, we will also discuss the feasibility in the integration of our drum resonator in microwave optomechanical circuits for exploring applications of optomechanical phonon thermometer.

1.4 Objectives of this thesis

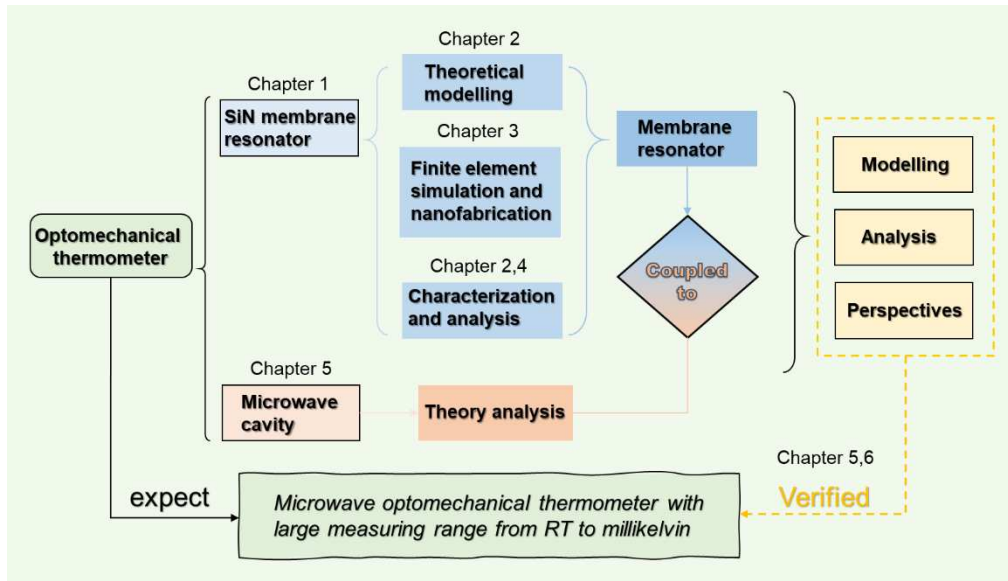


Figure 1.4.1. Illustration of framework of this thesis.

This work presents a study of the device properties of SiN membrane nanomechanical resonators. It aims at exploring a microwave optomechanical thermometer based on this kind of membrane NEMS in the future work. As shown in **Fig. 1.4.1**, this thesis work consists of theoretical modelling of nanomechanical resonator in a capacitive coupling scheme, discussions of critical nanofabrication process in achieving the device, exploiting microwave scanning microscopy to investigate mechanical properties of SiN membrane, and discussions of experimental implementations in integrating membrane NEMS in microwave optomechanical circuits.

In Chapter 2, we present theoretical analysis of the membrane nanoelectromechanical resonator, driving in a capacitive coupling scheme. The methodology theories contain mechanical mode, resonance frequency and effective mass of SiN circular membrane. Then, nanoelectromechanics principles were carefully analysed based on such a capacitive coupling scheme by adding electrostatic forces through the mixing dc and ac voltages. Then, parametric pump scheme, having non-degenerate and degenerate cases, was introduced to this resonator,

which enables signal amplification and de-amplification. Besides, Duffing nonlinear behaviours in this mechanical resonator have also been analysed. So as to extend the applicable range to electromechanically induced transparency and amplification, an analog to the optomechanical experiment, double driving tones have been modelled and developed. Basic related measurements of our SiN circular membrane have been conducted in the electrical readout.

In Chapter 3, we present the feasible and detailed nanofabrication process for achieving SiN circular membranes, containing a SiN circular membrane covered with a thin aluminium layer capacitively coupled to a suspended top gate. The details of fabrication techniques, such as electron beam lithography, reactive ion etching, XeF₂ etcher tools, have been investigated and learnt. Before fabrication process, finite element simulation of a circular membrane was performed. Then, critical fabrication steps have been discussed, including the XeF₂ selective etching process to release SiN membrane from silicon substrate and the reflow process to fabricate a top gate of a suspended aluminium membrane. This ultra-clean and CMOS-compatible process allows the SiN membrane to have a high quality factor ($\sim 1.1 \times 10^4$) at room temperature, enabling electrical integration with external circuits with high efficiency.

In Chapter 4, we study the mechanical properties by using SMM techniques. In this part, we take an AFM-tip as a suspended top gate of the SiN circular membrane, which is used to excite and detect mechanical motions of the membrane. In this chapter, we first performed finite element simulations for understanding of the tip-membrane interactions based on electrostatic forces. Then, spatial mapping mechanical modes of the SiN circular membrane have been measured in the linear response region. In addition, in order to study membrane-tip mode coupling, we drive the membrane by using double-tone in order to study electromechanically induced transparency and amplification. In the final part, we demonstrate measurement of thermal Brownian motion of the SiN circular membrane by artificially heating up the membrane through adding extra white noise.

In Chapter 5, we give a general review of basic principle of cavity optomechanical scheme for applications of thermometers, including two important issues: the coupling strength and the optical spring effect. We quantitatively analysed the advantages of integrating our drum membrane nanomechanical resonator in the microwave optomechanical circuits for developing thermometer in the future. In addition, to help understanding classical features of optomechanics, comparisons between an optomechanical system and a phonon-cavity system

have been discussed regarding the optical spring effects. Several important parameters, such as coupling capacitance, cavity photon number, in achieving this kind of phonon thermometer have been discussed.

In Chapter 6, we summarize the main results of the throughout work. Besides, several future works have been proposed. One of the future works is to build the thermometry experiment setup for measuring the temperature ranging from RT to millikelvin. Besides, the optimization of the XeF₂ etching process and the capacitance theory optimization of the tip-membrane interactions could also be interesting for the future work.

Chapter 2 Theory and measurement results of nano-electro-mechanics

In this chapter, we first introduce the theory analysis of SiN circular membrane, including mechanical mode, resonance frequency and effective mass evaluation. Then, nanoelectromechanics of SiN membrane is analysed that shows how the AC and DC electrical signal control works in the nanoelectromechanical system. Moreover, parametric pump scheme is presented in order to show signal amplification and de-amplification in the capacitive coupling system. Nonlinearity is also important when signal response occurs in non-linear response region. Furthermore, the double-tone driving scheme, analog to optomechanical system, has been modelled and analysed in the two nanoelectromechanical resonators. Finally, characterization and analysis of SiN membrane nanoelectromechanical resonator are done, such as linear behaviour, resonance frequency modulation by DC voltages, etc.

2.1 High prestressed SiN circular membrane

2.1.1 Mechanical modes of circular membranes

We start by analysing membrane's mechanical mode shape, which helps us to calculate a resonance frequency for the mechanical mode. Then, we can assess how much effective mass is presented in a mechanical mode.

Theory analytics of circular membranes. We introduce a mechanical system that can be used to model an oscillatory motion. In general, circular membranes can be modelled by modified beam's and string's motion equation and can be reduced to a one-dimensional oscillation in form of $z(x,y,t)$, given by [103–105]

$$\frac{Eh^3}{12(1-\nu^2)}\nabla^4 z(x,y,t) - T\nabla^2 z(x,y,t) + \rho h \frac{\partial^2 z(x,y,t)}{\partial t^2} + \frac{\gamma^*}{w} \frac{\partial z(x,y,t)}{\partial t} = q(x,y) \quad \text{Eq. 2.1.1}$$

where $\nabla^4 = \frac{\partial^4}{\partial x^4} + 2 \frac{\partial^4}{\partial x^2 \partial y^2} + \frac{\partial^4}{\partial y^4}$ and $\nabla^2 = \frac{\partial^2}{\partial x^2} + \frac{\partial^2}{\partial y^2}$ is the Laplacian operator. E is the Young's modulus, ν is the Poisson coefficient, ρ is the mass density, h is the membrane thickness, $T = \frac{N}{w} = \sigma h$ is the tensile force per unit length at the membrane edge, N being the total force, σ the membrane biaxial stress and w the membrane perimeter, $q(x,y)$ is the loading force per unit area.

Here, the simplest case, membrane structure is considered by neglecting the first and fourth term because of the large xy -axial tension effects and taking the load $q(x, y)$ as zero.

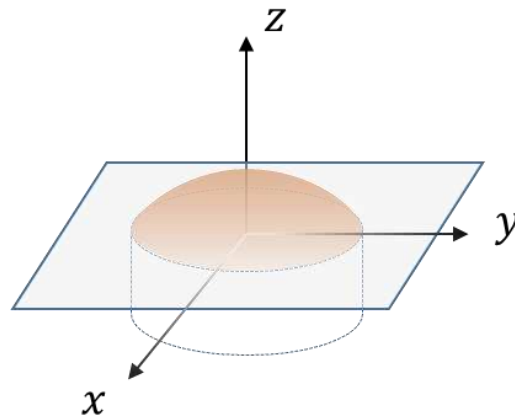


Figure 2.1.1. Oscillating motion of a circular membrane (light red) in the plane xy used in Cartesian coordinate system.

Thus, the description of the equation of free motion becomes

$$\frac{\partial^2 z}{\partial x^2} + \frac{\partial^2 z}{\partial y^2} - \frac{\rho}{\sigma} \frac{\partial^2 z}{\partial t^2} = 0 \quad \text{Eq. 2.1.2}$$

We noted that the circular membrane is symmetric in Cartesian coordinates, oscillating in form of $z(x, y, t)$, as shown in **Fig. 2.1.1**. To simplify the motion, we use cylindrical coordinates to describe the oscillation mechanics by reintroducing two-dimensional Laplacian operator $\nabla^2 = \partial^2/\partial x^2 + \partial^2/\partial y^2$. The converts from Cartesian coordinates to cylindrical coordinates are $x = r \cos \theta$ and $y = r \sin \theta$, as shown in **Fig. 2.1.2**.

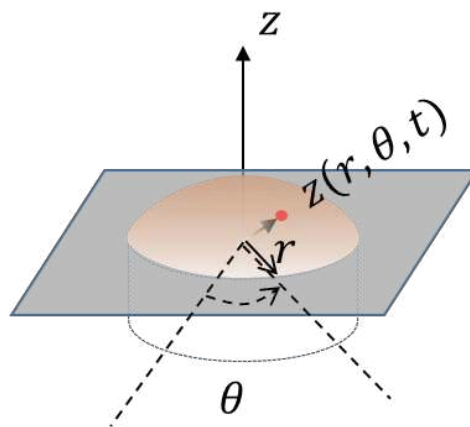


Figure 2.1.2. Oscillating motion of a circular membrane (light red) in the plane r, θ used in cylindrical coordinate system.

In the following, we will use the cylindrical coordinate system to describe the theoretical development progress. The converted equation becomes [106]

$$\frac{1}{r} \frac{\partial}{\partial r} \left(r \frac{\partial z}{\partial r} \right) + \frac{1}{r^2} \frac{\partial^2 z}{\partial \theta^2} - \frac{\rho}{\sigma} \frac{\partial^2 z}{\partial t^2} = 0 \quad \text{Eq. 2.1.3}$$

where the oscillation function in form of $z(x,y,t)$ to $z(r,\theta,t)$ is depicted in **Fig. 2.1.2**, r and θ are radial and angular coordinates reintroduced in cylindrical coordinates. We can find a solution of the transformed motion equation as

$$z(r, \theta, t) = \sum_m \sum_n a_{mn}(t) \psi_{mn}(r, \theta) \quad \text{Eq. 2.1.4}$$

where $a_{mn}(t)$ is the oscillating displacement of the membrane and $\psi_{mn}(r, \theta)$ is the mechanical mode shape controlled by r and θ coordinates. m and n are indices that will be defined later and related to the n_{th} positive root of the m_{th} order Bessel functions of the first kind.

Injecting Eq.2.1.4 into Eq.2.1.3 for each mode (m,n) can further be differentiated with separating time and spatial functions to be

$$\frac{1}{a_{m,n}} \frac{\partial^2 a_{mn}}{\partial t^2} = \frac{\sigma}{\rho} \frac{1}{\psi_{mn}} \nabla^2 \psi_{mn} \quad \text{Eq. 2.1.5}$$

Since the left member depends on time only and the right member on spatial term only, we find that

$$\frac{1}{a_{m,n}} \frac{\partial^2 a_{mn}}{\partial t^2} = cst. \quad \text{Eq. 2.1.6}$$

where this constant can be written as $-\omega_{mn}^2$, since it is homogeneous to a squared frequency and realistic physical solutions will be oscillating.

According to the one-dimensional oscillating motion, we describe the oscillating as

$$a_{mn}(t) = A_{mn} \cos(\omega_{mn}t) + B_{mn} \sin(\omega_{mn}t) \quad \text{Eq. 2.1.7}$$

where A_{mn} and B_{mn} are the prefactors of the oscillating magnitude, ω_{mn} is the angular resonance frequency corresponding to the mechanical mode.

To solve the equation of motion Eq. 2.1.5, we look for a solution of mechanical mode of the membrane in formalism of

$$\psi_{mn}(r, \theta) = \mathfrak{R}(r)\theta(\theta) \quad \text{Eq. 2.1.8}$$

We noticed an extended product of $\mathfrak{R}(r)$ and $\theta(\theta)$. Eq. 2.1.6 can be written as

$$\frac{\partial^2 a_{mn}}{\partial t^2} + \omega_{mn}^2 a_{mn} = 0 \quad \text{Eq. 2.1.9}$$

Putting back Eq. 2.1.8 and Eq. 2.1.9 into Eq. 2.1.5, we can separate functions $\mathfrak{R}(r)$ and $\theta(\theta)$ and Eq.2.1.5 can be derived to be

$$\theta \frac{1}{r} \frac{\partial}{\partial r} \left(r \frac{\partial \mathfrak{R}}{\partial r} \right) + \frac{\mathfrak{R}}{r^2} \frac{\partial^2 \theta}{\partial \theta^2} + \frac{\rho}{\sigma} \omega_{mn}^2 \mathfrak{R} \theta = 0 \quad \text{Eq. 2.1.10}$$

Therefore, using Eq. 2.1.10 describes the motion of the circular membrane since the left two members depending on r and the right member on the angle θ only. Usually, circular membranes satisfy two boundary conditions. When the circular membrane is defined with a radius of a in experiments, one of boundaries as $\psi_{mn}(a, \theta) = 0$ must be obeyed due to the clamping edge. To ensure $\psi_{mn}(r, \theta)$ in the cylindrical coordinate system as a single value, another well-known boundary condition is $\psi_{mn}(r, \theta) = \psi_{mn}(r, \theta + 2m\pi)$ where it follows $m \in \mathbb{Z}$. By separating functions $\mathfrak{R}(r)$ and $\theta(\theta)$, Eq. 2.1.10 can be rewritten as

$$\frac{1}{r} \frac{\partial}{\partial r} \left(r \frac{\partial \mathfrak{R}}{\partial r} \right) + \frac{\rho}{\sigma} \omega_{mn}^2 \mathfrak{R} = -\frac{1}{\theta} \frac{\mathfrak{R}}{r^2} \frac{\partial^2 \theta}{\partial \theta^2} \quad \text{Eq. 2.1.10a}$$

Since the left member depends on r only and the right member on the angle θ only, we deduce that both terms are constant and we can write $-\frac{1}{\theta} \frac{\partial^2 \theta}{\partial \theta^2} = m^2$. Eq. 2.1.10a can be related to the definition of Bessel function and we look for a possible solution for $\mathfrak{R}(r)$ in form of

$$\mathfrak{R}(r) = J_m \left(\frac{\alpha_{mn} r}{a} \right) \quad \text{Eq. 2.1.11}$$

where J_m is Bessel function of the first kind and α_{mn} is the n th positive root of the Bessel function for the m th order of the first kind to fulfil the boundary condition: $\mathfrak{R}(a) = J_m(\alpha_{mn}) = 0$. From Eq. 2.1.10a, we can also deduce that

$$\theta(\theta) = \cos(m\theta) \quad \text{Eq. 2.1.12}$$

Noting that the boundary condition $\psi_{mn}(a, \theta) = 0$ implies that $\theta(\theta)$ has sine or cosine function formalisms. In fact, all solutions will be in $\cos(m\theta + \phi)$ but we can consider the particular case $\phi = 0$ by choosing θ conveniently.

We subsequently investigate the mechanical mode function of the circular membrane to become [103]

$$\psi_{mn}(r, \theta) = \cos(m\theta) J_m\left(\frac{\alpha_{mn}r}{a}\right) \quad \text{Eq. 2.1.13}$$

According to Eq. 2.1.7 and Eq. 2.1.13, we take the mechanical motion of the circular membrane to be

$$z(r, \theta, t) = \sum_m \sum_n C_{mn} \cos(\omega_{mn}t) \cos(m\theta) J_m\left(\frac{\alpha_{mn}r}{a}\right) \quad \text{Eq. 2.1.14}$$

where C_{mn} is the prefactor of the oscillatory motion. Note that the time reference can be chosen so as to consider only the first term of Eq. 2.1.7.

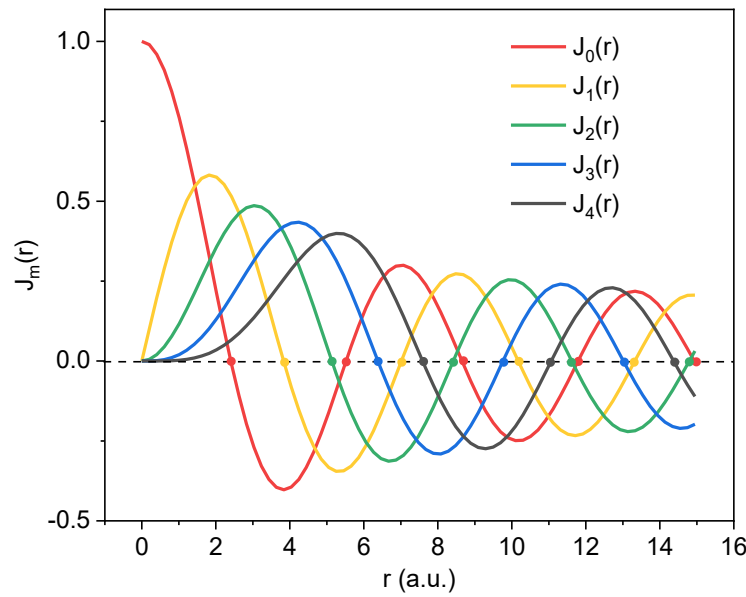


Figure 2.1.3. Plots of Bessel functions of m_{th} order of the first kind. The n_{th} zeros can be extracted in the curves intersected with $J_m(r) = 0, r > 0$.

Fig. 2.1.3 shows the mechanical motion modelled as the Bessel functions of the first kind. It gives n_{th} positive roots of the m_{th} order Bessel functions of the first kind, namely the value of α_{mn} .

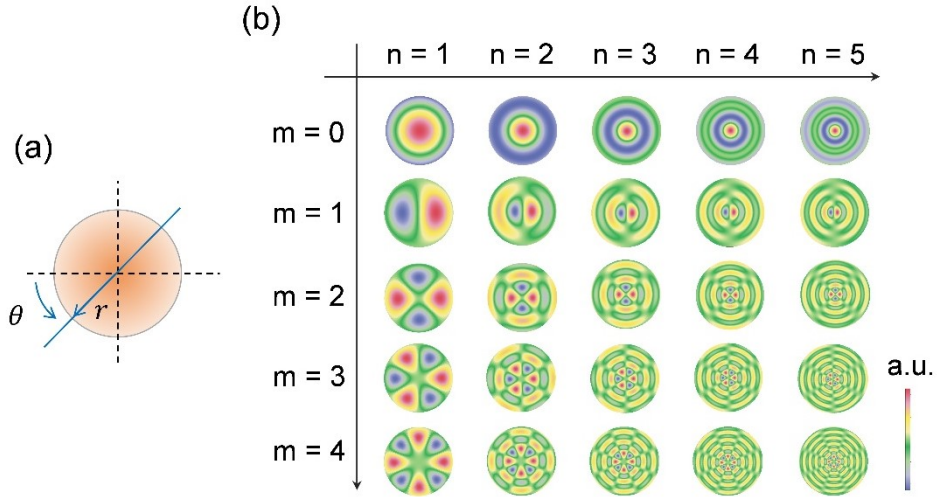


Figure 2.1.4. Simulations. (a) Top view of the oscillatory motion of a circular membrane (light red), in which the grey line is the clamped edge. (b) Mechanical mode shapes for first 25 modes of the circular membrane, derived from the oscillatory motion function Eq.2.1.14. The colour bar is arbitrary amplitude.

Table 2.1.1 α_{mn} values of the n_{th} zeros for the m_{th} order Bessel functions of the first kind, taken from Fig. 2.1.4. The first 25 mechanical modes here are shown.

Table 2.1.1. Analytical values of α_{mn} for each mechanical mode

| Mode (m,n) | n = 1 | n = 2 | n = 3 | n = 4 | n = 5 |
|------------|--------|---------|---------|---------|---------|
| m = 0 | 2.4048 | 5.5201 | 8.6537 | 11.7915 | 14.9309 |
| m = 1 | 3.8317 | 7.0156 | 10.1735 | 13.3237 | 16.4706 |
| m = 2 | 5.1356 | 8.4172 | 11.6198 | 14.7960 | 17.9598 |
| m = 3 | 6.3802 | 9.7610 | 13.0152 | 16.2235 | 19.4094 |
| m = 4 | 7.5883 | 11.0647 | 14.3725 | 17.6160 | 20.8269 |

In Eq. 2.1.14, oscillating motion function includes the oscillating function $\cos(\omega_{mn}t)$ and mode shape function $\cos(m\theta)J_m\left(\frac{\alpha_{mn}r}{a}\right)$. Fig. 2.1.4(a) shows a top view of the oscillating. Fig.2.1.4(b) shows simulations of circular membranes for the first 25 mechanical modes, which were analysed using cylindrical coordinate system based on Eq.2.1.14. According to the mode

shape patterns, they are able to affect the corresponding actuating forces. The higher mechanical modes are, the higher the driving forces we require, the more difficult to detect mechanical vibrations.

When order $m=0$, variations of the radial mode n indicate that the mechanical vibrations exhibit circularly symmetric amplitudes. If the index m to be $m > 0$, it will divide the circular membrane along azimuthal direction. For instance, when the azimuthal index $m = 1$, mechanical vibrations for modes $(1,n)$ can be observed in this case.

2.1.2 Resonance frequency of circular membranes

The resonance frequencies of the circular membrane are discussed. According to the rigorous equations solving in the above, a relationship between α_{mn} and angular frequency ω_{mn} is also introduced. The azimuthal portion of the membrane is described to be

$$\frac{\partial^2 \theta}{\partial \theta^2} + m^2 \theta = 0 \quad Eq. 2.1.15$$

which is already deduced in Eq.2.1.12, it is worth to note that using a m square here will be more convenient since m will be the index of the solution of ψ_{mn} . Then, Eq.2.1.10 can be written as

$$\frac{1}{r} \frac{\partial \mathfrak{R}}{\partial r} + \frac{\partial^2 \mathfrak{R}}{\partial r^2} + \frac{1}{r^2} (-m^2) \mathfrak{R} + \frac{\rho}{\sigma} \omega_{mn}^2 \mathfrak{R} = 0 \quad Eq. 2.1.16$$

Furthermore, this Eq.2.1.16 is reorganized as

$$r^2 \frac{\partial^2 \mathfrak{R}}{\partial r^2} + r \frac{\partial \mathfrak{R}}{\partial r} + \left(\frac{\rho}{\sigma} \omega_{mn}^2 r^2 - m^2 \right) \mathfrak{R} = 0 \quad Eq. 2.1.17$$

Then, a standard Bessel function can be derived from Eq. 2.1.17 unless the third term equal to 0. Here, m as m_{th} order Bessel function to obtain α_{mn} is defined. Using Eq.2.1.11, we must have $\left(\frac{\alpha_{mn} r}{a} \right)^2 = \frac{\rho}{\sigma} \omega_{mn}^2 r^2$ that is given by

$$\frac{\rho}{\sigma} \omega_{mn}^2 a^2 - \alpha_{mn}^2 = 0 \quad Eq. 2.1.18$$

Each angular frequency corresponding to different modes can be given to be

$$\omega_{mn} = \sqrt{\frac{\sigma}{\rho} \frac{\alpha_{mn}}{a}} \quad Eq. 2.1.19$$

where ω_{mn} is the angular frequency corresponding to each mode, σ is the tensile stress, ρ is the effective mass density.

Table 2.1.2 Values of f_{mn}/f_{01} ratio calculated from **Table 2.1.1**, for each mechanical mode with the factor α_{mn} . The resonance frequency f_{01} is referred to a fundamental mechanical mode (0,1).

Table 2.1.2. Analytical values of $\frac{f_{mn}}{f_{01}} = \alpha_{mn} / \alpha_{01}$ ratio for each mechanical mode

| Mode (m,n) | n = 1 | n = 2 | n = 3 | n = 4 | n = 5 |
|------------|--------|--------|--------|--------|--------|
| m = 0 | 1 | 2.2954 | 3.5985 | 4.9033 | 6.2087 |
| m = 1 | 1.5933 | 2.9173 | 4.2304 | 5.5404 | 6.8490 |
| m = 2 | 2.1355 | 3.5001 | 4.8319 | 6.1526 | 7.4683 |
| m = 3 | 2.6531 | 4.0589 | 5.4121 | 6.7462 | 8.0711 |
| m = 4 | 3.1554 | 4.6010 | 5.9765 | 7.3253 | 8.6605 |

In the next section 2.3, experimental measurements of a SiN circular membrane with tensile stress of 1.0 GPa, effective mass density of 3084 kg/m³, and a membrane diameter of 30 μm will be analysed. Using our experimental settings, we calculate Eq.2.1.19 to predict the ratio of resonance frequency for each mechanical mode.

Table 2.1.2 shows f_{mn}/f_{01} resonance frequency ratios corresponding to mechanical modes. It is obvious that the value of the ratio follows the ratio of the solution for the Bessel function of the first kind. It brings convenience for verifying the resonance frequency of one mechanical mode. As far as the table shows, the measured resonance frequency $f_{01} \sim 11.83$ MHz for the mode (0,1) on a 30 μm diameter membrane is much smaller than the calculated result 21.79MHz if we assume a tensile stress of 1.0 GPa. Actually, 11.83 MHz corresponds to a tensile stress of about 294.6 MPa. The measured tensile stress is by 70 % lower than the defined value of about 1.0 GPa assumed from the sample data sheet. For this case, there are several possible reasons: first, the nanoscale holes ~ 300 nm pattern that forms on the circular membrane causes the tensile stress changing of the biaxial stress mode [36]. Second, the release process also reduces the tensile stress of the membrane, greatly decreasing the resonance frequency. Third, the etch step also creates a realistic undercut, which increases the defined membrane's diameter from 30 to 32 μm. This can increase effective masses and reduce the wanted resonance frequency. In fact, for our measurements, the measured resonance frequencies of the resonator were truly far lower than theoretical calculation results.

2.1.3 Effective mass of circular membranes

The calculation of the effective mass allows to simplify motion equation into a second order differential equation. Despite the calculations of the effective mass performed in [105,107–109], in our case, the effective mass of the circular membrane is still important and its calculation is critical.

The equipartition theorem is chosen to define the effective mass of the circular membrane. A circular membrane that is infinitely decomposed into small volume elements is analysed in the following. To describe the membrane as a damped harmonic oscillator model, a correction term referred to the effective mass is introduced [105]. An uncorrected amplitude of the circular membrane is also introduced, demonstrating truly its physical displacement at any arbitrary position. In this case, the circular membrane with a resonance frequency ω_{mn} is thought of the mechanical mode (m,n), which has been infinite small elements of volume dV at a position (x, y) . As previous literature reports [105], the potential energy of such small volume element dV corresponding to each mass element $dm = \rho(x, y)dV$, where $\rho(x, y)$ is a position-dependent density. Here, such density is a constant ρ_0 due to the membrane uniformity. The kinetic energy for each small volume element of the circular membrane can be given by

$$dU(x, y, t) = \frac{1}{2} \rho_0 \omega_{mn}^2 |z(x, y, t)|^2 dV \quad Eq. 2.1.20$$

where $z(x, y, t) = a_{mn}(t)\psi_{mn}(x, y, t)$ is the oscillatory motion as shown in **Fig. 2.1.1**.

Then Cartesian coordinate system can be transformed to cylindrical coordinate system as shown in **Fig. 2.1.2** by exploiting $x = r \cos \theta$ and $y = r \sin \theta$. In this below, the theory derivations are based on cylindrical coordinate system.

So, the potential energy occupied in each small volume element becomes

$$dU(r, \theta, t) = \frac{1}{2} \rho_0 \omega_{mn}^2 |z(r, \theta, t)|^2 dV \quad Eq. 2.1.21$$

To figure out the total kinetic energy, we integrated over the entire structure of the circular membrane. The integrated formulism further is given by

$$U_{tot}(t) = \frac{1}{2} \omega_{mn}^2 |a_{mn}(t)|^2 \iiint \rho_0 |\psi_{mn}(r, \theta)|^2 dV \quad Eq. 2.1.22$$

The kinetic energy of the full membrane is taken equal to the kinetic of an equivalent local mass at position (r_0, θ_0) , it can be

$$\begin{aligned} \frac{1}{2} \omega_{mn}^2 |a_{mn}(t)|^2 \iiint \rho_0 |\psi_{mn}(r, \theta)|^2 dV \\ = \frac{1}{2} \omega_{mn}^2 |a_{mn}(t)|^2 m_{eff,m,n} |\psi_{mn}(r_0, \theta_0)|^2 \quad Eq. 2.1.23 \end{aligned}$$

Then, the definition of the effective mass can be given by

$$m_{eff,mn}^{nor}(r_0, \theta_0) = \iiint \rho_0 \left| \frac{\psi_{mn}(r, \theta)}{\psi_{mn}(r_0, \theta_0)} \right|^2 dV \quad Eq. 2.1.24$$

where $dV = h dS$ and $\rho_0 h = \rho_s$ is the surface mass density.

If a general $\psi_{mn}(r_0, \theta_0)$ is not at the exact maximum position, it induces a larger position-dependent effective mass. If measuring the mechanical mode (0,1), we simply achieve the maximum amplitude at its centre position (0,0) of the circular membrane, enabling the smallest effective mass. To simplify the expression of effective mass, infinite small volume elements with a uniform thickness h of the circular membrane are regarded. The effective mass further can be recast as

$$m_{eff,mn}^{nor}(r_0, \theta_0) = \rho_0 h \int_0^{2\pi} d\theta \int_0^a |u_{mn}(r, \theta)|^2 r dr \quad Eq. 2.1.25$$

where $u_{mn}(r, \theta) = \psi_{mn}(r, \theta) / \psi_{mn}(r_0, \theta_0)$ is a normalized mode shape of the circular membrane.

From Eq. 2.1.25, we can deduce the ratio between the effective mass and total mass, $M = \rho_0 h \pi a^2$, of the membrane to be

$$\frac{m_{eff,mn}^{nor}(r_0, \theta_0)}{M} = \frac{1}{\pi a^2} \int_0^{2\pi} d\theta \int_0^a \left| \frac{\psi_{mn}(r, \theta)}{\psi_{mn}(r_0, \theta_0)} \right|^2 r dr \quad Eq. 2.1.26$$

Using this ratio, we can discuss the mechanical mode of the circular membrane. In subsection 2.1.2, Bessel functions for the m th order have been discussed with two different conditions: when $m=0$ relating to the boundary condition $J_m(\alpha_{mn}) = 0$, we reach a simple solution because of obvious the maximum amplitude at membrane's centre; when discussing $m>0$, we introduce an argument for examining where the maximum amplitude of $\psi_{mn}(r_0, 2\pi) = J_m\left(\frac{\alpha_{mn} r_0}{a}\right)$ is. We

define η_{max} as the argument for determining the maximum amplitude and forming the justification $J_m(\eta)$. Here, the determination can be given by [103,105]

$$\frac{dJ_m(\eta)}{d\eta} = \frac{1}{2} [J_{m-1}(\eta) - J_{m+1}(\eta)] = 0 \quad Eq. 2.1.27$$

which means the extrema of $J_m(\eta)$ can be determined by searching for $J_{m-1}(\eta) = J_{m+1}(\eta)$. By using this justification, η_{max} will be found analytically.

We thus provide the ratios ($m_{eff,mn}/M$) of the effective mass of the circular membrane to be

$$\frac{m_{eff,mn}^{nor}(r_0, \theta_0)}{M} = \begin{cases} [J_1(\alpha_{0n})]^2 & \text{if } m = 0 \\ \frac{K_m^2}{2} [J_{m+1}(\alpha_{mn})]^2 & \text{if } m > 0 \end{cases} \quad Eq. 2.1.28$$

where $K_m = 1/\psi_{mn}(r_0, \theta_0) = 1/J_m(\eta_{max})$ are the normalization constants of ψ_{mn} .

Table 2.1.3 Values of $m_{eff,mn}/m$ ratio calculated from **Table 2.1.1** for each mechanical mode with each factor α_{mn} .

Table 2.1.3. Analytical values of $m_{eff,mn}/M$ ratio for each mechanical mode

| Mode (m,n) | n = 1 | n = 2 | n = 3 | n = 4 | n = 5 |
|------------|--------|--------|--------|--------|--------|
| m = 0 | 0.2695 | 0.1158 | 0.0737 | 0.0540 | 0.0427 |
| m = 1 | 0.2396 | 0.1330 | 0.0921 | 0.0704 | 0.0570 |
| m = 2 | 0.2437 | 0.1556 | 0.1141 | 0.0901 | 0.0744 |
| m = 3 | 0.2357 | 0.1648 | 0.1262 | 0.1022 | 0.0859 |
| m = 4 | 0.2255 | 0.1683 | 0.1333 | 0.1102 | 0.0939 |

Above all, a circular membrane with the effective mass is analysed to predict the device frequency performance. These calculation results clearly demonstrate that the values of effective masses of mechanical resonator depend on the mode shapes. **Table 2.1.3** shows if the azimuthal index m does not change, the values of the effective mass ratio decrease with increasing the radial index n . In this overall thesis work, for simplicity, the effective mass $m_{eff} = m_{eff,mn}^{nor}(r_0, \theta_0)$ corresponding to each mode has been renamed as m_{eff} . That means

the ratio relevant to each mode (m,n) has been considered, namely $m_{eff} = m_{eff,mn}^{nor}(r_0, \theta_0) = \frac{m_{eff,mn}^{nor}(r_0, \theta_0)}{M} \cdot M$, where $\frac{m_{eff,mn}^{nor}(r_0, \theta_0)}{M}$ is the effective mass ratio and M is the total mass of the membrane.

2.1.4 Summary

The theory method that includes motion equation of free motion and its simplification has been introduced and analysed by considering circular membranes. To solve it, we separate the r, θ, t variables from the motion equation in order to achieve physical functions for motion oscillation and mechanical mode shape. Through exploiting boundary conditions, the solution of motion equation of free motion has been done. By using this solution, there are three interesting and important mechanical parameters discussed, they are mechanical mode, resonance frequency and the ratio of effective mass of the circular membrane. According to these derived calculation expressions, they are helpful for us to verify whether a mechanical mode can reach, which is usually comparable to the measured frequency. Finally, the ratio of effective mass is calculated referring to as which mechanical modes preferable. It also correlates to mechanical mode and its resonance frequency.

2.2 Nanoelectromechanics in a capacitive driving scheme

In this part, motion equations of nanoelectromechanical resonator are analysed in the capacitively driving scheme. Then, parametric pumping scheme, having non-degenerate and degenerate cases, are analysed. Duffing nonlinearity is also analysed. Thereafter, double-tone driving scheme, an analogy to optomechanical system, is analytically modelled and analysed in the nanoelectromechanical system, consisting of SiN membrane capacitively coupled to aluminium suspended top gate drum.

The displacement calculated here will be one of an extended nanomechanical resonator of effective mass ($m_{eff} = m_{eff,mn}^{nor}(r_0, \theta_0)$) given by Eq.2.1.25. Similar to the effective mass calculation, the externally force $F(t)$ applied to the local mass can be deduced from the potential energy E obtained by integrating the energy of the local load over a small volume and then using $F = -\partial E/\partial x$ at the position (r_0, θ_0) .

2.2.1 Motion equation of nanoelectromechanical resonator driving through a capacitively coupling scheme

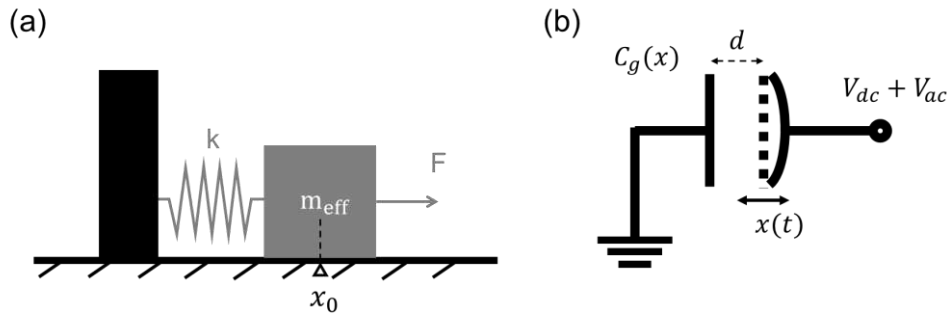


Figure 2.2.1.1. (a) Schematic of an object, attached with a spring with spring constant k and effective mass m_{eff} , driven by an external force F . (b) A mechanical resonator, consisting of parallel plates, in which one is a fixed plate and the other one is a mechanical movable element[110], which is electrostatically excited by a mixing voltage $V_{dc} + V_{ac}$.

Here, a harmonic oscillator system is taken into accounts as shown in **Fig. 2.2.1.1(a)**. It consists of an object, with mass m_{eff} , which is attached to a spring and driven by an externally applied force $F(t)$. Besides, we also add the damping force generated by a friction force, namely $-m_{eff}\gamma_m\dot{x}$, where γ_m is the damping rate of the system. According to Newton's laws, the motion equation of this object is given by

$$m_{eff}\ddot{x} + m_{eff}\gamma_m\dot{x} = F - kx \quad Eq. 2.2.1.1$$

where x is the mechanical displacement of the object and k is the spring constant. Now, we extend this harmonic oscillator system to a capacitively coupled electromechanical resonator shown in the **Fig. 2.2.1.1(b)**. By adding V_{dc} and V_{ac} voltages, electrostatic forces can be generated to excite the movable element. The electrostatic force ($F = -\partial E/\partial x$) can be derived through the energy ($E = C_g(x)V^2/2$) that is stored in the capacitance. Here, V is the applied voltage, including DC voltage V_{dc} and AC voltage $V_{ac} \cos(\omega_d t)$ driving at a frequency ω_d , namely $V = V_{dc} + V_{ac} \cos(\omega_d t)$. The $C_g(x)$ is the effective coupling capacitance between the mechanical element and its gate, namely $C_g(x) = \epsilon S/(d + x)$. Here, ϵ is dielectric constant, S is the actuation area of mechanical resonator, d is the initial distance between mechanical element and its coupled gate. The capacitance $C_g(x)$ can be rewritten in the form of Eq.2.2.1.2 by using Taylor expansion due to $\frac{x}{d} \ll 1$, with an initial definition of $C_{g0} = \epsilon S/d$. To further understand the electrostatic driving, we extend the V^2 to the series of the voltage as shown in Eq.2.2.1.3.

$$C_g(x) = C_{g0} \left(1 - \frac{x}{d} + \frac{x^2}{d^2} - \dots \right) \quad Eq. 2.2.1.2$$

$$V^2 = V_{dc}^2 + 2V_{dc}V_{ac} \cos(\omega_d t) + V_{ac}^2 \cos^2(\omega_d t) \quad Eq. 2.2.1.3$$

For the first term, V_{dc}^2 contributes to tuning a resonance frequency of the mechanical resonator and it is an independent term of time variable; For the second term, $V_{dc}V_{ac} \cos(\omega_d t)$ is a common use to excite mechanical resonator oscillating in real experiments when V_{dc} is set to be far more than the V_{ac} in the measurement settings; For the third term, $V_{ac}^2 \cos^2(\omega_d t)$ can also be exploited by choosing $\omega_d \sim \Omega_m/2$ or $\omega_d \sim \Omega_m$ for performing parametric pumping as can be seen in section 2.2.2.

Mechanical response by an external force with frequency $\sim \Omega_m$. Based on resonance frequency modulation for the mechanical resonator, we prefer to find a desirable resonance frequency to do several experiments of interests. It enables the improvement of mechanical responses. In this case, we discuss the second and third terms $2V_{dc}V_{ac} \cos(\omega_d t)$ and $V_{ac}^2 \cos^2(\omega_d t)$ with an oscillating frequency of $\sim \Omega_m$ to drive the mechanical resonator. Because the one oscillating frequency is two times than the other, the two mechanical

response magnitudes are competing with each other. In order to describe the driving force $F(t) = \partial(C_g(x)V^2/2)/\partial x$, we substitute the Eq.2.2.1.3 to it and derive the Eq.2.2.1.4. When taking into account the second drive term $V_{dc}V_{ac} \cos(\omega_d t)$, we find a solution in form of the displacement $x = \frac{\mu_x}{2} e^{-i\omega_d t} + c.c$ to solve the motion equation Eq.2.2.1.1, where the μ_x is the mechanical amplitude.

$$F(t) \approx \frac{C_{g0}}{2d} \left(V_{dc}^2 + 2V_{dc}V_{ac} \cos(\omega_d t) + V_{ac}^2 \cos^2(\omega_d t) \right) \quad Eq. 2.2.1.4$$

So, we look for a solution by the second term force $C_{g0}V_{dc}V_{ac} \cos(\omega_d t)/d$ driving mechanical resonator. Then, we obtain a mechanical amplitude μ_x and the phase φ_x as presented

$$\mu_x(\omega_d) = \frac{C_{g0}V_{dc}V_{ac}}{m_{eff}d} \frac{1}{\Omega_m^2 - \omega_d^2 - i\omega_d\gamma_m} \quad Eq. 2.2.1.5$$

$$\varphi_x(\omega_d) = \tan^{-1} \left(\frac{Im[\mu_x(\omega_d)]}{Re[\mu_x(\omega_d)]} \right) \quad Eq. 2.2.1.6$$

where ω_d is the driving frequency, m_{eff} is the effective mass of mechanical resonator and γ_m is the damping rate of mechanical resonator and $\Omega_m = \sqrt{k/m_{eff}}$ is the resonance frequency. It is worth noting that the mechanical resonator has an approximate amplitude maximum when driving frequency $\omega_d \approx \Omega_m$.

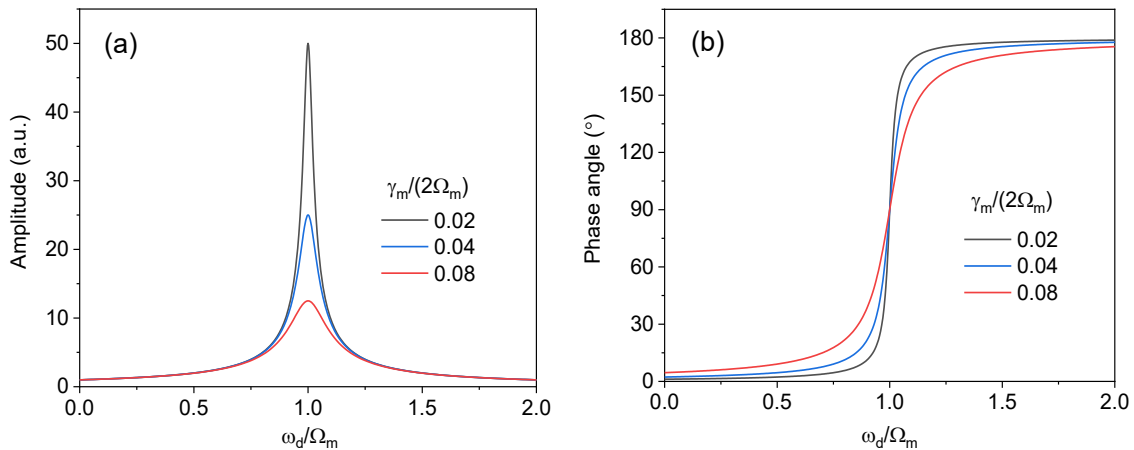


Figure 2.2.1.2. Plots of amplitude (a) and phase angle (b) as function of the ratio of excitation frequency to the resonance frequency ω_d/Ω_m , for different damping ratio $\gamma_m/(2\Omega_m)$. The prefactor of amplitude, namely $\frac{F}{2m_{eff}\Omega_m^2} = \frac{C_{g0}V_{dc}V_{ac}}{2m_{eff}\Omega_m^2d}$ is defined to be 1 in order to see the changing trends of the amplitude and phase. Resonance frequency value is also arbitrary.

From the **Fig. 2.2.1.2(a)**, we see that the amplitude of mechanical resonator increased as the ratio $\gamma_m/(2\Omega_m)$ decreases. That means the magnitude of amplitude depending on the damping control. In fact, **Fig. 2.2.1.2(b)** shows the corresponding phase angle transition range 180° no matter how the damping level is. With the ratio $\gamma_m/(2\Omega_m)$ reducing, the transition tilt is going sharp; otherwise, it turns out to be smooth. It indicates the damping plays an important role in controlling the mechanical amplitude corresponding to these phase shifts.

Modulation of resonance frequency by using DC voltages. Once a certain DC voltage actuating the movable part, it is able to be displaced from the initial equilibrium position because of the elastic properties subject to a basis of Hooke's law. After absorbing the DC voltage driving energy, the contribution of DC voltage-induced spring constant δk_{dc} to the displacement is to be rewritten with the intrinsic spring constant of the membrane. Hereafter, the motion equation Eq.2.2.1.1 can be transformed to Eq.2.2.1.7 by adding a DC voltage-induced spring constant variation δk_{dc} [111].

$$m_{eff}\ddot{x} + m_{eff}\gamma_m\dot{x} = F(t) - (k + \delta k_{dc})x \quad Eq. 2.2.1.7$$

where a driving force $F(t)$ depending on time variable is indicated.

We begin by analysing on how the additional spring constant δk_{dc} works in this simple mechanical system. When a certain DC voltage is acted onto the membrane, the energy ($E_{dc} = C_g(x)V_{dc}^2/2$) stored in this coupled capacitor can be changed leading to the relevant electrostatic force ($\delta F_{dc} = -\partial E_{dc}/\partial x$) changed and given by Eq.2.2.1.8. Notably, the negative symbol indicates force direction, here it is attractive force.

$$\delta F_{dc} \approx -\frac{V_{dc}^2}{2} \frac{\partial C_g(x)}{\partial x} \Big|_{x=\delta x} \quad Eq. 2.2.1.8$$

Furthermore, the additional spring constant dependent of the electrostatic force controlled by DC voltages can be rewritten as

$$\delta k_{dc} \approx -\frac{V_{dc}^2}{2} \frac{\partial^2 C_g(x)}{\partial x^2} \Big|_{x=\delta x} \quad Eq. 2.2.1.9$$

Based on the frequency modulation dependent of the spring constants as shown in Eq.2.2.1.10, we can find the modulation relationship between resonant frequency and spring constant variation induced by DC voltages.

$$\Omega_m = \sqrt{\frac{k + \delta k_{dc}}{m_{eff}}} = \Omega_{01} \sqrt{1 + \frac{\delta k_{dc}}{k}} \quad Eq. 2.2.1.10$$

Combining Eq.2.2.1.9 with Eq.2.2.1.10, Taylor expansion series depicted in Eq.2.2.1.2 can be truncated in second-order to achieve

$$\Omega_m \approx \Omega_{01} \left(1 - \frac{C_{g0} V_{dc}^2}{2kd^2} \right) \quad Eq. 2.2.1.11$$

where Ω_m is the resonance frequency of mechanical resonator, $\Omega_{01} = \sqrt{k/m_{eff}}$ is the fundamental resonance frequency of mechanical resonator, k is the intrinsic spring constant and d is the initial distance of the two plates.

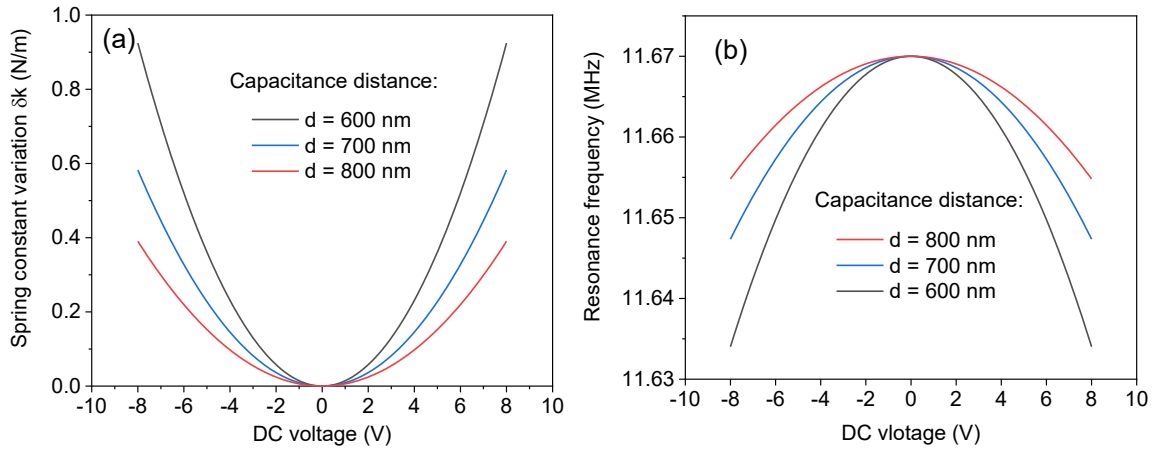


Figure 2.2.1.3. Plots of spring constant variation (a) and resonance frequency (b) as function of DC voltages, due to different capacitance distances. Here, 100 nm thick SiN drum membrane with tensile stress of 1.0 GPa is fixed to be 30 μm in diameter, the fundamental frequency and spring constant are achieved to be 11.67 MHz and 300 N/m.

Fig. 2.2.1.3(a) shows the modulation of spring constant is performed larger as the distance reduces. This indicates the spring variation of membrane can be induced by electrostatic forces. The electrostatic force is tuned by the capacitance because of the distance changing. **Fig. 2.2.1.3(b)** shows the resonance frequency tuned larger with the distance decreasing. This is consistent with the spring constant variation induced by electrostatic force. The modulation of resonance frequency for the mechanical resonator is proportional to V_{dc}^2 , which means Ω_m as a quadratic function of V_{dc} . It is worth noticing that $V_{dc} \gg |V_{ac}|$ is supposed to be the measurement condition. The other terms $2V_{dc}V_{ac} \cos(\omega_d t)$ and $V_{ac}^2 \cos^2(\omega_d t)$ in the

expression Eq.2.2.1.3 allow to perform experiments with an oscillating force at a driving frequency of $\omega_d \approx \Omega_m$ or $\Omega_m/2$, for different purposes as can be seen in section 2.2.2.

2.2.2 Mechanical parametric pumping

Parametric amplifications have been investigated in a variety of domains, such as optics, electronics, and mechanics [111–113]. Parametric pumping plays very important role in electronics. The basic principle is to use one signal (so called pump) to modulate one of the parameters in the system in order to transfer the energy from the pump tone to the system.

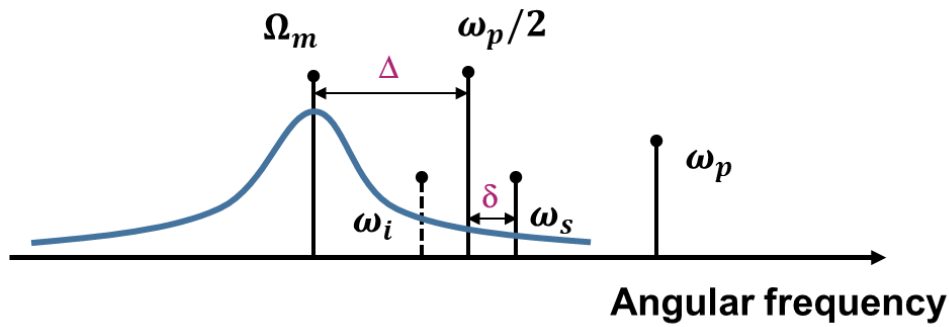


Figure 2.2.2.1. Operation spectrum landscape, for a general parametric pumping scheme

As shown in **Fig. 2.2.2.1**, a mechanical resonator with resonance frequency Ω_m is probed by a signal with frequency ω_s and is pumped by a signal with frequency ω_p . Here, Δ is the frequency difference between the half pump frequency and the mechanical resonance frequency, namely $\Delta = \omega_p/2 - \Omega_m$. δ is the frequency detuning between $\omega_p/2$ and ω_s , namely $\delta = \omega_s - \omega_p/2$. Based on these important definitions, we derive formalisms corresponding to two pumping schemes (i) non-degenerate case: $\omega_p \neq 2\omega_s$ and $\omega_p = \omega_s + \omega_i$. Note that ω_i is the frequency of idler signal, which is generated due to frequency mixing between the pump and the probe signal. (ii) degenerate case: $\omega_p = 2\omega_s$ with $\delta=0$, therefore, there is no idler term.

In this part, 100 nm thick SiN drum membrane with a tensile stress of 1.0 GPa and with a diameter of 30 μm is chosen for achieving resonance frequency around 11.1 MHz and the capacitive coupling distance is defined to be 500 nm for calculating a desired capacitance value $C_{g0}(d = 500 \text{ nm}, D = 30 \mu m) = 1.251 \times 10^{-14} F$.

2.2.2.1 Non-degenerate analytical calculation

According to operation spectrum landscape depicted in **Fig. 2.2.2.1**, a mechanical resonator with a parametric pump is described by a well-known equation of motion [36]

$$m_{eff}\ddot{x} + m_{eff}\gamma_m\dot{x} + (k + \delta k \sin(\omega_p t))x = F_d \quad Eq. 2.2.2.1$$

In order to find a form of solution while satisfying frequency relations $\omega_p = \omega_s + \omega_i$, we look for a displacement x in form of $\frac{\mu_s}{2}e^{-j\omega_s t} + \frac{\mu_i}{2}e^{-j\omega_i t} + c.c$ and write a drive force in a form of $F_d = \frac{f_d}{2}e^{-i\omega_s t} + c.c$. The modulation of spring constant, δk , is proportional to pump force f_p (see derivations in 2.2.1). It is worth to note that $\delta k \approx \frac{2C_{go}V_{ac}V_{dc}}{d^2}$ and $f_p \approx \frac{C_{go}V_{ac}V_{dc}}{d}$ are used here. The equation of motion thus can be transformed to be

$$m_{eff}\mu_s((\Omega_m^2 - \omega_s^2) - i\gamma_m\omega_s)e^{-i\omega_s t} + i\frac{\delta k}{2}\mu_i^*e^{-i(\omega_p - \omega_i)t} = f_d e^{-i\omega_s t} \quad Eq. 2.2.2.2(a)$$

$$m_{eff}\mu_i((\Omega_m^2 - \omega_i^2) - i\gamma_m\omega_i)e^{-i\omega_i t} + i\frac{\delta k}{2}\mu_s^*e^{-i(\omega_p - \omega_s)t} = 0 \quad Eq. 2.2.2.2(b)$$

Then, equations can be simplified to be

$$2m_{eff}\Omega_m\mu_s\chi_s^{-1}e^{-i\omega_s t} + i\frac{\delta k}{2}\mu_i^*e^{-i(\omega_p - \omega_i)t} = f_d e^{-i\omega_s t} \quad Eq. 2.2.2.3(a)$$

$$2m_{eff}\Omega_m\mu_i\chi_i^{-1}e^{-i\omega_i t} + i\frac{\delta k}{2}\mu_s^*e^{-i(\omega_p - \omega_s)t} = 0 \quad Eq. 2.2.2.3(b)$$

where two mechanical susceptibilities are defined as $\chi_s = \left(\Delta - \delta - \frac{i\gamma_m}{2}\right)^{-1}$ and $\chi_i = \left(\Delta + \delta - \frac{i\gamma_m}{2}\right)^{-1}$.

Amplitudes of the mechanical resonator, corresponding to μ_s and μ_i , arrive to be

$$|\mu_s(\Delta, \delta, \delta k)| = \left| \frac{2m_{eff}\Omega_m\chi_i^*f_d}{(2m_{eff}\Omega_m)^2\chi_s^{-1}\chi_i^{*-1} - \frac{\delta k^2}{4}} \right| \quad Eq. 2.2.2.4(a)$$

$$|\mu_i(\Delta, \delta, \delta k)| = \left| \frac{-\frac{\delta k}{2}f_d^*}{(2m_{eff}\Omega_m)^2\chi_s^{-1}\chi_i^{*-1} - \frac{\delta k^2}{4}} \right| \quad Eq. 2.2.2.4(b)$$

Furthermore, the associated mechanical gain can be obtained from the ratio of signal amplitudes corresponding to pump on and pump off, $\text{Sig}[\delta k \neq 0] / \text{Sig}[\delta k = 0]$ as shown in

$$G(\Delta, \delta, \delta k) = \frac{1}{\left| 1 - \frac{\delta k^2}{16(m_{eff}\Omega_m)^2\chi_s^{-1}\chi_i^{*-1}} \right|} \quad Eq. 2.2.2.5$$

In the following, we choose the same essential simulation parameters, including resonance frequency 11.1 MHz , damping rate 948.7 Hz , quality factor 11700 , and then start to analyse mechanical system with amplitude gain G as functions of several parameters, e.g., Δ , δ , and so on. These variable parameters are helpful to understand the critical condition in using parametric pumping.

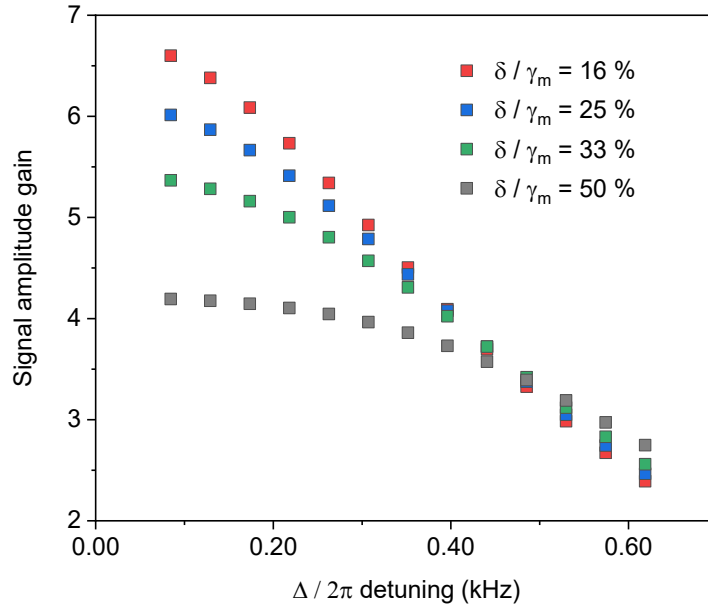


Figure 2.2.2.2. Calculations of non-degenerate condition of signal amplitude gain vs. $\Delta = \frac{\omega_p}{2} - \Omega_m$, corresponding to different ratios of δ/γ_m . In these calculations, pumping force (f_p) and mechanical damping rate γ_m were kept as constants. Note that the pump force is $f_{p,sim}(V_{dc} = 8V, V_{acp} = 50 \text{ mV}, C_{g0} = 1.251 \times 10^{-14} \text{ F}) = 10 \text{ nN}$.

Fig. 2.2.2.2 shows signal amplitude gains as a function of Δ , corresponding to different values of δ . The G decreases with increasing Δ . It means that the pump will lose its efficiency in transferring energy to mechanical system, when $\frac{\omega_p}{2}$ is far from the resonance frequency Ω_m . In addition, when we decrease the frequency detuning δ , the larger signal amplitude gain was obtained. Therefore, for a fixed pumping force, an ideal pumping is to decrease both Δ and δ in order to obtain the large signal gain, G .

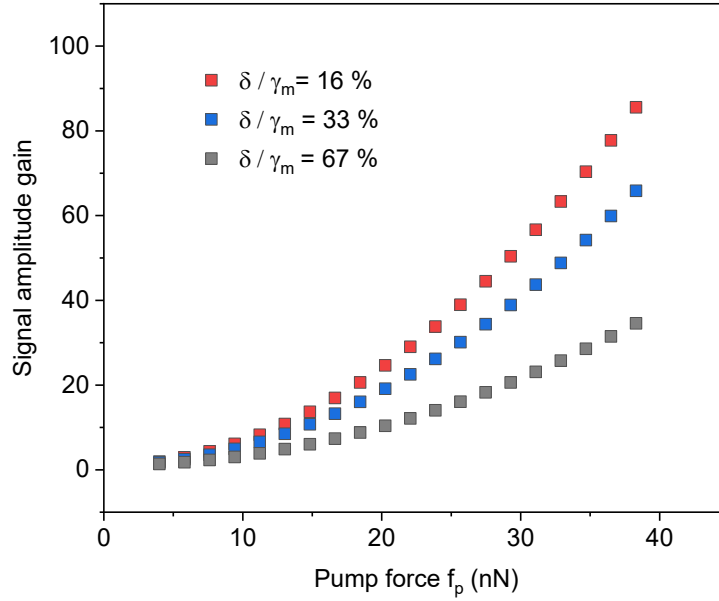


Figure 2.2.2.3. Calculations of non-degenerate condition of signal amplitude gain vs. pump force (f_p). Here γ_m is fixed as a constant and we set $\Delta = \omega_p/2 - \Omega_m = 0$.

Besides the frequency, we also should pay attention to the pump force (f_p), which defines modulation quantity of spring constant δk . **Fig. 2.2.2.3** shows signal amplitude gains can be enhanced with increasing the pump forces. It presents that the stronger pumping force gives the larger the modulation of spring constant, resulting in the larger signal amplitude gain. However, the pump force must not increase too much because the pump force will reach $1 - \frac{\delta k^2}{16(m_{eff}\Omega_m)^2 \chi_s^{-1} \chi_i^{*-1}} = 0$, in Eq. 2.2.2.5. At this condition, the mechanical system goes into auto-oscillation states.

2.2.2.2 Degenerate analytical calculation

Degenerate pumping scheme as a particular instance: $\delta=0$, it means the pump frequency is exactly two times of the signal frequency, namely $\omega_s = \frac{\omega_p}{2}$. Therefore, there is no generation of idle signal.

According to these analytics, we can look for a form of displacement x with $\frac{\mu_s}{2} e^{-i\omega_s t} + c.c.$ and write a drive force in a complex form, $F_d = \frac{f_d}{2} e^{-i\omega_s t} + c.c.$ Note that we introduce a pump

phase φ in the pump signal. We thus inject the derivatives related to this form into the motion equation. The motion equation becomes

$$m_{eff}\mu_s((\Omega_m^2 - \omega_s^2) - i\gamma_m\omega_s)e^{-i\omega_s t} + i\frac{\delta k}{2}\mu_s^*e^{-i[(\omega_p - \omega_s)t - \varphi]} = f_d e^{-i\omega_s t} \quad Eq. 2.2.2.6$$

Through an approximation $\Omega_m^2 - \omega_s^2 \approx 2\Omega_m(\Omega_m - \omega_s)$, we simplify this equation to be

$$2m_{eff}\Omega_m\mu_s\chi_s^{-1}e^{-i\omega_s t} + i\frac{\delta k}{2}\mu_s^*e^{-i[(\omega_p - \omega_s)t - \varphi]} = f_d e^{-i\omega_s t} \quad Eq. 2.2.2.7$$

Here, we consider the equation of motion using the degenerate condition and deduce the amplitude of the mechanical displacement x to be

$$|\mu_s(\Delta, \delta k, \varphi)| = f_d \left| \frac{\left[2m_{eff}\Omega_m\Delta + \frac{\delta k}{2}\sin(\varphi) \right] + i\left[\frac{k}{Q} - \frac{\delta k}{2}\cos(\varphi) \right]}{(2m_{eff}\Omega_m\Delta)^2 - \left[\left(\frac{\delta k}{2} \right)^2 - \left(\frac{k}{Q} \right)^2 \right]} \right| \quad Eq. 2.2.2.8$$

Furthermore, the associated mechanical gain can be derived again from the ratio of the signal amplitudes of the pump on to the pump off as

$$\begin{aligned} Gain(\Delta, \delta k, \varphi) &= \left| \frac{(2m_{eff}\Omega_m\Delta)^2 + \left(\frac{k}{Q} \right)^2}{(2m_{eff}\Omega_m\Delta)^2 - \left[\left(\frac{\delta k}{2} \right)^2 - \left(\frac{k}{Q} \right)^2 \right]} \right| \\ &\times \left| \frac{\left[2m_{eff}\Omega_m\Delta + \frac{\delta k}{2}\sin(\varphi) \right] + i\left[\frac{k}{Q} - \frac{\delta k}{2}\cos(\varphi) \right]}{2m_{eff}\Omega_m\Delta + i\frac{k}{Q}} \right| \quad Eq. 2.2.3.10 \end{aligned}$$

In particular, if $\Delta = 0$, the amplitude gain Eq.2.2.3.10 should be given by

$$Gain(\Delta = 0, \delta k, \varphi) = \left| \frac{1 - \left(\frac{Q\delta k}{2k} \right) \cos(\varphi) - i\left(\frac{Q\delta k}{2k} \right) \sin(\varphi)}{\left(\frac{Q\delta k}{2k} \right)^2 - 1} \right| \quad Eq. 2.2.3.11$$

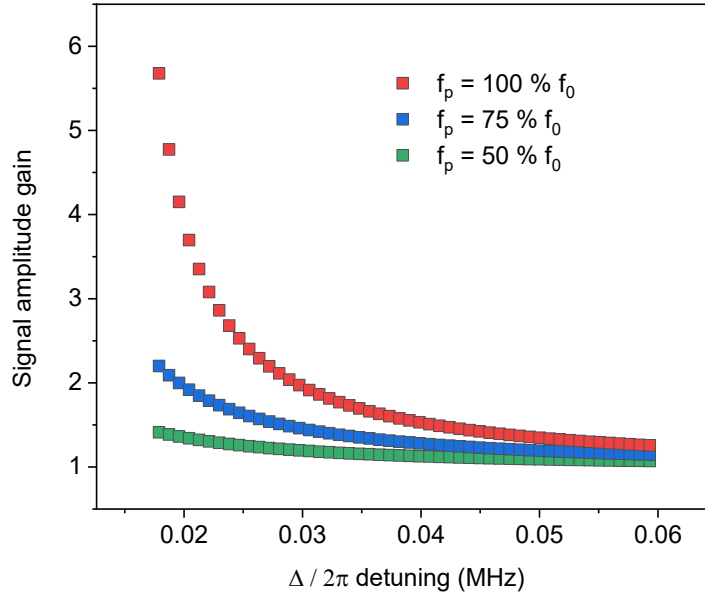


Figure 2.2.2.4. Calculations of signal amplitude gain vs. Δ detuning, for degenerate case. Here, signal amplitude gains are tuned through pumping force f_p , when the phase difference between pump and drive signal is given to be $\pi/2$.

To simplify the quantity of the pump force, we define a pump force $f_0 (V_{dc} = 8V, V_{acp} = 0.8V, C_{g0} = 1.251 \times 10^{-14}F) = 160 \text{ nN}$. Using the degenerate analytical results, we consider signal amplitude gains as a function of Δ detuning, as shown in **Fig. 2.2.2.4**. It shows that signal amplitude gain of the resonator increases with decreasing the frequency detuning $\Delta = \omega_p/2 - \Omega_m$. Likewise, the signal amplitude gains grow if the pump force ratio increases. It exhibits the same tendency with non-degenerate case.

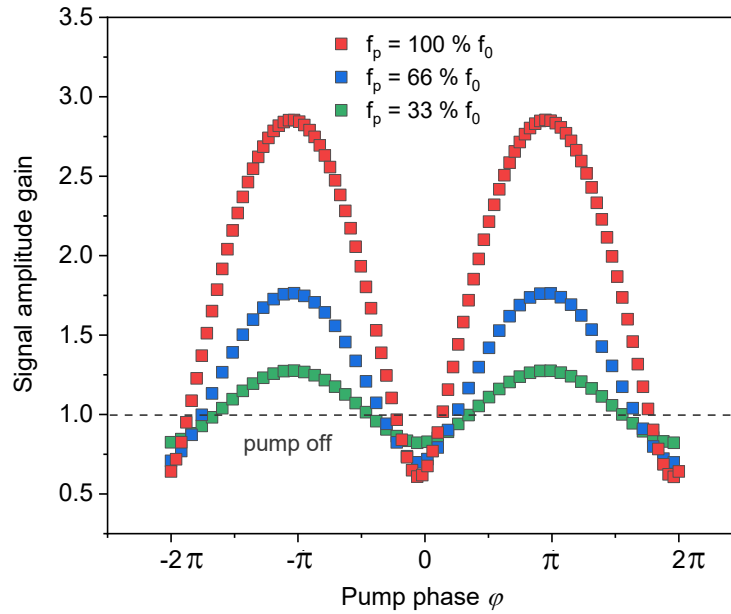


Figure 2.2.2.5. Calculations of signal amplitude gain vs. the phase difference between the pump and drive signal, in degenerate condition. These plots are calculated by taking $\Delta/\Omega_m = 0.002$. Note that a defined pump force $f_0 (V_{dc} = 8V, V_{ac} = 0.6V, C_{g0} = 1.251 \times 10^{-14}F) = 120 \text{ nN}$.

Compared to the non-degenerate pumping scheme, the degenerate pumping scheme gives an interesting feature that signal gain relies on the pump phase, φ . **Fig. 2.2.2.5** shows signal amplitude gains periodically modified by rotating the phase about 2π , corresponding to different pumping forces. It is worth to note that the dashed line has been remarked to represent the gain about 1. Obviously, in degenerate case, we can achieve in amplification and de-amplification of an input signal through manipulating the pump phase (also for noise).

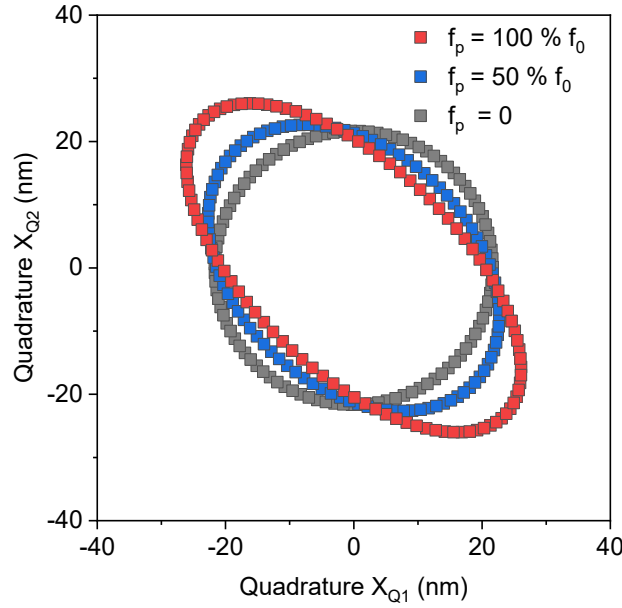


Figure 2.2.2.6. Calculation results of two-quadrature X_{Q1} and X_{Q2} , in the degenerate case. The parametric plots are plotted by the rotating phase frame $(0, 2\pi)$. Here, these plots are calculated by fixing $\Delta/\Omega_m = 0.01$, a defined pump force is $f_0(V_{dc} = 8V, V_{ac} = 1.6V, C_{g0} = 1.251 \times 10^{-14}F) = 320 \text{ nN}$.

Fig. 2.2.2.6 shows parametric plots of both quadratures related to the formalism of $x(t) = X_{Q1}(t) \cos(\Omega_m t) + X_{Q2}(t) \sin(\Omega_m t)$ in a rotating frame. When the pumping force increases, the larger compressed quadrature ellipses have been achieved, which are different from the one without the pumping force (as shown in **Fig. 2.2.2.6**, the special case $f_p = 0$). Degenerate pumping gives more flexibility that we could exploit it to amplify one of the quadrature and de-amplify the other one through controlling the phase.

2.2.2.3 Summary

We have discussed parametric pumping scheme in an electromechanical resonator, based on (i) non-degenerate pumping scheme: $\omega_p = \omega_s + \omega_i$, $\omega_p/2 = \omega_s + \delta$, where there is a idler frequency that is generated due to frequency mixing between the pump and the probe signal and (ii) degenerate pumping scheme: $\omega_p = 2\omega_s$, where this case does not present a idler. In general, the non-degenerate case leads electromechanical system to achieving amplification used for mechanical amplifier applications; on the other hand, the degenerate case enables electromechanical system to de-amplify and amplify signals, which are frequently applied in signal-to-noise ratio improvement and thermal noise squeezing applications. Besides, signal gain, in both cases, also depends on frequency detuning between $\omega_p/2$ and mechanical resonance frequency, namely $\Delta = \omega_p/2 - \Omega_m$.

2.2.3 Duffing nonlinearity

In this section, we start to consider Duffing nonlinear mechanical resonator with linear and nonlinear terms, which is driven by an external sinusoidal force. This mechanical resonator is described as [36]

$$\ddot{x} + \gamma_m \dot{x} + \Omega_m^2 x + \alpha x^3 = \frac{F}{m_{eff}} \cos(\omega_d t) \quad Eq. 2.2.3.1$$

where x is the mechanical displacement, m is the effective mass, γ_m is the damping rate, Ω_m is the intrinsic resonant frequency, α is the nonlinear parameter, F is the amplitude of driving force, and ω_d is the driving frequency.

To solve this Duffing mechanical resonator, we use a solution in form of $x = \frac{\mu_x(t)}{2} e^{-i\omega_d t} + c.c$, where $\mu_x(t)$ is the complex amplitude dependent of time variable. The relevant derivatives of x are deduced and derived as described in Eq.2.2.3.2 and Eq.2.2.3.3. Eq.2.2.3.4 gives the term in $e^{-i\omega_d t}$ coming from x^3 .

$$\dot{x} = \frac{\dot{\mu}_x}{2} e^{-i\omega_d t} + \frac{\mu_x}{2} e^{-i\omega_d t} (-i\omega_d) + c.c \quad Eq. 2.2.3.2$$

$$\ddot{x} = \frac{\ddot{\mu}_x}{2} e^{-i\omega_d t} + \frac{\dot{\mu}_x}{2} e^{-i\omega_d t} (-2i\omega_d) + \frac{\mu_x}{2} e^{-i\omega_d t} (-\omega_d^2) + c.c \quad Eq. 2.2.3.3$$

$$x^3 = \left(\frac{\mu_x}{2} e^{-i\omega_d t} + \frac{\mu_x^*}{2} e^{i\omega_d t} \right)^3 \text{ gives}$$

$$\frac{3}{8} |\mu_x|^2 \mu_x e^{-i\omega_d t} + c.c \quad Eq. 2.2.3.4$$

Then substituting these terms back into Eq.2.2.3.1, it becomes

$$\ddot{\mu}_x + \dot{\mu}_x (\gamma_m - 2i\omega_d) + \mu_x (\Omega_m^2 - \omega_d^2 - i\omega_d \gamma_m) + \frac{3}{4} \alpha |\mu_x|^2 \mu_x = \frac{F}{m_{eff}} \quad Eq. 2.2.3.5$$

For the purpose of secular perturbation theory, we neglect $\ddot{\mu}_x$ here. At the same moment, the $\dot{\mu}_x (\gamma_m - 2i\omega_d)$ makes an approximation to $\dot{\mu}_x (-2i\omega_d)$ attributing to $\gamma_m \ll \omega_d$. Concurrently, letting $\omega_d \sim \Omega_m$ gets an approximate mechanical amplitude maximum. Furthermore, Eq.2.2.3.5 is re-written as

$$\frac{2\dot{\mu}_x}{\gamma_m} = \frac{2i(\omega_d - \Omega_m)\mu_x}{\gamma_m} - \mu_x - \frac{3i\alpha |\mu_x|^2 \mu_x}{4\gamma_m \Omega_m} + \frac{iF}{m_{eff} \gamma_m \Omega_m} \quad Eq. 2.2.3.6$$

A rescaled time variable and amplitude comparable back to the original physical motion equation Eq.2.2.3.1 are reintroduced, and the derivatives of time variable and amplitude have been described in Eq.2.2.3.7 and Eq.2.2.3.8 respectively.

$$\frac{2}{\gamma_m} \frac{d\mu_x}{dt} = \frac{d\mu_x}{d\tilde{t}} \quad \text{Eq. 2.2.3.7}$$

where $\tilde{t} = \gamma_m t/2$ is defined with larger magnitude than the original time variable t , ascribing to the multiplication factor of γ_m .

$$a = \sqrt{\frac{\alpha}{\gamma_m \Omega_m}} \mu_x \quad \text{Eq. 2.2.3.8}$$

Simplifying the motion Eq.2.2.3.6, we can introduce an intermediate variable as present in Eq.2.2.3.8. When injecting Eq.2.2.3.7 and Eq.2.2.3.8 into Eq.2.2.3.6, the motion equation Eq.2.2.3.9 for solving the proportional amplitude μ_x is derived.

$$\frac{da}{d\tilde{t}} = \frac{2i(\omega_d - \Omega_m)a}{\gamma_m} - a - \frac{3i}{4}|a|^2 a + \frac{iF}{m_{eff}\gamma_m\Omega_m} \sqrt{\frac{\alpha}{\gamma_m\Omega_m}} \quad \text{Eq. 2.2.3.9}$$

This equation can be used for secular perturbation theory while the $da/d\tilde{t}$ approximating zero, so that it is not divergent. Therefore, a certain mechanical amplitude a is found and becomes

$$a \left(2\Omega_x + \frac{3}{4}|a|^2 - i \right) = g \quad \text{Eq. 2.2.3.10}$$

where $\Omega_x = (\Omega_m - \omega_d)/\gamma_m$, $a = x\sqrt{\alpha/\gamma_m\Omega_m}$, and $g = (F/m_{eff}\gamma_m\Omega_m)\sqrt{\alpha/\gamma_m\Omega_m}$.

Finally, the proportional amplitude corresponding to Eq.2.2.3.10 can be given by

$$|a|^2 = \frac{g^2}{\left(2\Omega_x \pm \frac{3}{4}|a|^2 \right)^2 + 1} \quad \text{Eq. 2.2.3.11}$$

By analysing this rescaled equation, we can substitute the scaled terms and return back to the original physical motion equation Eq.2.2.3.1. Correspondingly, the original amplitude is approached to be

$$|\mu_x|^2 = \frac{\left(\frac{F}{m_{eff}\gamma_m\Omega_m} \right)^2}{\left(\frac{2(\Omega_m - \omega_d)}{\gamma_m} \pm \frac{3\alpha}{4\gamma_m\Omega_m} |\mu_x|^2 \right)^2 + 1} \quad \text{Eq. 2.2.3.12}$$

By deducing Eq.2.2.3.11, we achieve the maximum mechanical amplitude when taking the denominator $2\Omega_x \pm \frac{3}{4}|a|^2 = 0$. Note that the symbol “+” and “-” correspond to Duffing softening and hardening nonlinear responses respectively. We will show the discussion as following.

In this part, 100 nm thick SiN drum membrane with a tensile stress of 1.0 GPa and with a diameter of 30 μm is chosen for achieving resonance frequency around 11.67 MHz, and capacitive distance is defined to be around 790 nm for approximating the experimental capacitance value.

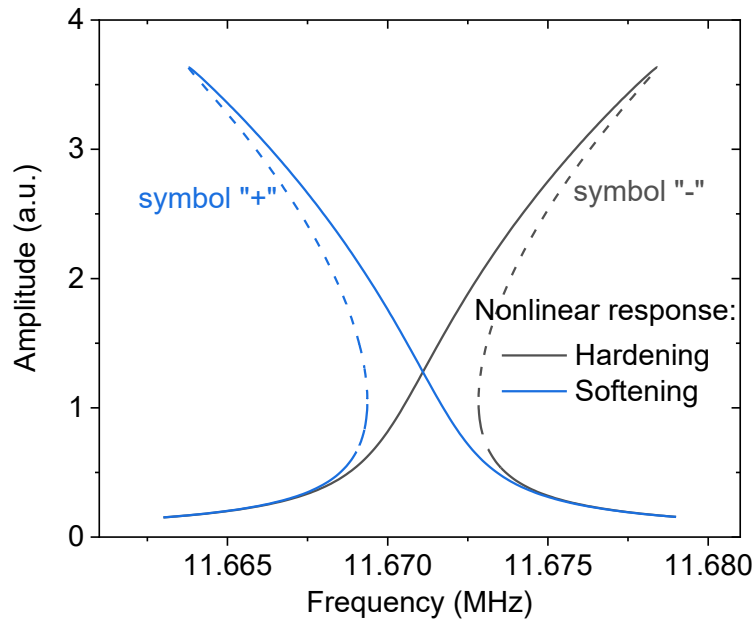


Figure 2.2.3.1. Calculation results of softening and hardening Duffing nonlinear responses as function of driving frequency. Note that the dashed lines are unstable solutions.

Nonlinearity is one of important features of a mechanical system applied for signal processing or ultrasensitive sensor [114,115]. In general, a mechanical resonator is driven in the linear region, so we can neglect the impact of nonlinear term on the mechanical system. However, if the nonlinear term cannot be neglected, we need to consider it. In other words, if nonlinear term αx^3 in Eq.2.2.3.1 is comparable with the linear term $\Omega_m^2 x$, forming a comparable expression $\Omega_m^2 (1 + \frac{\alpha|x|^2}{\Omega_m^2})x$, nonlinearity should not be neglected because it does shift mechanical resonance frequency. **Fig. 2.2.3.1** shows the calculated results of Duffing nonlinearity, including the softening (“+”) and hardening (“-”) nonlinear curves. Here, nonlinear parameter, driving

force, effective mass, resonant frequency and quality factor are $\alpha = 6.8 \times 10^{27} \text{ m}^{-2} \cdot \text{s}^{-2}$, $f_d = 500 \text{ pN}$, $m_{eff} = 4.4 \times 10^{-14} \text{ kg}$, $\frac{\Omega_m}{2\pi} = 11.6711 \text{ MHz}$ and $Q = 17200$, respectively.

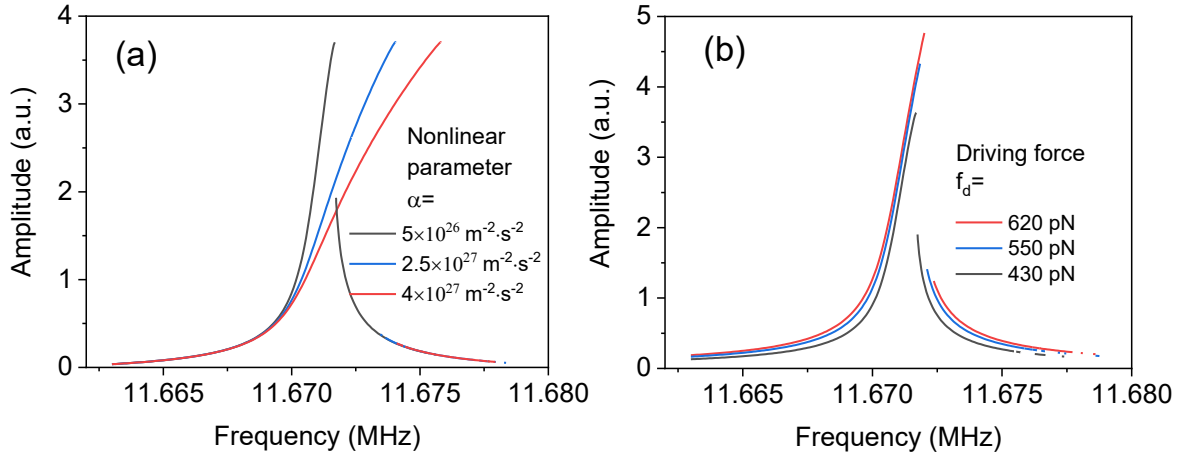


Figure 2.2.3.2. Calculation results of Duffing mechanical responses. (a) Nonlinear amplitude as a function of frequency with α increasing. (b) Nonlinear amplitude as function of frequency with the driving force increasing. The calculation static capacitance $C_{g0}(d \approx 790 \text{ nm}, D \approx 30 \mu\text{m}) \approx 7.918 \times 10^{-15} \text{ F}$ is used here.

Besides, the specific hardening nonlinearity can be discussed further. **Fig. 2.2.3.2(a)** shows the nonlinearity can be modulated by the control of nonlinear parameter while fixing driving force, effective mass, resonance frequency and quality factor being $f_d = 450 \text{ pN}$, $m_{eff} = 4.4 \times 10^{-14} \text{ kg}$, $\frac{\Omega_m}{2\pi} = 11.6711 \text{ MHz}$, and $Q = 20000$, respectively. This is helpful for us to understand whether, or not, a suitable nonlinear curve shape can be approached. **Fig. 2.2.3.2(b)** shows the nonlinearity is able to approach the higher amplitude when increasing the drive force. In this case, nonlinear parameter, driving force, effective mass, resonance frequency and quality factor being $\alpha = 5.6 \times 10^{26} \text{ m}^{-2} \cdot \text{s}^{-2}$, $m_{eff} = 4.4 \times 10^{-14} \text{ kg}$, $\frac{\Omega_m}{2\pi} = 11.6711 \text{ MHz}$, $Q = 20000$ have been used as well.

2.2.4 Double-tone driving scheme in nanoelectromechanics, an analogy to optomechanical system

In previous section 2.2.1 and 2.2.2, both single tone driving scheme and parametric pumping scheme have been introduced. In this subsection, we start to analyse a double-tone driving scheme in a coupled nanoelectromechanical system, consisting of two capacitively coupled nanoelectromechanical resonators. One of the coupled resonators, having the higher resonance frequency, is chosen as a phonon-cavity, in order to perform an analog to the optomechanical system. Classical optomechanical systems [116] contain a mechanical resonator (e.g., membrane) that is embedded and connected to the optical cavity. Through semi-reflected mirror side, light waves in forms of photons with a driving frequency are input into the cavity interacting with the movable object, namely mechanical resonator. Light waves confined in the cavity with higher frequency can be optical cavity mode, and the mechanical resonator with relatively low resonance frequency can be mechanical mode, thus establishing the energy transduction between the both. Such phenomena have also been observed in the nanoelectromechanical systems [117,118].

In this double-tone scheme, we use one RF signal to probe one of the coupled resonators and take the other RF signal to pump the phonon-cavity at its sideband. More details in both experiment and modelling have been reported by Pokharel et al [93].

2.2.4.1 Analytical modelling of the double tone driving scheme

We consider a nanoelectromechanical system as a capacitor consisting of two parallel and movable plates, namely $C_g(X_1, X_2)$, as shown in **Fig. 2.2.4.1**, where the displacements X_1 and X_2 correspond to the plates resonating at the frequencies Ω_1 and Ω_2 respectively.

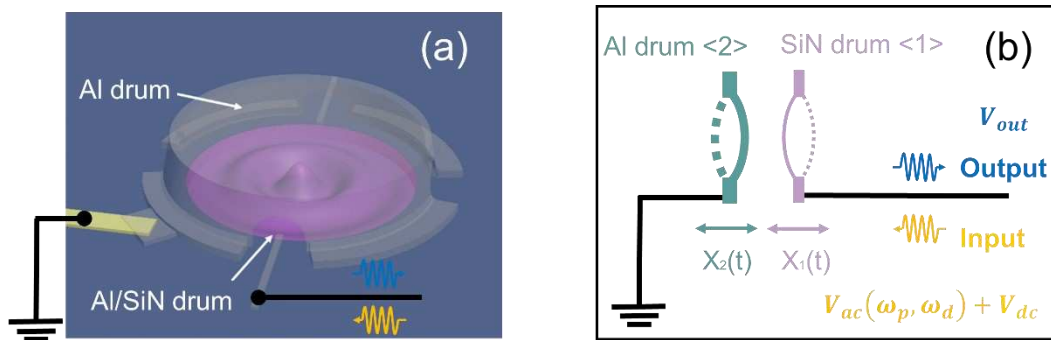


Figure 2.2.4.1. (a) Sketch of a bottom drum resonator capacitively coupled to a top gate drum resonator. (b) Structure of the capacitively coupled two membrane resonators. Note that $V_{ac}(\omega_p, \omega_d)$ contains two ac signals, namely sideband pump signal with frequency ω_p and

probe signal with frequency ω_d . Here, probe signal can drive either SiN drum or Al drum, therefore having frequency labelled later by ω_{d1} or ω_{d2} , respectively.

The driving force of the mechanical system is given by

$$F_1(X_1, X_2) = \frac{V^2}{2} \frac{\partial C_g(X_1, X_2)}{\partial X_1} \quad \text{Eq. 2.2.4.1}$$

where driving voltage is $V = V_{dc} + V_{ac}$, more details can be found in section 2.2.1.

Here we think of this driving force with second order Taylor expansion of the capacitance approximation $C_g(x) \approx C_{g0}(1 - \frac{x}{d} + \frac{x^2}{d^2})$, where we define $x(t) = X_2(t) - X_1(t)$. Therefore, the driving force can be extended to be

$$F_1(X_1, X_2) = \frac{V^2 C_{g0}}{2} \frac{\partial}{\partial X_1} \left(1 - \frac{(X_2 - X_1)}{d} + \frac{(X_2 - X_1)^2}{d^2} \right) \quad \text{Eq. 2.2.4.2}$$

The motion equations of the mechanical resonators are given by [93]

$$\ddot{X}_1 + \gamma_1 \dot{X}_1 + \Omega_1^2 X_1 = \frac{V^2 C_{g0}}{2dm_1} \left(1 - \frac{2(X_2 - X_1)}{d} \right) \quad \text{Eq. 2.2.4.3(a)}$$

$$\ddot{X}_2 + \gamma_2 \dot{X}_2 + \Omega_2^2 X_2 = \frac{V^2 C_{g0}}{2dm_2} \left(-1 + \frac{2(X_2 - X_1)}{d} \right) \quad \text{Eq. 2.2.4.3(b)}$$

where $\gamma_{1,2}$ is the damping rate, $m_{1,2}$ is the effective mass and C_{g0} is the initial capacitance between two parallel circular membranes with a capacitive distance d .

We have discussed the V^2 in the section 2.2.1, and take $2V_{ac}V_{dc}$ to analyse the equations. To make an electromechanical analog to optomechanical experiments, we made several important definitions. First, a resonator having a higher resonance frequency in the coupled mechanical system is defined as a phonon-cavity and labelled as the mechanical resonator <1>; the other coupled resonator is labelled as <2>. In the following, we will discuss four kinds of double-tone driving schemes.

Table 2.2.4.1. Red sideband pump the phonon cavity and probe the phonon cavity

| Parameter | SiN drum resonator <1> | Al drum resonator <2> |
|--|--|--|
| Resonance frequency | Ω_1 | Ω_2 |
| Displacement | $X_1(t) = \frac{x_1(t)}{2} e^{-i\Omega_{d1}t} + c.c$ | $X_2(t) = \frac{x_2(t)}{2} e^{i(\Omega_p - \Omega_{d1})t} + c.c$ |
| Probe signal | $\Omega_{d1} = \Omega_1 + \delta$ | No |
| Pump signal | $\Omega_p = \Omega_1 - \Omega_2 + \Delta$ | No |
| Mechanical susceptibility | $\chi_1[\Omega_{d1}] = \frac{1}{\Omega_1 - \Omega_{d1} - i\frac{\gamma_1}{2}}$ | $\chi_2[\Omega_{d2}] = \frac{1}{\Omega_2 - \Omega_{d2} - i\frac{\gamma_2}{2}}$ |
| Definitions of mechanical susceptibility | $\chi_1^{red} = \frac{1}{-\delta - i\frac{\gamma_1}{2}}$ | $\chi_2^{red} = \frac{1}{\Delta - \delta - i\frac{\gamma_2}{2}}$ |
| Solution of displacement | $x_1 = \frac{f_{d1}}{2m_1\Omega_1} \frac{1}{\chi_1^{-1}[\Omega_{d1}] - \frac{ f_p ^2 \chi_2[\Omega_{d2}]}{4m_1m_2d^2\Omega_1\Omega_2}}$ | $x_2 = -\frac{f_p^*}{2m_2\Omega_2} \frac{x_1}{d} \chi_2[\Omega_{d2}]$ |
| Effective damping rate | $\gamma_{eff1}^{red} = \gamma_1 + \frac{ f_p ^2}{4m_1m_2d^2\Omega_1\Omega_2} \frac{\gamma_2}{(\Omega_2 - \Omega_{d2})^2 + \frac{\gamma_2^2}{4}}$ | No |

Red sideband pump the phonon cavity and probe the phonon cavity. We first use one signal with frequency Ω_{d1} to probe around mechanical resonator <1>, namely $\Omega_{d1} = \Omega_1 + \delta$. Here, δ is a small value, indicating a frequency detuning from Ω_1 . Then, we use the other sideband

signal to pump the phonon cavity at its red sideband $\sim \Omega_1 - \Omega_2$. A small pump frequency detuning Δ is defined to be $\Omega_p = \Omega_1 - \Omega_2 + \Delta$.

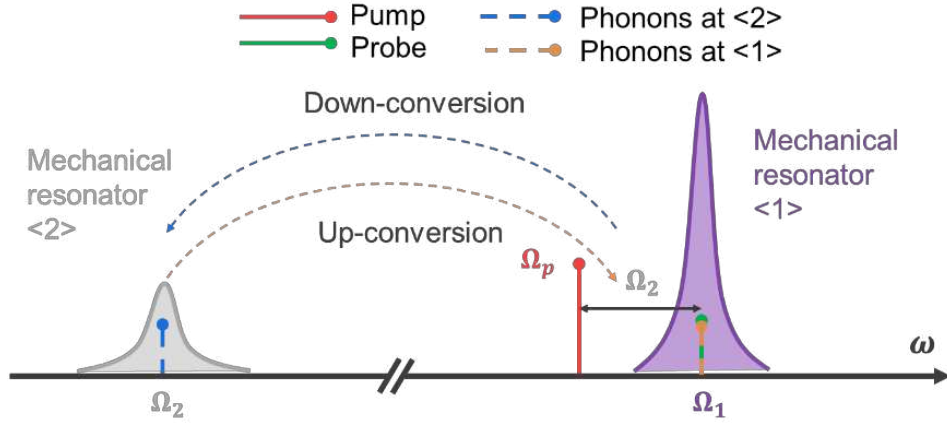


Figure 2.2.4.2. Spectrum landscape at red sideband pumping scheme while probing the phonon-cavity. Purple and grey colors are the mechanical resonator <1> with higher frequency Ω_1 and the mechanical resonator <2> with the low resonance frequency Ω_2 . Green color is a probe signal with the frequency $\Omega_{d1} = \Omega_1 + \delta$ at the phonon cavity. Red color is red sideband pumping with the frequency $\Omega_p = \Omega_1 - \Omega_2 + \Delta$. Blue and orange dashed signal bars describe the down-conversion phonons at mechanical resonator <2> and the feedback phonons at the phonon-cavity mechanical resonator <1>.

Because the phonon cavity, corresponding to the displacement X_1 , is driving with Ω_{d1} , we look for Eq. 2.2.4.3(a) frequency match with $e^{-i\Omega_{d1}t}$. Considering that the mechanical system is driving with two tones, namely the probe and the pump, we have the voltage $V_{ac}(\omega_p, \omega_{d1}) = \frac{\mu_p}{2}e^{-i\Omega_p t} + \frac{\mu_s}{2}e^{-i\Omega_{d1}t} + c.c.$. We also define the probed mechanical resonator $X_1(t) = \frac{x_1(t)}{2}e^{-i\Omega_{d1}t} + c.c$ and the other coupled mechanical resonator $X_2(t) = \frac{x_2(t)}{2}e^{i(\Omega_p - \Omega_{d1})t} + c.c.$ The frequency match is given by selecting these terms containing $e^{-i\Omega_{d1}t}$. Therefore, Eq.2.2.4.3(a) can be modified by

$$\begin{aligned}
& \frac{V_{dc}C_{g0}}{2dm_1} \left(1 - \frac{2(X_2 - X_1)}{d}\right) \cdot V_{ac}(\omega_p, \omega_{d1}) \\
&= \frac{V_{dc}C_{g0}}{2dm_1} \left(1 - \frac{2\left(\frac{x_2(t)}{2}e^{i(\Omega_p - \Omega_{d1})t} - \frac{x_1(t)}{2}e^{-i\Omega_{d1}t} + c.c\right)}{d}\right) \\
&\cdot \left(\frac{\mu_p}{2}e^{-i\Omega_p t} + \frac{\mu_s}{2}e^{-i\Omega_{d1}t} + c.c\right) \quad \text{Eq. 2.2.4.4(a)}
\end{aligned}$$

To select the terms related to $e^{-i\Omega_{d1}t}$, we discuss each term in Eq.2.2.4.4(a) exhibiting below:

$$1 \cdot \left(\frac{\mu_p}{2}e^{-i\Omega_p t} + \frac{\mu_s}{2}e^{-i\Omega_{d1}t} + c.c\right) \quad \text{Eq. 2.2.4.5(1)}$$

The term $\frac{\mu_p}{2}e^{-i\Omega_p t}$ can be neglected due to there no frequency mixing with $e^{-i\Omega_{d1}t}$ and the term $\frac{\mu_s}{2}e^{-i\Omega_{d1}t}$ can be kept because of its exact same with $e^{-i\Omega_{d1}t}$;

$$\frac{x_2(t)}{2}e^{i(\Omega_p - \Omega_{d1})t} \cdot \left(\frac{\mu_p}{2}e^{-i\Omega_p t} + \frac{\mu_s}{2}e^{-i\Omega_{d1}t} + c.c\right) \quad \text{Eq. 2.2.4.5(2)}$$

The term $\frac{x_2(t)}{2}e^{i(\Omega_p - \Omega_{d1})t}$ multiplying with $\frac{\mu_p}{2}e^{-i\Omega_p t}$ can be kept due to a frequency mixing with $e^{-i\Omega_{d1}t}$, and the term $\frac{x_2(t)}{2}e^{i(\Omega_p - \Omega_{d1})t}$ multiplying with $\frac{\mu_s}{2}e^{-i\Omega_{d1}t}$ can be neglected because of there no frequency mixing with $e^{-i\Omega_{d1}t}$;

$$\frac{x_1(t)}{2}e^{-i\Omega_{d1}t} \cdot \left(\frac{\mu_p}{2}e^{-i\Omega_p t} + \frac{\mu_s}{2}e^{-i\Omega_{d1}t} + c.c\right) \quad \text{Eq. 2.2.4.5(3)}$$

The term $\frac{x_1(t)}{2}e^{-i\Omega_{d1}t}$ multiplying with other terms can all be neglected because there is no frequency mixing with $e^{-i\Omega_{d1}t}$.

We summarize our analysis by selecting the terms containing $e^{-i\Omega_{d1}t}$, which is given by

$$\frac{V_{dc}C_{g0}}{2dm_1} \left(1 - \frac{2(X_2 - X_1)}{d}\right) \cdot V_{ac}(\omega_p, \omega_{d1}) \stackrel{\text{def}}{=} \frac{V_{dc}C_{g0}}{dm_1} \left(\frac{x_{1s}}{2} - \frac{\mu_p x_2}{2d}\right) e^{-i\Omega_{d1}t} \quad \text{Eq. 2.2.4.6(a)}$$

Similarly, Eq.2.2.4.3(b) can be modified by

$$\begin{aligned}
& \frac{V_{dc}C_{g0}}{2dm_2} \left(-1 + \frac{2(X_2 - X_1)}{d} \right) \cdot V_{ac}(\omega_p) \\
&= \frac{V_{dc}C_{g0}}{2dm_2} \left(-1 + \frac{2 \left(\frac{x_2(t)}{2} e^{i(\Omega_p - \Omega_{d1})t} - \frac{x_1(t)}{2} e^{-i\Omega_{d1}t} + c.c \right)}{d} \right) \\
& \cdot \left(\frac{\mu_p^*}{2} e^{i\Omega_p t} + c.c \right) \quad \text{Eq. 2.2.4.4(b)}
\end{aligned}$$

To select the terms related to $e^{-i\Omega_{d2}t}$, we discuss each term in Eq.2.2.4.4(b) exhibiting below:

$$-1 \cdot \left(\frac{\mu_p^*}{2} e^{i\Omega_p t} + c.c \right) \quad \text{Eq. 2.2.4.7(1)}$$

The term $\frac{\mu_p^*}{2} e^{i\Omega_p t}$ can be neglected due to there no frequency mixing with $e^{-i\Omega_{d2}t}$;

$$\frac{x_2(t)}{2} e^{i(\Omega_p - \Omega_{d1})t} \cdot \left(\frac{\mu_p^*}{2} e^{i\Omega_p t} + c.c \right) \quad \text{Eq. 2.2.4.7(2)}$$

The term $\frac{x_2(t)}{2} e^{i(\Omega_p - \Omega_{d1})t}$ multiplying with $\frac{\mu_p^*}{2} e^{i\Omega_p t}$ can be neglected due to there no a frequency mixing with $e^{-i\Omega_{d2}t}$;

$$\frac{x_1(t)}{2} e^{-i\Omega_{d1}t} \cdot \left(\frac{\mu_p^*}{2} e^{i\Omega_p t} + c.c \right) \quad \text{Eq. 2.2.4.7(3)}$$

The term $\frac{x_1(t)}{2} e^{-i\Omega_{d1}t}$ multiplying with $\frac{\mu_p^*}{2} e^{i\Omega_p t}$ can be kept because of there a frequency mixing $e^{i(\Omega_p - \Omega_{d1})t}$ with $e^{-i\Omega_{d2}t}$.

We summarize our analysis by selecting the terms containing $e^{-i\Omega_{d2}t}$, which is given by

$$\frac{V_{dc}C_{g0}}{2dm_2} \left(-1 + \frac{2(X_2 - X_1)}{d} \right) \cdot V_{ac}(\omega_p) \stackrel{\text{def}}{=} -\frac{V_{dc}C_{g0}}{dm_2} \frac{\mu_p^* x_1}{2d} e^{-i\Omega_{d2}t} \quad \text{Eq. 2.2.4.6(b)}$$

After mixing the frequencies, we derive the analytical motion equations to be

$$\ddot{X}_1 + \gamma_1 \dot{X}_1 + \Omega_1^2 X_1 = \frac{V_{dc}C_{g0}}{dm_1} \left(\frac{x_{1s}}{2} - \frac{\mu_p x_2}{2d} \right) e^{-i\Omega_{d1}t} \quad \text{Eq. 2.2.4.8(a)}$$

$$\ddot{X}_2 + \gamma_2 \dot{X}_2 + \Omega_2^2 X_2 = -\frac{V_{dc}C_{g0}}{dm_2} \frac{\mu_p^* x_1}{2d} e^{-i\Omega_{d2}t} \quad \text{Eq. 2.2.4.8(b)}$$

Based on $\Omega_{d1} = \Omega_1 + \delta$ and $\Omega_{d2} = \Omega_2 + \delta - \Delta$, if $\Delta, \delta \rightarrow 0$, we get approximations to be $\Omega_1^2 - \Omega_{d1}^2 \approx 2\Omega_1(\Omega_1 - \Omega_{d1})$ and $\Omega_2^2 - \Omega_{d2}^2 \approx 2\Omega_2(\Omega_2 - \Omega_{d2})$. The equations are recast by

$$\Omega_1 \chi_1^{-1}[\Omega_{d1}] x_1 = \frac{V_{dc} C_{g0}}{dm_1} \left(\frac{\mu_s}{2} - \frac{\mu_p x_2}{2d} \right) \quad Eq. 2.2.4.9(a)$$

$$\Omega_2 \chi_2^{-1}[\Omega_{d2}] x_2 = -\frac{V_{dc} C_{g0} \mu_p^* x_1}{dm_2} \frac{1}{2d} \quad Eq. 2.2.4.9(b)$$

where $\chi_1[\Omega_{d1}] = \frac{1}{\Omega_1 - \Omega_{d1} - i\frac{\gamma_1}{2}}$ and $\chi_2[\Omega_{d2}] = \frac{1}{\Omega_2 - \Omega_{d2} - i\frac{\gamma_2}{2}}$ are the mechanical susceptibilities, μ_s is a probe signal amplitude, x_1 and x_2 are the slow varying complex amplitudes corresponding to the mechanical displacements.

Because the mechanical displacements in this electromechanical system exhibiting similar a behaviour to the optomechanically induced transparency [119][120], the analytical solutions from Eq.2.2.4.9 can be described by

$$x_1 = \frac{f_{d1}}{2m_1\Omega_1} \frac{1}{\chi_1^{-1}[\Omega_{d1}] - \frac{|f_p|^2 \chi_2[\Omega_{d2}]}{4m_1m_2d^2\Omega_1\Omega_2}} \quad Eq. 2.2.4.10(a)$$

$$x_2 = -\frac{f_p^*}{2m_2\Omega_2} \frac{x_1}{d} \chi_2[\Omega_{d2}] \quad Eq. 2.2.4.10(b)$$

where $f_{d1} = \frac{V_{dc} C_{g0} \mu_s}{d}$ is the probe force and $f_p^* = \frac{V_{dc} C_{g0} \mu_p^*}{d}$ is the conjugate pump force.

Furthermore, the effective damping rate at red sideband is given by

$$\gamma_{eff1}^{red} = \gamma_1 + \frac{|f_p|^2}{4m_1m_2d^2\Omega_1\Omega_2} \frac{\gamma_2}{(\Omega_2 - \Omega_{d2})^2 + \frac{\gamma_2^2}{4}} \quad Eq. 2.2.4.11$$

To make the frequency operation clear, we define the mechanical susceptibilities $\chi_{1,2}^{red}$ when probing at the frequency $\Omega_{d1} = \Omega_1 + \delta$ and red sideband pumping at the frequency $\Omega_p = \Omega_1 - \Omega_2 + \Delta$. Then, they are given by

$$\chi_1^{red} = \frac{1}{-\delta - i\frac{\gamma_1}{2}} \quad Eq. 2.2.4.12(a)$$

$$\chi_2^{red} = \frac{1}{\Delta - \delta - i\frac{\gamma_2}{2}} \quad Eq. 2.2.4.12(b)$$

Table 2.2.4.2. Blue sideband pump the phonon cavity and probe the phonon cavity

| Parameter | SiN drum resonator <1> | Al drum resonator <2> |
|--|---|--|
| Resonance frequency | Ω_1 | Ω_2 |
| Displacement | $X_1(t) = \frac{x_1(t)}{2} e^{-i\Omega_{d1}t} + c.c$ | $X_2(t) = \frac{x_2(t)}{2} e^{i(\Omega_p - \Omega_{d1})t} + c.c$ |
| Probe signal | $\Omega_{d1} = \Omega_1 + \delta$ | No |
| Pump signal | $\Omega_p = \Omega_1 + \Omega_2 + \Delta$ | No |
| Mechanical susceptibility | $\chi_1[\Omega_{d1}] = \frac{1}{\Omega_1 - \Omega_{d1} - i\frac{\gamma_1}{2}}$ | $\chi_2[\Omega_{d2}] = \frac{1}{\Omega_2 - \Omega_{d2} - i\frac{\gamma_2}{2}}$ |
| Definitions of mechanical susceptibility | $\chi_1^{blue} = \frac{1}{-\delta - i\frac{\gamma_1}{2}}$ | $\chi_2^{blue} = \frac{1}{\delta - \Delta - i\frac{\gamma_2}{2}}$ |
| Solution of displacement | $x_1 = \frac{f_{d1}}{2m_1\Omega_1} \frac{1}{\chi_1^{-1}[\Omega_{d1}] + \frac{ f_p ^2 \chi_2[\Omega_{d2}]}{4m_1m_2d^2\Omega_1\Omega_2}}$ | $x_2 = -\frac{f_p}{2m_2\Omega_2} \frac{x_1^*}{d} \chi_2[\Omega_{d2}]$ |
| Effective damping rate | $\gamma_{eff1}^{blue} = \gamma_1 - \frac{ f_p ^2}{4m_1m_2d^2\Omega_1\Omega_2} \frac{\gamma_2}{(\Omega_2 - \Omega_{d2})^2 + \frac{\gamma_2^2}{4}}$ | No |

Blue sideband pump the phonon cavity and probe the phonon cavity. We still use one signal with frequency Ω_{d1} to probe around mechanical resonator <1>, namely $\Omega_{d1} = \Omega_1 + \delta$. Then in this time, we use the other sideband signal to pump the phonon cavity at its blue sideband $\sim \Omega_1 + \Omega_2$. A small pump frequency detuning Δ is defined to be $\Omega_p = \Omega_1 + \Omega_2 + \Delta$.

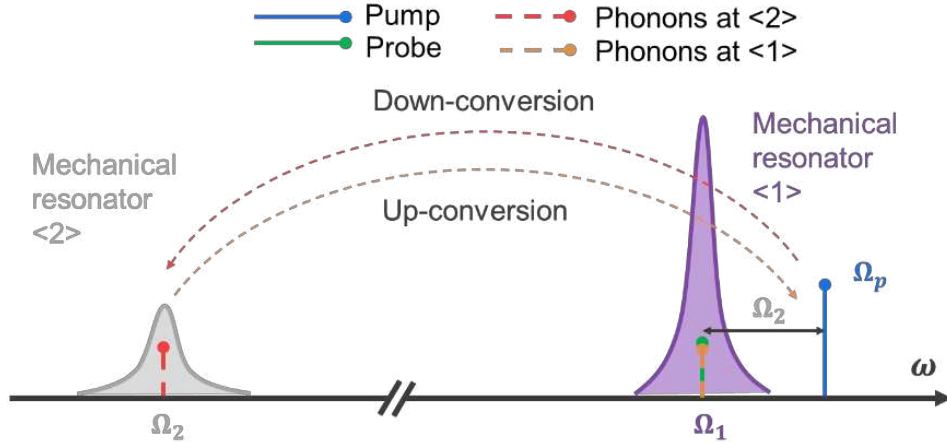


Figure 2.2.4.3. Spectrum landscape at blue sideband pumping scheme while probing the phonon-cavity. Purple and grey colors are the mechanical resonator $\langle 1 \rangle$ with higher frequency Ω_1 and the mechanical resonator $\langle 2 \rangle$ with the low resonance frequency Ω_2 . Green color is a probe signal with the frequency $\Omega_{d1} = \Omega_1 + \delta$ at the phonon-cavity. Blue color is blue sideband pumping with the frequency $\Omega_p = \Omega_1 + \Omega_2 + \Delta$. Red and orange dashed signal bars are the down-conversion phonons at mechanical resonator $\langle 2 \rangle$ and the feedback phonons at the phonon cavity mechanical resonator $\langle 1 \rangle$.

Because the phonon cavity, corresponding to the displacement X_1 , is driving with Ω_{d1} , we look for the Eq. 2.2.4.3(a) frequency match with $e^{-i\Omega_{d1}t}$. Considering that the system is driving with two tones, namely the probe and the pump, we get the $V_{ac}(\omega_p, \omega_{d1}) = \frac{\mu_p}{2} e^{-i\Omega_p t} + \frac{\mu_s}{2} e^{-i\Omega_{d1}t} + c. c$. We also defined the probed mechanical resonator $X_1(t) = \frac{x_1(t)}{2} e^{-i\Omega_{d1}t} + c. c$ and the other coupled mechanical resonator $X_2(t) = \frac{x_2^*(t)}{2} e^{i(\Omega_p - \Omega_{d1})t} + c. c$. The frequency match is given by selecting these terms containing $e^{-i\Omega_{d1}t}$. Eq.2.2.4.3(a) can be modified by

$$\begin{aligned} & \frac{V_{dc}C_{g0}}{2dm_1} \left(1 - \frac{2(X_2 - X_1)}{d} \right) \cdot V_{ac}(\omega_p, \omega_{d1}) \\ &= \frac{V_{dc}C_{g0}}{2dm_1} \left(1 - \frac{2 \left(\frac{x_2^*(t)}{2} e^{i(\Omega_p - \Omega_{d1})t} - \frac{x_1^*(t)}{2} e^{i\Omega_{d1}t} + c. c \right)}{d} \right) \\ & \cdot \left(\frac{\mu_p}{2} e^{-i\Omega_p t} + \frac{\mu_s}{2} e^{-i\Omega_{d1}t} + c. c \right) \quad \text{Eq. 2.2.4.13(a)} \end{aligned}$$

To select the terms related to $e^{-i\Omega_{d1}t}$, we discuss each term in Eq.2.2.4.13(a) exhibiting below:

$$1 \cdot \left(\frac{\mu_p}{2} e^{-i\Omega_p t} + \frac{\mu_s}{2} e^{-i\Omega_{d1} t} + c.c \right) \quad Eq. 2.2.4.14(1)$$

The term $\frac{\mu_p}{2} e^{-i\Omega_p t}$ can be neglected due to there no frequency mixing with $e^{-i\Omega_{d1} t}$ and the term $\frac{\mu_s}{2} e^{-i\Omega_{d1} t}$ can be kept because of its exact mixing with $e^{-i\Omega_{d1} t}$;

$$\frac{x_2^*(t)}{2} e^{i(\Omega_p - \Omega_{d1})t} \cdot \left(\frac{\mu_p}{2} e^{-i\Omega_p t} + \frac{\mu_s}{2} e^{-i\Omega_{d1} t} + c.c \right) \quad Eq. 2.2.4.14(2)$$

The term $\frac{x_2^*(t)}{2} e^{i(\Omega_p - \Omega_{d1})t}$ multiplying with $\frac{\mu_p}{2} e^{-i\Omega_p t}$ can be kept due to a frequency mixing with $e^{-i\Omega_{d1} t}$, and the term $\frac{x_2^*(t)}{2} e^{i(\Omega_p - \Omega_{d1})t}$ multiplying with $\frac{\mu_s}{2} e^{-i\Omega_{d1} t}$ can be neglected because of there no frequency mixing with $e^{-i\Omega_{d1} t}$;

$$\frac{x_1^*(t)}{2} e^{i\Omega_{d1} t} \cdot \left(\frac{\mu_p}{2} e^{-i\Omega_p t} + \frac{\mu_s}{2} e^{-i\Omega_{d1} t} + c.c \right) \quad Eq. 2.2.4.14(3)$$

The term $\frac{x_1^*(t)}{2} e^{i\Omega_{d1} t}$ multiplying with other terms can be neglected because there is no frequency mixing with $e^{-i\Omega_{d1} t}$.

We summarize our analysis by selecting the terms containing $e^{-i\Omega_{d1} t}$. It is given by

$$\frac{V_{dc} C_{g0}}{2dm_1} \left(1 - \frac{2(X_2 - X_1)}{d} \right) \cdot V_{ac}(\omega_p, \omega_{d1}) \stackrel{\text{def}}{=} \frac{V_{dc} C_{g0}}{dm_1} \left(\frac{x_{1s}}{2} - \frac{\mu_p x_2^*}{2d} \right) e^{-i\Omega_{d1} t} \quad Eq. 2.2.4.15(a)$$

Similarly, Eq.2.2.4.3(b) can be modified by

$$\begin{aligned} & \frac{V_{dc} C_{g0}}{2dm_2} \left(-1 + \frac{2(X_2 - X_1)}{d} \right) \cdot V_{ac}(\omega_p) \\ &= \frac{V_{dc} C_{g0}}{2dm_2} \left(-1 + \frac{2 \left(\frac{x_2^*(t)}{2} e^{i(\Omega_p - \Omega_{d1})t} - \frac{x_1^*(t)}{2} e^{i\Omega_{d1} t} + c.c \right)}{d} \right) \\ & \cdot \left(\frac{\mu_p}{2} e^{-i\Omega_p t} + c.c \right) \quad Eq. 2.2.4.13(b) \end{aligned}$$

To select the term related to $e^{-i\Omega_{d2} t}$, we discuss each term in Eq.2.2.4.13(b) exhibiting below:

$$-1 \cdot \left(\frac{\mu_p}{2} e^{-i\Omega_p t} + c.c \right) \quad Eq. 2.2.4.16(1)$$

The term $\frac{\mu_p}{2} e^{-i\Omega_p t}$ can be neglected due to there no frequency mixing with $e^{-i\Omega_{d2} t}$;

$$\frac{x_2^*(t)}{2} e^{i(\Omega_p - \Omega_{d1})t} \cdot \left(\frac{\mu_p}{2} e^{-i\Omega_p t} + c.c \right) \quad Eq. 2.2.4.16(2)$$

The term $\frac{x_2^*(t)}{2} e^{i(\Omega_p - \Omega_{d1})t}$ multiplying with $\frac{\mu_p}{2} e^{-i\Omega_p t}$ can be neglected due to there no a frequency mixing with $e^{-i\Omega_{d2}t}$;

$$\frac{x_1^*(t)}{2} e^{i\Omega_{d1}t} \cdot \left(\frac{\mu_p}{2} e^{-i\Omega_p t} + c.c \right) \quad Eq. 2.2.4.16(3)$$

The term $\frac{x_1^*(t)}{2} e^{i\Omega_{d1}t}$ multiplying with $\frac{\mu_p}{2} e^{-i\Omega_p t}$ can be kept because of there a frequency mixing $e^{i(-\Omega_p + \Omega_{d1})t}$ with $e^{-i\Omega_{d2}t}$.

We summarize our analysis by selecting the terms containing $e^{-i\Omega_{d2}t}$. It is given by

$$\frac{V_{dc} C_{g0}}{2dm_2} \left(-1 + \frac{2(X_2 - X_1)}{d} \right) \cdot V_{ac}(\omega_p) \stackrel{\text{def}}{=} -\frac{V_{dc} C_{g0}}{dm_2} \frac{\mu_p x_1^*}{2d} e^{-i\Omega_{d2}t} \quad Eq. 2.2.4.15(b)$$

After mixing the frequencies, the analytical equations are derived to be

$$\ddot{X}_1 + \gamma_1 \dot{X}_1 + \Omega_1^2 X_1 = \frac{V_{dc} C_{g0}}{dm_1} \left(\frac{x_{1s}}{2} - \frac{\mu_p x_2^*}{2d} \right) e^{-i\Omega_{d1}t} \quad Eq. 2.2.4.17(a)$$

$$\ddot{X}_2 + \gamma_2 \dot{X}_2 + \Omega_2^2 X_2 = -\frac{V_{dc} C_{g0}}{dm_2} \frac{\mu_p x_1^*}{2d} e^{-i\Omega_{d2}t} \quad Eq. 2.2.4.17(b)$$

Based on $\Omega_{d1} = \Omega_1 + \delta$ and $\Omega_{d2} = \Omega_2 + \Delta - \delta$, if $\Delta, \delta \rightarrow 0$, we have approximations to be $\Omega_1^2 - \Omega_{d1}^2 \approx 2\Omega_1(\Omega_1 - \Omega_{d1})$ and $\Omega_2^2 - \Omega_{d2}^2 \approx 2\Omega_2(\Omega_2 - \Omega_{d2})$, the corresponding equations are given by

$$\Omega_1 \chi_1^{-1}[\Omega_{d1}] x_1 = \frac{V_{dc} C_{g0}}{dm_1} \left(\frac{\mu_s}{2} - \frac{\mu_p x_2^*}{2d} \right) \quad Eq. 2.2.4.18(a)$$

$$\Omega_2 \chi_2^{-1}[\Omega_{d2}] x_2 = -\frac{V_{dc} C_{g0}}{dm_2} \frac{\mu_p x_1^*}{2d} \quad Eq. 2.2.4.18(b)$$

Due to the mechanical displacements featuring a similar behaviour to the optomechanically induced amplification [120],[117], the analytical solutions from Eq.2.2.4.18 can be written by

$$x_1 = \frac{f_{d1}}{2m_1 \Omega_1} \frac{1}{\chi_1^{-1}[\Omega_{d1}] + \frac{|f_p|^2 \chi_2[\Omega_{d2}]}{4m_1 m_2 d^2 \Omega_1 \Omega_2}} \quad Eq. 2.2.4.19(a)$$

$$x_2 = -\frac{f_p}{2m_2\Omega_2} \frac{x_1^*}{d} \chi_2[\Omega_{d2}] \quad Eq. 2.2.4.19(b)$$

where $f_{d1} = \frac{V_{dc}C_{g0}\mu_s}{d}$ is the probe force and $f_p = \frac{V_{dc}C_{g0}\mu_p}{d}$ is the pump force.

Likewise, the effective damping rate at blue sideband is given by

$$\gamma_{eff1}^{blue} = \gamma_1 - \frac{|f_p|^2}{4m_1m_2d^2\Omega_1\Omega_2} \frac{\gamma_2}{(\Omega_2 - \Omega_{d2})^2 + \frac{\gamma_2^2}{4}} \quad Eq. 2.2.4.20$$

We similarly define the mechanical susceptibilities $\chi_{1,2}^{blue}$ when probing at the frequency $\Omega_{d1} = \Omega_1 + \delta$ and blue sideband pumping at the frequency $\Omega_p = \Omega_1 + \Omega_2 + \Delta$. Then, the mechanical susceptibilities $\chi_{1,2}^{blue}$ at blue sideband become

$$\chi_1^{blue} = \frac{1}{-\delta - i\frac{\gamma_1}{2}} \quad Eq. 2.2.4.21(a)$$

$$\chi_2^{blue} = \frac{1}{\delta - \Delta - i\frac{\gamma_2}{2}} \quad Eq. 2.2.4.21(b)$$

We compare the mechanical susceptibilities between at red and blue sidebands. An analytical result is seen as $\chi_2^{red} = -\chi_2^{*blue}$. Thus, we rewrite the analytical solutions to be

$$x_1 = \frac{f_d}{2m_1\Omega_1} \frac{1}{\chi_1^{-1}[\Omega_{d1}] \pm \frac{|f_p|^2 \chi_2[\Omega_{d2}]}{4m_1m_2d^2\Omega_1\Omega_2}} \quad Eq. 2.2.4.22$$

where the symbols ‘-’ and ‘+’ are red and blue sideband.

Table 2.2.4.3. Red sideband pump the phonon cavity and probe the coupled Al drum

| Parameter | SiN drum resonator <1> | Al drum resonator <2> |
|--|--|--|
| Resonance frequency | Ω_1 | Ω_2 |
| Displacement | $X_1(t) = \frac{x_1(t)}{2} e^{-i(\Omega_p + \Omega_{d2})t} + c.c$ | $X_2(t) = \frac{x_2(t)}{2} e^{-i\Omega_{d2}t} + c.c$ |
| Probe signal | No | $\Omega_{d2} = \Omega_2 + \delta$ |
| Pump signal | $\Omega_p = \Omega_1 - \Omega_2 + \Delta$ | No |
| Mechanical susceptibility | $\chi_1[\Omega_{d1}] = \frac{1}{\Omega_1 - \Omega_{d1} - i\frac{\gamma_1}{2}}$ | $\chi_2[\Omega_{d2}] = \frac{1}{\Omega_2 - \Omega_{d2} - i\frac{\gamma_2}{2}}$ |
| Definitions of mechanical susceptibility | $\chi_1^{red} = \frac{1}{-\Delta - \delta - i\frac{\gamma_1}{2}}$ | $\chi_2^{red} = \frac{1}{-\delta - i\frac{\gamma_2}{2}}$ |
| Solution of displacement | $x_1 = -\frac{f_p}{2m_1\Omega_1} \frac{x_2}{d} \chi_1[\Omega_{d1}]$ | $x_2 = -\frac{f_{d2}}{2m_2\Omega_2} \frac{1}{\chi_2^{-1}[\Omega_{d2}] - \frac{ f_p ^2 \chi_1[\Omega_{d1}]}{4m_1m_2d^2\Omega_1\Omega_2}}$ |
| Effective damping rate | No | $\gamma_{eff2}^{red} = \gamma_2 + \frac{ f_p ^2}{4m_1m_2d^2\Omega_1\Omega_2} \frac{\gamma_1}{(\Omega_1 - \Omega_{d1})^2 + \frac{\gamma_1^2}{4}}$ |

Red sideband pump the phonon-cavity and probe the coupled Al drum. We present the similar analytical analysis to the red sideband pumping abovementioned by Eq.2.2.4.4. We first use one signal with frequency Ω_{d2} to probe around mechanical resonator <2>, namely $\Omega_{d2} = \Omega_2 + \delta$. Here, δ indicates a frequency detuning from Ω_2 . Then, we use the other sideband signal to pump the phonon cavity at its red sideband $\sim \Omega_1 - \Omega_2$. A small pump frequency detuning Δ is defined to be $\Omega_p = \Omega_1 - \Omega_2 + \Delta$.

Considering that the mechanical system is driving with the probe and the pump, we have the $V_{ac}(\omega_p, \omega_{d2}) = \frac{\mu_p}{2} e^{-i\Omega_p t} + \frac{\mu_s}{2} e^{-i\Omega_{d2} t} + c. c$. We also define the probed mechanical resonator $X_2(t) = \frac{x_2(t)}{2} e^{-i\Omega_{d2} t} + c. c$ and the other coupled mechanical resonator $X_1(t) = \frac{x_2(t)}{2} e^{-i(\Omega_p + \Omega_{d2}) t} + c. c$. The frequency match is given by selecting these terms containing $e^{-i\Omega_{d1} t}$. Therefore, Eq.2.2.4.3(a) can be analysed and given by

$$\ddot{X}_1 + \gamma_1 \dot{X}_1 + \Omega_1^2 X_1 = -\frac{V_{dc} C_{g0} \mu_p x_2}{dm_1} \frac{1}{2d} e^{-i\Omega_{d1} t} \quad \text{Eq. 2.2.4.23(a)}$$

$$\ddot{X}_2 + \gamma_2 \dot{X}_2 + \Omega_2^2 X_2 = \frac{V_{dc} C_{g0}}{dm_2} \left(-\frac{x_{2s}}{2} - \frac{\mu_p^* x_1}{2d} \right) e^{-i\Omega_{d2} t} \quad \text{Eq. 2.2.4.23(b)}$$

Based on $\Omega_{d2} = \Omega_2 + \delta$ and $\Omega_{d1} = \Omega_1 + \Delta + \delta$, if $\Delta, \delta \rightarrow 0$, we have approximations $\Omega_1^2 - \Omega_{d1}^2 \approx 2\Omega_1(\Omega_1 - \Omega_{d1})$ and $\Omega_2^2 - \Omega_{d2}^2 \approx 2\Omega_2(\Omega_2 - \Omega_{d2})$. The analytical equations are modified by

$$\Omega_1 \chi_1^{-1}[\Omega_{d1}] x_1 = -\frac{V_{dc} C_{g0} \mu_p x_2}{dm_1} \frac{1}{2d} \quad \text{Eq. 2.2.4.24(a)}$$

$$\Omega_2 \chi_2^{-1}[\Omega_{d2}] x_2 = \frac{V_{dc} C_{g0}}{dm_2} \left(-\frac{\mu_s}{2} - \frac{\mu_p^* x_1}{2d} \right) \quad \text{Eq. 2.2.4.24(b)}$$

where $\chi_1[\Omega_{d1}] = \frac{1}{\Omega_1 - \Omega_{d1} - i\frac{\gamma_1}{2}}$ and $\chi_2[\Omega_{d2}] = \frac{1}{\Omega_2 - \Omega_{d2} - i\frac{\gamma_2}{2}}$ are the mechanical susceptibilities, μ_s is a probe signal amplitude, x_1 and x_2 are the slow varying complex amplitudes of the mechanical displacements as before.

So, the analytical solutions from Eq.2.2.4.24 are given by

$$x_1 = -\frac{f_p}{2m_1\Omega_1} \frac{x_2}{d} \chi_1[\Omega_{d1}] \quad \text{Eq. 2.2.4.25(a)}$$

$$x_2 = -\frac{f_{d2}}{2m_2\Omega_2} \frac{1}{\chi_2^{-1}[\Omega_{d2}] - \frac{|f_p|^2 \chi_1[\Omega_{d1}]}{4m_1 m_2 d^2 \Omega_1 \Omega_2}} \quad \text{Eq. 2.2.4.25(b)}$$

where $f_{d2} = \frac{V_{dc} C_{g0} \mu_s}{d}$ is the probe force and $f_p = \frac{V_{dc} C_{g0} \mu_p}{d}$ is the pump force.

Then, the effective damping rate at red sideband is given by

$$\gamma_{eff2}^{red} = \gamma_2 + \frac{|f_p|^2}{4m_1m_2d^2\Omega_1\Omega_2} \frac{\gamma_1}{(\Omega_1 - \Omega_{d1})^2 + \frac{\gamma_1^2}{4}} \quad Eq. 2.2.4.26$$

We define the mechanical susceptibilities $\chi_{1,2}^{red}$ when probing at the frequency $\Omega_{d2} = \Omega_2 + \delta$ and red sideband pumping at the frequency $\Omega_p = \Omega_1 - \Omega_2 + \Delta$. They are given by

$$\chi_1^{red} = \frac{1}{-\Delta - \delta - i\frac{\gamma_1}{2}} \quad Eq. 2.2.4.27(a)$$

$$\chi_2^{red} = \frac{1}{-\delta - i\frac{\gamma_2}{2}} \quad Eq. 2.2.4.27(b)$$

Table 2.2.4.4. Blue sideband pump the phonon cavity and probe the coupled Al drum

| Parameter | SiN drum resonator <1> | Al drum resonator <2> |
|--|--|---|
| Resonance frequency | Ω_1 | Ω_2 |
| Displacement | $X_1(t) = \frac{x_1(t)}{2} e^{-i(\Omega_p + \Omega_{d2})t} + c.c$ | $X_2(t) = \frac{x_2(t)}{2} e^{-i\Omega_{d2}t} + c.c$ |
| Probe signal | No | $\Omega_{d2} = \Omega_2 + \delta$ |
| Pump signal | $\Omega_p = \Omega_1 + \Omega_2 + \Delta$ | No |
| Mechanical susceptibility | $\chi_1[\Omega_{d1}] = \frac{1}{\Omega_1 - \Omega_{d1} - i\frac{\gamma_1}{2}}$ | $\chi_2[\Omega_{d2}] = \frac{1}{\Omega_2 - \Omega_{d2} - i\frac{\gamma_2}{2}}$ |
| Definitions of mechanical susceptibility | $\chi_1^{blue} = \frac{1}{\delta - \Delta - i\frac{\gamma_1}{2}}$ | $\chi_2^{blue} = \frac{1}{-\delta - i\frac{\gamma_2}{2}}$ |
| Solution of displacement | $x_1 = -\frac{f_p}{2m_1\Omega_1} \frac{x_2^*}{d} \chi_1[\Omega_{d1}]$ | $x_2 = -\frac{f_{d2}}{2m_2\Omega_2} \frac{1}{\chi_2^{-1}[\Omega_{d2}] - \frac{ f_p ^2 \chi_1^*[\Omega_{d1}]}{4m_1m_2d^2\Omega_1\Omega_2}}$ |
| Effective damping rate | No | $\gamma_{eff2}^{blue} = \gamma_2 - \frac{ f_p ^2}{4m_1m_2d^2\Omega_1\Omega_2} \frac{\gamma_1}{(\Omega_1 - \Omega_{d1})^2 + \frac{\gamma_1^2}{4}}$ |

Blue sideband pump the phonon-cavity and probe the coupled Al drum. We follow the similar analysis to the blue sideband pumping abovementioned by Eq.2.2.4.13. We remain probing around the mechanical resonator <2> with the frequency $\Omega_{d2} = \Omega_2 + \delta$ and pumping the phonon cavity mechanical resonator <1> with a blue sideband at the frequency $\Omega_p = \Omega_1 + \Omega_2 + \Delta$. The analytical motion equations can be analysed and given by

$$\ddot{X}_1 + \gamma_1 \dot{X}_1 + \Omega_1^2 X_1 = -\frac{V_{dc} C_{g0} \mu_p x_2^*}{dm_1} e^{-i\Omega_{d1}t} \quad Eq. 2.2.4.28(a)$$

$$\ddot{X}_2 + \gamma_2 \dot{X}_2 + \Omega_2^2 X_2 = \frac{V_{dc} C_{g0}}{dm_2} \left(-\frac{\mu_s}{2} - \frac{\mu_p x_1^*}{2d} \right) e^{-i\Omega_{d2}t} \quad Eq. 2.2.4.28(b)$$

Based on $\Omega_{d2} = \Omega_2 + \delta$ and $\Omega_{d1} = \Omega_1 + \Delta - \delta$, if $\Delta, \delta \rightarrow 0$, we have approximations $\Omega_1^2 - \Omega_{d1}^2 \approx 2\Omega_1(\Omega_1 - \Omega_{d1})$ and $\Omega_2^2 - \Omega_{d2}^2 \approx 2\Omega_2(\Omega_2 - \Omega_{d2})$. The modified equations become

$$\Omega_1 \chi_1^{-1}[\Omega_{d1}] x_1 = -\frac{V_{dc} C_{g0} \mu_p x_2^*}{dm_1} \quad Eq. 2.2.4.29(a)$$

$$\Omega_2 \chi_2^{-1}[\Omega_{d2}] x_2 = \frac{V_{dc} C_{g0}}{dm_2} \left(-\frac{\mu_s}{2} - \frac{\mu_p x_1^*}{2d} \right) \quad Eq. 2.2.4.29(b)$$

where $\chi_1[\Omega_{d1}] = \frac{1}{\Omega_1 - \Omega_{d1} - i\frac{\gamma_1}{2}}$ and $\chi_2[\Omega_{d2}] = \frac{1}{\Omega_2 - \Omega_{d2} - i\frac{\gamma_2}{2}}$ are the mechanical susceptibilities, μ_s is a probe signal amplitude, x_1 and x_2 are the slow varying complex amplitudes of the mechanical displacements.

Therefore, the analytical solutions from Eq.2.2.4.29 are given by

$$x_1 = -\frac{f_p}{2m_1\Omega_1} \frac{x_2^*}{d} \chi_1[\Omega_{d1}] \quad Eq. 2.2.4.30(a)$$

$$x_2 = -\frac{f_{d2}}{2m_2\Omega_2} \frac{1}{\chi_2^{-1}[\Omega_{d2}] - \frac{|f_p|^2 \chi_1^*[\Omega_{d1}]}{4m_1 m_2 d^2 \Omega_1 \Omega_2}} \quad Eq. 2.2.4.30(b)$$

where $f_{d2} = \frac{V_{dc} C_{g0} \mu_s}{d}$ is the probe force and $f_p = \frac{V_{dc} C_{g0} \mu_p}{d}$ is the pump force.

Moreover, the effective damping rate at blue sideband is given by

$$\gamma_{eff2}^{blue} = \gamma_2 - \frac{|f_p|^2}{4m_1 m_2 d^2 \Omega_1 \Omega_2} \frac{\gamma_1}{(\Omega_1 - \Omega_{d1})^2 + \frac{\gamma_1^2}{4}} \quad Eq. 2.2.4.31$$

We define the mechanical susceptibilities $\chi_{1,2}^{blue}$ when using probe signal at the frequency $\Omega_{d2} = \Omega_2 + \delta$ and red sideband pump at the frequency $\Omega_p = \Omega_1 + \Omega_2 + \Delta$. Then, the mechanical susceptibilities $\chi_{1,2}^{blue}$ at blue sideband are given by

$$\chi_1^{blue} = \frac{1}{\delta - \Delta - i\frac{\gamma_1}{2}} \quad Eq. 2.2.4.32(a)$$

$$\chi_2^{blue} = \frac{1}{-\delta - i\frac{\gamma_2}{2}} \quad Eq. 2.2.4.32(b)$$

Again, we compare the mechanical susceptibilities between at red and blue sidebands. In this case, no relevant analytical result is seen due to $\chi_1^{red} \neq -\chi_1^{*blue}$. Hence, we cannot rewrite the analytical red and blue sideband solutions together, which differs from the case that we probe the signal at the phonon-cavity resonator $\langle 1 \rangle$.

2.2.4.2 Simulation results of the nanoelectromechanically induced transparency and amplification

In order to build the electromechanical phonon interference analog to the optomechanical system, we write the coupling strength of the mechanical resonator $\langle 1 \rangle$ as $G = \frac{\partial \Omega_1}{\partial X_2} \approx \frac{\partial \Omega_1}{\partial C_g} \frac{\partial C_g}{\partial X_2} \approx -\frac{\Omega_1}{2d}$. Using it, we provide single phonon coupling rate $g_0 = G x_{zpf}$, where $x_{zpf} = \sqrt{\frac{\hbar}{2m_2\Omega_2}}$ is zero-point fluctuation of the coupled mechanical resonator $\langle 2 \rangle$ with the low resonance frequency Ω_2 . We therefore take a transform of $\frac{|f_p|^2}{4m_1m_2d^2\Omega_1\Omega_2}$ to $n_p g_0^2 \approx \frac{2|f_p|^2}{m_1\Omega_1^2} \frac{g_0^2}{\hbar\Omega_p}$, where n_p is a definition of the phonon number generated by pump tone. Because the mechanical system is driven by the probe and pump, the analytical solutions of the coupled mechanical resonators at red and blue sidebands can be rewritten by

$$x_1 = \frac{f_{d1}}{2m_1\Omega_1} \frac{1}{\chi_1^{-1}[\Omega_{d1}] \pm n_p g_0^2 \chi_2[\Omega_{d2}]} \quad Eq. 2.2.4.33$$

where ‘-’ and ‘+’ are red and blue sidebands.

In this part, 100 nm thick SiN drum membrane with a tensile stress of 1.0 GPa and with a diameter of 40 μm is chosen for achieving resonance frequency around 11.78 MHz. Capacitive coupling distance between SiN drum and Al top gate is defined to be 500 nm for calculating a desired capacitance value $C_{g0}(d = 500 \text{ nm}, D = 40 \mu m) = 2.22 \times 10^{-14} \text{ F}$.

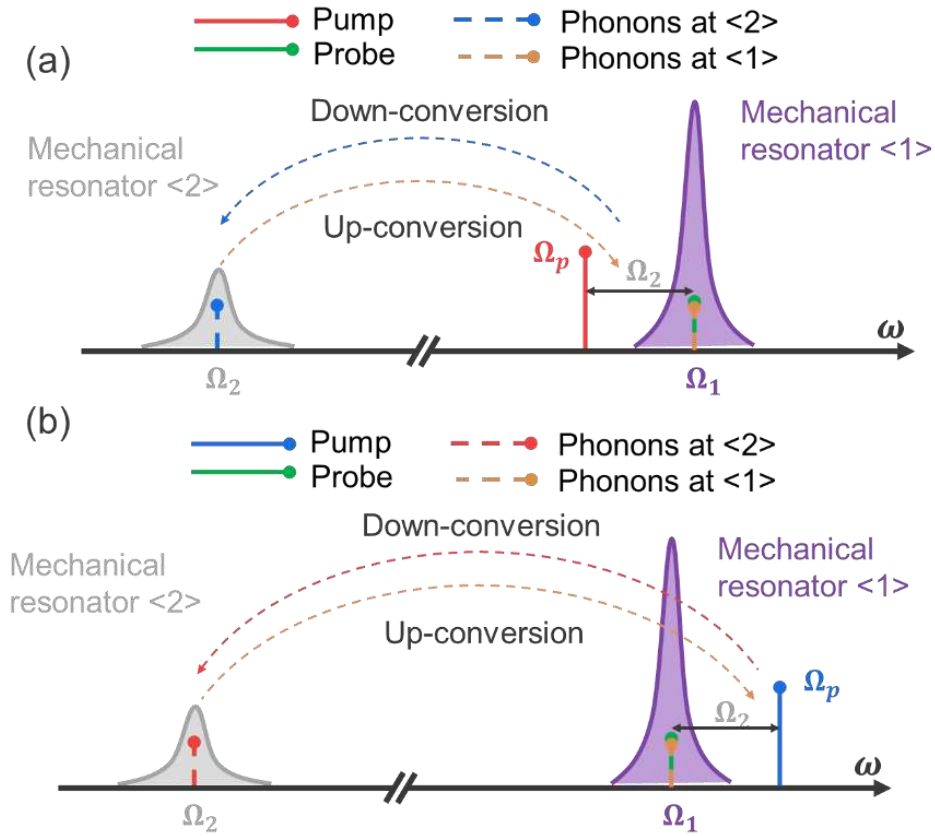


Figure 2.2.4.4. Spectrum landscape at red and blue sideband pumping while probing the phonon cavity. Green color is the probe signal, (a) red color is the red sideband pump signal; (b) blue color is the blue sideband pump signal.

Fig. 2.2.4.4 shows red and blue sideband pumping the phonon-cavity mechanical resonator $\langle 1 \rangle$ can generate phonons transferring to the unprobed mechanical resonator $\langle 2 \rangle$. Then, the phonons stored in the mechanical resonator $\langle 2 \rangle$ corresponding to the term $n_p g_0^2 \chi_2[\Omega_{d2}]$ can be fed back to the initial probed mechanical resonator $\langle 1 \rangle$ related to the term of $\chi_1[\Omega_{d1}]$ through controlling the pump tone. As the mechanical system consisting of two circular membranes modelled in Eq.2.2.4.33, the number creation of phonons depends on n_p from the pump tone. The interference efficiency therefore can be enhanced when controlling the number of phonons.

Red sideband pump the phonon-cavity and probe the phonon cavity.

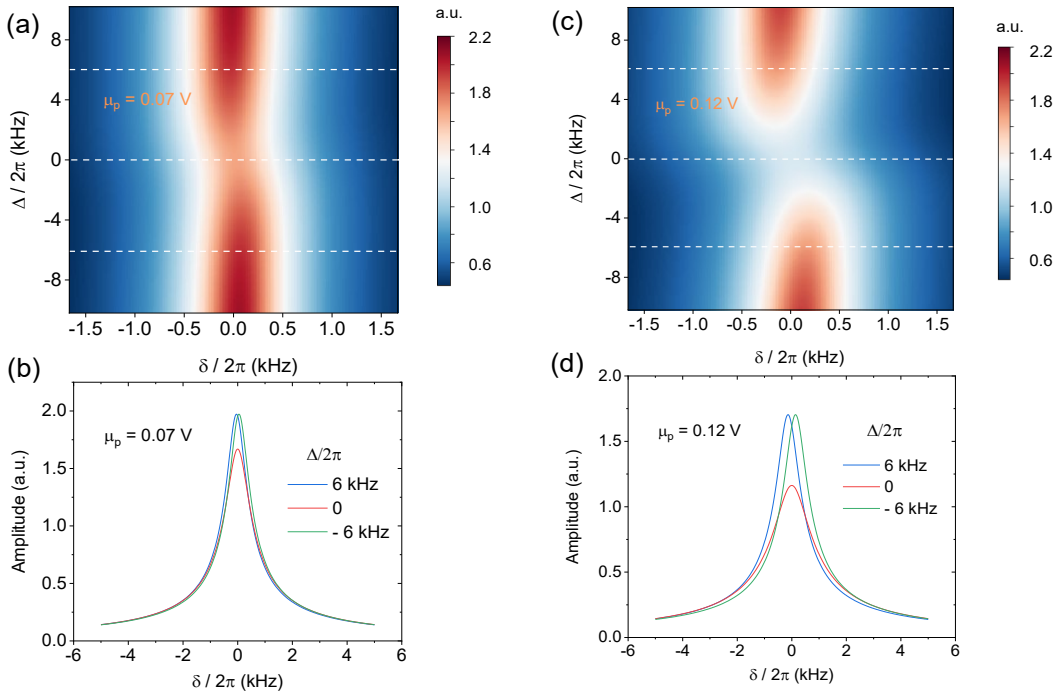


Figure 2.2.4.5. Simulation results of electromechanically induced transparency at red sideband pumping scheme. (a) Mechanical amplitude mapping for the phonon-cavity mechanical resonator $\langle 1 \rangle$, where Δ and δ are the detunings from red sideband and the probe signal respectively. (b) Lorentzian curves are extracted from the white dashed lines in (a), with $\frac{\Delta}{2\pi} = 6, 0, -6$ kHz. The color bar is mechanical amplitude. (a,b) The pump amplitude is $\mu_p = 0.07$ V; (c,d) The pump amplitude is $\mu_p = 0.12$ V.

Fig. 2.2.4.5(a) shows simulated results of electromechanically induced transparency [119][120] when red sideband pumping at the phonon cavity. In this simulation, we use essential parameters including the high frequency $\frac{\Omega_1}{2\pi} = 11.78$ MHz, the low frequency $\frac{\Omega_2}{2\pi} = 2.94$ MHz, effective masses of mechanical resonator $\langle 1 \rangle$ about $m_1 = 4.4 \times 10^{-14}$ kg and mechanical resonator $\langle 2 \rangle$ about $m_2 = 4.41 \times 10^{-13}$ kg, a capacitive gap distance of about 500 nm, and a diameter of circular membrane about 40 μm . Based on pump amplitude $\mu_p = 0.07$ V, we use red sideband $\Omega_p = \Omega_1 - \Omega_2 + \Delta$ to pump the phonon cavity with Δ sweeping window from -10 to 10 kHz, and weakly probe the phonon-cavity mechanical resonator $\langle 1 \rangle$ with δ sweeping window from -1.5 to 1.5 kHz. When choosing the detuning $\frac{\Delta}{2\pi} = 6, 0, -6$ kHz, the amplitude of the phonon cavity can be achieved in **Fig. 2.2.4.5(b)**. It means the amplitude of phonon cavity

also depends on the detuning $\frac{\Delta}{2\pi}$ when keeping the pump amplitude same. For the physics, the pump signal acting on the phonon cavity can provide enough phonons to the coupled mechanical resonator <2>, namely an energy transfer station. The stored phonons at <2> can be fed back to the probed resonator <1>. At this red sideband, destructive phonon interference between the probed phonons and phonons induced by the pump can be established.

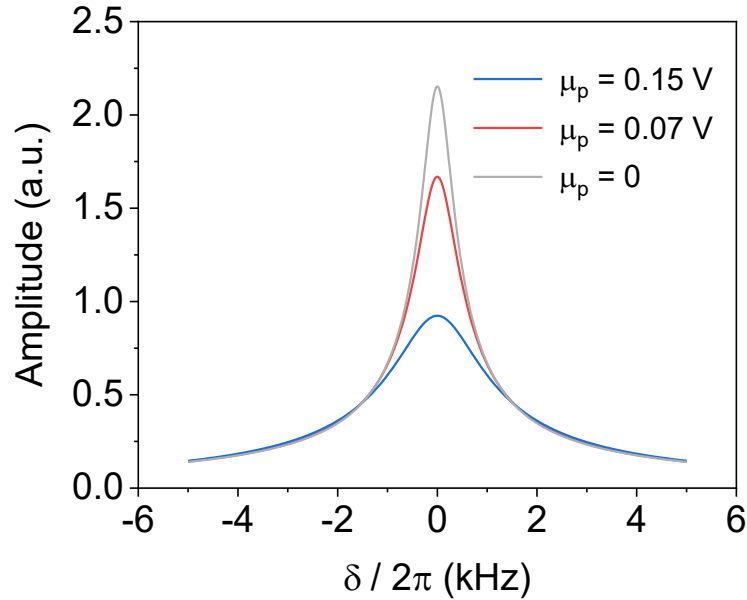


Figure 2.2.4.6. Simulation results of electromechanically induced transparency at red sideband pumping scheme. Three red, blue and grey curves performing at $\frac{\Delta}{2\pi} = 0$ correspond to different pump amounts.

Different pump amplitudes are set to pump the electromechanical system to vary the mechanical amplitude of the phonon cavity referring to as the resonator <1>. **Fig. 2.2.4.6** shows strong suppression of mechanical amplitudes when increasing pump amplitude from 0 to 0.15 V.

When looking back to Eq.2.2.4.11, we noticed that the effective damping rate $\gamma_{eff1}^{red} = \gamma_1 + \frac{|f_p|^2}{4m_1m_2d^2\Omega_1\Omega_2} \frac{\gamma_2}{(\Omega_2 - \Omega_{d2})^2 + \frac{\gamma_2^2}{4}}$ can be increased with the pump amplitude increasing, suppressing

the mechanical responses much more when $\Omega_2 \sim \Omega_{d2}$. That is the reason that we see clearly the mechanical amplitude decreasing in the centre of the sweeping window.

Blue sideband pump the phonon cavity and probe the phonon cavity.

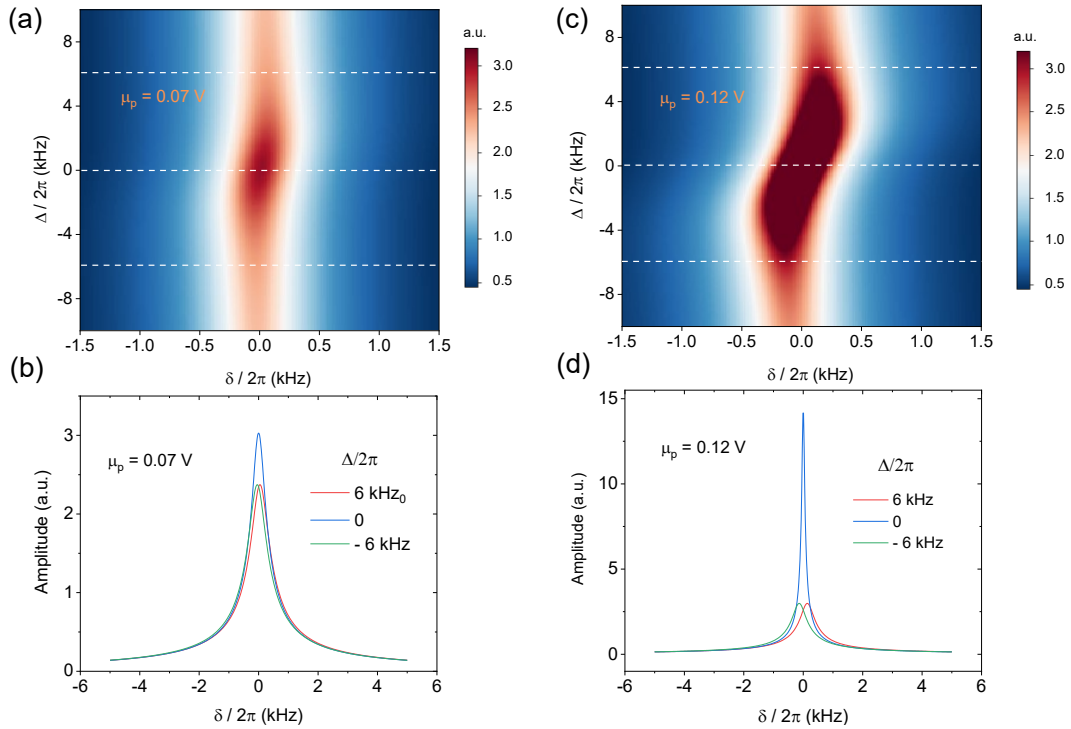


Figure 2.2.4.7. Simulation results of electromechanically induced amplification at blue sideband pumping scheme. (a) Mechanical amplitude mapping for the phonon-cavity mechanical resonator $\langle 1 \rangle$, where Δ is detuned from blue sideband and δ is detuned from the probe signal. (b) Lorentzian curves are extracted from the white dashed lines in (a), with $\frac{\Delta}{2\pi} = 6, 0, -6$ kHz. The color bar is mechanical amplitude. (a,b) The pump amplitude is $\mu_p = 0.07$ V; (c,d) The pump amplitude is $\mu_p = 0.12$ V.

Fig. 2.2.4.7(a) shows simulated results of electromechanically induced amplification [117] [120] when blue sideband pumping at the phonon cavity. In this simulation, we use same simulation parameters with the red sideband. Based on mechanical amplitude $\mu_p = 0.07$ V, we use blue sideband $\Omega_p = \Omega_1 + \Omega_2 + \Delta$ to pump the phonon cavity with Δ sweeping from -10 to 10 kHz, and weakly probe the phonon-cavity mechanical resonator $\langle 1 \rangle$ with δ sweeping from -1.5 to 1.5 kHz. When choosing the detuning $\frac{\Delta}{2\pi} = 6, 0, -6$ kHz, the mechanical amplitudes of the phonon cavity are able to be observed in **Fig. 2.2.4.7(b)**. For this blue sideband case, the phonon cavity can create down-conversion phonons to the coupled mechanical resonator $\langle 2 \rangle$. The stored phonons at $\langle 2 \rangle$ can be up-conversion fed back to the probed resonator $\langle 1 \rangle$. For this

physics, constructive phonon interference between the probed phonons and phonons from the pump can be established.

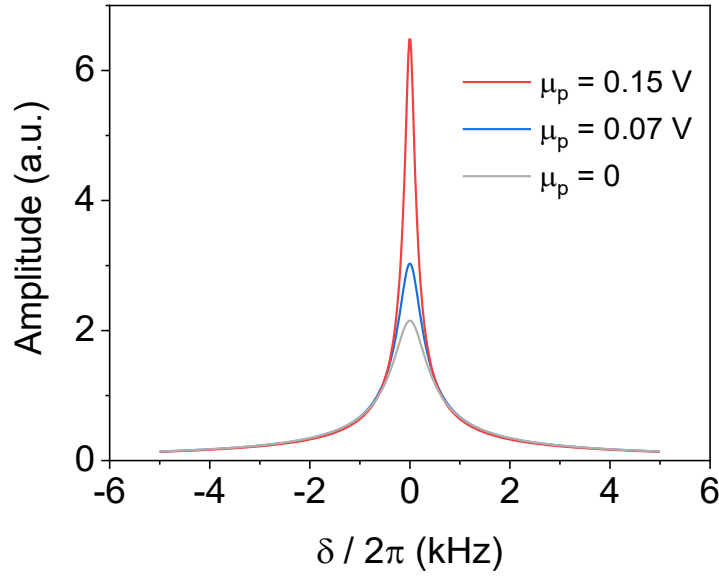


Figure 2.2.4.8. Simulation results of electromechanically induced amplification at blue sideband pumping scheme. Three blue, red and grey curves performing at $\frac{\Delta}{2\pi} = 0$ correspond to different pump amounts.

Different pump amplitudes onto pump the electromechanical system are used, so that they routinely vary the mechanical amplitude of the resonator $\langle 1 \rangle$. **Fig. 2.2.4.8** shows an amplification trend of mechanical amplitudes when the pump intensity increases from 0 to 0.15V. When looking back to Eq.2.2.4.20, we noted a decrease of the effective damping rate,

namely $\gamma_{eff1}^{blue} = \gamma_1 - \frac{|f_p|^2}{4m_1m_2d^2\Omega_1\Omega_2} \frac{\gamma_2}{(\Omega_2 - \Omega_{d2})^2 + \frac{\gamma_2^2}{4}}$, amplifying the mechanical amplitudes when

$\Omega_2 \sim \Omega_{d2}$. We therefore see the mechanical amplitude increasing in the centre of the sweeping window.

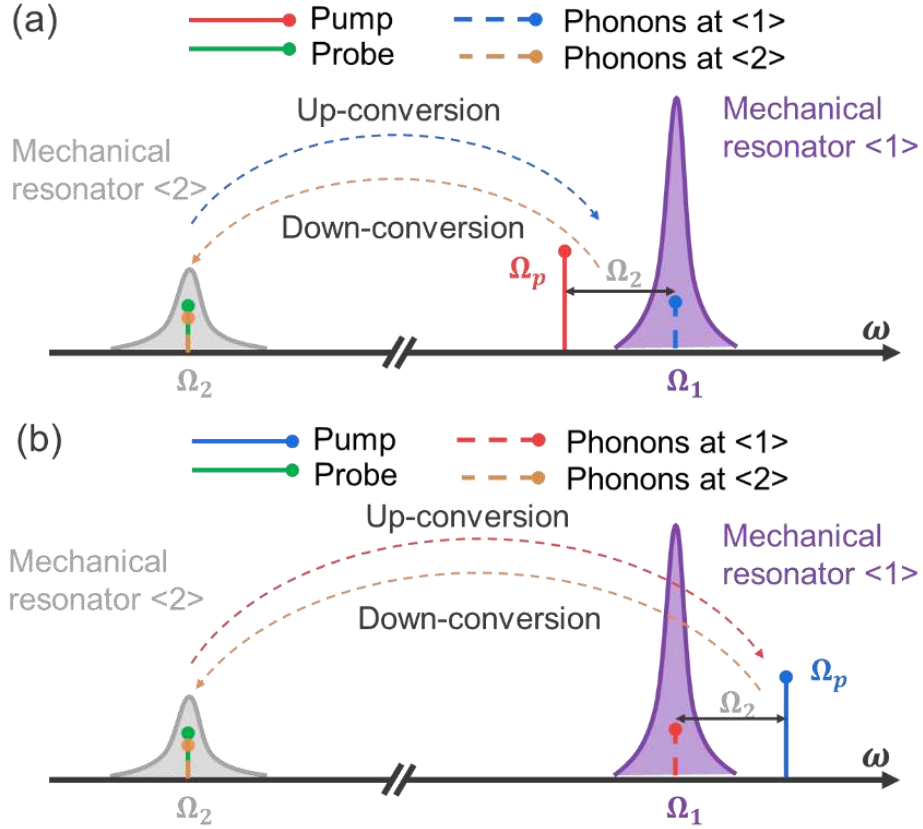


Figure 2.2.4.9. Spectrum landscape at red and blue sideband pumping while probing the coupled mechanical resonator $\langle 2 \rangle$. Green color is the probe signal, (a) red signal bar is the red sideband pump signal; (b) blue signal bar is the blue sideband pump signal.

Fig. 2.2.4.9 shows while probing the coupled mechanical resonator $\langle 2 \rangle$, red and blue sideband pumping the phonon-cavity mechanical resonator $\langle 1 \rangle$ can generate transferring phonons at the unprobed mechanical resonator. Then, the phonons stored in the mechanical resonator $\langle 1 \rangle$ corresponding to the term $n_p g_0^2 \chi_1[\Omega_{d2}]$ or $n_p g_0^2 \chi_1^*[\Omega_{d1}]$ can be fed back to the initial probed mechanical resonator $\langle 2 \rangle$ related to the term of $\chi_2[\Omega_{d2}]$ through controlling the pump tone. As the mechanical system modelled in Eq.2.2.4.25 and Eq.2.2.4.30, the number of phonons depends on n_p from the pump tone. Therefore, the interference efficiency can be enhanced when controlling the number of phonons.

Red sideband pump the phonon cavity and probe the coupled Al drum.

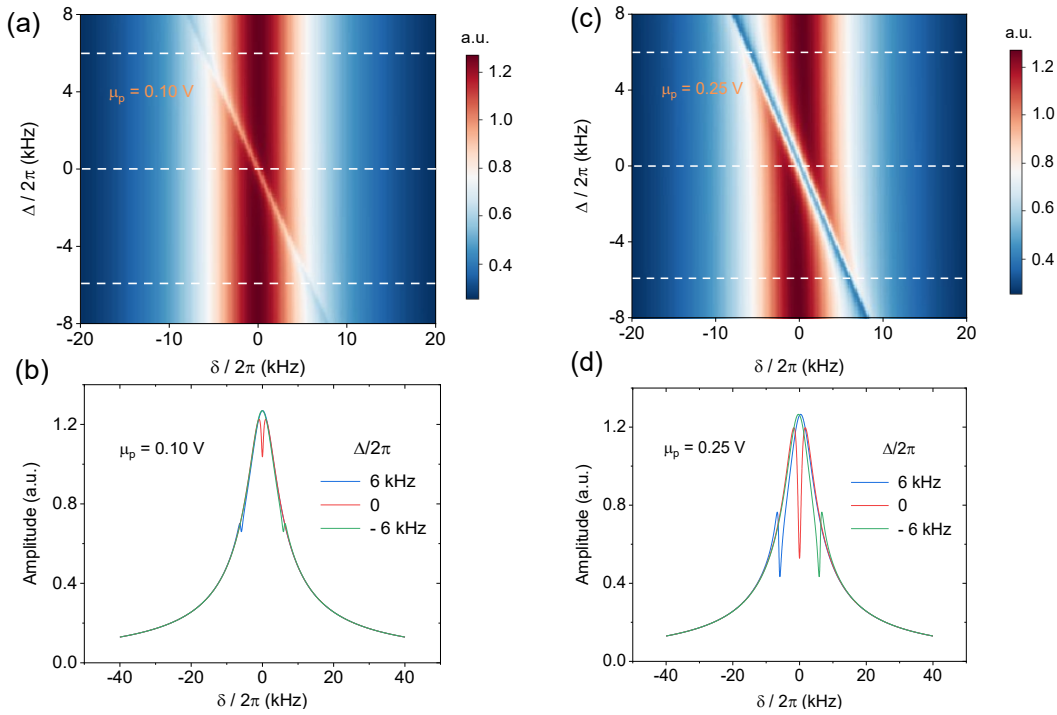


Figure 2.2.4.10. Simulation results of electromechanically induced transparency at red sideband pumping scheme. (a) Mechanical amplitude mapping for the coupled mechanical resonators $\langle 2 \rangle$, where Δ is detuned from red sideband and δ is detuned from the probe signal. (b) Lorentzian curves are extracted from the white dashed lines in (a), with $\frac{\Delta}{2\pi} = 6, 0, -6$ kHz. The color bar is mechanical amplitude. (a,b) The pump amplitude is $\mu_p = 0.1$ V; (c,d) The pump amplitude is $\mu_p = 0.25$ V.

Fig. 2.2.4.10(a) shows simulated results of electromechanically induced transparency [119][120] when red sideband pumping at the phonon cavity. In this simulation, we use simulation parameters including the high frequency $\frac{\Omega_1}{2\pi} = 11.78$ MHz, the low frequency $\frac{\Omega_2}{2\pi} = 2.94$ MHz, effective masses of mechanical resonator $\langle 1 \rangle$ about $m_1 = 4.4 \times 10^{-14}$ kg and mechanical resonator $\langle 2 \rangle$ about $m_2 = 4.41 \times 10^{-13}$ kg, a capacitive gap distance of about 500 nm, and a diameter of circular membrane about 40 μm . By using the pump amplitude $\mu_p = 0.1$ V, we use red sideband $\Omega_p = \Omega_1 - \Omega_2 + \Delta$ to pump the phonon cavity with Δ sweeping window from -8 to 8 kHz, and weakly probe the coupled mechanical resonator $\langle 2 \rangle$ with δ sweeping window from -20 to 20 kHz. When choosing the detuning $\frac{\Delta}{2\pi} = 6, 0, -6$ kHz, the mechanical amplitude for the coupled resonator $\langle 2 \rangle$ can be captured in **Fig.2.2.4.10(b)**. It indicates that the

mechanical response also relies on the detuning $\frac{\Delta}{2\pi}$. In this red sideband case, probing the coupled resonator $\langle 2 \rangle$ can generate phonons acting onto the phonon cavity $\langle 1 \rangle$. These phonons subsequently go back to the probed the resonator $\langle 2 \rangle$. For the physics, destructive phonon interference between the phonons at $\langle 2 \rangle$ from the probe signal and the phonons at $\langle 1 \rangle$ from the pump signal is established.

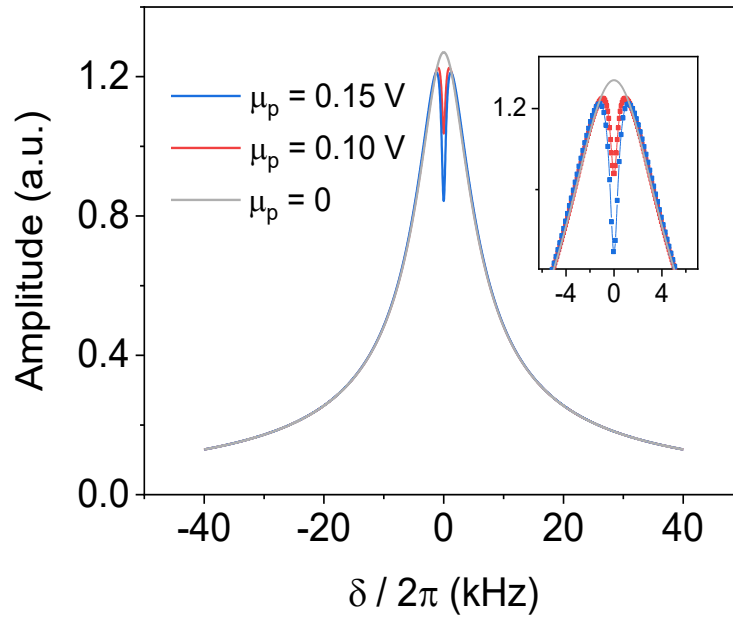


Figure 2.2.4.11. Simulation results of electromechanically induced transparency at red sideband pumping scheme. Three red, blue and grey curves performing at $\frac{\Delta}{2\pi} = 0$ correspond to different pump amounts. Inset shows the enlarged region.

Different pump amplitudes are implemented to pump the mechanical system to vary the mechanical amplitude for the coupled mechanical resonator $\langle 2 \rangle$. **Fig. 2.2.4.11** shows a suppression trend of mechanical amplitudes when the pump intensity increases from 0 to 0.15V. When looking back to Eq.2.2.4.26, we noted that the effective damping rate $\gamma_{eff2}^{red} = \gamma_2 + \frac{|f_p|^2}{4m_1m_2d^2\Omega_1\Omega_2} \frac{\gamma_1}{(\Omega_1 - \Omega_{d1})^2 + \frac{\gamma_1^2}{4}}$ can be increased, suppressing the mechanical amplitudes when $\Omega_1 \sim \Omega_{d1}$. While satisfying the damping rates $\gamma_1 > \gamma_2$, we observe Lorentz simulation curves of mechanical amplitudes with a much narrower dip in the transparency frequency window, where the dip is clear due to the frequency bandwidth of the transparency effect effected by the damping rate of the unprobed mechanical resonator $\langle 1 \rangle$.

Blue sideband pump the phonon cavity and probe the coupled Al drum.

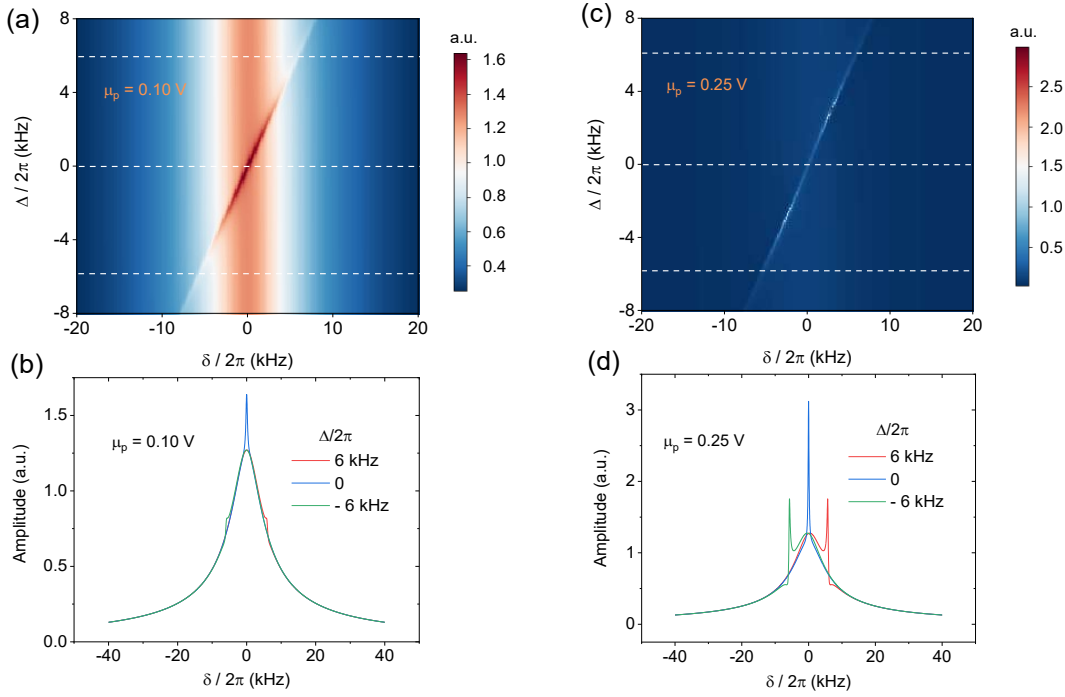


Figure 2.2.4.12. Simulation results of electromechanically induced amplification at blue sideband pumping scheme. (a) Mechanical amplitude mapping for the coupled mechanical resonator $\langle 2 \rangle$, where Δ detuned from blue sideband and δ detuned from the probe signal. (b) Lorentzian simulation curves are extracted from the white dashed lines in (a), with $\frac{\Delta}{2\pi} = 6, 0, -6$ kHz. The color bar is mechanical amplitude. (a,b) The pump amplitude is $\mu_p = 0.1 \text{ V}$; (c,d) The pump amplitude is $\mu_p = 0.25 \text{ V}$.

Fig. 2.2.4.12(a) shows simulated results of electromechanically induced amplification [120][117] when blue sideband pumping at the phonon cavity. In this simulation, we use same simulated parameters with the red sideband. When using $\mu_p = 0.1 \text{ V}$, we use blue sideband $\Omega_p = \Omega_1 + \Omega_2 + \Delta$ to pump the phonon cavity with Δ sweeping from -8 to 8 kHz, and weakly probe the coupled mechanical resonator $\langle 2 \rangle$ with δ sweeping from -20 to 20 kHz. Choosing the detuning $\frac{\Delta}{2\pi} = 6, 0, -6$ kHz, the mechanical amplitude of the coupled resonator $\langle 2 \rangle$ can be shown in **Fig. 2.2.4.12(b)**. It proves that the amplitude correlates to the detuning Δ . For this blue sideband manipulation, the coupled mechanical resonator $\langle 2 \rangle$ creates up-conversion phonons onto the phonon-cavity mechanical resonator $\langle 1 \rangle$. These phonons then can be down-conversion fed back to the probed resonator $\langle 2 \rangle$. For this blue sideband physics,

constructive phonon interference between the phonons at $\langle 2 \rangle$ and phonons at $\langle 1 \rangle$ can be established.

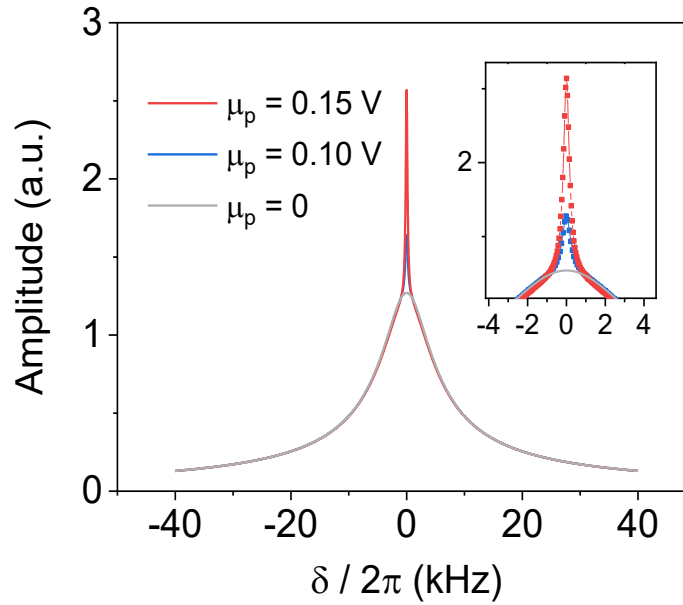


Figure 2.2.4.13. Simulation results of electromechanically induced amplification at blue sideband pumping scheme. Three blue, red and grey curves performing at $\frac{\Delta}{2\pi} = 0$ correspond to different pump amounts. Inset shows the enlarged region.

Different pump amplitudes pump the mechanical system to investigate the mechanical amplitude of the coupled mechanical resonator $\langle 2 \rangle$. **Fig. 2.2.4.13** shows an amplification trend of mechanical amplitudes when the pump intensity increases from 0 to 0.15 V. Looking back to Eq.2.2.4.31, we noticed that the effective damping rate $\gamma_{eff2}^{blue} = \gamma_2 - \frac{|f_p|^2}{4m_1m_2d^2\Omega_1\Omega_2} \frac{\gamma_1}{(\Omega_1 - \Omega_{d1})^2 + \frac{\gamma_1^2}{4}}$ gets to be decreased, amplifying the mechanical amplitudes when $\Omega_1 \sim \Omega_{d1}$. In terms of satisfying the damping rates $\gamma_1 > \gamma_2$, we observe clearly Lorentz simulation curves of mechanical amplitudes with a narrow peak in the amplification frequency window. It indicates that the smaller damping rate from the phonon cavity determines the frequency bandwidth window from the coupled mechanical resonator $\langle 2 \rangle$.

2.2.4.3 Motion behaviours between two parallel circular membranes in the nanoelectromechanical system

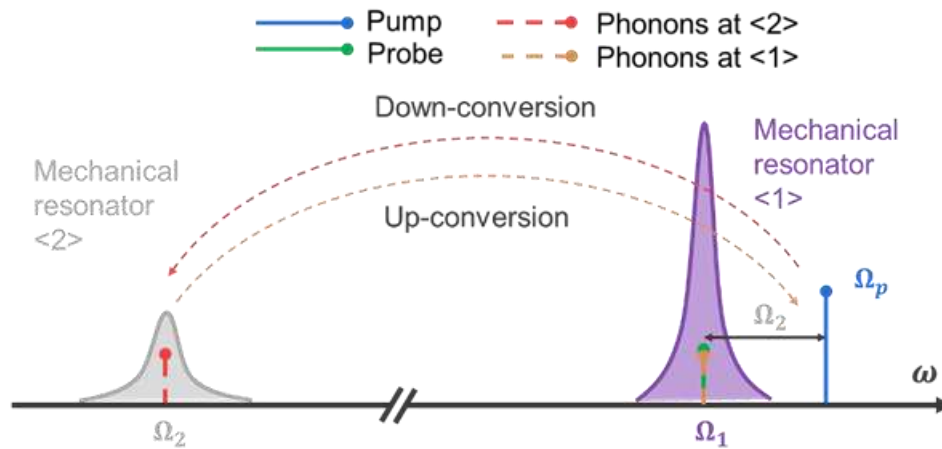


Figure 2.2.4.14. Blue sideband pump the phonon cavity and probe the phonon cavity. Green color is the probe signal and blue color is the blue sideband pump signal.

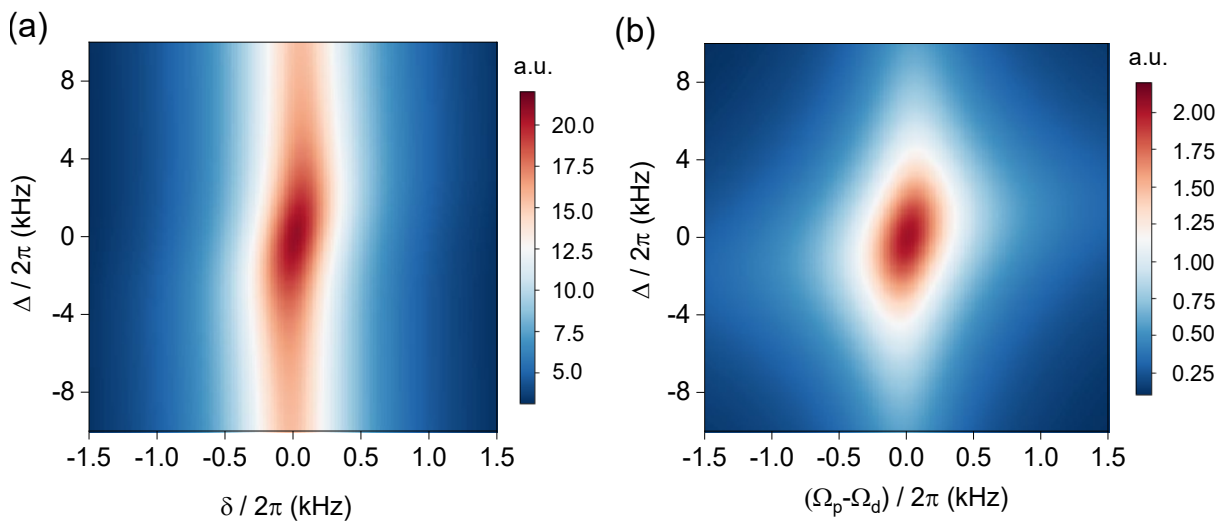


Figure 2.2.4.15. Simulation results of electromechanically induced amplification at blue sideband pumping while probing the phonon-cavity mechanical resonator $\langle 1 \rangle$. (a) Mechanical amplitude mapping for the phonon-cavity mechanical resonator $\langle 1 \rangle$. (b) Simultaneous mechanical amplitude mapping for the coupled mechanical resonator $\langle 2 \rangle$. The color bar is mechanical amplitude. The pump amplitude is $\mu_p = 0.07$ V.

Blue sideband to pump the phonon-cavity mechanical resonator $\langle 1 \rangle$ is used while probing the phonon cavity itself. **Fig. 2.2.4.15(a)** analytically calculated by Eq. 2.2.4.19(a) shows simulating the electromechanically induced amplification [120][117] at blue sideband pumping, indicating the establishment of constructive phonon interference between the phonons from the probe and the pump. Correspondingly, **Fig. 2.2.4.15(b)** analytically calculated by Eq. 2.2.4.19(b) shows the interfered interaction of the coupled mechanical resonator $\langle 2 \rangle$ with the phonon cavity in this electromechanical system.

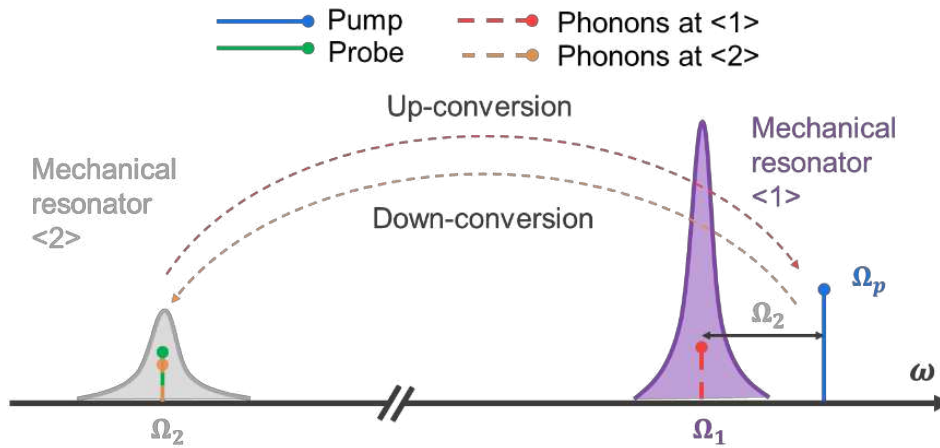


Figure 2.2.4.16. Blue sideband pump the phonon cavity and probe the coupled Al drum. Green color is the probe signal and blue color is the blue sideband pump signal.

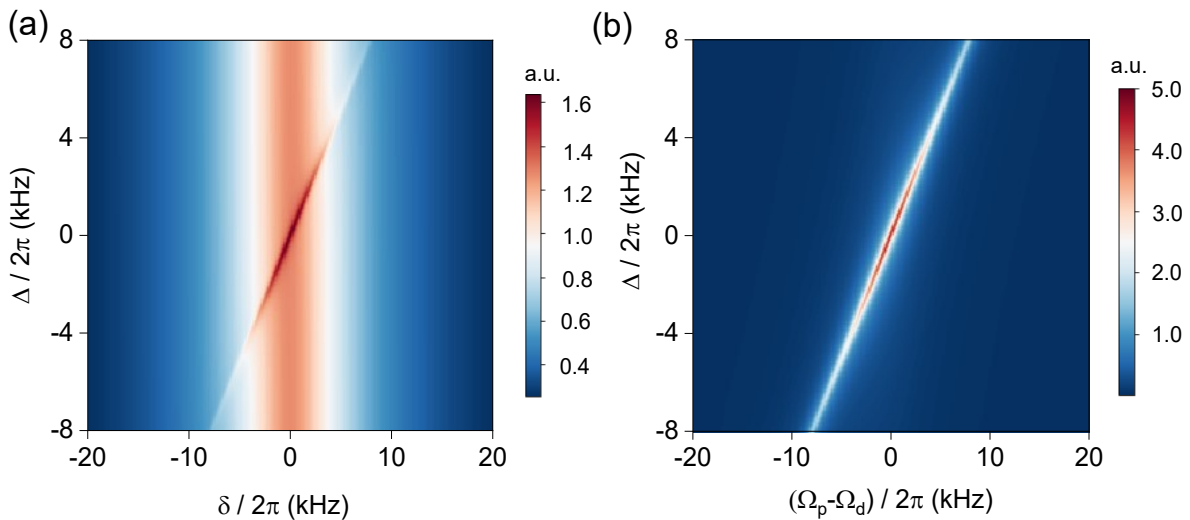


Figure 2.2.4.17. Simulation results of electromechanically induced amplification at blue sideband pumping while probing the mechanical resonator $\langle 2 \rangle$. (a) Mechanical amplitude for the coupled mechanical resonator $\langle 2 \rangle$. (b) Mechanical amplitude mapping for the phonon-

cavity mechanical resonator <1>. The color bar is mechanical amplitude. The pump amplitude is $\mu_p = 0.1$ V.

In addition, blue sideband can be employed to pump the phonon-cavity mechanical resonator <1> while probing the other coupled mechanical resonator <2>. **Fig. 2.2.4.17(a)** analytically calculated by Eq. 2.2.4.30(b) shows simulation of the electromechanically induced amplification [120][117] for the mechanical amplitude at blue sideband, indicating establishing constructive phonon interference between the phonons from the probe and the pump. **Fig.2.2.4.17(b)** analytically calculated by Eq. 2.2.4.30(a) shows the timely response of mechanical amplitude for the phonon-cavity mechanical resonator <1> in this electromechanical system.

2.2.4.4 Summary

The double-tones driving scheme modelling and simulations in the capacitively coupled two mechanical resonators have been done. We take an electromechanical analog to the optomechanical system, because one mechanical resonator with higher resonance frequency becomes a phonon cavity and the other coupled mechanical resonator with the low resonance frequency is regarded as an energy transfer station. In this coupled electromechanical system, one signal is used to probe one of mechanical resonators; another sideband signal is used to pump the phonon-cavity at its red or blue sideband. In order to manipulate the mechanical system, we present especial definitions of using red and blue sideband to control mechanical resonators. Subsequently, we analysed and simulated electromechanically induced transparency and amplification at red and blue sidebands. It is essential to explain the phonon interference between the phonons from probe tone and the phonons induced by the pump tone. The measurement results of coupled distinct nanoelectromechanical resonators, described by this modelling, has been carried out by Pokharel et al [93].

In Chapter 4, we will provide measurements in a coupled electromechanical system consisting of a metallic AFM-tip and a circular membrane by scanning microwave microscopy (SMM). The results can also be described by using this theoretical model.

2.3 Experiment setup and basic related measurement results

We introduce the room temperature experiment setup that is used for measuring the electromechanical system. It consists of SiN drum membrane capacitively coupled to an Al top gate. Then, we show analysis of the measurement results. In this thesis work, the experiment setup is built by X. Zhou. In this part, SiN drum nanoelectromechanical resonator coupled to an Al suspended top gate was fabricated by S. Venkatachalam. To make clear for the measurement data taken, it needs to distinguish that the data from section 2.3.2, 2.3.3 and 2.3.4 were taken by H. Xu and the data from section 2.3.5 were measured by A. Pokharel.

2.3.1 Experiment setup

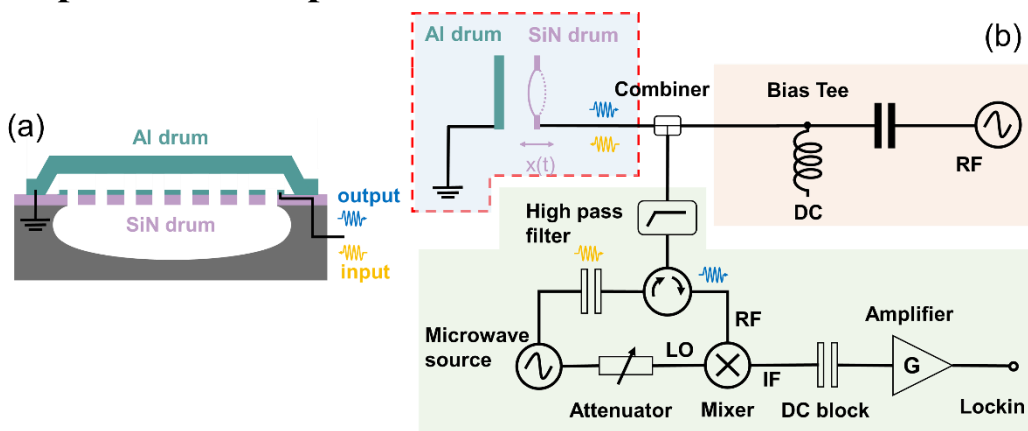


Figure 2.3.1. Experiment setup. (a) Cross sectional view of the electromechanical system. (b) Schematic diagram of the measurement setup. A microwave source is used to generate a microwave signal (yellow) to detect the mechanical displacement of the Al/SiN drum membrane system which is excited by the RF signal. The detection feedback signal (blue) returns the modulated RF component to be mixed with the reference signal for frequency down conversion. Finally, the mechanical displacement is readout by the Lockin amplifier.

Fig. 2.3.1. depicts the measurement setup in the electrical readout scheme. To apply each electrical component, we analyse and explain their properties through an analog to the optical components. The measurement setup can be divided into blue, red and green three parts. They are (i) device under test (DUT), (ii) electrical drive and (iii) microwave emission/detection respectively.

(i) DUT part (blue) is key. In particular, the bottom mechanical resonator through the top gate can be integrated with the compliant electrical circuits. Then, we can add electrical dc and ac signals onto the mechanical system, so that the mechanical resonator can be excited.

(ii) electrical drive part (red) includes electrical bias tee containing ac signal and dc signal. These two driving signals play analog roles as to actuation signals in an optical excitation/readout scheme. They control the capacitive actuation of the membrane. SiN and Al membranes can be actuated by selecting the frequency range around the mechanical resonance frequency. ac and dc driving signals can be added through combiner component analog to an optical beam splitter.

(iii) the microwave detection part (green) has several electrical components including microwave source, attenuator, high pass filter, circulator, mixer, DC block and amplifier. They can be analog to laser source, optical attenuator, spectral filter, optical circulator, optical beam splitter, spectral filter and amplifier in the optical readout scheme. According to the detection part (green), a microwave source signal with a high frequency ω_c is splitted into two signals. One signal is going to detect the mechanical system through high pass filter, circulator and combiner; the other signal reaches the LO port of mixer as a reference with a frequency ω_c through an attenuator. The yellow signal is the incident microwave signal. Afterwards, the feedback signal from the mechanical system is reflected to the mixer component through circulator. It carries a signal with a higher frequency $\omega_c + \Omega_m$ to the RF port of the mixer. By mixing the feedback signal and the LO signal in the mixer component, a signal featuring a frequency $\sim \Omega_m$ is detected by the Lockin amplifier. In the following, we provide the signal processing method with equivalent circuits of the reflectometry.

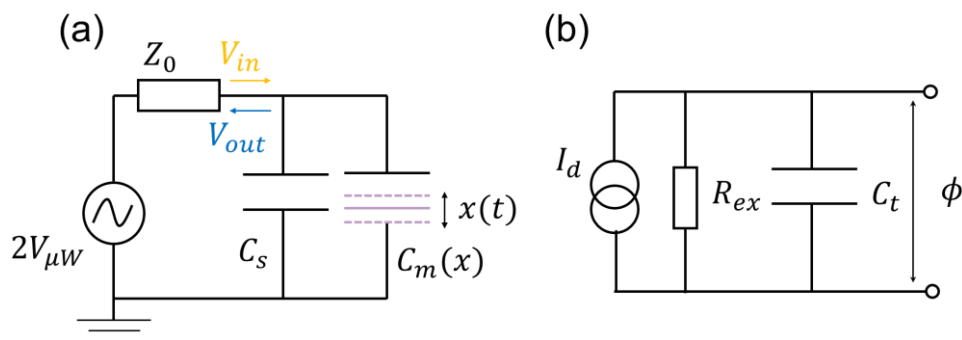


Figure 2.3.2. Microwave detection part. (a) Equivalent circuit of reflectometry. The impedance of the detection part is $Z_0 = 50$ Ohm and $V_{in} = V_{\mu W}$ is the microwave amplitude with a frequency ω_c delivered to the mechanical resonator. Here, we have inner impedance about 50 Ohm inside

the voltage source. (b) Its equivalent parallel RC circuit. $C_t = C_s + C_m(x)$ is the total capacitor, where C_s is the circuit stray capacitor induced by electrode pads and $C_m(x)$ is the movable capacitor, $x(t)$ is the displacement of the capacitor, I_d is the equivalent current source, R_{ex} is the equivalent external resistance, and $\phi(t)$ is the flux in the circuit [36,110].

We consider the mechanical resonator as a movable capacitor model $C_m(x)$. By using Norton's theorem, we can simplify the equivalent circuit of the reflectometry to a parallel circuit with a current source. **Fig. 2.3.2** shows the circuit equivalence for the detection part, where the total capacitance $C_t = C_s + C_m(x)$. In order to transform the series voltage source circuit to a parallel RC circuit, the effective components of the Norton drive circuit can be defined in formalism of real part and imaginary part of the complex admittance [110], $Y_t(\omega_c) = (Z_0 + \frac{1}{i\omega_c C_t})^{-1}$. Here, $Re[Y_t(\omega_c)] = \frac{1}{R_{ex}}$, then the equivalent external resistance $R_{ex} \approx 1/(\omega_c^2 C_t^2 Z_0)$. To analyse the circuits, we can rewrite the total capacitance $C_t = C_{t0} - C_{m0} \frac{x(t)}{d}$ due to the $C_m(x)$ as a function of the mechanical displacement $x(t)$. C_{t0} is the total static capacitance and d is the initial capacitor distance. Therefore, an analytical motion equation of the flux ϕ biased on the $C_m(x)$ can be given by [110]

$$\frac{\partial}{\partial t} \left(\left(C_{t0} - \frac{C_{m0}x(t)}{d} \right) \frac{\partial \phi}{\partial t} \right) + \frac{1}{R_{ex}} \frac{\partial \phi}{\partial t} = I_d \quad Eq. 2.3.1$$

where the total current can be described by $I_d = i\omega_c C_t V_{\mu W}$, which is also written in the form of $I_d(t) = \frac{I}{2} e^{-i\omega_c t} + c.c$, where I is the complex amplitude of the current. The mechanical displacement is written in form of $x(t) = \frac{A(t)}{2} e^{-i\Omega_m t} + c.c$, where the $A(t)$ is the complex amplitude with the frequency around Ω_m . Therefore, we can find an exact solution using the *ansatz*

$$\phi(t) = \sum_{n=-\infty}^{+\infty} \frac{\mu_n(t)}{2} e^{-i(\omega_c + n\Omega_m)t} + c.c \quad Eq. 2.3.2$$

To solve Eq. 2.3.1, we look for the solution V_{out} with the frequency $\omega_c + \Omega_m$, which was measured in the experiments. Derivatives of the relevant amplitudes can be given by

$$\frac{\partial \phi_1}{\partial t} = \frac{\mu_1(t)}{2} e^{-i(\omega_c + \Omega_m)t} (-i(\omega_c + \Omega_m)) + c.c \quad Eq. 2.3.3$$

$$\frac{\partial^2 \phi_1}{\partial t^2} = \frac{\mu_1(t)}{2} e^{-i(\omega_c + \Omega_m)t} (-(\omega_c + \Omega_m)^2) + c.c \quad Eq. 2.3.4$$

$$\frac{\partial x}{\partial t} = \frac{A(t)}{2} e^{-i\Omega_m t} (-i\Omega_m) + c.c \quad Eq. 2.3.5$$

Based on detection frequency $\omega_c \gg \Omega_m$, we get reasonable approximation $\omega_c/(\omega_c + \Omega_m) \sim 1$. Because the typical stray capacitance C_s is the pF range, we also have a reasonable estimate $\omega_c C_{t0} Z_0 \ll 1$. In addition, the equivalent parallel RC circuit is a current source circuit, featuring a constant total current I_d . Combining with input-output theory [110], we can solve the motion equation Eq.2.3.1. It is finally given by

$$V_{out} = \omega_c Z_0 \frac{C_m |x|}{d} \frac{1}{2} V_{\mu W} \quad Eq. 2.3.6$$

Here, V_{out} relates to the flux complex amplitude μ_1 with the frequency $\omega_c + \Omega_m$, $V_{\mu W}$ relates to the flux complex amplitude μ_0 with the frequency ω_c .

Using Eq.2.3.6, we can measure and analyse the mechanical displacement x through this microwave reflectometry scheme. Here, we use ac signal generated by the Lockin to excite the mechanical resonator, and detect it using a microwave signal $V_{\mu W}$ with the high frequency $\omega_c/2\pi = 4.8 \text{ GHz}$. As mentioned above, we convert the V_{out} to low frequency signal around Ω_m through demodulating it with a signal ω_c . All of the measurements at room temperature performed under the vacuum ($\sim 10^{-6} \text{ mbar}$).

2.3.2 Mechanical response vs. frequency (in the linear region)

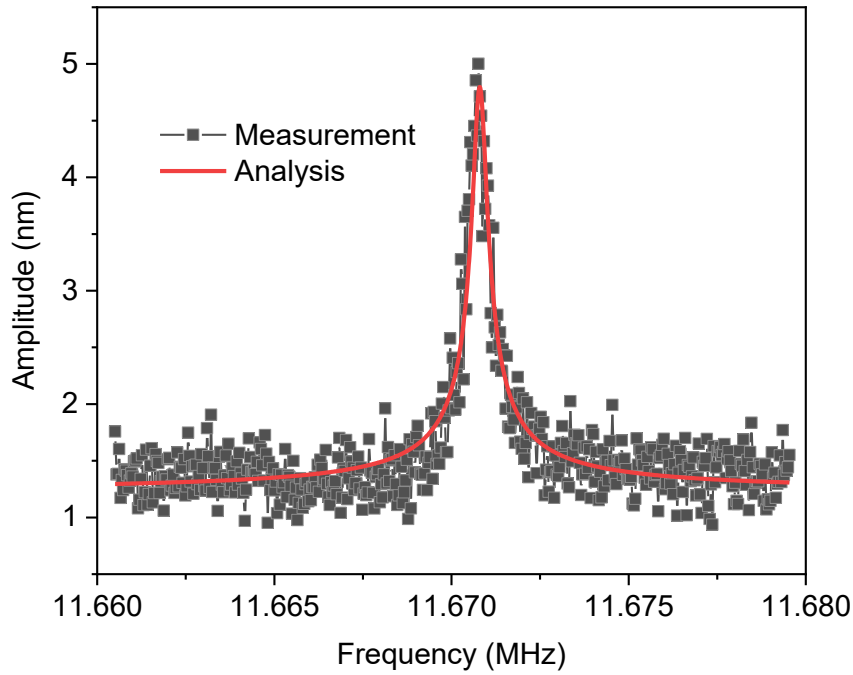


Figure 2.3.3. Amplitude of the mechanical resonator driven by DC+AC voltages in the linear region. Grey squares are the measurement data and red solid line is a fitting result. The amplitude has been adjusted to fit the measurement data.

| Table 2.3.1. Linear mechanical amplitude vs. frequency | | |
|--|--|--|
| Parameter | Experiment, mode (0, 1) | Analysis, mode (0, 1) |
| Resonance frequency (MHz) | 11.671 | 14.51 ($\sigma = 1 \text{ GPa}$, $\rho = 3084 \text{ kg/cm}^3$, $\alpha_{01} = 2.4048$, $D = 30 \mu\text{m}$) |
| Capacitance (F) | $\sim 7.819 \times 10^{-15}$ ($d = 800 \text{ nm}$, $D = 30 \mu\text{m}$) | $\sim 7.918 \times 10^{-15}$ ($d \approx 790 \text{ nm}$, $D \approx 30 \mu\text{m}$) |
| Effective mass (m_{eff}/kg) | range: $4.28 - 6.11 \times 10^{-14}$ | 4.4×10^{-14} |
| Quality factor (Q) | > 10000 | 27800 |
| Driving force (pN) | 30.06 ($V_{ac} = 2 \text{ V}$, $V_{acs} = 1.5 \text{ mV}_p$) | 30.39 |

In this part, **Table 2.3.1** analytically shows SiN drum membrane with a tensile stress of 1.0 GPa and a diameter of 30 μm is defined in order to achieve resonance frequency around 14.51 MHz, the value of which is evaluated based on the formula $\frac{\omega_{mn}}{2\pi} = \frac{1}{2\pi} \sqrt{\frac{\sigma}{\rho}} \frac{\alpha_{mn}}{a}$ (see section 2.1.2). Here, the fundamental mode (0,1) is measured, therefore having the factor $\alpha_{01} = 2.4048$ (see Table 2.1.1 in section 2.1.1). Similarly, other modes, e.g., (1,1), (0,2), corresponding to different resonance frequencies, can also be analysed.

Experimentally, we show using AC voltages to drive the mechanical resonator in the linear region. We choose a DC voltage of 2 V to modulate spring constant to enable a resonance frequency of the mechanical resonator. **Fig. 2.3.3** shows mechanical response of the resonator, in which the measurement data are fitted well by a square root of Lorentzian shape function $|\mu_x(\omega_d)| = \frac{f_d}{m_{eff}} \frac{1}{|\Omega_m^2 - \omega_d^2 - i\omega_d\gamma_m|}$, where f_d is the driving force $\frac{C_{g0}V_{dc}V_{acs}}{d}$ (V_{acs} is the V_p peak voltage during measurements). Then, the following parameters are used for fitting: driving force $f_{d,fit} \approx 30.39 \text{ pN}$, the capacitance $C_{g0}(d \approx 790 \text{ nm}, D \approx 30 \mu\text{m}) \approx 7.918 \times 10^{-15} \text{ F}$, the effective mass $m_{eff} \approx 4.4 \times 10^{-14} \text{ kg}$, and the quality factor $Q \approx 27800$, which agrees with our setting driving force $f_{d,set}(V_{dc} = 2 \text{ V}, V_{acs} = 1.5 \text{ mV}_p) \approx 30.06 \text{ pN}$. However, experimental resonance frequency around 11.671 MHz is achieved, less than the defined one around 14.51 MHz. There are two main causes to explain: in nanofabrication process, first, releasing of SiN drum membrane actually reduces the tensile stress of the membrane, leading to the decrease of resonance frequency; second, the realistic undercut goes larger, namely the diameter of drum $> 30 \mu\text{m}$, thus reducing the resonance frequency of the membrane. Besides, the effective mass range around $4.28 - 6.11 \times 10^{-14} \text{ kg}$ is evaluated because the minimal or maximal mass of the membrane can be evaluated through removing nanohole materials or not. Here, we use the exact calculation of a square root of the Lorentzian function and adjusted the amplitude with experimental measurements to fit.

2.3.3 Resonance frequency vs. DC voltage (the modulation of spring constant)

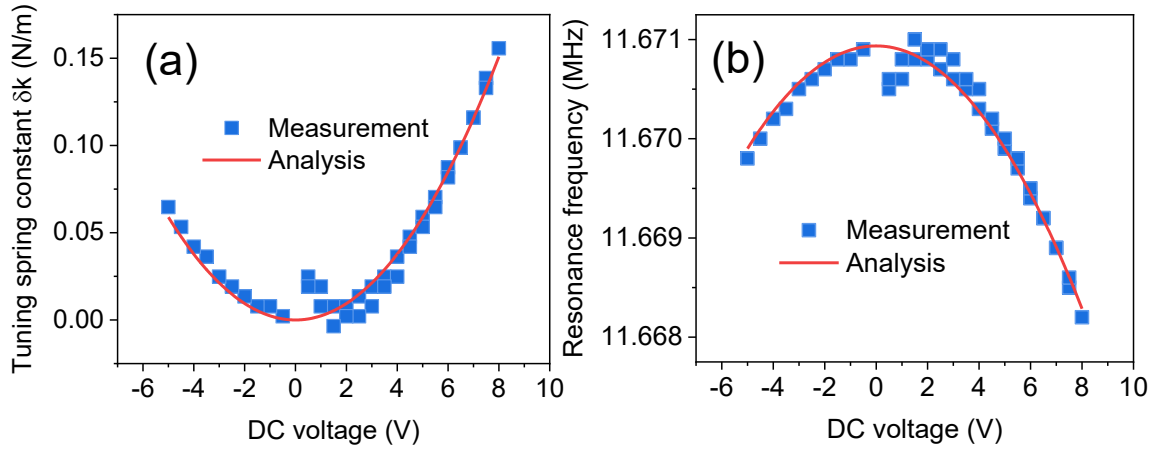


Figure 2.3.4. (a) Spring constant modulation of the mechanical resonator by DC voltages. (b) Mechanical resonance frequency modulation by DC voltages. Blue squares are the measurement data and red solid lines are fitting results.

In this part, we focus on mechanical resonance frequency modulation by DC voltage. **Fig.2.3.4(a)** shows tuning spring constant variation δk as a function of DC voltage, in which the measurement data are well fit by a quadratic description $\delta k \approx \frac{C_{g0}V_{dc}^2}{d^2}$. **Fig. 2.3.4(b)** shows resonance frequency modulation by DC voltages, which presents a good quadratic fitting based on $\Omega_m \approx \Omega_{01}(1 - \frac{C_{g0}V_{dc}^2}{2kd^2})$, where Ω_{01} is the resonance frequency of the fundamental mode (0,1), C_{g0} is the initial capacitance, k is the intrinsic spring constant and d is the capacitor distance. Here, we have reasonable fitting parameters $C_{g0}(d = 800 \pm 37 \text{ nm}, D = 30 \mu\text{m}, \epsilon \approx 1.708 \times 10^{-12} \text{ F} \cdot \text{m}^{-1}) \approx 1.509 \times 10^{-15} \text{ F}$ and $k_{fit} \approx 332 \text{ N/m}$. It is obvious that this fit capacitance value differs from the capacitance in section 2.3.2, which is because charging effects happened as the leak current effect related to the device gate has been observed at the voltage -5.5 V. This effect generates the dielectric cancellation of the capacitor device, reducing the capacitance value. Besides, this fit spring constant number is a bit smaller than the theoretical analysis value ($k_{set} \approx 365 \text{ N/m}$) calculated according to the formula $k = m_{eff} \cdot \omega_{mn}^2$, where $m_{eff} \approx 4.4 \times 10^{-14} \text{ kg}$ and $\frac{\omega_{01}}{2\pi} \approx 14.51 \text{ MHz}$. As mentioned above, it is reasonable because the resonance frequency reduces, generating the decrease of experimental

spring constant. It is worth noting that measurement signals around $V_{dc}=0$ almost have no forces. When V_{dc} bias goes quite small, mechanical resonator is driven by the small forces, yielding signal perished in the noise level. Therefore, when the data taken corresponding to $V_{dc}\sim 0$, the mechanical vibrations cannot be detected well.

2.3.4 Duffing mechanical response vs. frequency (in the nonlinear region)

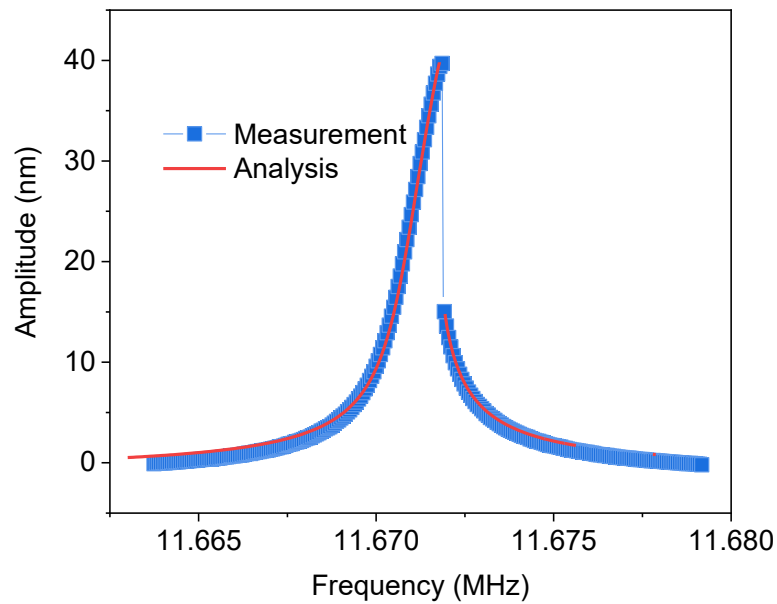


Figure 2.3.5. Measurement data of Duffing mechanical responses. Blue squares are the measurement data and red solid line is a fitting result. The amplitude has been adjusted to fit the measurement data.

| Table 2.3.2. Nonlinear mechanical amplitude vs. frequency | | |
|---|-------------------------|-------------------------|
| Parameters | Fitting results | Setting values |
| DC voltage | - | 2 V |
| Drive voltage (V_{acs}) | - | 20 mV _p |
| Capacitance (F) | 7.918×10^{-15} | 7.918×10^{-15} |
| Nonlinear parameter ($\alpha/m^{-2}s^{-2}$) | 5.6×10^{26} | - |
| Quality factor (Q) | 2×10^4 | - |
| Effective mass (m_{eff}/kg) | 4.4×10^{-14} | - |
| Driving force (pN) | 500 | 400.91 |

In this part, we fit our measurement data by using analytical calculations of Duffing mechanical resonator. As analysed in the previous section 2.2.3, a mechanical amplitude has been given by

$|a|^2 = \frac{g^2}{(2\Omega_x + \frac{4}{3}|a|^2)^2 + 1}$, where $\Omega_x = Q(\omega_d/\Omega_m - 1)$, $a = x\sqrt{\alpha Q/\Omega_m^2}$ and $g = (F/\Omega_m^3)\sqrt{\alpha Q^3/m_{eff}^2}$. We perform data fitting by this. **Fig. 2.3.5** shows the measurement data have been well fit by Duffing resonator function $|a|^2 = \frac{g^2}{(2\Omega_x + \frac{4}{3}|a|^2)^2 + 1}$. Then, we have fitting parameters to be the capacitance $C_{g0}(d \approx 790 \text{ nm}, D \approx 30 \text{ }\mu\text{m}) \approx 7.918 \times 10^{-15} \text{ F}$, nonlinear parameter $\alpha \approx 5.6 \times 10^{26} \text{ m}^{-2}\text{s}^{-2}$, effective mass $m_{eff} \approx 4.4 \times 10^{-14} \text{ kg}$, quality factor $Q \approx 20000$, and driving force $f_{d,fit} \approx 500 \text{ pN}$, which are in agreement with our setting driving force $f_{d,set}(V_{dc} = 2 \text{ V}, V_{acs} = 20 \text{ mV}_p) \approx 400.91 \text{ pN}$ (V_{acs} are the V_p peak voltage during measurements).

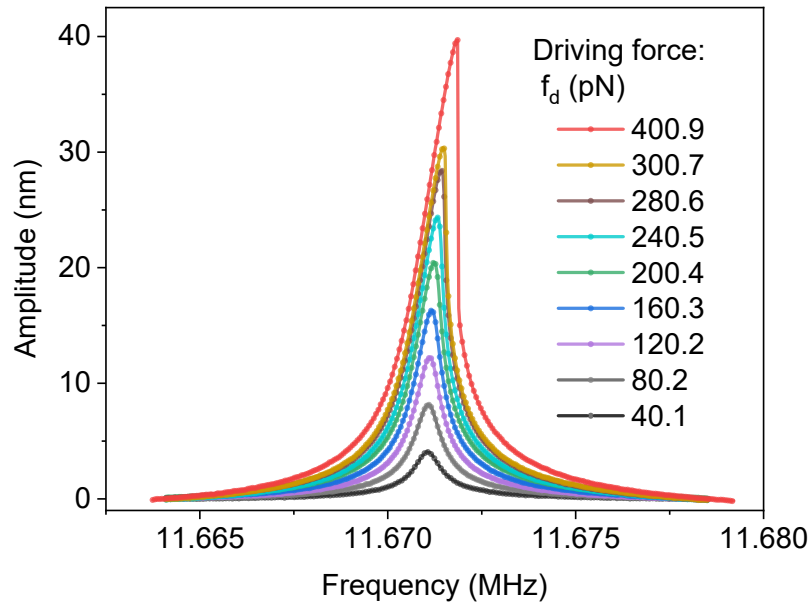


Figure 2.3.6. Measurement data of Duffing mechanical resonator. Solid circle lines are the measurement data. The amplitude has been adjusted to fit the measurement data.

To observe nonlinear behaviours of Duffing mechanical resonator, we have also measured couples of mechanical responses. **Fig. 2.3.6** shows mechanical amplitudes as function of driving frequency, which exhibits nonlinearity clear at the driving force around 400.9 pN.

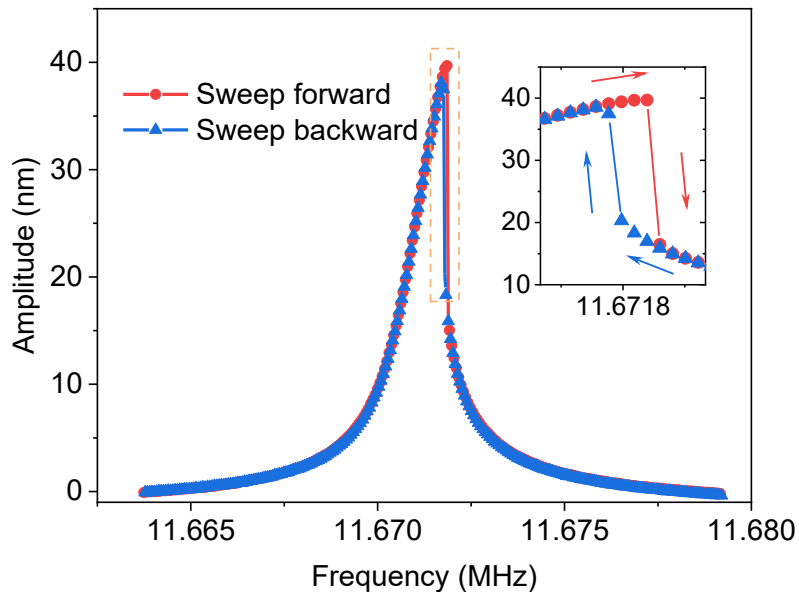


Figure 2.3.7. Measurement data of sweeping forward and backward for Duffing resonator. Red circle lines are the sweep forward data and blue triangle lines are the sweep backward data. The amplitude has been adjusted to fit the measurement data.

Duffing mechanical resonator also enables transducing small signals between forward and backward sweeping bistable states. This phenomena have been observed in several mechanical resonators driven by strong electrostatic forces [114,115,121,122]. We have also observed this switching feature in our mechanical resonator and demonstrate the switch capability of Duffing nonlinearity to perform signal detection. **Fig. 2.3.7** shows frequency forward and backward sweeping that allow bistable states in the hysteresis. Our results show a switching rate about 100 Hz in such a kind of high quality factor $\sim 3 \times 10^4$ [115]. The inset shows the zoom-in forward and backward sweeping directions. They describe the hysteresis window including bistable states with stochastic forces assisted switching. This Duffing mechanical resonator opens up possibilities to realize potentially signal processing [123,124].

2.3.5 Parametric pumping applications (gain amplification and de-amplification)

Through combining an electrical ac signal V_{ac} and a dc signal V_{dc} for driving the mechanical system, we used this microwave reflectometer for readout [36]. We measured a drum mechanical resonator with a diameter of 30 μm , having the resonance frequency $\Omega_{01}/2\pi \sim 11.83\text{MHz}$ at RT [81]. Experimentally, parametric amplification is implemented onto the resonator using an ac power supply (Keysight 33500B). A drive signal V_{acs} with an angular frequency ω_s and another one pump signal V_{acp} with an angular frequency ω_p can be used combining with a controlled phase shift φ . Their amplitudes and frequencies can be adjusted so that V_{acs} drives the resonator vibrating around its resonance frequency [125].

First, we need to verify the contributions from nonlinearity, and then discuss whether or not we could reach an infinite mechanical parametric amplification gain, and then examine that it is reasonable or not to ignore nonlinearities. Considering the Duffing term, we have the Duffing nonlinearity of this drum resonator. Now, we make an analytical comparison between nonlinear term $\alpha|x|^2$ and the linear term Ω_m^2 . Note that if $\alpha|x|^2$ is comparable with the value of Ω_m^2 , forming a comparable expression of the shifted resonance frequency $\left(\frac{\Omega_m}{2\pi}\right)^2 \cdot \left(1 + \frac{3}{8} \frac{\alpha|x|^2}{\left(\frac{\Omega_m}{2\pi}\right)^2}\right)$, the nonlinearity should not be neglected because it does shift the mechanical resonance frequency.

Second, as we mentioned above in the nondegenerate case, the pump force cannot increase too much because the pump force will yield $1 - \frac{\delta k^2}{16(m_{eff}\Omega_m)^2 \chi_s^{-1} \chi_i^{*-1}} = 0$, the mechanical resonator

will enter auto-oscillation states as described in $G(\Delta, \delta, \delta k) = \frac{1}{\left|1 - \frac{\delta k^2}{16(m_{eff}\Omega_m)^2 \chi_s^{-1} \chi_i^{*-1}}\right|}$.

Usually, the parametric amplification gain cannot be infinite because of the nonlinear term not working and the working state far away from the auto-oscillation states.

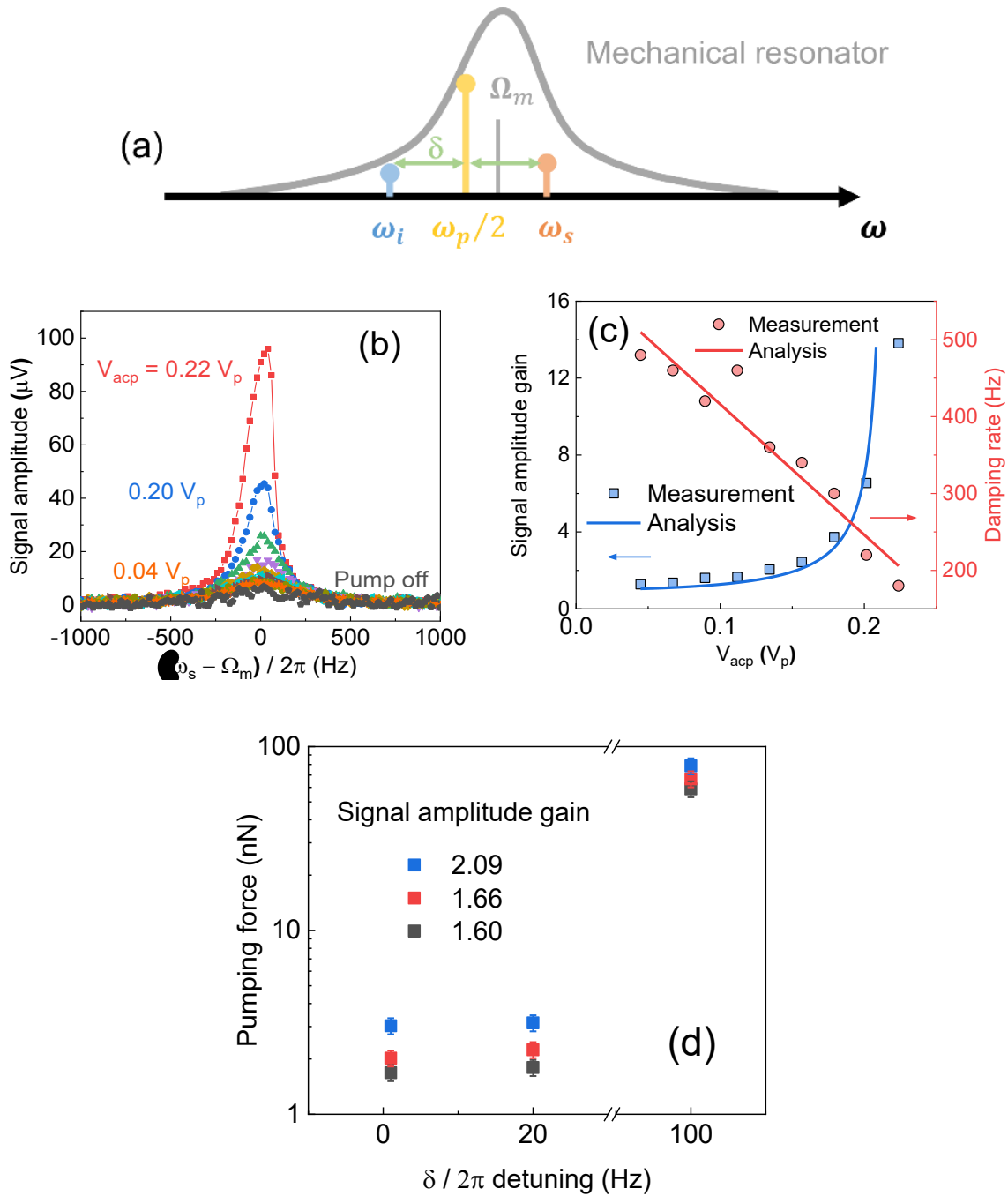


Figure 2.3.8. Nondegenerate parametric pumping scheme. (a) Spectrum operation of the resonator, which is parametrically probed with driving frequency $\omega_s = \omega_p/2 + \delta$. The vertical bars are the position of the angular frequencies related to the schematic amplitude. (b) Mechanical amplitude vs. $(\omega_s - \Omega_m)/2\pi$, with pump amplitude V_{acp} varying from 0 to $0.22 V_p$. (c) Signal amplitude gain is measured at $\delta/2\pi = 20$ Hz. (d) Pumping forces correspond to different $\delta/2\pi = 1, 20, 100$ Hz detunings when reaching the same signal amplitude gain 2.09, 1.66, and 1.60 respectively.

| Table 2.3.3. Non-degenerate parametric pumping scheme | | |
|---|-----------------------|-------------------------|
| Parameters | Fitting results | Setting values |
| DC voltage | - | 2 V |
| Drive voltage (V_{acs}) | - | 111.9 μV_p |
| Pump voltage (V_{acp}) | - | 0 ~ 0.22 V_p |
| Capacitance (F) | - | 7.918×10^{-15} |
| Effective mass (m_{eff}/kg) | 4.4×10^{-14} | - |
| Resonance frequency (MHz) | - | 11.83 MHz |
| Detuning δ (Hz) | - | 20 |

Fig. 2.3.8(a) shows nondegenerate parametric pumping scheme, namely $\Delta = 0, \delta = \omega_s - \omega_p/2 \neq 0$. We investigate the mechanical resonator actuation by probing it with the frequency $\omega_s = \omega_p/2 + \delta$, where δ is a detuning from $\frac{\omega_p}{2}$. Then, we start pumping it with $\omega_p = 2\Omega_{01}$. Since $\omega_s \neq \omega_p/2$, both frequencies mixture give rise to a resonator idler response at $\omega_i = \omega_p - \omega_s$. In the measurement, we used the experimental drive signal voltages $V_{dc} = 2V, V_{acs} = 111.9 \mu V_p$ (V_{acs} is the V_p peak voltage) and vary the pump force in form of $\partial(C_{g0}V^2/2)/\partial x \approx C_{g0}V_{dc}V_{acp}/d$ to reach the same amplitude gain, corresponding to different frequency detuning $\delta/2\pi = 1$ Hz, 20 Hz, 100 Hz, respectively. In this mechanical system, the modulation of spring constant δk in form of $\partial f_p/\partial x \approx 2 C_{g0}V_{dc}V_{acp}/d^2$ (V_{acp} is already the V_p peak voltage) can be induced by pumping force. **Fig. 2.3.8(b)** shows mechanical responses dependent of varying pump forces ranging from 0 to 0.22 V_p in the interval of 0.02 V_p . When V_{acp} is kept off during the experiment, the initial drive still excites the mechanical resonator. This may be due to slightly different work functions from two inter-electrodes forming the capacitance. Besides, it is worth to note that it is observable for $V_{acp} = 0.22 V_p$ starting to perform slightly nonlinearity. **Fig. 2.3.8(c)** shows signal amplitude gain exhibiting a tendency at the frequency $\omega_s = \Omega_m$ that can be described as

$$G(\Delta=0, \delta k, \delta) = \left| \frac{1}{1 + \delta k^2 / 16 m_{eff}^2 \Omega_m^2 \left(\delta + \frac{i\gamma_m}{2} \right)^2} \right| \quad Eq. 2.3.7$$

The measurement data can be fitted in good agreement with this non-degenerate model,

achieving effective mass $m_{eff} \approx 4.4 \times 10^{-14} \text{ kg}$. Moreover, **Fig. 2.3.8(c)** also shows more energy is able to be transduced to the mechanical system as the pump amplitude increasing, resulting in the higher amplitude gain and the lower damping rates. Besides, **Fig. 2.3.8(d)** shows the pumping forces and corresponding $\delta/2\pi$ detuning to a given gain. We see that the pump forces due to $\frac{\delta}{2\pi} = 100 \text{ Hz}$ are stronger than those the forces at 20 Hz or 1 Hz while reaching the same signal amplitude gain.

As discussed above, pump power cannot increase too much into the mechanical system because the pump force will yield $1 - \frac{\delta k^2}{16(m_{eff}\Omega_m)^2 \chi_s^{-1} \chi_i^{*-1}} = 0$, thus mechanical resonator entering auto-oscillation states. In order to find the critical pumping force, we set the denominator of Eq.2.3.7 to be zero, corresponding to mechanical self-auto oscillations. Then, we are able to give the critical modulation $\delta k_c = 2k/Q$ by taking $\Delta = 0$ and $\delta = 0$. When the parametric pump is more efficient to transfer energy to the system, mechanical resonator achieves the higher quality factor.

| Table 2.3.4. Degenerate parametric pumping scheme | | |
|---|----------------------|-------------------------|
| Parameters | Fitting results | Setting values |
| DC voltage | - | 2 V |
| Drive amplitude (V_{acs}) | - | 201.42 μV_p |
| Pump amplitude (V_{acp}) | - | 0.19 V_p |
| Capacitance (F) | - | 7.918×10^{-15} |
| Quality factor (Q) | 1.1×10^4 | - |
| Spring constant k (N/m) | 82 | - |
| Modulations of spring constant δk (N/m) | 1.2×10^{-2} | - |
| Pumping force (nN) | 4.74 | 3.81 |

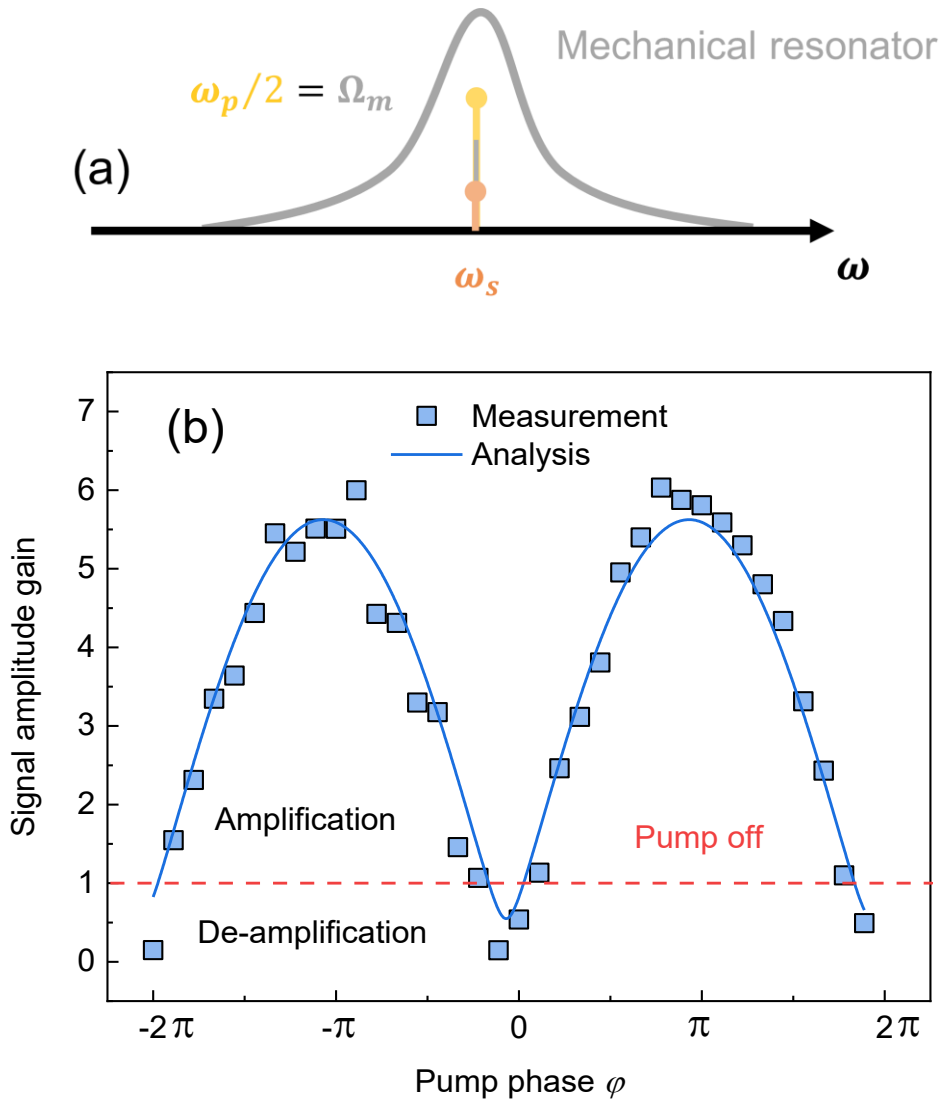


Figure 2.3.9. Degenerate parametric pumping scheme. (a) Spectrum operation of the resonator, which is parametrically pumped at a pumping frequency $\omega_p = 2\Omega_m$ and actuated at $\omega_s = \Omega_m$. The vertical bars represent the position of the angular frequencies related to the schematic amplitude. (b) Signal amplitude gain measured with $\omega_s = \omega_p/2$ (solid squares) and fit by analytical calculation (solid line).

Fig. 2.3.9(a) shows a degenerate parametric pumping scheme, namely $\Delta = 0, \delta = \omega_s - \omega_p/2 = 0$. In general, the frequency response of the resonator is present only at frequencies $n\omega_s$ (n being an integer) since ω_p is a multiple factor of ω_s and will mix with ω_s to offer those frequencies. Here, we just consider a simple case, namely $n = 1$. We drive the mechanical system by implementing $V_{dc} = 2 V, V_{acs} = 201.42 \mu V_p$ and pumping it by $V_{acp} = 0.19 V_p$. The signal amplitude gain is given by

$$G(\Delta=0, \delta k, \varphi) = \frac{\left| 1 - \left(\frac{Q\delta k}{2k}\right) \cos(\varphi) - i \left(\frac{Q\delta k}{2k}\right) \sin(\varphi) \right|}{\left| \left(\frac{Q\delta k}{2k}\right)^2 - 1 \right|} \quad \text{Eq. 2.3.8}$$

Note that it is the signal amplitude ratio between pump on and pump off.

Fig. 2.3.9(b) shows that the amplitude gain sensitivity to the phase allows a signal transition between amplification and de-amplification, the measurement data of which can be fitted well by using the above analysis, achieving fitting parameters of quality factor about $Q_{fit} \approx 1.1 \times 10^4$, spring constant $k_{fit} \approx 82 \text{ N/m}$, and pump force $f_{p,fit} (\delta k \approx 1.2 \times 10^{-2} \text{ N/m}) \approx 4.74 \text{ nN}$. It is obvious that the fitting pump force agrees with the experiment pump setting $f_{p,set} (V_{dc} = 2 \text{ V}, V_{acp} = 0.19 V_p, C_{g0} \approx 7.918 \times 10^{-15} \text{ F}) \approx 3.81 \text{ nN}$, where V_{acp} is already the V_p peak voltage. Besides, the horizontal red line corresponds to the pump off ($V_{acp} = 0$). This degenerate parametric pumping scheme can be potentially used for various applications either in signal enhancement or for noise squeezing.

Chapter 3 Fabrication of SiN membrane nano-electro-mechanical resonator

In this chapter, several essential equipments, including electron beam lithography (EBL), reactive ion etching (RIE), and xenon difluoride etching (XeF_2 etcher) will be first introduced, which have been used for fabricating these SiN membrane mechanical resonators. Then, COMSOL simulation for designing the circular SiN membrane will be introduced and discussed. In the following, critical fabrication process for achieving SiN membrane mechanical resonator will be discussed. In the last part, fabrication process of successful SiN membrane mechanical resonators will be summarized.

3.1 Introduction to fabrication tools

3.1.1 Electron beam lithography (EBL)

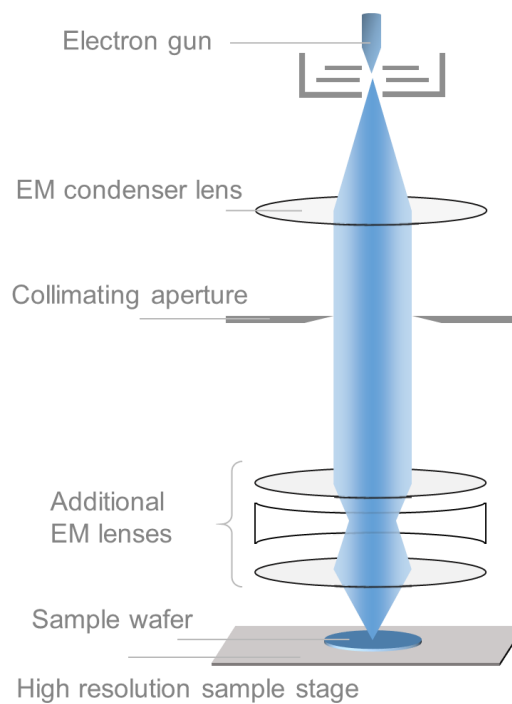


Figure 3.1.1. Schematic of equivalent EBL system, consisting of an electron gun, electromagnetic (EM) condenser lens, collimating aperture and sets of electron optics lenses used to focus and scan the electron beam [126,127].

Electron beam lithography (EBL) system (in **Fig. 3.1.1**) is one of useful instruments to fabricate micro/nanoscale devices. Comparing optical lithography process, EBL gives an access to fabricate devices in sub-micron scales. In general, the whole EBL process includes following steps: first, patterns design is an early and key step, because it plays an important role in designing device structure with writing field, EBL step, EB resist types, dosages and writing time. Second, the designed patterns can be translated from GDSII data to a machine-exposable file for patterns preparation. Third, sample preparation is to fix samples on a machine-recognized holder and sample surface height is to be adjusted by using laser-equipped optical microscopy. Fourth, machine calibration relates to electron beam focus on the sample surface. Fifth, exposure includes setting write dose and write time. Sixth, effects of development on writing features lie in developing temperature and the time.

Nowadays, numerous micro/nano-devices have been used in the reality but their fabricating cost-time depends on write fields, write dosage and write beam current. The write time per an area in EBL system can be estimated [127]

$$Dose[\mu C/cm^2] \times Area[cm^2] = Time[s] \times Beamcurrent[nA] \quad Eq. 3.1.1$$

where Dose is how many electrons per unit area of exposure on the resist, Area is the exposed area, Time is the total exposure time across exposing area, and Beam current is the current of the electron beam.

EBL system consists of an electron gun, EM condenser lens, collimating aperture and series of electron optics lenses [126]. Similar to scanning electron microscopy (SEM) system, EBL system is by adding additional an EBL electron gun scanning the beam onto a sample. The sample can be written accurate according to the instructions produced by the designed patterns. In terms of device design, Layout Editor software, interfacing the operator terminal with EBL machine (EBPG 5000 PLUS, RAITH, Germany) to translate and convert the device design is first critical step. In this step, researchers require to consider essential parameters, such as EB resists, write fields, write dosages and write beam current. In order to prepare samples for EBL writing, sample holder chosen usually allows sample to adjust its surface height by applying laser beam to measure in a range of about $\pm 40 \mu m$. From the operator's interface in EBL system, achieving desired features relies on the machine calibration, because initial system settings help the machine to recognize alignment marks and position the beam on the patterns. Exposure is to expose designed patterns, where an electron beam interacts with EB resists,

positively degrading EB resists in the exposure region. It should be noted that specific development manner and time must be treated carefully because of fine features requiring.

Layout Editor drawing pattern.

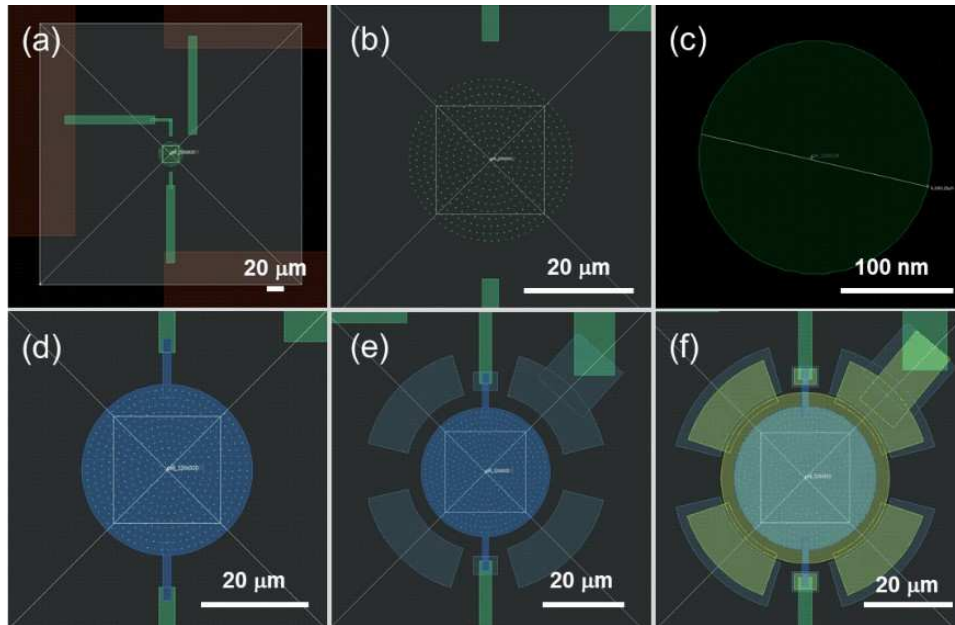


Figure 3.1.2. Layout Editor drawing of all layer dimensions of SiN drum mechanical resonator with an example diameter of 30 μm . It includes contact lines (green) and pads (red) in (a), holes pattern (still green) on SiN film in (b), zoomed-in single hole on SiN film in (c), bottom electrode Al coating (blue) in (d), support feet (light blue) helping suspended top gate to be fabricated in (e), and top-gated pattern (yellow) in (f).

In this thesis, SiN drum mechanical resonator has been designed and developed by Zhou et al [36]. To describe the overall layer dimensions of the device, Layout Editor drawing is presented in **Fig. 3.1.2**. These patterns are designed to be adapted for 320 $\mu\text{m} \times 320 \mu\text{m}$ cell, required by EBL system. The writing resolution is 50 nm, corresponding to current in ranges of 100 nA and 2 nA. While design preparing, we can translate and convert the design format of GDS.file to EBL machine by using pattern generator workflow.

EB resists selection and spin coating.

In EBL process, EB resists are of great importance for EB lithography manufacturing. Because the focus of the electron beam scans onto a sample, the beam spot is able to change the chemical

solubility of EB resists, resulting in an electron-sensitive feature sizes. Since an electron resist poly-(methyl methacrylate) (PMMA) was discovered in IBM Watson Research Center in 1968 [128] and used for microfabrication in 1969 [129], it has been used well in EBL community, for various applications ranging from microelectronic/photonic integrated circuits to microfluidics. Since another commercial electron resist ZEP520 was reported in 1987 [130] and improved in 1992 [131] for quantum wire fabrication, it has also been a good choice for nanofabrication. With the dry etching development of process stability, high resolution, high contrast and high sensitivity, Chemical Semi-Amplified positive tone EB resists (CSAR62) have emerged in 2013 [132]. Copolymer structures similar to ZEP520, it has main composition copolymer of poly(a-methylstyrene-co-a-chloromethacrylate) with a concentration of 9% in anisole reported in 2014 [133]. CSAR62 resist has also been evidenced with 10 times higher sensitivity to electron beam than PMMA while maintaining the same resolution. It is widely used in dry etching process for plasma etch stability.

EB resists exposure.

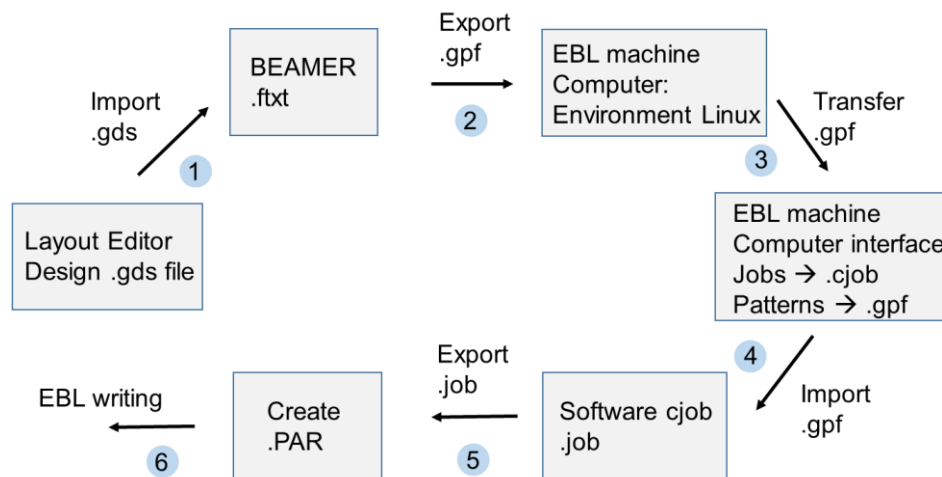


Figure 3.1.3. File preparing process from .gds file to .PAR file through cjob software in EBL.

The exposure step launched under a vacuum chamber ($\sim 10^{-6}$ Torr). In IEMN, the designed gds file is converted into gpf file for EBL system. The JOB.file is used to expose patterns described in gpf file, which contains information of sample holder, current, dose, and the patterns. The PAR file is to excute the exposure. The file preparation process is shown in **Fig.3.1.3**.

3.1.2 Reactive ion etching (RIE)

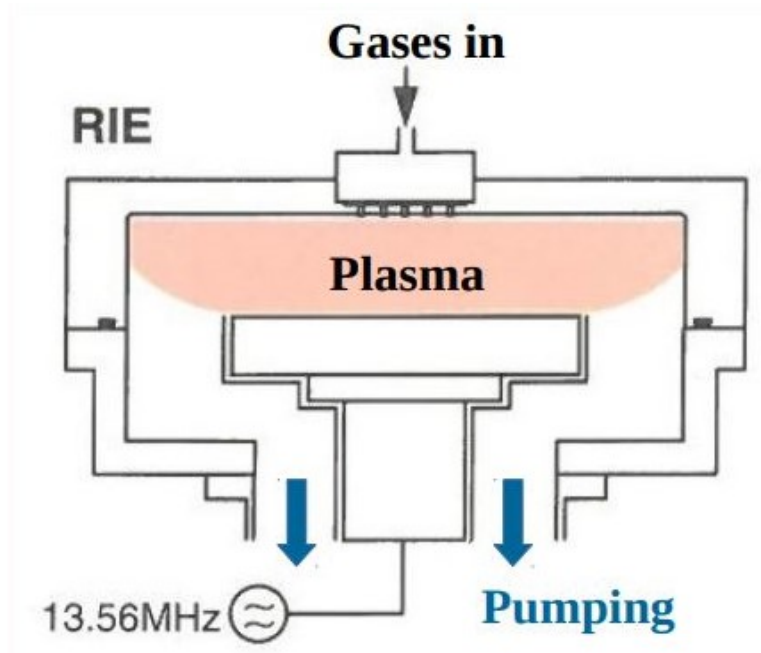


Figure 3.1.4. Schematic of RIE system, which is a kind of capacitively coupled plasma system. It consists of RF generator, RF match network, main reactive chamber and sample stage chunk etc [134,135]. (Photo courtesy to IEMN)

Reactive ion etching (RIE) (in **Fig. 3.1.4**) is a plasma-processing tool that is widely applied in modern semiconductor industries. Dry etching process to remove some materials can be done by RIE process. When some radicals and neutrals that can be chemically formed on the specimen surface produce volatile precursors, positive ions can be accelerated across plasma sheath in the inter-electrode space, so as to add sufficient ions energy forming ions bombardment [136]. This ions bombardment plays an important role in creating anisotropic profiles, etching rate improvement and surface materials removal. Besides, another approach to electron density control in capacitively coupled plasma has also been meaningful [137]. It is able to avoid etching instabilities, e.g., process reproducibility.

In this thesis, a standard capacitively coupled plasma RIE equipment (PlasmaLab 80 Plus, OIPT, UK) is used for selective etching of the SiN/silicon against CSAR62 resist. In order to control RIE etch process, several parameters, such as etchant passivation gas, etch time, gas flow rate, chamber pressure and RF power are considered. They are collectively major effects on etch rate and etch profile.

3.1.3 Xenon difluoride etching (XeF_2)

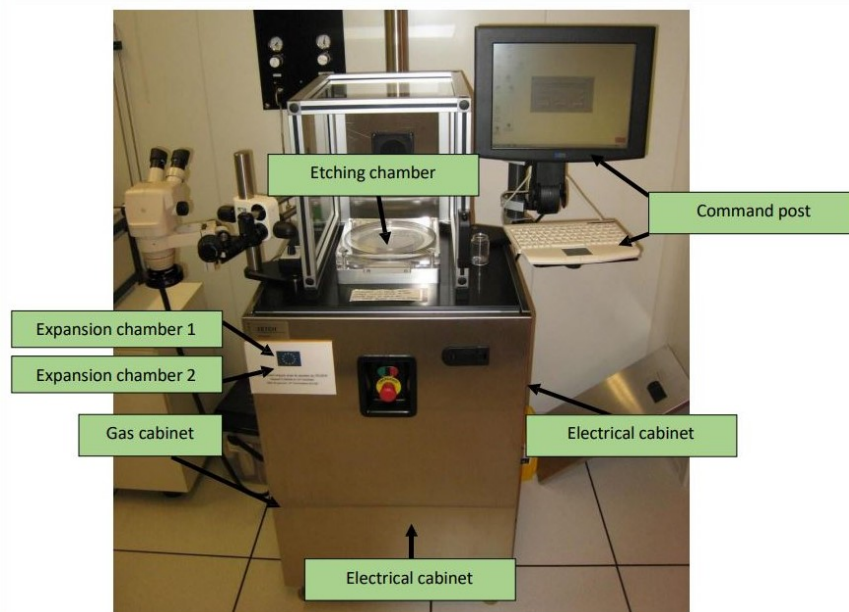


Figure 3.1.5. Schematic of XeF_2 etcher system. It consists of nitrogen source, XeF_2 crystals source, expansion chamber, etch chamber, vacuum pump, series of control valves and PC controller [138]. (Photo courtesy to IEMN)

Xenon difluoride (XeF_2) etcher system (in **Fig. 3.1.5**) is an isotropic silicon-etching tool, which is also engaged for modern microelectronics fabrication. This tool is able to use XeF_2 gas as an etchant to selectively etch the target silicon. Since XeF_2 gas was first discovered in Argonne National Laboratory in 1962 [139], Winters et al in IBM Research Laboratory in 1979 [140] reported for the first time on the etching of silicon with XeF_2 vapour. Their work investigated the changing of etch rates with different pressures and found the selectivity of XeF_2 for silicon with respect to SiC , SiO_2 , and stoichiometric SiN . Over the past long time till 1995, Hoffman et al [141] and Chang et al [138] reported the selectivity of etching silicon with XeF_2 to photoresist, aluminium, SiO_2 etc and used this high etch selectivity in standard CMOS fabrication process and MEMS fabrication. In recent years, Vähänissi et al in 2019 [142] have also uncovered the selectivity of etching silicon with XeF_2 against different compounds, such as Ti/Mo , stoichiometric SiN , SiO_2 , Al_2O_3 , and AlN etc. They revealed the etching selectivity ratio between the silicon and the SiN about 30:1 in the fabrication of microelectromechanical devices. Rondé et al in 2021 [143] have increased the etch selectivity of silicon against SiN by 68%, by reducing the processing temperature because of the sensitive proximity effect on a

silicon sacrificial layer. Therefore, XeF_2 gas as an etchant to etch selectively silicon is a promising method and it has been used well in MEMS applications.

In XeF_2 etcher system, it includes nitrogen source, XeF_2 crystals source, expansion chamber, main etch chamber and vacuum systems. By using cycle mode, this etcher system can expose the target specimen to XeF_2 gas atmosphere. Using expansion chamber, XeF_2 gas from the source can be controlled with a pressure. Then, the gas is going to enter the etch chamber to perform etch process. A standard XeF_2 etcher machine (Xetch Xactix X3B, Xactix, USA) is employed in this work for the selectivity of etching silicon with XeF_2 against EB resist CSAR62 and stoichiometric SiN. In order to control the XeF_2 etching process, several necessary parameters, namely etch mode, etch time, cycle number, gas pressure and pump out pressure have to be taken into account. It facilitates wanted etch rate, etch profile and selectivity of mask to materials.

Besides those equipments mentioned above, a standard EB evaporator machine (MEB 500S, Plassys, France) is utilized for depositing the target metal materials (e.g., Ti, Au, Al) on a wafer under a vacuum. In this thesis work, all metallization process is performed by a professional engineer, Marc Dewitte in IEMN. In the process, we choose the deposition speed, e.g., 1 nm/s, and pre-clean process (e.g., argon ion cleaning process), and the desired metal thickness.

3.2 Design of SiN circular membrane by finite element simulation

Before the release of SiN membranes from the silicon substrate, the optimization and analysis of clamping losses of the SiN membrane are performed by using finite element method (FEM) by means of COMSOL multiphysics. A circular SiN membrane with a fixed tensile stress of 1.0 GPa and diameter of 30 μm is simulated, giving a resonance frequency of 1.353 MHz. The clamping occupation ratio (\mathfrak{R}) is defined with the total arc length ($4l$) of the clamping edge divided by the circumference ($2\pi r$) of the membrane.

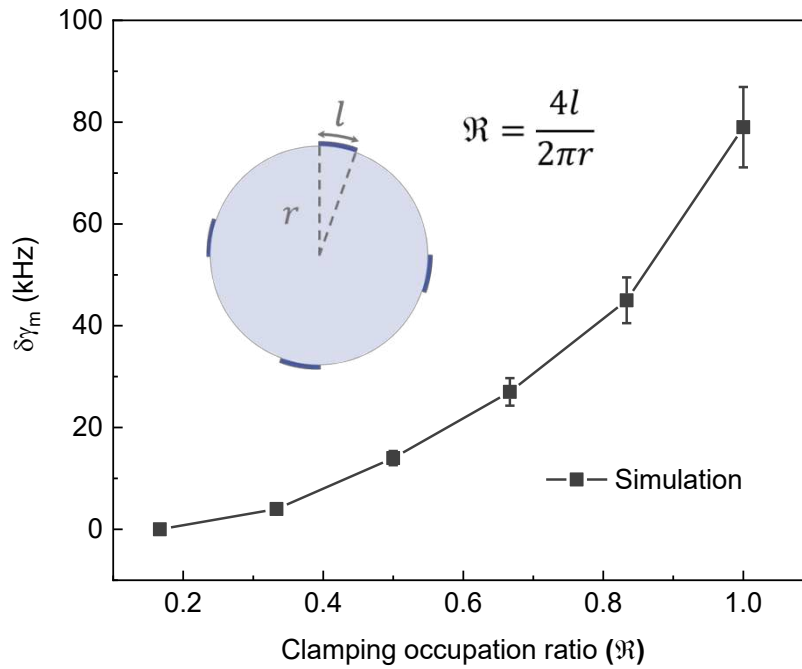


Figure 3.2.1. Simulation results of mechanical damping rates of SiN circular membrane, corresponding to different clamping ratio $\mathfrak{R} = \frac{4l}{2\pi r}$. The insets are the schematic for the definition of clamping occupation ratio, where the dark blue shows the clamping part of the membrane. Here, r is the radius of the circular membrane.

Fig. 3.2.1 shows the simulation results of damping rate varying $\delta\gamma_m$ that is obtained by normalizing the damping rate γ_m with the initial damping rate $\gamma_m/2\pi = 9.4$ kHz. It is simulated with the clamping occupation ratio value $\mathfrak{R} = \frac{1}{6}$, namely $\delta\gamma_m = \gamma_m - \gamma_m(\mathfrak{R} = \frac{1}{6})$. Its specific patterns are subsequently shown in **Fig. 3.2.2**. In this simulation, we observed the values of $\delta\gamma_m$ increasing with the clamping occupation ratio \mathfrak{R} increasing. It indicates that the clamping losses of the circular membrane gradually increase while the clamping edge is

occupied larger on the circumference. It is worth to mention that this simulated circular membrane is based on bare silicon nitride membrane. In fact, our final device structure consists of two circular membranes, namely the aluminium membrane acting as a suspended top gate and the SiN membrane drum. Here, silicon nitride membrane covered by a thin aluminium has not yet been simulated, but this kind of concern has been considered in the Fig. 4.2.6 of section 4.2.1 in chapter 4. The simulation circular membrane consists of silicon nitride circular membrane covered with a thin aluminium. For the SiN membrane nanoelectromechanical resonators, the dissipation is highly diluted by its high tensile stress [144]. Moreover, the mechanical properties of the SiN/Al membrane are still dominated by the silicon nitride with high tensile stress, generating the resonant frequency of the membrane remaining silicon nitride membrane (also mentioned in section 3.3.3 in chapter 3).

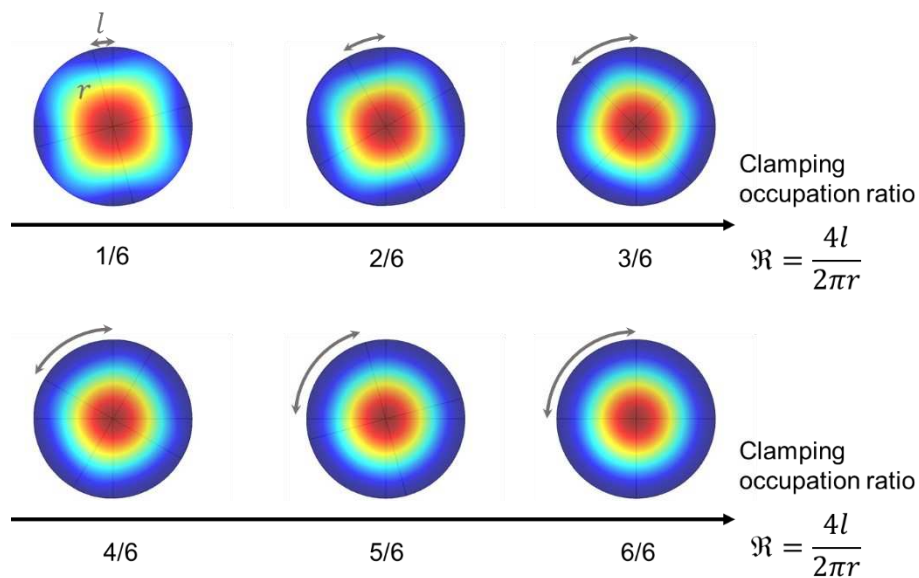


Figure 3.2.2. Simulation results of mechanical vibration of SiN circular membrane. The clamping occupation ratio $\mathfrak{R} = \frac{4l}{2\pi r}$ ranging from 1/6 to 6/6. The color on the membrane is mechanical amplitude arbitrary (units). The lines on the membrane are referred lines.

This simulation results provide us with a feasible evaluation to achieve a compromise between membrane fabrication and low clamping losses. In recent years, soft clamping schemes have been exploited to further reduce damping effects, where most of the SiN membrane edges are etched away to avoid full clamping [80]. Such membrane nanoelectromechanical resonators are well suited for applications in optical readout schemes. It is very challenging to achieve electrical integration for this type membranes, as the membrane becomes too fragile to fabricate

a suspended top gate. Considering the difficulties in the fabrication process, we therefore design the SiN membrane to be a fully clamped scheme (namely $\mathfrak{R} = 1$) in this thesis work. In order to have a capacitive coupling scheme, a thin aluminium layer will be deposited on surface of the SiN membrane. It is designed not to cover the entire clamping edge of the SiN membrane, but only the edge where the two leads are connected later in **Fig.3.3.15(a)**, with the $\mathfrak{R} < 0.2$, so as to reduce additional clamping losses. Besides, we would like to mention that the aluminium top gate is also a nanoelectromechanical resonator, with resonance frequency around ~ 3 MHz [93]. In order to reduce its clamping losses, the clamping ratio of Al top gate drum $\mathfrak{R} = 0.5$ is chosen in this thesis work.

3.3 Fabrication process of SiN membrane nano-electro-mechanical resonator

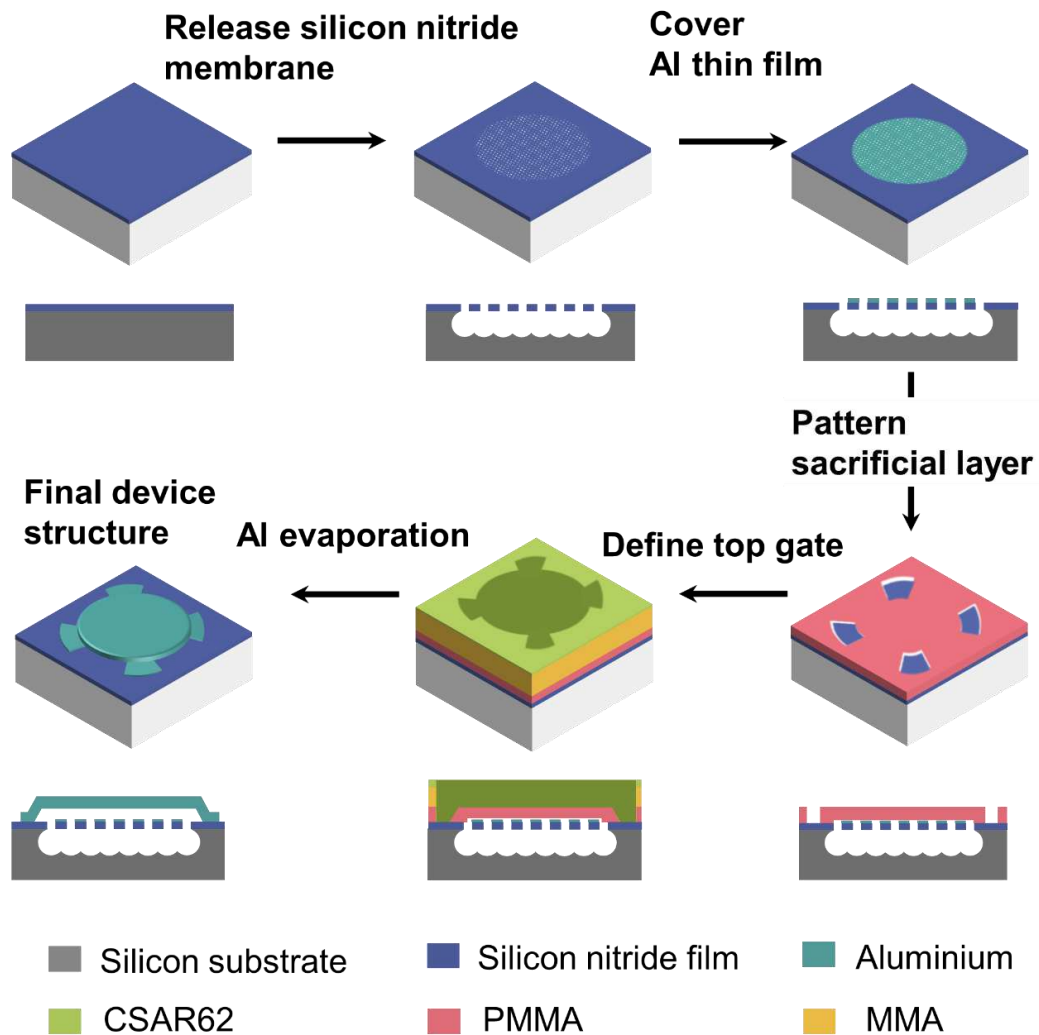


Figure 3.3.1. Schematic of nanofabrication process for a SiN membrane nanoelectromechanical resonator. It includes the dry etching process to release the membrane from silicon substrate, the deposition of aluminium thin layer on the surface of the membrane, and the two-step EB lithography process to create a suspended aluminium top gate.

Fig. 3.3.1 contains the following specific fabrication steps:

- (i) alignment marks, contact lines and pads,
- (ii) release of SiN membrane from the silicon substrate,

(iii) aluminium thin film deposition on the SiN membrane,

(iv) aluminium suspended top gate on the top of the SiN membrane.

In this fabrication process, SiN drum mechanical resonators were fabricated from a high resistivity ($\sim 10 \text{ k}\Omega\cdot\text{cm}$) silicon substrate deposited with stoichiometric SiN (Si_3N_4) thin film of about 100 nm with high tensile stress of about 1.0 GPa.

Before spin coating process, sample clean is always proceeded (see **Table 3.3.1**). It plays a major role in MEMS fabrication process because the fabricated devices are strongly dependent of effective masses. Dirty particles carry extra masses to the devices and further hinder the use of devices. Therefore, clean process mainly includes two steps, namely clean wafer and examine the wafer in optical microscopy.

| Process | Parameters |
|--|--|
| Coating photoresist SPR 220 | 2500 rpm_speed, 1000 rpm/s_acc., 15 s_time, Bake 100 °C for 2 min |
| Wafer laser cutting in IEMN | Achieving $1.7\text{cm} \times 1.7\text{cm}$ samples |
| Cleaning wafers | SVC-14 solvent 70 °C for 3 hour, IPA rinsing, N ₂ blowing |
| Wafers examination by optical microscopy | Magnitude: $\times 10$, $\times 20$ etc |

3.3.1 Alignment marks, contact lines and pads

These alignment marks (see process in **Table 3.3.2**) are used to define the relative coordinates of each pattern. They allow EB machine to write patterns, for each layer, in the described positions on the chip.

| Table 3.3.2. Fabrication process of alignment marks, contact lines and pads | |
|--|---|
| Process | Parameters |
| Cleaning wafers | SVC-14 solvent 70 °C for 3 hour, IPA rinsing, N ₂ blowing |
| Activating the surface by HDMS+ EL 13%_ | 3000 rpm_speed, 1000 rpm/s_acc., 12 s_time, 170 °C for 5 min |
| Spin coating EB resist PMMA 3% | 3000 rpm_speed, 1000 rpm/s_acc., 12 s_time, 170 °C for 5 min |
| EBL writing patterns | Exposure dose 650 $\mu\text{C}/\text{cm}^2$, Current 50na (marks+lines), 100na (pads), Cell size 320 $\mu\text{m} \times 320 \mu\text{m}$ |
| Developing | MIBK (30 ml) : IPA (60 ml) for 1 min 40 s, IPA rinsing for 10 s and N ₂ blowing |
| Metal deposition | Ar pre-etching for 60s, Ti 30 nm at 0.2 nm/s, Au 250 nm at 0.5 nm/s |
| Lift-off | SVC-14 solvent at 70 °C for 3 hours, Acetone + IPA rinsing, and N ₂ blowing |

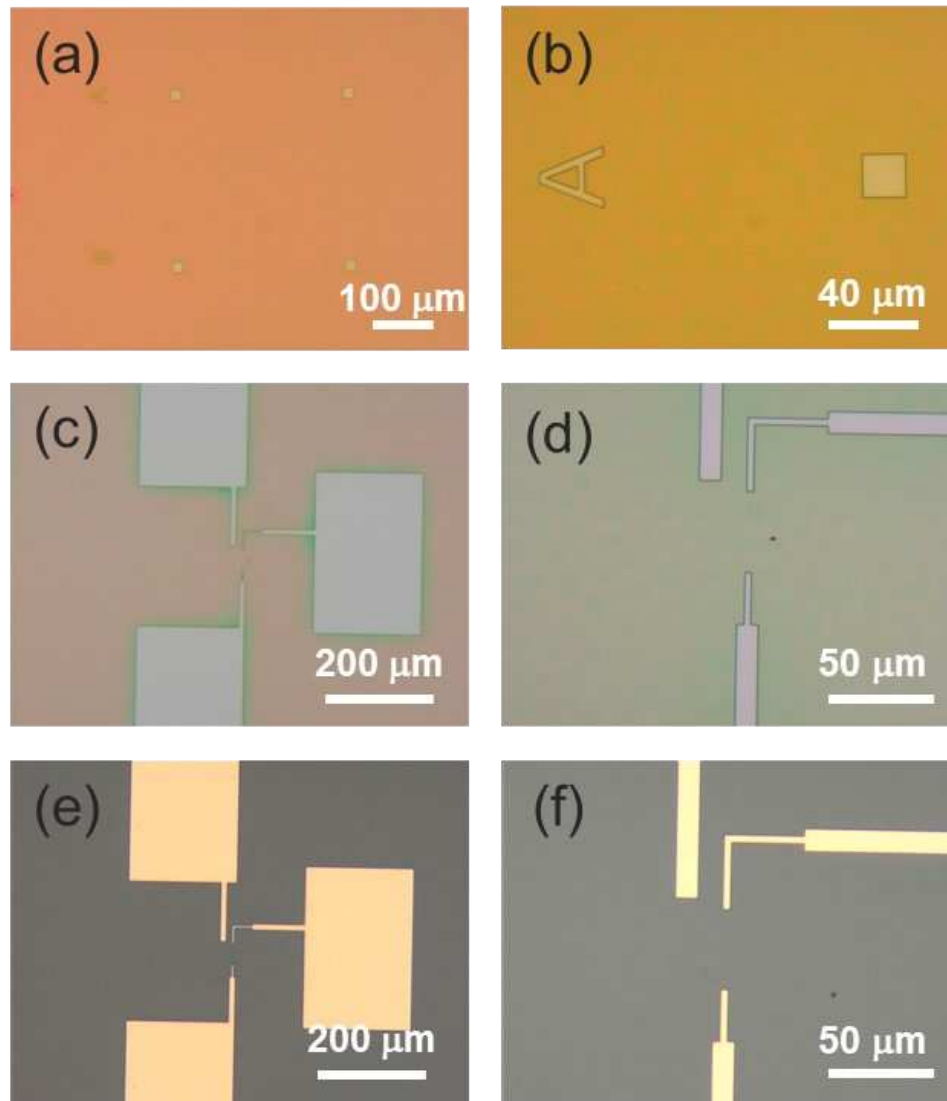


Figure 3.3.2. Optical micrographs of alignment marks, contact lines and pads after development (a-d), and contact lines and pads after metal deposition (e,f). Note that Au about 250 nm is used for alignment marks and Al about 250 nm is used for contact lines and pads here.

First of all, we start to fabricate the alignment marks, contact line and pads. They are useful as fabrication coordinate references in the device fabrication process. The alignment marks allow EBL machine to locate and expose pattern features for each fabrication step. **Fig. 3.3.2(a,b)** show alignment marks, which are about $20\ \mu\text{m}$ long \times $20\ \mu\text{m}$ wide and enable electron beam to recognize the wanted location for allocating patterns exposure. **Fig.3.3.2(c-f)** show contact lines and pads, which are about $100\ \mu\text{m}$ \times $10\ \mu\text{m}$ and $300\ \mu\text{m}$ \times $200\ \mu\text{m}$, respectively. In our process, Al layer 250 nm in thickness is deposited. All depositions are followed by lift off process so as

to transfer the metals on the wafer surface. Contact lines connecting with larger contact pads allows mechanical resonator devices to be connected with external circuits through wire bonding.

3.3.2 Release of SiN membrane from silicon substrate

The release method of SiN membrane from the Si substrate includes two-steps dry etching process. Because we have defined the circular holes patterns on the SiN membrane through CSAR62 resist, RIE is first used for etching SiN/Si materials in order to expose the Si material to the XeF_2 gas; XeF_2 etcher system is then employed for the selectivity of etching Si material. Besides, it is worth mentioning that SiN membranes have also been technically released from silicon dioxide on silicon substrate by using hydrofluoric acid vapour through critical point drying [87]. Here, we have a novel double dry etching process (namely RIE and XeF_2 etching) to release our SiN membranes from silicon substrate.

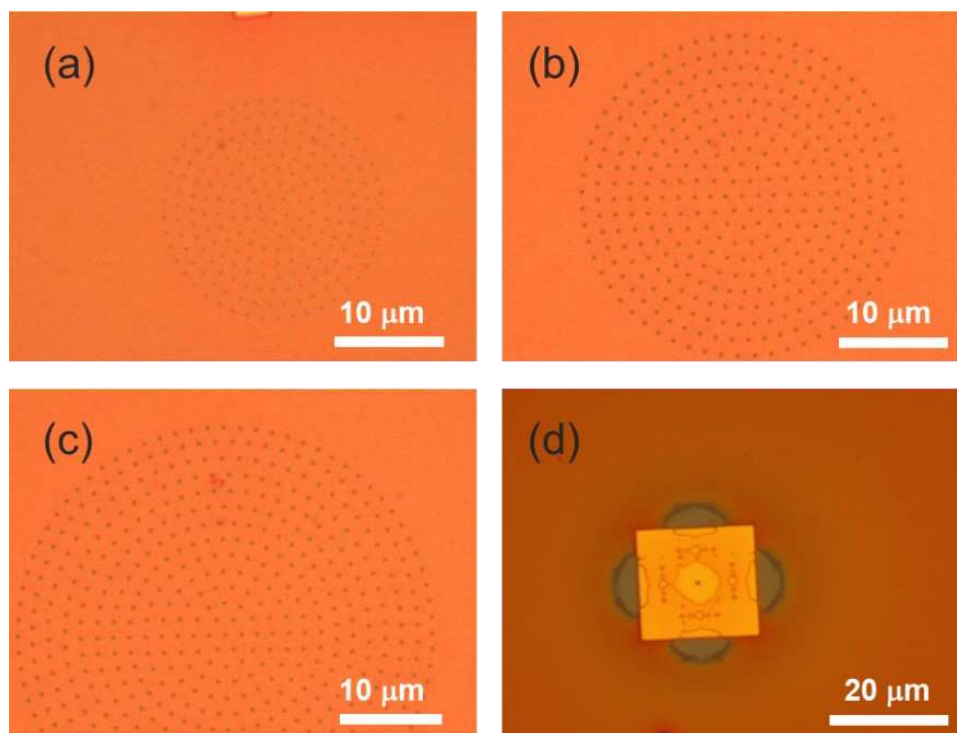


Figure 3.3.3. Optical micrographs of CSAR62 resist on SiN membranes. These membranes are of 20 μm (a), 30 μm (b) and 40 μm (c) in diameters with nominal holes patterns of 300 nm in diameter. (d) The alignment mark enables EBL exposure for the pattern position check. Note that here CSAR62 resist is used as a mask.

The nominal vibrating membranes with different diameters are defined by using EBL and development process is followed to pattern circular symmetric holes on the CSAR62 resist. Notably, the release of SiN membrane is possible when the underneath of the SiN film, the silicon, is exposed to reactive etchant gas. To facilitate Si etching and thus release SiN membrane, circular symmetric holes of 300 nm in diameter spaced by about 1.3 μm are defined and they are EB lithographically exposed on the CSAR62 resist, followed by development. Then, the pattern is able to be transferred from the resist to the SiN thin film by RIE through these circular holes to remove unwanted parts. Fig. 3.3.3(a-c) show optical images of EBL exposed patterns, showing the circular membranes with 20 μm , 30 μm and 40 μm diameters definitions. For each definition, we define holes patterns all with 300 nm diameter to be exposed for the purpose of SiN membrane release. Fig. 3.3.3(d) shows the readout of alignment marks in EB writing process. These patterns on CSAR62 resist mask will be used in the following RIE and XeF_2 etch steps.

| Table 3.3.3. Release of SiN membrane from silicon substrate | |
|--|---|
| Process | Parameters |
| Spin coating EB resist CSAR62 | 3000 rpm_speed, 1000 rpm/s_acc., 12 s_time, heating at 150 °C for 1 min |
| EBL writing hole patterns | Exposure dose 630 $\mu\text{C}/\text{cm}^2$, Current 1na, Cell size 320 $\mu\text{m} \times 320 \mu\text{m}$ |
| Developing | AR-600-546 solvent for 50 s, IPA rinsing for 10 s and N ₂ blowing |
| RIE etching SiN/Si | Cleaning for 6 mins, SF ₆ /Ar 10 sccm/10 sccm, RF Power 30W, Pressure 10 mTorr |
| Release SiN film by XeF ₂ etching Si | Advanced Normal, 1 cycle, 50 s, 3.0 Torr, 800 mTorr |
| Remove CSAR62 | SVC-14 solvent at 70 °C for 1 hour, Acetone + IPA rinsing, and N ₂ blowing |

RIE etching is used to transfer the pattern from the CSAR62 mask to SiN film and locally etch the SiN film with sulphur hexafluoride(SF₆)/Argon(Ar) chemical gases (flow rate:10 sccm /10 sccm) and active plasma power 30 Watt. It gives the etching rate of SiN about 20 nm/min. After removing SiN parts, the RIE process continues to remove Si parts about 350 nm from the substrate. Opening SiN holes through the CSAR62 mask is crucial for the subsequent XeF₂ etching. In case of incomplete SiN layer etch, it would leave an ultrathin layer (< 100 nm) of SiN membrane, thereby inhibiting XeF₂ gas etching and failing to release SiN membrane from the substrate.

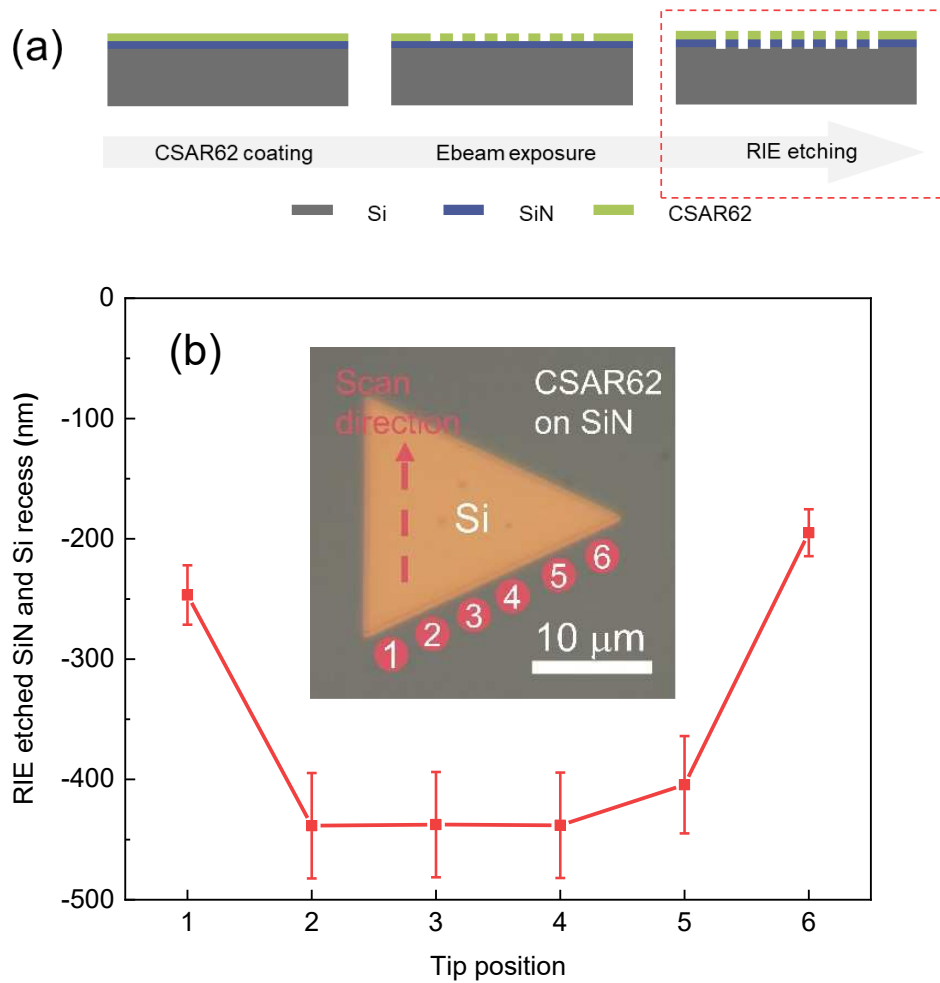


Figure 3.3.4. Recess characterization of RIE etching SiN thin film. (a) Schematic of cross sectional view. (b) Profilometry measurement results and the inset showing an optical image of a triangle pattern. The tip scan direction marked by red dashed line and its position marked by numbered red circles are present. Note that, CSAR62 resist mask (grey) on silicon remained and triangle pattern (yellow location) shows RIE etch cause.

In order to remark the fabrication, etch process logics is thought of as: (a) Etch test of RIE process, (b) Etch test of XeF₂ process, and (c) Releasing of SiN membrane.

(a) Etch test of RIE process.

Fig. 3.3.4 (a) shows RIE etch step of SiN thin film. In order to estimate a membrane fully being released or not, etching test is performed in our process. Here, a triangle pattern is defined with a dimension of about 20 μm. RIE etch is employed to transfer the triangle pattern from the CSAR62 mask to SiN membrane, hence obtaining an inverted pyramid trench. **Fig. 3.3.4 (b)**

inset shows the RIE etched triangle pattern. After analysing measurement resultant each sweep line of the tip on each start position, all the measured results can be rebuilt. The recesses exceed about 430 nm, implying SiN membrane about 100 nm in thickness and Si about 330 nm in thickness. They both have been removed at the centre part of this pattern. While, for the position edge, only about 200 nm materials have been etched away. These measurement results are important to have evidenced buried Si substrate exposing to reactive etchant gas.

(b) Etch test of XeF₂ process.

XeF₂ etcher tool (Xetch Xactix X3B) is engaged to continue to selectively etch Si material after RIE etch. This is because RIE etched holes pattern on SiN membrane exposed successfully Si material to XeF₂ gas. As XeF₂ gas has highly selective etching rate between Si and SiN[138], this rate is about 100 :1 in this process. Our aim is to use XeF₂ gas to etch isotropically the Si material to release the target SiN thin film from the substrate, thus forming a vibrating SiN membrane. To well release the SiN membrane, the chamber is maintained at 2.2 Torr and two cycles of etching are carried out with 30 seconds etch time per cycle. This gives the maximal etching rate of Si material about 70.4 nm/s. This rate highly depends on the exposure area and the doping density of the Si substrate. In this process, this XeF₂ etcher is able to choose “etch cycles” at a pressure and time for highly-efficient control of the Si material etching, and it also enables high selectivity of etching Si with XeF₂ by using CSAR62 resist and SiN masks.

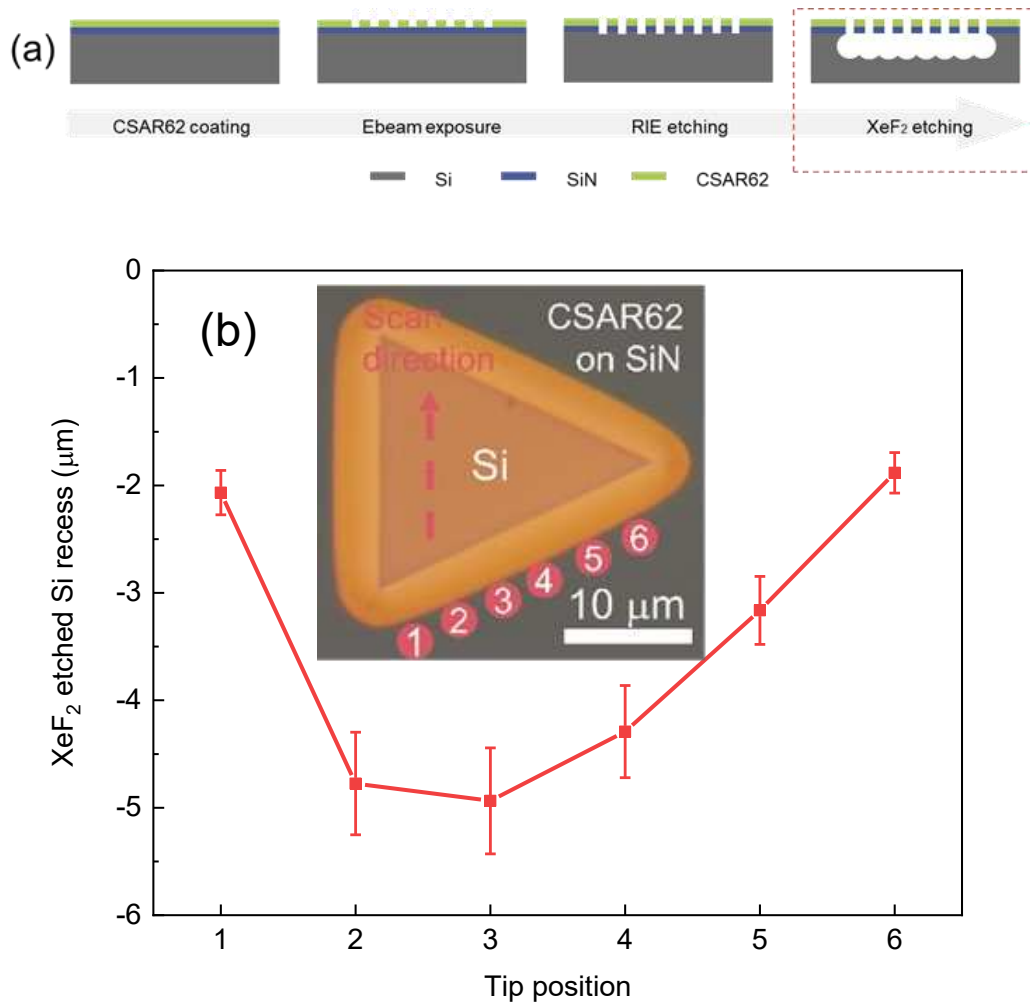


Figure 3.3.5. Recess characterization of XeF₂ etching the silicon material. (a) Schematic of cross sectional view for XeF₂ etching step. (b) Profilometry measurement results and the inset showing a triangle pattern. The tip scan direction marked by red dashed line and its position marked by numbered red circles are present. Note that, CSAR62 resist mask (grey region) is still on silicon and triangle pattern (yellow region) shows XeF₂ etch cause.

As described in RIE etched process, this triangle pattern etch went beyond at least 200 nm near the edge. So the silicon underneath of the SiN film has been exposed successfully. **Fig. 3.3.5 (a)** shows XeF₂ etched step, which continues with the RIE process. **Fig.3.3.5(b)** shows profilometry measurement results, where the pattern recess etched at the position edge over at least 2 μm and at the centre at least 4 μm . At the same time, the **Fig. 3.3.5** inset shows the undercut of the triangle pattern about 3 μm , indicating the etch depending on the exposure area. From this test observation, the silicon material etched by XeF₂ gas can be confirmed.

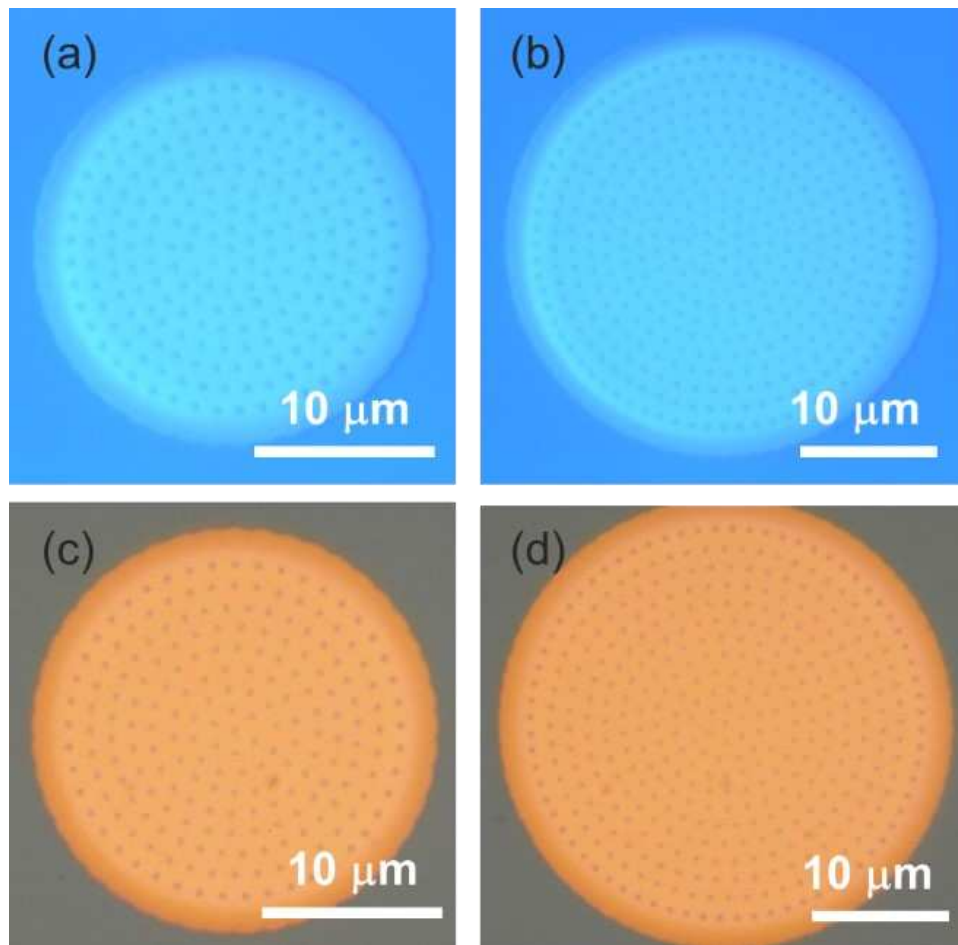
(c) Releasing of SiN membrane

Figure 3.3.6. Optical micrographs of released SiN membranes before (a,b) and after removing (c,d) CSAR62 resist mask.

Well etched SiN membrane, or not, can be determined based on three key points: first, The residue under the SiN should be checked, second, check the width of undercuts, third, check the edge shapes. According to the above analysis of the triangle pattern test, the released SiN membrane in principle can be achieved. Preliminary examinations on well-releasing SiN or not can be done by using optical microscope. **Fig. 3.3.6** shows well-released SiN membranes without and with removing the CSAR62 resist mask. The undercuts have been larger than the distance between the neighbouring holes $\sim 1.3 \mu\text{m}$, indicating a good release of SiN from the silicon substrate.

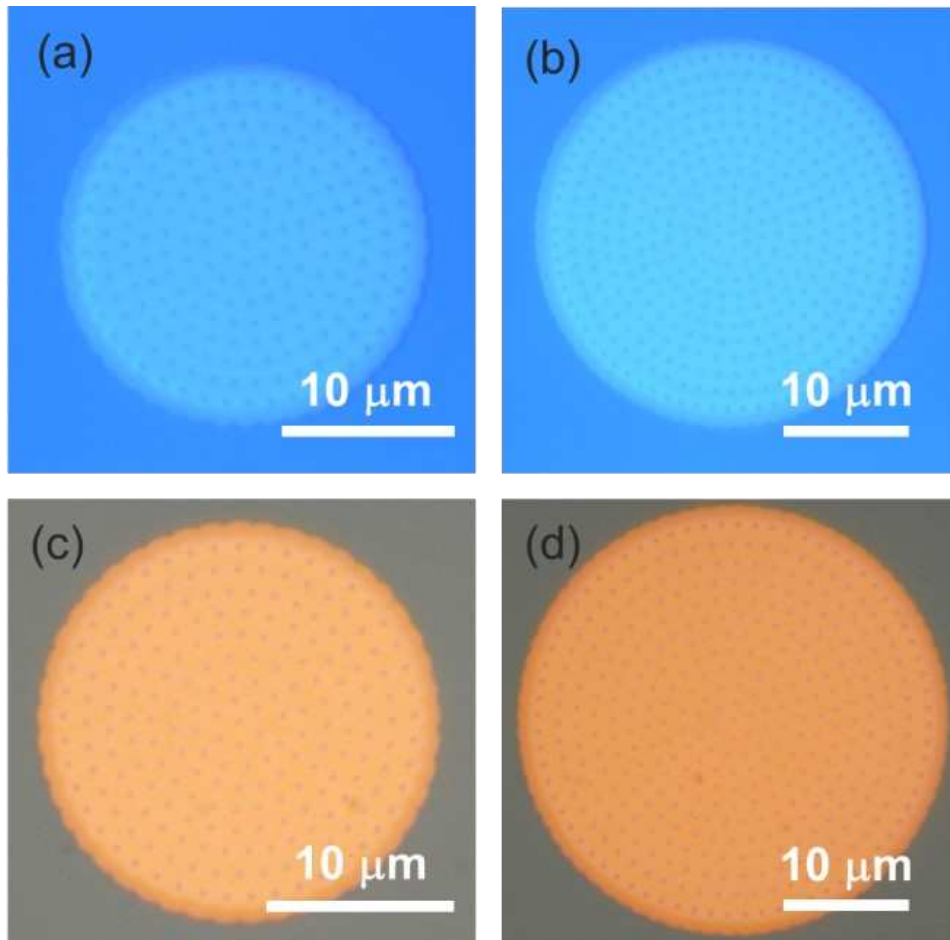


Figure 3.3.7. Optical micrographs of partly-released SiN membranes before (a,b) and after (c,d) removing CSAR62 resist masks.

Comparing with the well-released SiN membranes in **Fig. 3.3.6**, **Fig. 3.3.7** shows the partly-released SiN membranes. In these figures, the undercuts can be examined less than the distance between the neighbouring holes $\sim 1.3 \mu\text{m}$. It means the incomplete release of the SiN film, as results of some residues still underneath the SiN film. This problem will be discussed below to gather with SEM images. In the nanofabrication part, all SEM images were taken by C. Boyaval and X. Zhou.

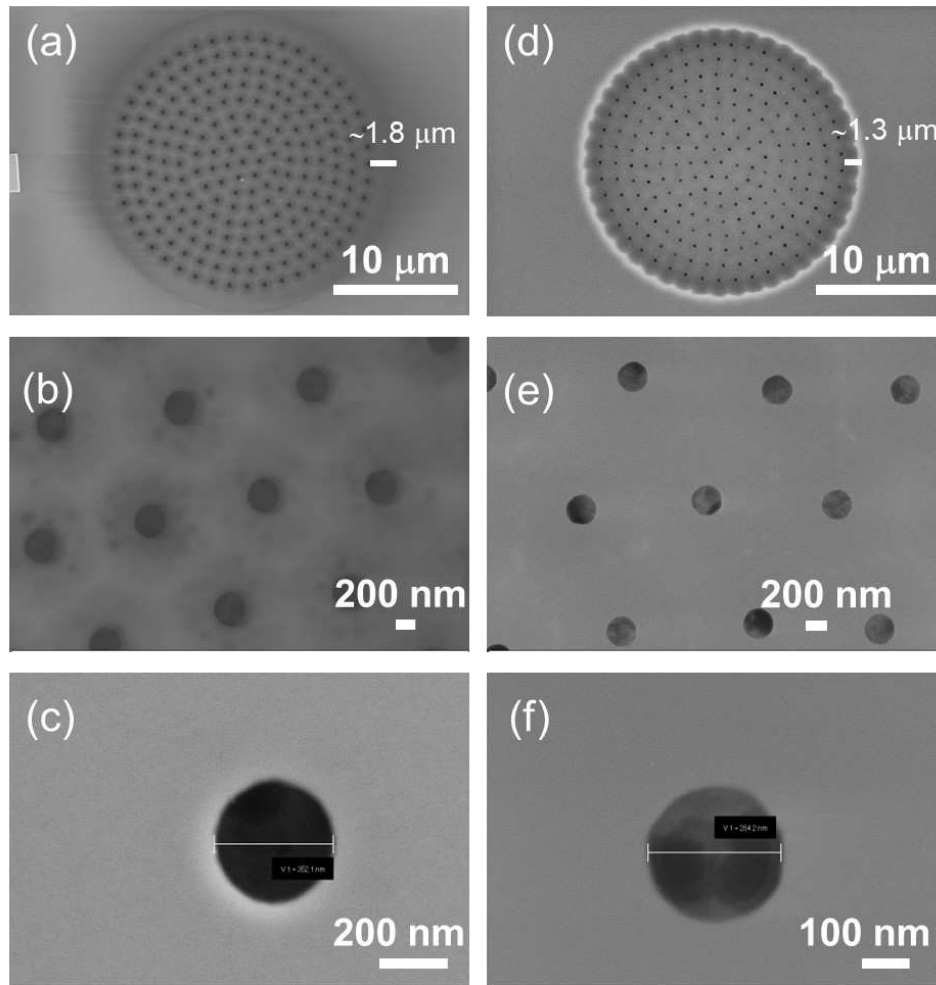


Figure 3.3.8. SEM micrographs of the released SiN membranes with 20 μm in diameter. (a-c) images show well-released SiN membrane after XeF_2 etching, in which holes are about 352 nm in diameter. (d-f) images show partly-released SiN membrane.

SEM microscope is employed to investigate the etch undercut. Unlike optical microscopy, SEM tool with electron beam scanning is able to not only examine the XeF_2 etched silicon material under the SiN film, but also observe whether the residues remain below the membrane or not. If residues are observed, it means SiN membranes vibrating are affected. Therefore, this kind membrane cannot be used to perform following nanofabrication process. **Fig. 3.3.8** shows a release comparison of SiN membranes. **Fig. 3.3.8(a-c)** show well-released SiN membranes, in which (c) shows pattern holes of about 352 nm in diameter observed by SEM. It indicates the well release of SiN membrane from silicon substrate, due to no residues observed as well. Besides, the high selectivity of etching silicon with XeF_2 gas is an orient independent (isotropic) etch, yet yielding a visible undercut about 1.8 μm next to the outer hole. This value is larger

than the distance between nearest neighboring holes. In addition, the edge shape of membrane is perfect circular. Thus, it also proves the membrane is well released. On the contrary, **Fig.3.3.8(d-f)** show partly-released SiN membrane examples. XeF₂ etching silicon residues are observed through these etching holes. The observable residues are attached under the SiN membrane, making the membrane difficult to vibrate. And they will lead to imperfect device performance. Specifically, **Fig. 3.3.8(d)** shows flower-like undercut edge exhibiting an underetch about 1.3 μm , in which (f) enlarges the hole appearance showing a diameter of about 284 nm, adversely coexisting the residues with the pattern holes. this flower-like undercut edge differs from the circular undercut edge. These phenomena are also observed in larger diameters in **Fig. 3.3.9**.

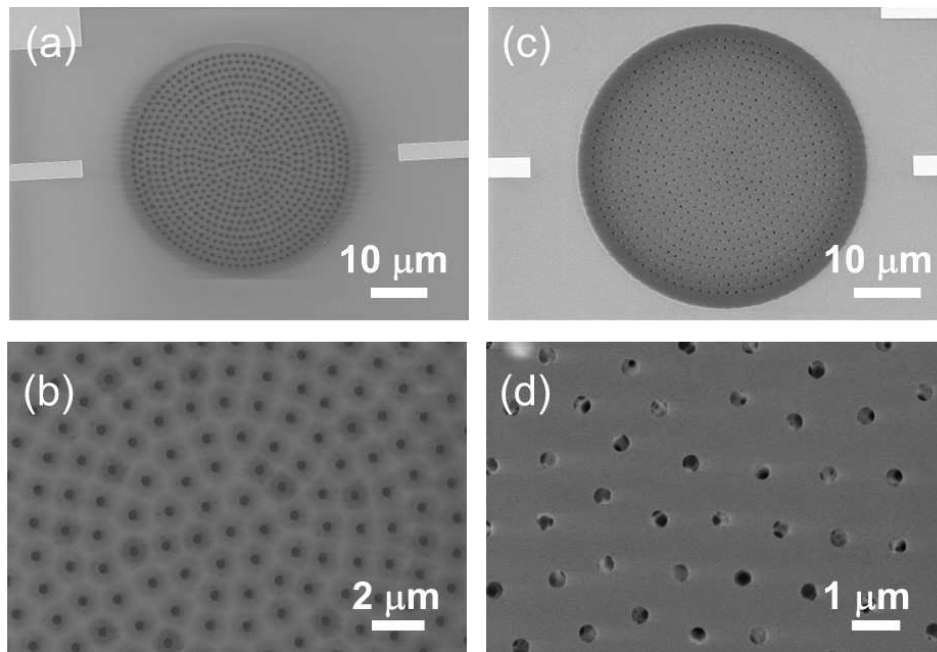


Figure 3.3.9. SEM micrographs of the released SiN membranes with 40 μm in diameter. (a,b) images have well-released SiN membrane, in which holes are about 355 nm diameter. (c,d) the SiN membranes have not well been released.

For the fabrication efficiency of SiN membranes, it needs to point out high efficiency depending on the well control of RIE and XeF₂ etching. Unfortunately, SiN membranes with contaminants are sometimes observed after optical microscopy checking. The fabrication efficiency of SiN membranes is defined by the ratio between the numbers of well-released clean membrane and all devices. For most high fabrication efficiency of SiN membranes, we have obtained the membrane success rate 95% at least (namely 60 devices out of 64 devices on a chip).

3.3.3 Aluminium film deposition on the released SiN membrane

In order to allow the SiN membrane to be capacitively coupled to an external gate electrode and to be electrostatically driven, a thin conductive film on SiN membranes are required, due to the insulating feature of SiN material. Here, three critical steps are included: first, EB resist spin coating on the released SiN membranes; second, EB lithographically exposing the drum patterns; third, metal evaporation performs for achieving a thin conductive film.

| Table 3.3.4. Aluminium thin film evaporation on SiN membrane | |
|---|---|
| Process | Parameters |
| Spin coating EB resist PMMA 4% | 2500 rpm speed, 1000 rpm/s_acc., 12 s_time, heating at 160 °C for 2 min |
| EBL writing drum patterns | Exposure dose 650 $\mu\text{C}/\text{cm}^2$, Current 50 na, Cell size 320 $\mu\text{m} \times 320 \mu\text{m}$ |
| Developing | MIBK (30 ml) : IPA (60 ml) for 1 min 40s, IPA rinsing for 10 s and N ₂ blowing |
| Metal evaporation | Ar pre-etching for 60s, Al 30nm at 0.1 nm/s |
| Lift off | SVC-14 solvent at 70 °C for 4 hour, Acetone + IPA rinsing, and N ₂ blowing |

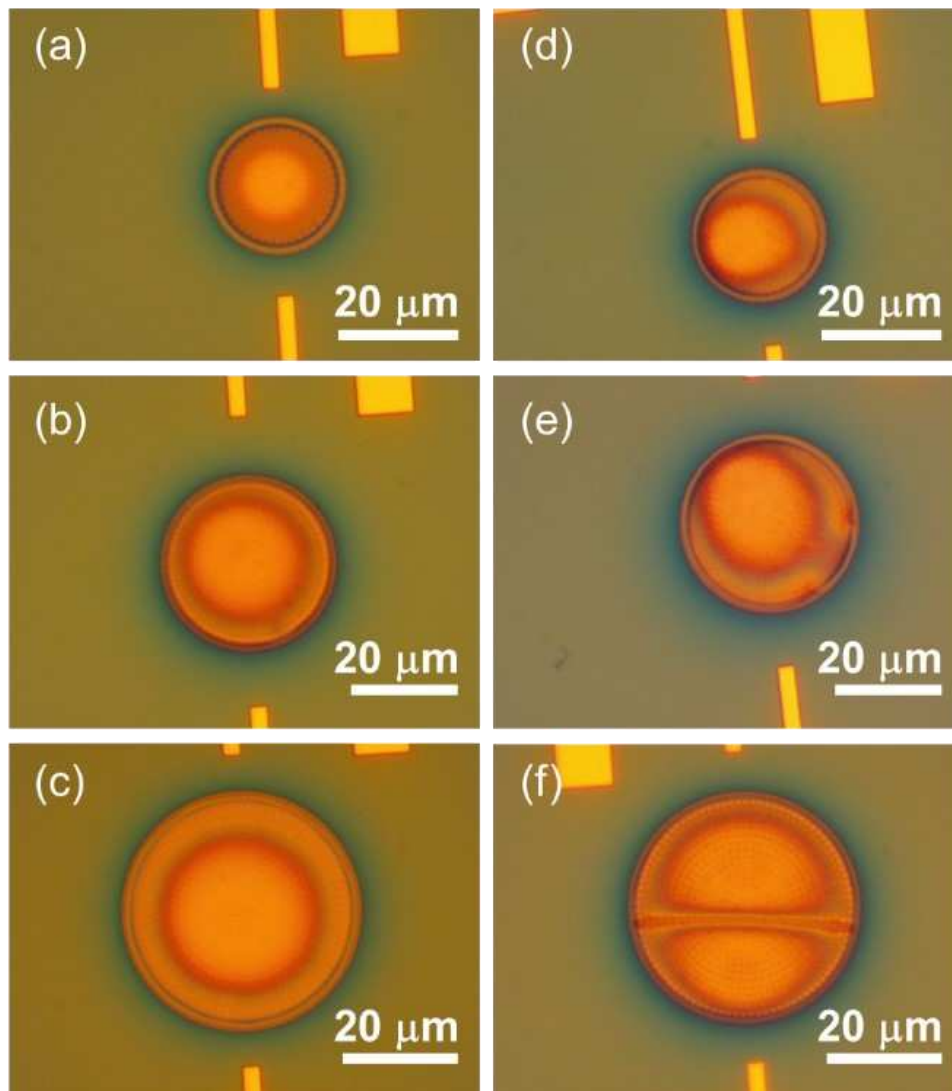


Figure 3.3.10. Optical micrographs of EB resists coating on the released SiN membranes with 20, 30 and 40 μm in diameters. (a-c) spin coating on SiN membranes is perfect. (d-f) spin coating on SiN membranes is imperfect. Note that PMMA EB resist coats on SiN membranes.

Fig. 3.3.10 shows optical images of EB resist on the released SiN membranes after coating. They present facing problems for metallization, including two spin coating issues: First issue is that EB resist covers uniformly on the SiN membranes in images (a-c). The phenomenon is inferred due to the buckling deformation when SiN membranes is released from silicon substrate. Second issue is not perfect coating on the SiN membranes in images (d-f) because of possible problems generated by spin-coating parameters, e.g., spin speed. If the bad impact arises from spin coating control, we are usually able to avoid the issue and use this membrane. This is because the morphologies are just not perfect, but do not affect membranes themselves,

EBL exposure and later processes. If some bad impacts arise from the contaminants on membranes, they are most of possibilities unable to be used, the mechanical resonator featuring very fragile SiN membrane does not suggest using ultrasonication machine to remove particles in spite of contaminations.

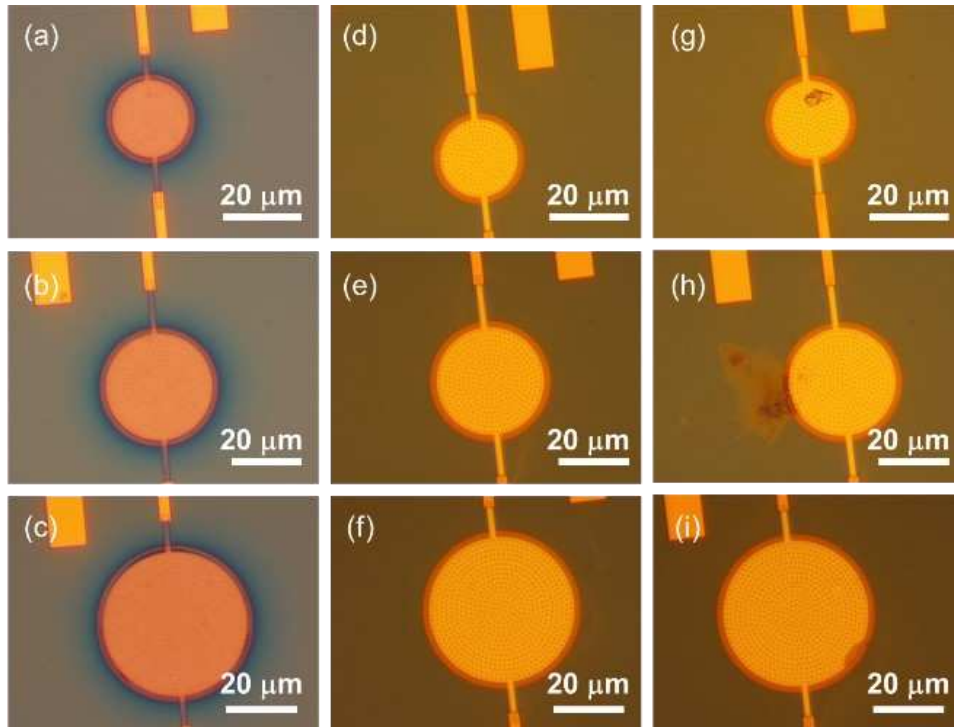


Figure 3.3.11. Optical micrographs of drum patterns and metal deposition. (a-c) EBL writing drum patterns, followed by development. (d-f) clean drum patterns, followed by lift-off process. (e-i) contaminants on drum patterns.

Fig. 3.3.11(a-c) show optical images of the developed drum patterns, which can be used for metal evaporation further. **Fig. 3.3.11 (d-f)** show optical images of perfect lift-off Al film on SiN membranes. In our process, Al metal is used, because its mechanical properties, e.g., tensile stress, are similarly close to SiN membranes and it is also measured in superconducting circuits at cryogenic condition [9]. **Fig. 3.3.11 (g-i)** show optical images of some contaminants on SiN drum membranes. This indicates SiN membranes cannot serve as mechanical resonator devices, because these contaminants result in high effective masses, following with reduction of the mechanical resonance frequency. It could also lead to low quality factor of the mechanical resonator. Besides, only 30 nm thin Al film is deposited on the SiN membranes, it is trivial for

affecting the performance of the SiN membranes. Despite the deposition going through the holes to the etched silicon cavity, forming a stray capacitance, the etched cavity depth at the pattern edge is at least 2 μm , this stray capacitance is quite small compared to the gate capacitance. Therefore, we are able to neglect its effect on the overall electrical performance of the device. The mechanical properties of the membrane are still dominated by the SiN membrane having high tensile stress, and the resonant frequency of the membrane is not reduced too much by the extra mass added by this thin Al layer.

3.3.4 Aluminium suspended top gate on the top of the SiN membrane

In order to form a capacitive coupling scheme, a suspended Al top gate on the top of the SiN membrane can be fabricated. This process is inspired by nanofabrication process of air bridge in superconducting quantum circuits [145]. In our process, sacrificial EB resist layer is first fabricated for supporting Al suspended top gate and then EBL is used to expose top gate patterns.

3.3.4.1 Coating of EB resist sacrificial layer

EB resists (either PMMA or PMGI) is exploited as sacrificial layer to spin coat on the Al/SiN membranes. As discussed in section 3.1.1, a desired thickness layer of EB resist is defined to achieve a distance between the SiN membrane and its suspended top gate.

| Table 3.3.5. Coating PMMA resist as sacrificial layer on SiN membrane | |
|--|--|
| Process | Parameters |
| Coating EB resist PMMA 4% | 4000 rpm_speed, 1000 rpm/s_acc., 12s time, heating at 150 °C for 2 min |
| Coating EB resist PMMA 5% | 3000 rpm_speed, 1000 rpm/s_acc., 12s time, heating at 150 °C for 2 min |
| EBL writing feet patterns | Exposure dose 650 μ C/cm ² , Current 50na, Cell size 320 μ m \times 320 μ m |
| Developing | MIBK (30 ml) : IPA (60 ml) for 1 min 40s, IPA rinsing for 30 s and N2 blowing |
| Bake and reflowing | temperature at 180 °C for 3 mins |

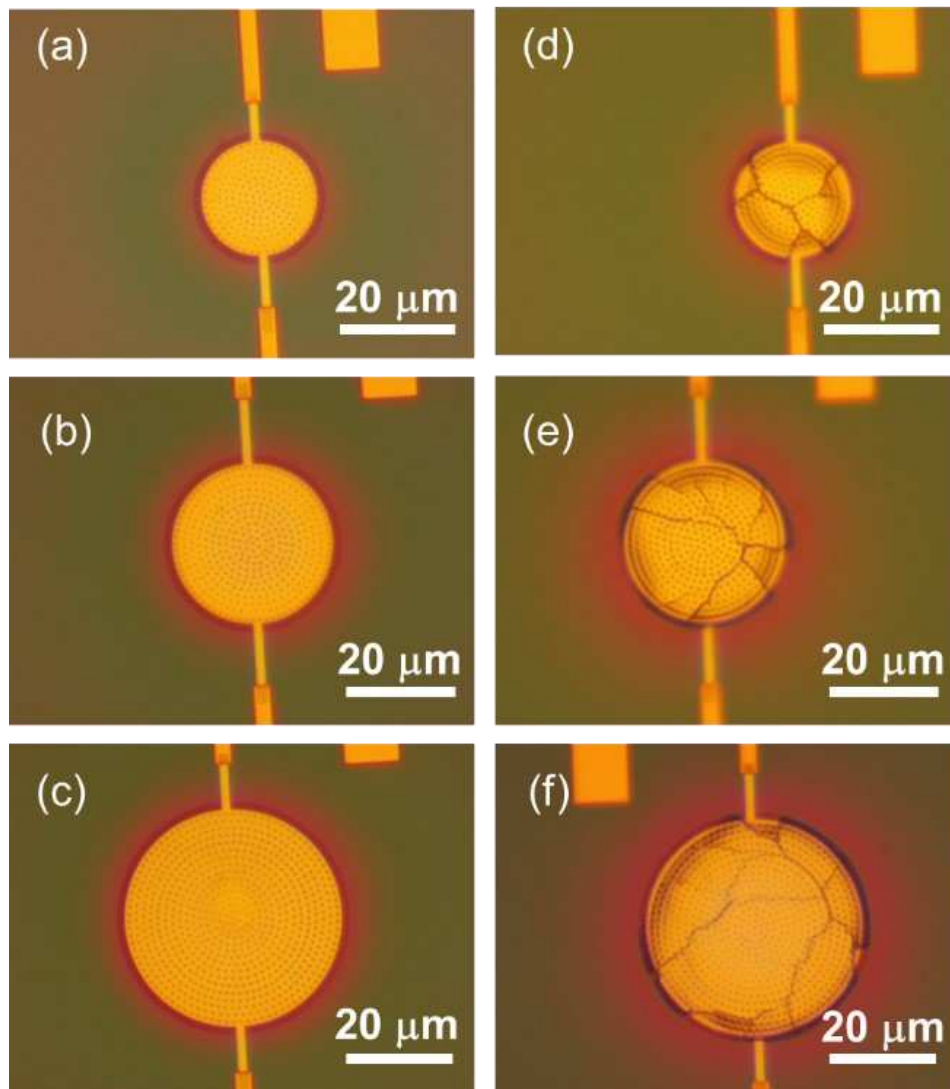


Figure 3.3.12. Optical micrographs of EB resists spin coating on Al/SiN membranes. (a-c) perfect Al/SiN membranes after coating and baking; (d-f) broken Al/SiN membranes after coating and baking.

This EB resist will first be soft baked at the relatively low temperature about 150 °C. **Fig. 3.3.12** shows optical images of EB resists spin coating, which include perfect membranes and broken membranes. **Fig. 3.3.12(a-c)** show perfect examples of Al/SiN membranes. They are 20 μm, 30 μm, and 40 μm in diameters. Comparing with these ideal Al/SiN membranes, **Fig. 3.3.12 (d-f)** show some broken examples of the Al/SiN membranes. They present broken features, illustrating their properties unable to be used further. The broken phenomena can be inferred because of possible soft baking. Baking atmosphere is able to yield heating to form a soft solid

EB resist film on the membrane surfaces. This solid EB resist film may deform and break the membranes to the generated strain.

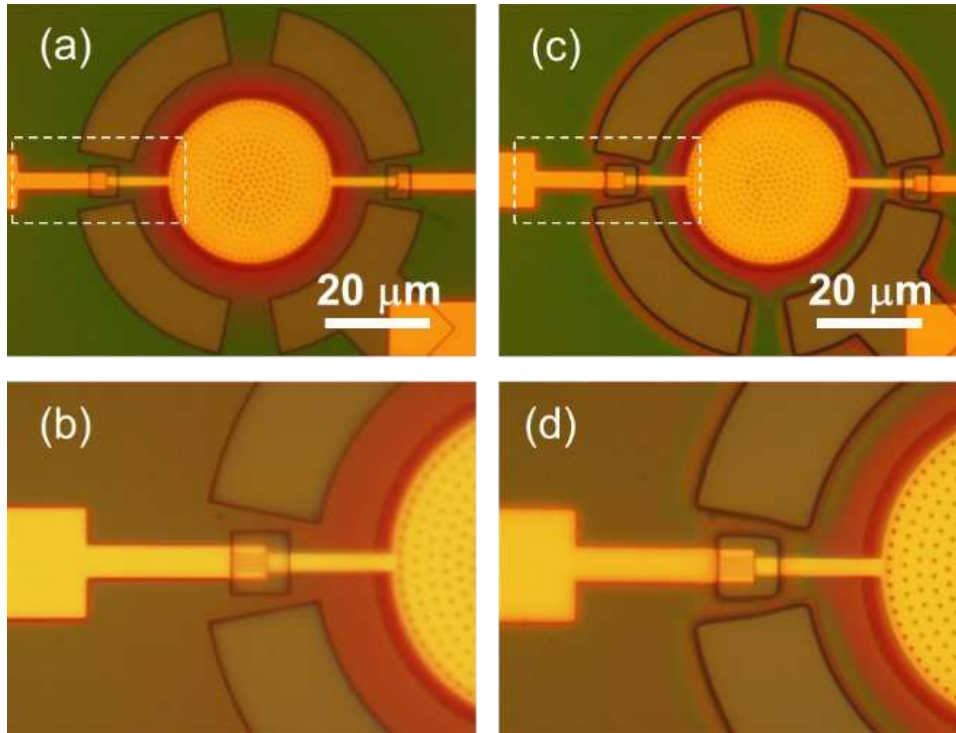


Figure 3.3.13. Optical micrographs of EBL writing support feet, showing examples of 30 μm diameter drum pattern after development. (a,b) before and (c,d) after soft baking.

After patterning the feet of the suspended gate through EBL, followed by development, the resist is then baked again at the higher temperature about 180 $^{\circ}\text{C}$. It is well known as the reflow process [145], where the patterns edges are rounded, thereby avoiding the following lift-off process. **Fig. 3.3.13(a,b)** show before soft baking patterns with fine development features, exhibiting observable sidewalls. After soft baking at the higher temperature about 180 $^{\circ}\text{C}$, **Fig.3.3.13(c,d)** show the reflowing process of feet patterns, resulting in the rounded edge. Profilometry is further used to measure the thickness of PMMA coating, showing soft-baked rounded effects after its development. **Fig. 3.3.14** below shows an example of PMMA coating thickness about 750 nm which defines the distance between the SiN/Al membrane and its suspended top gate.

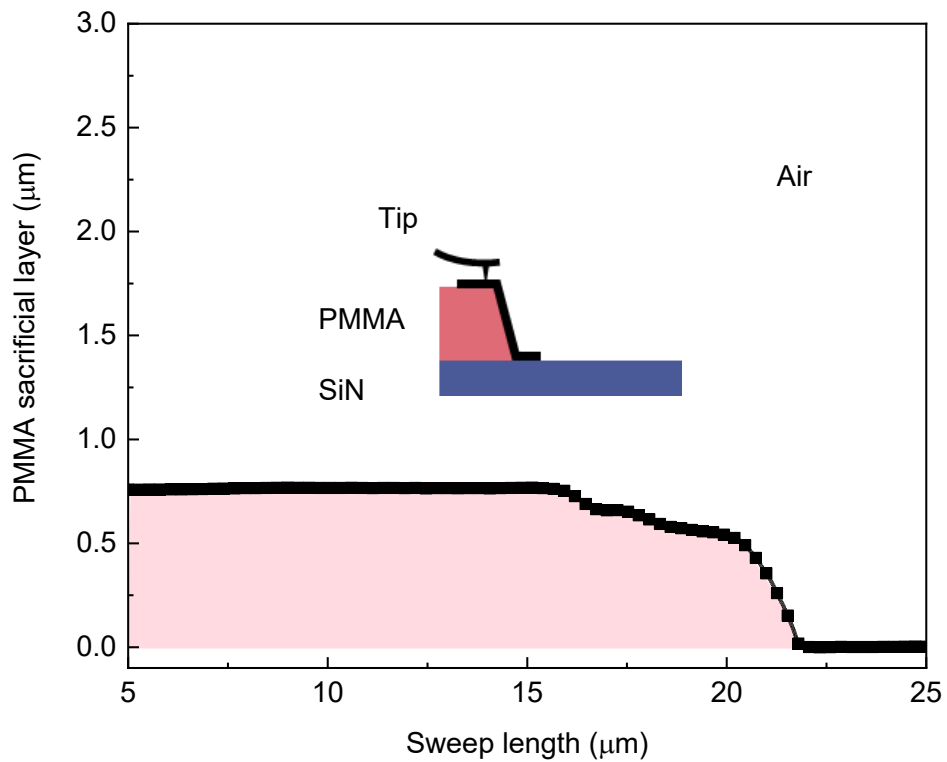


Figure 3.3.14. Profilometry measurement of EB resist coating on the Al/SiN membranes. Pink region is PMMA, the height of which is measured by the tip (insert).

3.3.4.2 Formation of suspended Al top gate on the top of SiN membrane

A bilayer of EB resists are spin coated, namely 2 μm thick MMA (methyl methacrylate), and ~ 120 nm thin CSAR62 resist, which helps a suitable critical lift-off process later. The final top-gate is patterned on this bilayer EB resists through EBL, which is followed with development and evaporated with ~ 550 nm thin Al film. The device fabrication process has ended up after the lift-off process.

| Table 3.3.6. Formation of suspended Al top gate on the top of SiN membrane | |
|---|--|
| Process | Parameters |
| Spin coating EB resist MMA | 2500 rpm_speed, 1000 rpm/s_acc., 12s time, Softbaking at 130 °C for 2 min |
| Coating EB resist CSAR62 (1/0.5) | 1500 rpm_speed, 1000 rpm/s_acc., 12s_time Softbaking at 130 °C for 2 min |
| EBL writing top gate patterns | Exposure dose 300 $\mu\text{C}/\text{cm}^2$, Current 50na, Cell size 320 $\mu\text{m} \times 320 \mu\text{m}$ |
| Developing CSAR62 | AR600-546 developer for 30 s, IPA rinsing for 10 s and N ₂ blowing |
| Developing MMA | Methanol (10 ml) : IPA (30 ml) for 35 s IPA rinsing for 10 s and N ₂ blowing |
| Metal evaporation | Ar pre-etching for 60s, Al ~ 550 nm at 0.5 nm/s, |
| Lift off | SVC-14 solvent at 70 °C for 2 hour, Acetone + IPA rinsing, and N ₂ blowing |

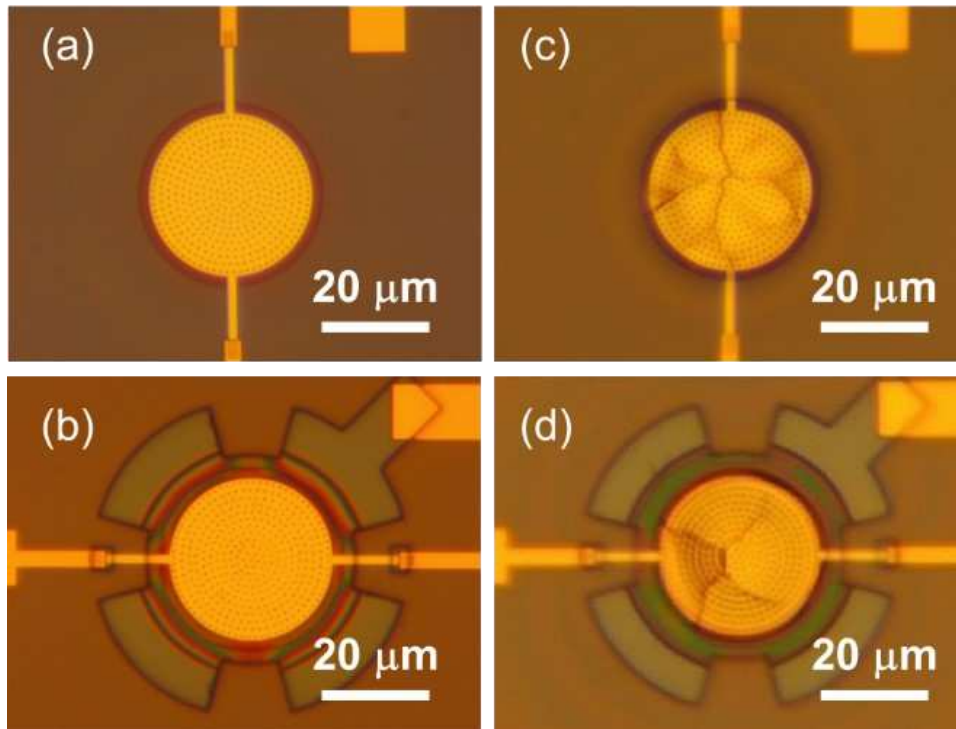


Figure 3.3.15. Optical micrographs of EB resists coating on the sacrificial layer. (a,b) spin coating showing uniform EB resists on Al/SiN membrane; (c,d) spin coating showing a broken example of Al/SiN membrane. Note that MMA and CSAR62 EB resists are used here.

Fig. 3.3.15(a,b) show optical micrographs of the final drum patterns (including support feet patterns). It indicates a successful sacrificial layer fabrication, contributing to Al suspended top gate formation. Besides, **Fig. 3.3.15(c,d)** show broken examples of the drum patterns. It evidences an unsuccessful case for suspending Al top gate. By optimising spin coating parameters, it is possible for us to avoid having broken membranes. There include two main factors: the first one is the droplets control of EB resists and the second factor is to reduce inner pressure during spin coating. For the latter one, we can leave spin coater's lid open so as to reduce pressure inside the machine.

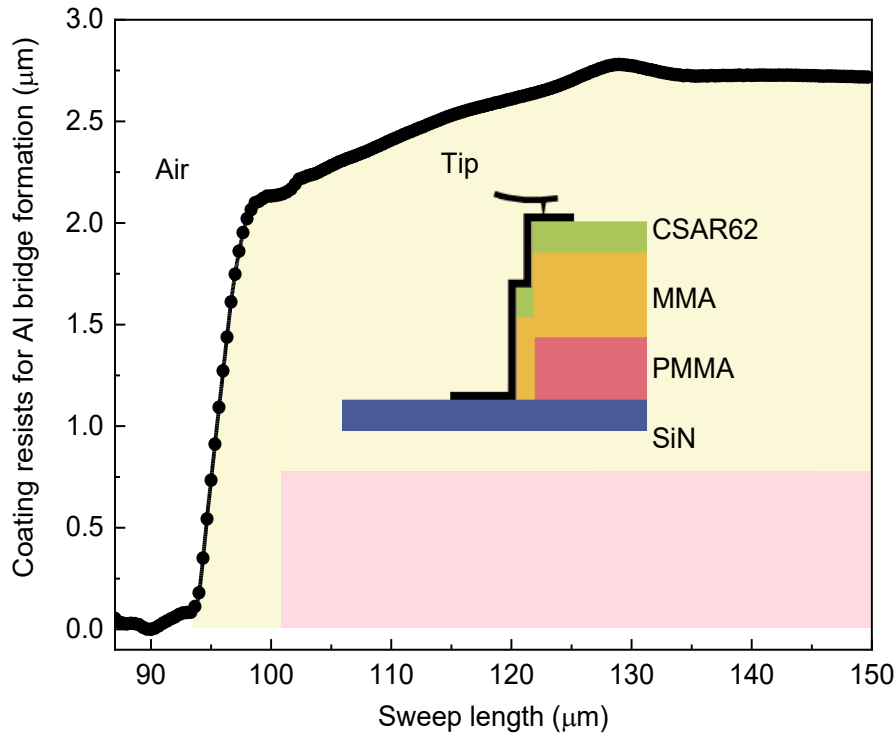


Figure 3.3.16. Profilometry measurement of EB resists coating on the sacrificial layer. Pink region is PMMA sacrificial layer and light yellow region is MMA-CSAR62 bilayer resists. Their total height is measured by the tip (insert illustration).

Fig. 3.3.16 shows the coating bilayer, namely both MMA and CSAR62 resists (light yellow). A total height of EB resists about 2.5 μm is measured. This height is higher 3 times than an expected Al deposition thickness so as to lead to a critical lift-off.

It is while worth noting that the final lift-off not only does remove the sacrificial resist (EB resist: PMMA) for supporting the top gate, but it also removes the bilayer resists (EB resists: MMA and CSAR62) coated on the top of the sacrificial layer for having lift-off of the Al film.

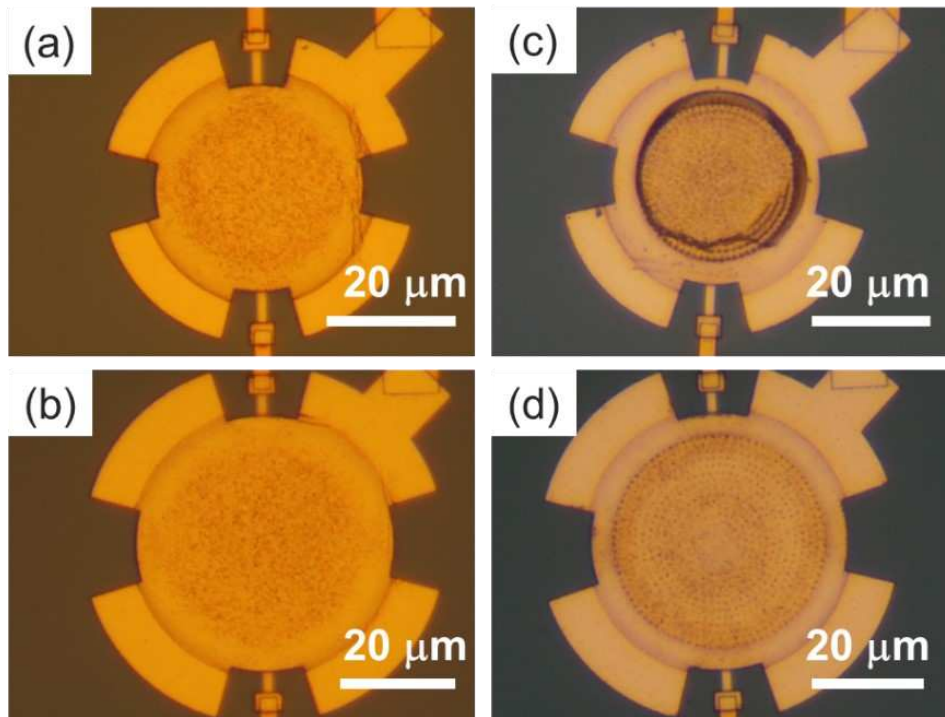


Figure 3.3.17. Optical micrographs of top view for the final SiN drum mechanical resonators. (a,b) successful examples and (c,d) unsuccessful examples of drum mechanical resonators. Note that Al about 550 nm is used for top gate here.

After full fabrication process, we achieved the final SiN drum mechanical resonator consisting of the Al/SiN drum membrane capacitively coupled to its Al suspended top gate. **Fig.3.3.17(a,b)** show successful examples of SiN drum mechanical resonators with 30 μm and 40 μm in diameters. On the contrary, **Fig. 3.3.17(c,d)** show failed examples of top gate of SiN drum mechanical resonators. These drum resonators are unable to be used further. When the Al top gate stick to the bottom drum, these holes on the top of sin drum can be clearly observed.

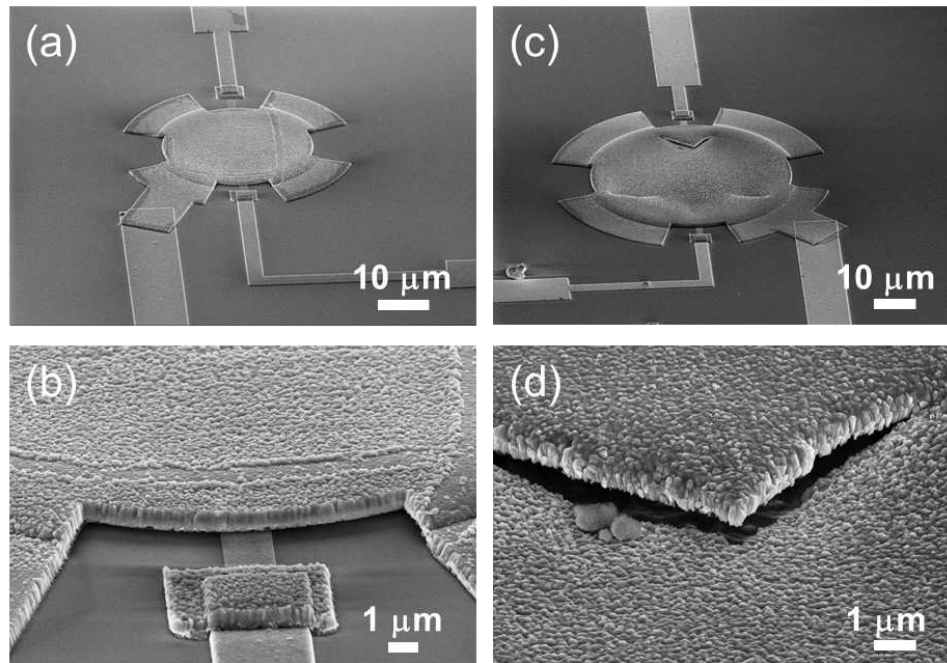


Figure 3.3.18. SEM micrographs of the final SiN drum mechanical resonator. (a,b) successful examples of the final drum resonator with 30 μm in diameter ; (c,d) failure examples of the final drum resonator with 40 μm in diameter.

Fig. 3.3.18(a,b) show a successful SiN drum mechanical resonator. From SEM image view, Al/SiN membrane under the top gate is connected to one contact line and the Al suspended top gate is linked to the other contact line. **Fig. 3.3.18(b)** shows close-side view of a distance gap. However, it cannot indicate the real distance due to the tilted observation angle. It is also worth to mention that real electrode gap can be measured by professional laser metrology; or, the real gaps have been obtained by measuring the devices and fitting the amplitude of the device. **Fig.3.3.18(c,d)** shows a failed top gate of SiN drum mechanical resonator. A broken open is presented on the top of Al suspended top gate. **Fig. 3.3.18(d)** shows an enlarged feature in the broken region. This case has two possible reasons: First, the collapsed SiN membrane underneath the top gate leads to device failure, Second, the resist has not yet been removed thoroughly, causing a top gate failure. For the fabrication efficiency of Al top gate membrane, its fabrication efficiency mainly depends on adding the reflow process (also mentioned in Figs.3.3.13 and 3.3.14). Unfortunately, the broken Al top gates are observed by optical microscopy examining. Therefore, most high fabrication efficiency of Al top gate is defined by the ratio between no broken Al top gates and all devices. We have obtained the final device success rate 22% (namely 14 devices out of 64 devices on a chip).

3.4 Summary

In this chapter, we introduced key fabrication tools used for nanofabrication process with tool's principle and basic critical steps. Besides, finite element method (FEM) simulation of mechanical damping rates of SiN drum membrane is performed so as to optimize the device design and help us to understand the trade-off between achieving low clamping losses and feasible fabrication process. Main fabrication steps have also been discussed, including (i) alignment marks, contact lines and pads, (ii) release of SiN membrane from the silicon substrate, (iii) aluminium thin film deposition on the released SiN membrane, and (iv) aluminium suspended top gate on the top of the SiN membrane, in order to provide essential and detailed guidance for the fabrication of SiN drum membrane mechanical resonator. In addition, two key fabrication steps, namely the release of SiN membrane and forming a suspended top gate, have been discussed carefully, so as to offer the critical dry XeF_2 selective etching process and reflow processes. Also, the failure of fabrication has been analysed mainly associated with the EB resists coating and lift-off processes.

Chapter 4 Scanning microwave microscopy for detecting mechanical vibration of SiN membrane

In this chapter, we will introduce a promising SMM technology that is used for investigating the mechanical vibrations of SiN drum membrane. Before simulations and experiments, the flexible functions of the AFM-tip, serving as a movable gate, will be introduced as it is able to accurately approach on a membrane surface with a gap in the nanoscale. Then, comsol simulations will be presented in order to help us for better understanding of the interactions between the AFM-tip and membrane. Later, characterizations of this SiN drum membrane through the AFM-tip will be performed that show basics of the device properties, such as linear, nonlinear behaviours and so on.

4.1 Scanning microwave microscopy

4.1.1 The overview and the state-of-the-art of scanning microwave microscopy

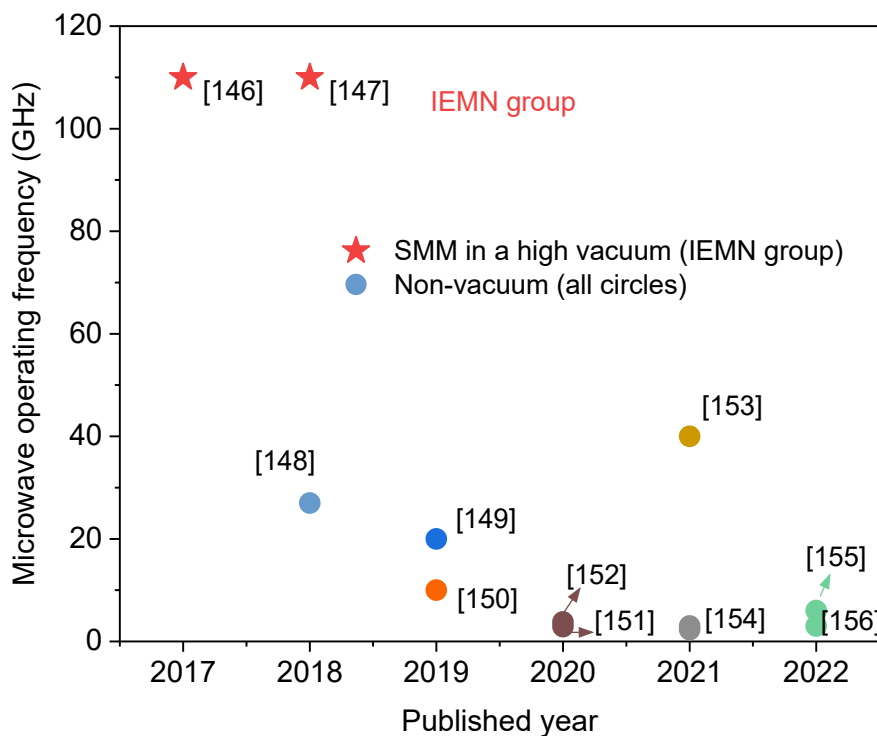


Figure 4.1.1. The development of SMM technique, with continuous contributions to the SMM imaging community[146–156]. Note that pentagram symbols (IEMN group) are representatives for SMM with the frequency up to 110 GHz in a high vacuum.

Scanning microwave microscopy (SMM), due to the local manipulation flexibility in the nanoscale and very high operating frequency, potentially up to 110 GHz, is an important technique for investigating quantitative nanoscale electrostatics. It mainly contains an atomic force microscope (AFM) and allows the metallic AFM-tip to be compliantly connected to external electrical measurement systems, such as vector network analyser (VNA). To date, investigations of materials' properties using SMM have been performed in imaging material topological phases [150,151,154,156], imaging and calibrating fF/aF-scale capacitances [153,157], impedance [158] and carrier densities [148], imaging buried materials nanostructures [159] and imaging biological live cells [160]. These previous investigations are important implementations beneficial for superconductivity, conductance or capacitance in stationary hetero-structures. Because some novel nanoscale structures with high impedance can be easily affected by parasitic capacitance, this effect leads to a long signal response time. [161] Therefore, high operating frequency will overcome this problem, making improvement of signal detecting speed. **Fig. 4.1.1** shows the development of SMM in the recent five years regarding to the microwave operation frequency, in particular IEMN group performing very high operating frequency up to 110 GHz since 2017 [146,162]. This high frequency has the potential to be applied in high-speed signal detection for nanoelectronic devices, such as single electron transistor [163] and carbon nanotube [164].

In this chapter, we show our efforts in extending SMM techniques to the investigations of nanoelectromechanical resonators. In the setup, a metallic tip is exploited as a suspended top gate over the SiN membrane that is covered with a thin aluminium layer. In our SMM equipment, the metallic AFM-tip is connected to a microwave measurement system by a coaxial cable. The microwave signal can be generated by either a VNA or a microwave source and is detected in a reflection mode. The AFM has also been integrated with a SEM in a vacuum chamber (7×10^{-4} mbar). Because of such a vacuum condition and the capacitive coupling scheme, the tiny displacement of SiN drum membrane is able to be excited and detected through a single metallic AFM tip.

Here, the AFM-tip-sample interface analysis is first introduced for presenting the AFM-in-SEM paramount capability of approaching to or retracting from the SiN sample. In order to excite the mechanical vibrations of the membrane, we use lockin amplifier to drive the membrane around its resonance frequency. A microwave signal is delivered to the coupled membrane through the AFM-tip. Its reflected signal carries the signal of the mechanical vibration back. By using such a SMM technique, our measurements are performed at room temperature and the

results discussion is made, including SiN membrane's linear mechanical response, resonance frequency modulation, Duffing nonlinear mechanical response, mechanical modes detection and double-tone driving scheme. White noise drive of SiN membrane has also been measured. Finally, we summarized the main results of this study.

4.1.2 AFM-tip-sample interface and principle

The distance between the AFM-tip and the sample surface plays an important role in detecting mechanical vibrations of the SiN membrane. In the case of capacitive coupling scheme, the capacitance value mainly depends on the actuation area and actuation distance between two capacitance electrodes. Fortunately, using SMM technique, the AFM-tip position can be adjusted for a wanted distance down to 10 nm, where an aF/fF-scale capacitance is convenient to be attainable. However, the tip-sample interface principle requires to be well understood.

Before introducing the operation of AFM-tip, the knowledge of interacting forces between the AFM-tip and sample is explained. The electrical potential distribution in the tip-sample interface can be influenced by work function variations due to sample surface adsorbates, crystallographic orientation, sample surface preparation and even contamination [165,166]. Fortunately, supplying electrical charges helps cancelling this kind of intrinsic electrical background effect, further contributing to the fF/aF-scale capacitance in experiments. Date back the year of 1970, a surface probe apparatus has been applied for investigating the distance dependence of van der Waals forces [167], requiring a small-distance force effect between two objects [168,169]. Today, AFM has still been a promising tool to measure the atomic level effects through its ultrasharp metallic tip, which can be adjusted to approach a sample surface. When AFM-tip-sample distance is in several tens of nanometers, the interacting forces are long-range forces. Therefore, van der Waals forces are weak and can be neglected in our case[170,171].

In the following part, we did not consider this electrical potential in our measurement, because its effect is negligible comparing with the potential generated by the large DC bias.

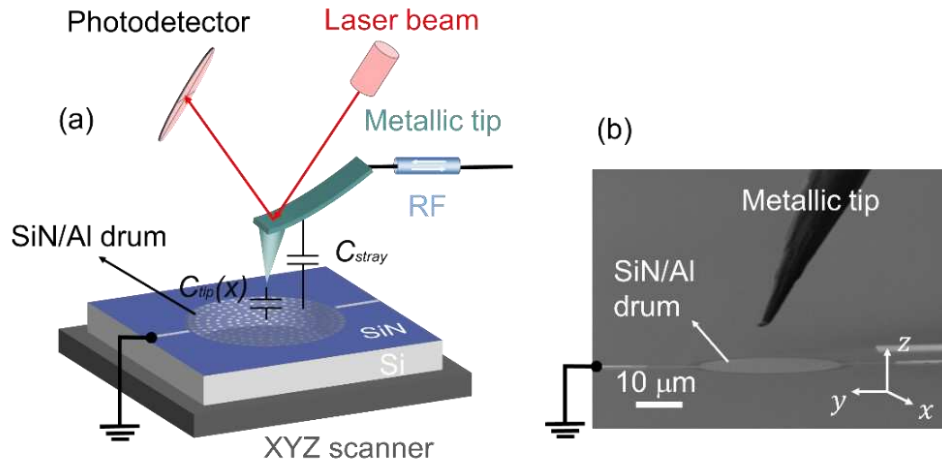


Figure 4.1.2. AFM-tip and sample interface. (a) Schematic of the interface between the AFM-tip and the SiN drum membrane. (b) SEM micrograph of the tip-sample interface, where the SiN/Al drum membrane is connected to the grounding through the connected leads and is capacitively coupled to the metallic AFM tip.

Fig. 4.1.2 shows a schematic of the interface mainly consisting of SiN/Al drum and a conductive AFM-tip. For such an interface, a small distance is able to be obtainable attributed to the high-resolution of the manipulation (about 10 nm) of the sample holder piezo-actuator scanner along X-Y-Z axes. Besides, if there are no electrical charges on the tip or sample surface, electrical potential energy should be zero, the corresponding Coulomb force is zero. For our capacitive coupling scheme, the two electrodes, namely the AFM-tip and SiN/Al drum membrane, are all conductive, having a tunable Coulomb force between these two objects.

For the AFM system, an ideal probe contains an ultrasharp tip and is mounted on a soft cantilever spring. The AFM-tip is usually fixed and the sample holder mounted on the piezo-actuator scanner can be moved flexibly along X-Y-Z axes with a maximum span of few tens of micrometers. The interacting forces between the AFM-tip and sample surface are able to be formed due to Coulomb electrostatic forces. Besides, a focused laser beam spot radiates on the right place of the cantilever end for monitoring the small interacting forces changing and it will be subsequently deflected to the photodetector window. By using a position-sensitive photodetector, the interacting forces variation is convenient to be collected and registered. In addition, the converted optical information is able to feed back the piezo-actuator scanner so as to maintain a deflection setpoint within a closed loop automation process. Therefore, a desired interaction force is reached based on such hybrid AFM controller platform.

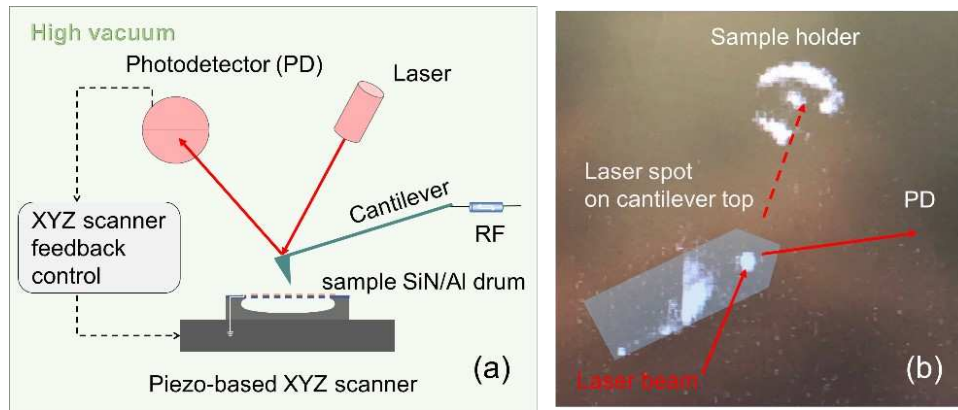


Figure 4.1.3. Illustration of the cross sectional view of the hybrid AFM-in-SEM setup. (a) A laser beam (650 nm) radiates on the top of cantilever end and is deflected to the photodetector (PD) to convert the laser intensity to the photoelectric voltage. This voltage signal is fed to the XYZ feedback controller to optimally move the piezo-based XYZ scanner [147]. (b) Real photo of laser spot ($\sim 30 \mu\text{m}$) on the cantilever end.

Fig. 4.1.3 illustrates schematically the hybrid AFM-in-SEM in a vacuum atmosphere, where the optical system is responsible for monitoring the interacting forces between the AFM-tip and the sample surface. The laser radiates a spot on the cantilever end that is reflected towards the photodetector window. In general, the interaction between the AFM-tip and sample surface can be monitored in several ways. In contact mode, the cantilever is deflected statically by the pressure exerted by the sample on the AFM cantilever. The deflection is registered on the photodetector and feeds back to the piezo-actuator scanner so as to reach a desirable deflection of the AFM-tip cantilever. In tapping mode, the cantilever is mechanically excited by a small piezoelectric actuator near its resonance frequency. The vibrating amplitude detected by the photodetector is then measured by a lock-in amplifier. When approaching the sample, the cantilever vibration amplitude reduces because of the interaction forces between the sample and the AFM-tip. The measured amplitude feeds back to the piezo-actuator scanner to reach a desirable small average distance between the AFM-tip and the sample surface. Here, the AFM-tip-in-SEM was designed to operate in contact mode (as can be seen in **Fig. 4.1.3** and **Fig. 4.1.4**).

Approaching sample surface is necessary for achieving a small inter-electrode distance. The better understanding of nanoscale manipulating origin of piezo-actuator XYZ scanner requires careful explanations using the approach-retract principle. Therefore, three aspects are discussed: (i) Control loop of photodetector feeding to piezo-actuator scanner; (ii) Contact scheme of the

AFM-tip approaching sample surface; (iii) Sensitivity measurement based on the approach-retract process.

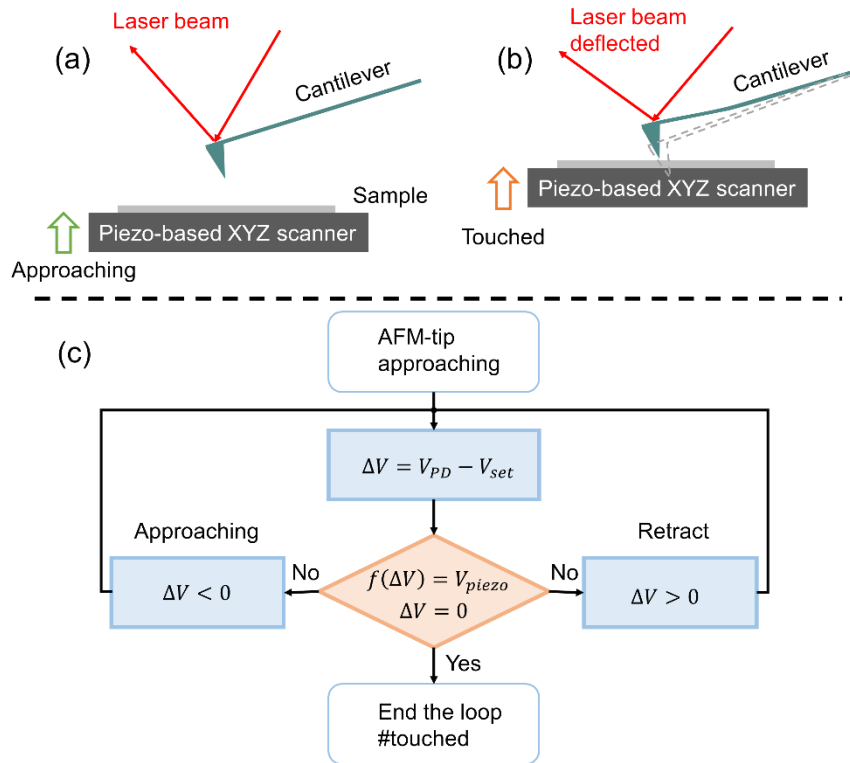


Figure 4.1.4. Piezo-actuator XYZ scanner movement along Z-axis. (a) Approaching and (b) Contact between the AFM-tip and sample surface. (c) Approach-retract loop flowchart, where V_{PD} , V_{set} and V_{piezo} are the voltages from the photodetector, controller voltage set-point and sample piezo-actuator scanner respectively. $V_{piezo} = f(\Delta V)$ is the embedded function dependent of ΔV for calculating the voltages to be applied on the piezo-actuator scanner so as to assess the approach-retract positioning.

(i) Control loop of photodetector feeding to piezo-actuator scanner

When the AFM-tip does not touch the sample surface, the laser beam radiates on the cantilever without bending and the spot is naturally reflected onto the photodetector window. In other words, with approaching the surface, the photoelectric signal from photodetector feeding to the piezo-actuator controller does not change. In practice, the initial reference voltage value from the photodetector is based on the non-contact mode (**Fig. 4.1.4(a)**). In fact, the cantilever consists of a thin beam that ends with the AFM-tip and behaves as a spring. Once the contact happens (**Fig. 4.1.4(b)**), as mentioned above, the “spring” cantilever is slightly bent, resulting

in a reflected optical intensity variation on the photodetector window. Its updated signal is straightforward converted to a voltage value to be transmitted to the piezo-actuator controller interacting with the AFM-tip.

In order to describe the approach-retract principle, a schematic of the loop flowchart is shown in **Fig. 4.1.4(c)**. A piezo-actuator scanner assessment with regards to the voltage signal (V_{piezo}) is introduced, which is able to assess the critical point value while approaching the sample surface. With the AFM-tip approaching, actually, the sample on piezo-actuator XYZ scanner approaches the AFM-tip. If $\Delta V < 0$, it means that the AFM-tip is not interacting with the surface, namely, which results in the continuation of the approaching process. If $\Delta V > 0$, it means that the AFM-tip has touched the surface and needs to be optimized in time while interacting with the controller. If $\Delta V = 0$, it means that the contact is reached as fixed by the set-point V_{set} .

(ii) Contact scheme of the AFM-tip approaching sample surface

| Table 4.1.1. Essential parameters of the AFM-tip contacting the surface | | | |
|--|------------------------|-------------------|------------------------------|
| Parameters | Setting values | Calculated values | Notes |
| f_c (nN) | 280 | - | nN to μ N |
| A_c (m^2) | 2.82×10^{-13} | - | AFM-tip apex |
| P_c (GPa) | - | 0.001 | AFM-tip apex |
| E_{sample} (GPa) | 280 | - | Young's modulus |
| $k_{cantilever}$ (N/m) | 22 | - | Nominal |
| Δz (nm) | - | 12.72 | Static cantilever deflection |
| S (mV/nm) | - | 0.23 | Sensitivity |
| $V_{horizontal}$ (mV) | - | 3 | If $\Delta z = 13$ nm |

Contact pressure. The evaluation of contact pressure on sample surface is important before measurements. To our knowledge, the interacting force of the AFM-tip with the sample surface is very small, usually the magnitude of order in the range from nN to μ N. Based on our measurement, we would introduce a formula as $f_c = k_{cantilever} \Delta z = \frac{k_{cantilever}}{S} V_{horizontal}$ and then evaluate the values, where the symbol S is the sensitivity, which is defined as $S = V_{horizontal}/\Delta z$. In our case, a contact force $f_c \approx 280$ nN is assessed. Moreover, an apex radius

of contact area approximately 300 nm is achieved. Then, the area of contact can be given by $A_c = \pi R^2$, achieving an area contact about $2.82 \times 10^{-13} \text{ m}^2$.

While having $f_c \approx 280 \text{ nN}$ and $A_c = 2.82 \times 10^{-13} \text{ m}^2$, the corresponding pressure is derived in order to verify whether the AFM-tip would damage sample surface. The contact pressure can be calculated to be approximately 1 MPa using the expression $P_c = f_c/A_c$. In comparison with Young's modulus about 280 GPa of the SiN sample surface, the pressure of contact is far less than the comparable value, thus evidencing that the contact of AFM-tip does not damage the SiN sample surface.

Contact sensitivity and voltage set-point. The sensitivity of the contact also plays a role in the calculation of the contact set-point V_{set} . In our measurement, the cantilever is a 25Pt300B probe purchased from Rocky Mountain Nanotechnology Company and is similar to a soft Pt strip spring with a spring constant of about 22 N/m according to the supplier's probe characteristics data (see at <https://rnmnano.com/>).

When choosing $f_c \approx 280 \text{ nN}$ together with a spring constant of the AFM-tip about nominal 22 N/m, the static displacement of contact about 12.72 nm is calculated using Hooke's law $f_c = k_{cantilever} \cdot \Delta z$. In order to follow with the experiment, we use the measured value of the sensitivity (S) about 0.23 mV/nm, which is related to the photodetector conversion. The determination of the sensitivity will be explained after. If evaluating $\Delta z \approx 13 \text{ nm}$, the horizontal voltage (namely set-point voltage, as mentioned above) is derived to be about 3 mV, which is an important parameter to determine whether the AFM-tip touches the sample surface. In our measurement, we rounded the set-point about 3 mV for simplification.

(iii) Sensitivity measurement based on the approach-retract process

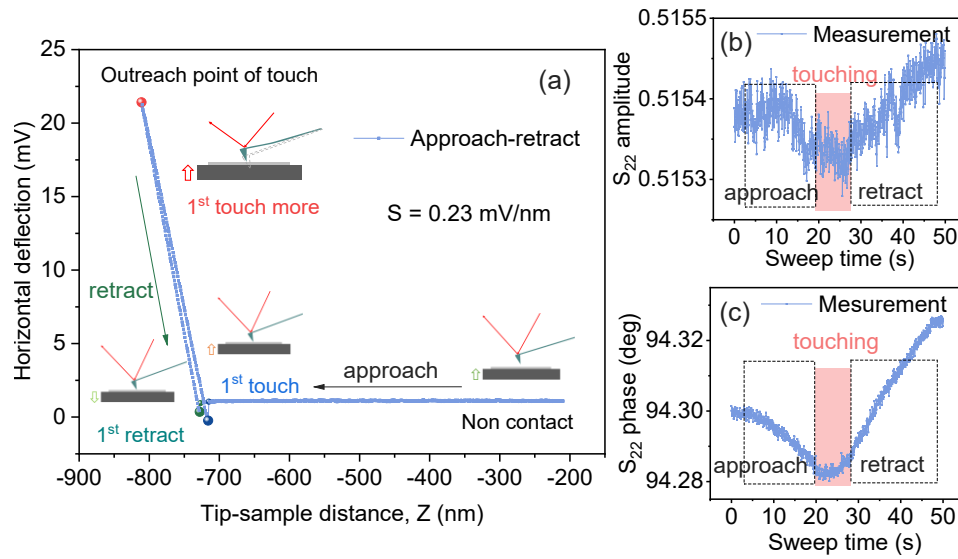


Figure 4.1.5. Sensitivity measurements based on the approach-retract process. (a) Schematic diagram of the measurement process. (b) S_{22} amplitude and (c) phase record when performing the approach-retract measurement.

During measurements, the evaluation of the sensitivity is essential, because the experimental horizontal voltage determines how much a set-point voltage should be set. Using approach-retract method, the horizontal deflection voltage as function of the approaching distance along Z -axis is investigated carefully, as shown in **Fig. 4.1.5(a)**. With approaching, the AFM-tip touches the sample surface in the position $z = -715$ nm for the first time (captioned by 1st touch). Because of the AFM-tip mounted on the spring cantilever, contact of the AFM-tip outreaches farthest the position $z = -810$ nm (captioned by 1st touch more), which means the tip presses the sample surface with a pressure. Then, the AFM-tip retracts at the position $z = -727$ nm (captioned by 1st retract), but having a small error difference between 1st touch and 1st retract positions because of the interacting forces between the AFM-tip and the sample surface. This error is also present in this experiment configuration although implementing all the measurements in a high vacuum. Several sensitivities of contact (see **Table 4.1.2**) have been measured and confirmed, achieving an average sensitivity value around 0.23 mV/nm.

| Measurement number | 1 st | 2 nd | 3 rd | 4 th |
|---------------------|-----------------|-----------------|-----------------|-----------------|
| Sensitivity (mV/nm) | 0.232 | 0.235 | 0.234 | 0.233 |

Besides, a VNA was also exploited at a microwave frequency of 1 GHz in order to observe the sensitivity near the contact and extract the signals. Based on the approach-retract method, S_{22} amplitude and phase measurements were performed at the same time. The interacting contact region between AFM-tip and the SiN sample surface is observed, as shown in **Fig. 4.1.5(b,c)**. As we can see, the S_{22} amplitude has much more noise than the phase, which may be attributed to the capacitive behaviour of the sample (see the Eq. 4.1.1). Although the S parameter may be dependent of the tip-sample distance, using it to precisely detect the contact point may not be suitable. As an evidence, the relevant measurement data are still shown in the following.

4.1.3 Vector network analyser measurement

Because the inter-distance between the AFM-tip and the sample surface is usually in the range of tens of nanometers, knowing their physical properties becomes very difficult. However, it is well known that there is an electric field distribution while the AFM-tip approaching sample surface with supplying electric charges. By measuring the electric field, achieving the local impedance and capacitance or conductance becomes convenient. Thus, scattering (so called S-) parameters were introduced with VNA apparatus[172,173]. A typical VNA consists of a RF source generator, a power splitter, a RF detector/receiver, and other digital signal processing circuitry [174]. It is able to measure the amplitude and phase of the transmission RF signal by a coaxial cable. RF signal is an electromagnetic wave, featuring a frequency range, amplitude and phase. Using the VNA analyser, a RF microwave signal generated at the VNA source is splitted into two signals. One signal is referred to the local oscillator (LO), serving as a signal reference, and the other RF signal is used for detecting the sample, comparable to the LO. Thereafter, the measured signal can be reflected to an embedded measurement channel. The outcome RF signal can finally be recorded in formalisms of amplitude and phase.

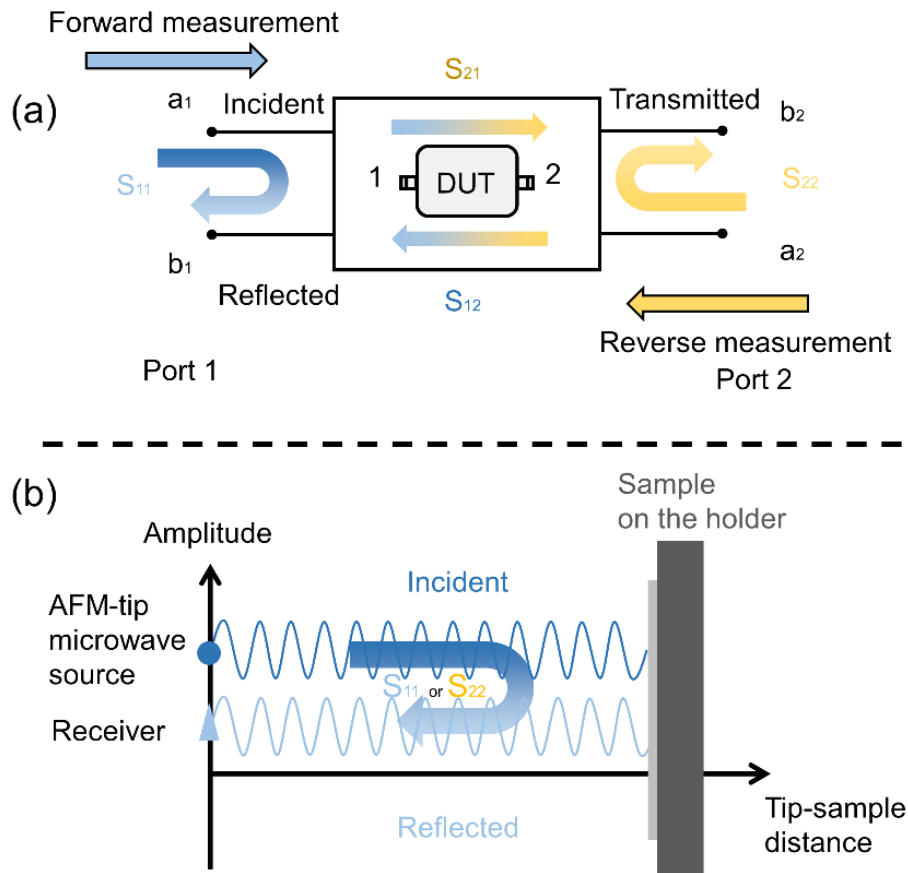


Figure 4.1.6. VNA measurement principles. (a) S-parameters of a two-port VNA network for DUT, namely S_{11} , S_{22} , S_{12} , S_{21} . (b) Schematic of using the AFM-tip to measure the sample surface.

So as to measure the S-parameters, the RF source is set with a frequency range, amplitude and phase to generate an incident microwave that is guided to the sample. This incident wave is for instance defined as a_1 . Once the incident wave arrives on the sample surface, it is reflected and comes back the RF receiver. The reflected wave signal is named as b_1 . The forward reflection coefficient (S_{11}) is defined and determined, namely $S_{11} = b_1/a_1$, as can be seen in **Fig.4.1.6(a)**. Since the VNA has two ports, a second reflection coefficient (S_{22}) is also determined as $S_{22} = b_2/a_2$. Additionally, when the microwave signal could go through the sample, such as a membrane, measuring a transmission signal is possible. The forward transmission coefficient (also called forward gain) (S_{21}) is defined, namely $S_{21} = b_2/a_1$ and the reverse transmission coefficient becomes $S_{12} = b_1/a_2$. Note that for the correct definition of S_{11} and S_{21} , a_2 must be null; similarly, for the correct definition of S_{12} and S_{22} , a_1 must be null.

When actually performing measurements, there are some necessary accessories including either amplifier or attenuator set for amplifying or attenuating a RF signal. Notably, an interfacing mismatch between the impedance of VNA and sample becomes a technical issue. The internal impedance of the VNA is referred to as $Z_{ref} = 50 \Omega$. Then, the forward reflection coefficient (S_{11}) as function of the local impedance is defined to be

$$S_{11} = \frac{Z_{in} - Z_{ref}}{Z_{in} + Z_{ref}} \quad Eq. 4.1.1$$

where Z_{in} is the impedance of the measured sample. In the present case, Z_{in} is very high, usually in the range of $M\Omega$. It is due to the measured capacitance usually in the magnitude of order about aF/fF-scale. Thus, the impedance Z_{in} is very far from the reference impedance of the VNA analyser setting, leading to inaccurate measurement results. In order to tackle such a technical issue, some[172] have used a lumped measurement resistance 50Ω to absorb spurious microwave signal from an incidence, causing much smaller uncertainty. It is because the almost 0 reflection effect in accordance to 50Ω resistance.

Here, the measurements were performed by connecting directly the VNA port to the AFM tip with -10 dBm input power and about -13 dBm at the probe tip. By varying the inter-distance, the distance-dependent S_{22} amplitude and phase are measured. As depicted in **Fig. 4.1.6(b)**, the microwave signal loss becomes larger with the tip-sample distance increasing, leading to a smaller capacitance. The details will also be discussed in the subsequent section 4.2.2. It is worthwhile noting that the measured amplitude and phase have different sensitivities to the distance change. The microwave amplitude intensity is little sensitive to tip-sample surface distance, because of the capacitive behaviour. The S-parameter phase is rather sensitive to the surface. All S-parameter measurement results are shown below based on this analysis.

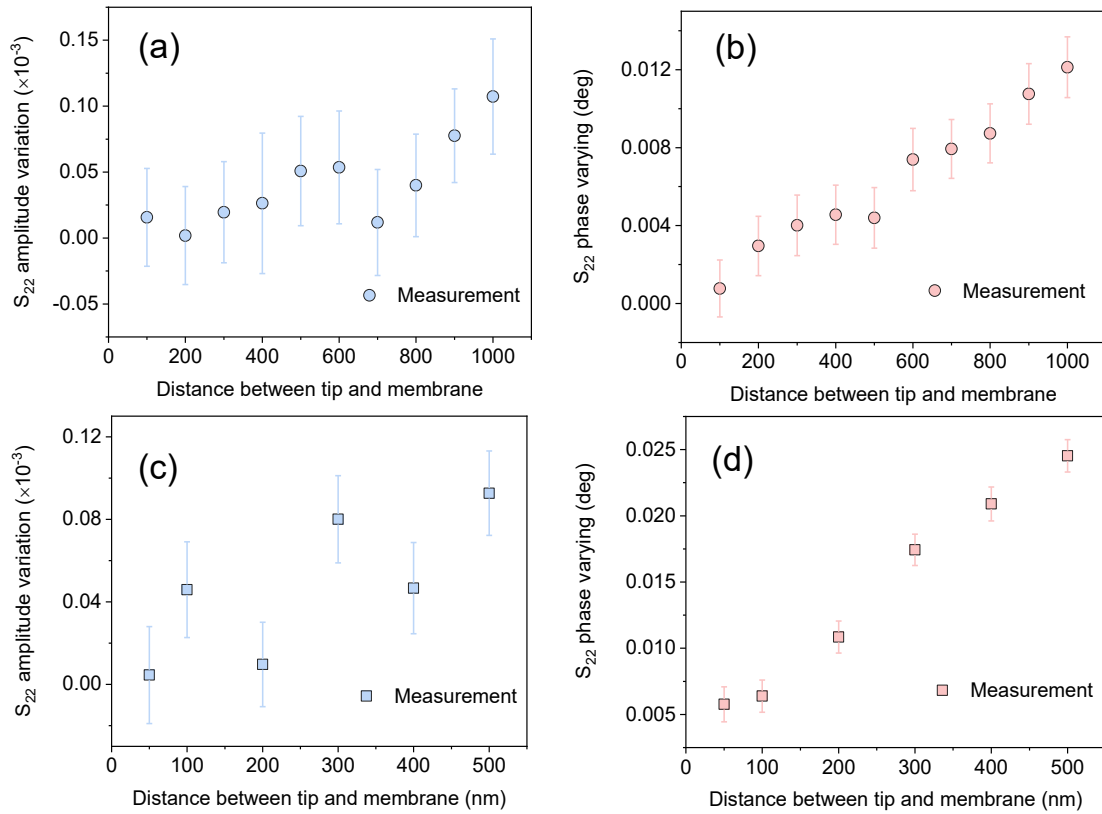


Figure 4.1.7. Evolution of the S_{22} parameter amplitude and phase with the tip-sample distance. For (a) and (b), the tip-sample distance ranging from 100 to 1000 nm and the measured frequency is 1 GHz. For (c) and (d), the tip-sample distance ranging from 50 to 500 nm and the measured frequency is 7 GHz.

A microwave signal is implemented with the frequency of 1 GHz or 7 GHz to measure the sample, as changing the distance. **Fig. 4.1.7(a,b)** shows the measured S_{22} amplitude and phase at frequency of 1 GHz for evaluating microwave signal as function of tip-sample distance. Comparing with the amplitude results, we observed the measured phase clearly depends on the distance. To confirm whether the measured results can be reproduced, **Fig. 4.1.7(c,d)** shows the measured S_{22} amplitude and phase at frequency of 7 GHz. Then, similar results were observed. The amplitude is still independent of the distance. But, the phase evolution is almost about seven times larger than that of the 1 GHz. Thus, we may use the S-parameter to measure the phase evolution, instead of the amplitude, so as to characterize the sample.

4.1.4 Measurement setup

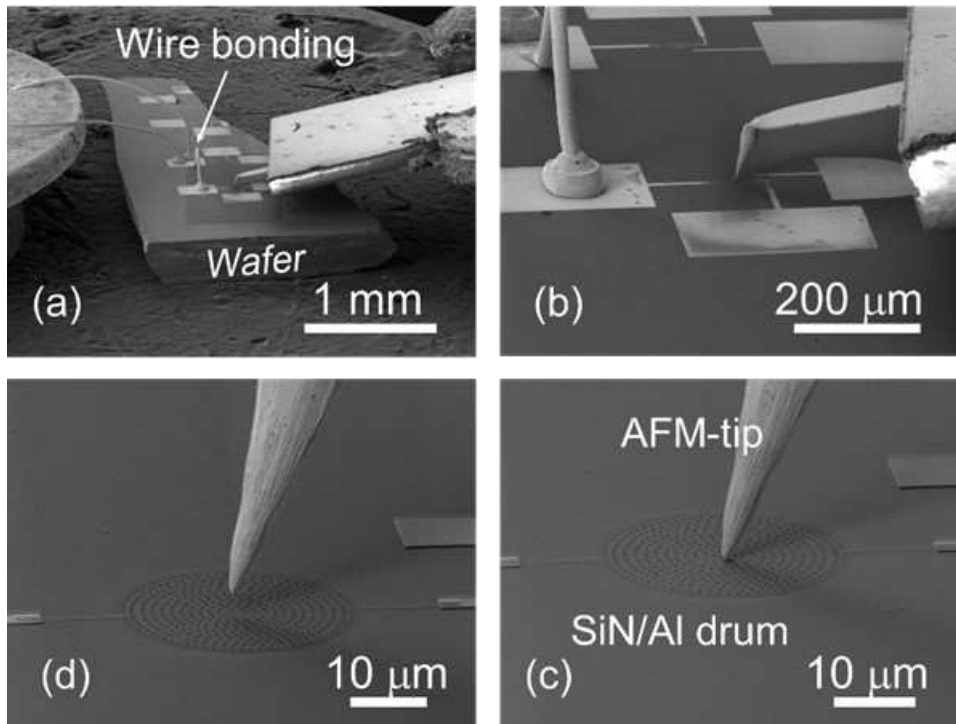


Figure 4.1.8. AFM-tip capacitively coupling with SiN membrane covered with thin aluminium film. (a) SiN membrane is connected to the grounding through wire bonding and zoomed in (b). (c) A close view of the tip-sample distance about 50 nm. (d) A retract operation of the AFM-tip from the surface.

The measurement configuration done by X. Zhou is the same with the previous section 2.3, which has been used to measure the membrane nanoelectromechanical resonator through a fixed aluminium top gate. Here, instead of the previous fixed aluminium top gate, an AFM-tip integrated with SEM in a vacuum (7×10^{-4} mbar) is employed to capacitively couple with a SiN drum membrane, as shown in **Fig. 4.1.8**. In this case, the SiN membrane is connected to the ground through bonding wires. More importantly, it is the position, corresponding to the fixed AFM-tip, that can be controlled and operated precisely by a piezo-actuator nano-positioner in X-Y-Z axes. The tip-membrane distance thus can be achieved as required. The simulation for this tip-membrane scheme will be shown in the following part.

4.2 Characterization and results discussion of mechanical vibration of SiN membrane

In the measurement, we used an AFM tip as a movable and suspended top gate to drive and detect mechanical vibrations of the SiN membrane resonator in a capacitive coupling scheme. In the following part, numerical simulations are first used to understand this coupling effect. Then, the analysis of the measurement results is presented. In this chapter, the measurement of the electromechanical properties of the membrane in a SMM scheme has been mainly carried out by X. Zhou and D. Theron.

4.2.1 Finite element method simulation of the tip-membrane scheme

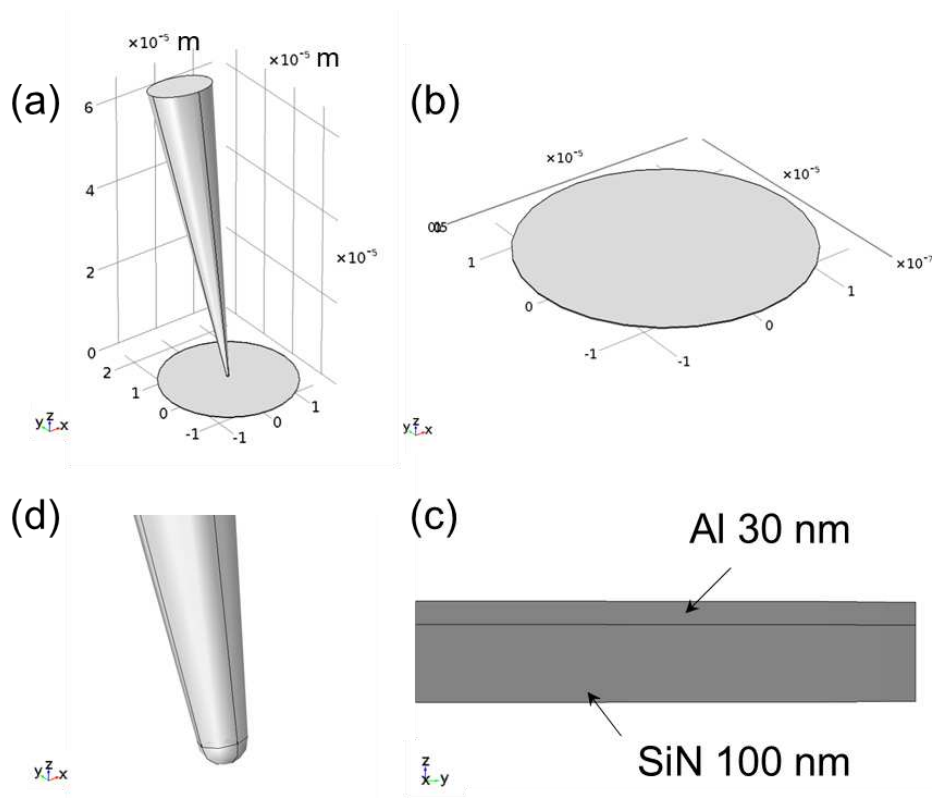


Figure 4.2.1. The geometry design. (a) The cone-like AFM-tip over the surface of the membrane. (b) The circular membrane. (c) The cross sectional view of the membrane. (d) The apex of the AFM-tip.

The finite element method (FEM) simulation is performed in order to understand interactions between the metallic tip and the vibration membrane, in a capacitive coupling scheme. The

electrostatics modules of COMSOL Multiphysics are chosen in our geometry, which includes functions of static capacitance, electric potential, electric field, electric charge and electrostatic force distributions based on the circular membrane through the actuation of the AFM-tip. The geometry structure (in **Fig. 4.2.1**), namely a metallic AFM-tip capacitively coupling with a conductive circular membrane, is designed and analysed in a vacuum box. The computation solves the Maxwell equations in the cases of differential and integral as described as

$$\nabla \cdot \mathbf{D} = \nabla \cdot (\epsilon_0 \epsilon_r \mathbf{E}_{electricfield}) = \rho_{charge} \quad Eq. 4.2.1$$

$$\oiint_{\partial\Omega} \mathbf{D} d\mathbf{S} = \iiint_{\Omega} \rho_{charge} dV = Q_{charge} \quad Eq. 4.2.2$$

where \mathbf{D} is the electric displacement vector, $\mathbf{E}_{electricfield}$ is the electric field vector, ϵ_0 is the dielectric constant in vacuum, ϵ_r is the relative dielectric, ρ_{charge} is the electric charge density surrounding the geometry structures, \mathbf{S} is the unit area on the geometry, V is the volume of the geometry, and Q_{charge} is the electric charge on the surface of the entire geometry.

In general, FEM simulation requires four steps for carrying on the studied model, including (i) the geometry design and boundary condition, (ii) choose materials, (iii) mesh in study, and (iv) computation and solution.

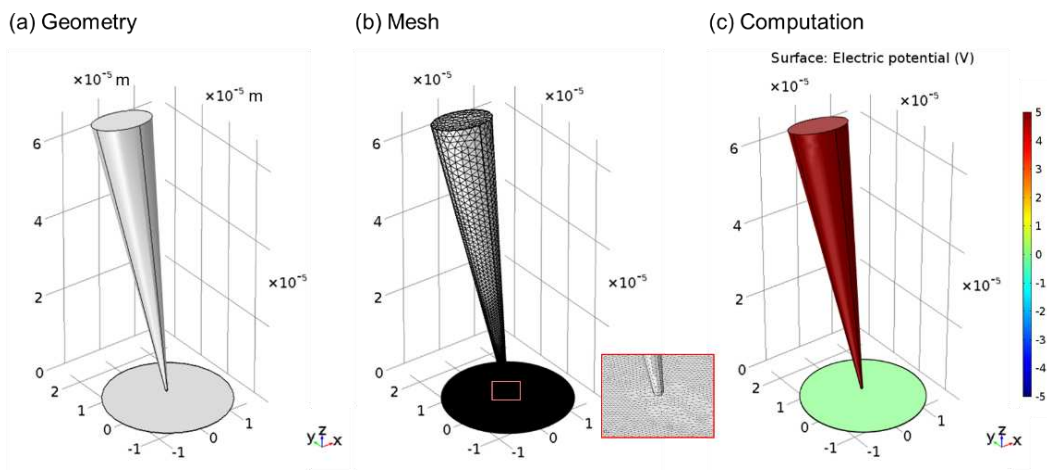


Figure 4.2.2. Schematic of the studied geometry, namely AFM-tip and SiN/Al circular membrane separated by a gap. (a) The geometry placed in the centre part of a defined vacuum cubic box. (b) The mesh of the entire studied geometry is performed. The right-corner inset enlarges the meshed result. (c) Computation solution showing the analysis of the studied geometry.

(i) Geometry design and boundary condition. The entire geometry structure studied here is elaborated as shown in the **Fig. 4.2.1** and optimized in **Fig. 4.2.2(a)**. The tip is similar to a cone with features a bottom diameter of 13.85 μm , an apex diameter of 600 nm and a conical height of 64.5 μm ; for the circular membrane, it is 100 nm thin SiN circular membrane covered with 30 nm thin Al, consistent with our experiment device. In our model, the gap distance between the AFM-tip and the circular membrane can be set as required, for example, 300 nm. Besides, specific boundary condition is considered based on electromagnetic propagation in the entire studied space. The outer boundary layer, that is defined by vacuum cubic box with dimensions of 150 $\mu\text{m} \times 150 \mu\text{m} \times 150 \mu\text{m}$, enough covers all of the studied geometries in order to absorb the residual electromagnetic energy, thereby simulating the electromagnetic waves fading towards the boundary edge.

(ii) Choose materials. Rendering dielectric properties of the materials has a key role in simulating the studied geometry. In order to describe conveniently, we use the relative permittivity (ϵ_r) of the material here, namely $\epsilon = \epsilon_r \epsilon_0$, where $\epsilon_0 = 8.85 \times 10^{-12} \text{ F} \cdot \text{m}^{-1}$ is the vacuum permittivity. The AFM-tip is made from platinum (Pt), thus rendering the relative permittivity value to be 1. SiN is the insulating material with the relative permittivity value to be 9.7. Al is a conductive material with a relative permittivity value to be 1.

(iii) Mesh in this study, we choose the most easiest way to mesh the whole geometry with “mesh fine”, offered automatically by the software. It is presented in **Fig. 4.2.2(b)**.

(iv) Computation and solution. The studied geometry can be further computed for solving the Maxwell's equations mentioned above. It is based on electrostatics modules chosen here where the solution results of electric potential, electric field and electric charge are contained in general. **Fig. 4.2.2(c)** shows the electric potential distribution surrounding the geometry.

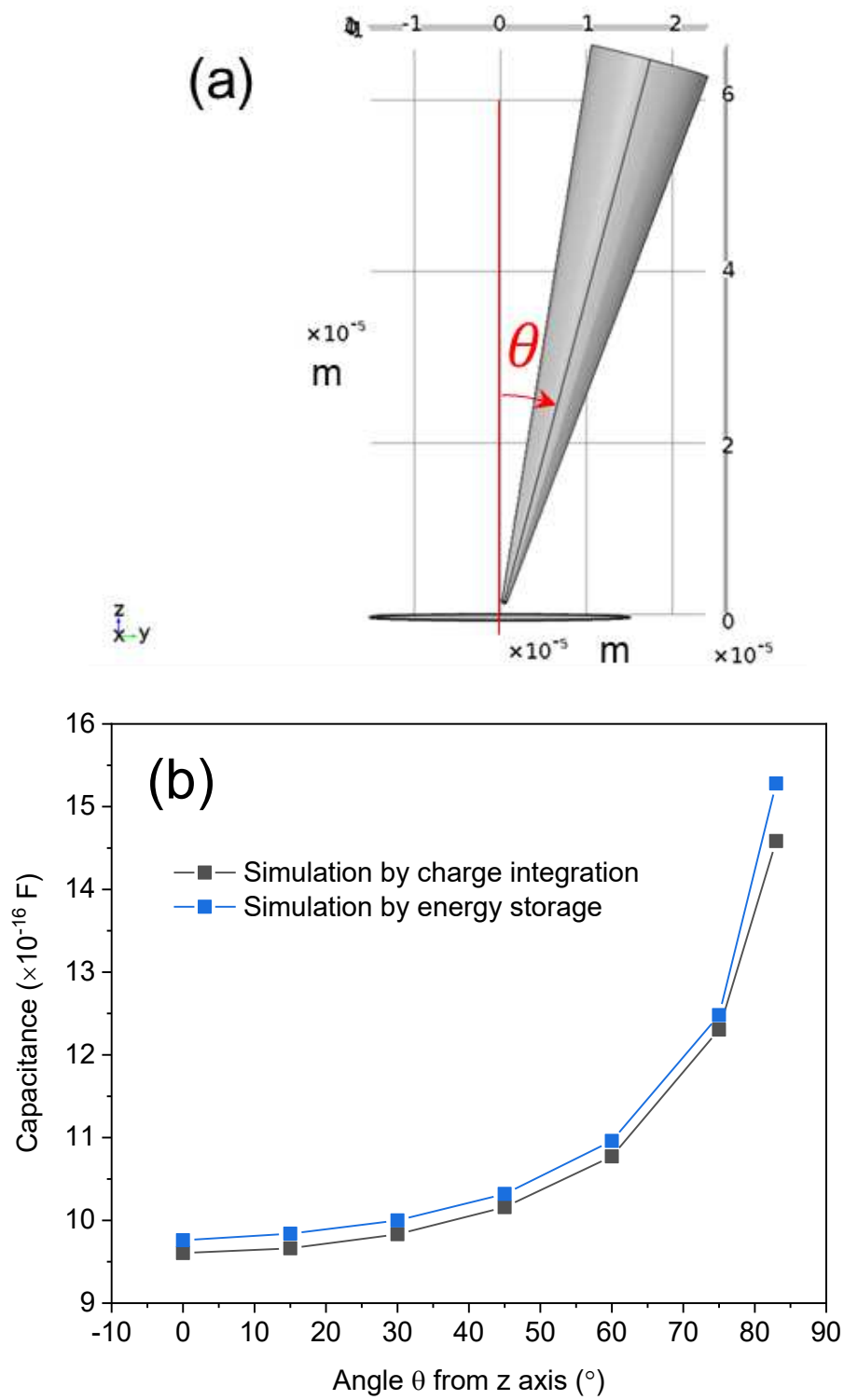


Figure 4.2.3. Simulation results of capacitance as function of the tilt angle θ . (a) The geometry of AFM-tip capacitively coupling with the circular membrane, tilted an angle θ from the Z-axis. (b) Simulation results of the capacitance as function of the angle θ .

Capacitance vs. the tilt angle. When performing the experiments, the capacitance takes a significant part in understanding and guiding our measurements. Therefore, we evaluate the coupling capacitance between the tip and the drum through the simulation. In order to approach the experimental conditions, we start to consider the effects of tip tile angle on the values of the coupling capacitance. **Fig. 4.2.3(a)** shows the side view of the studied geometry with the tilt angle changing. The gap has been fixed about 500 nm in this simulation. The simulated capacitance value strongly depends on the tilt angle θ , as shown in **Fig. 4.2.3(b)**. It is due to the active area between the tip and the drum increasing with increasing the tile angle. The results shown here are obtained by two different methods: for first one, the capacitance can be derived by stored energy inside the geometry. It can be specified by the general expression $E_t = CV^2/2$, where E_t is the total energy stored in the geometry and V is the applied voltage. For second one, the capacitance can be achieved by the integration of the surface charge on the entire circular membrane, based on the expression $Q_{charge} = CV$. As shown in **Fig. 4.2.3(b)**, they have same trends of the capacitance value to the angle, indicating that the actuation areas exponentially increase as the angle increases. These results ascertain the capacitance of the geometry strongly depending on the tilt angle that can be adjusted and optimized in our real experiment setup.

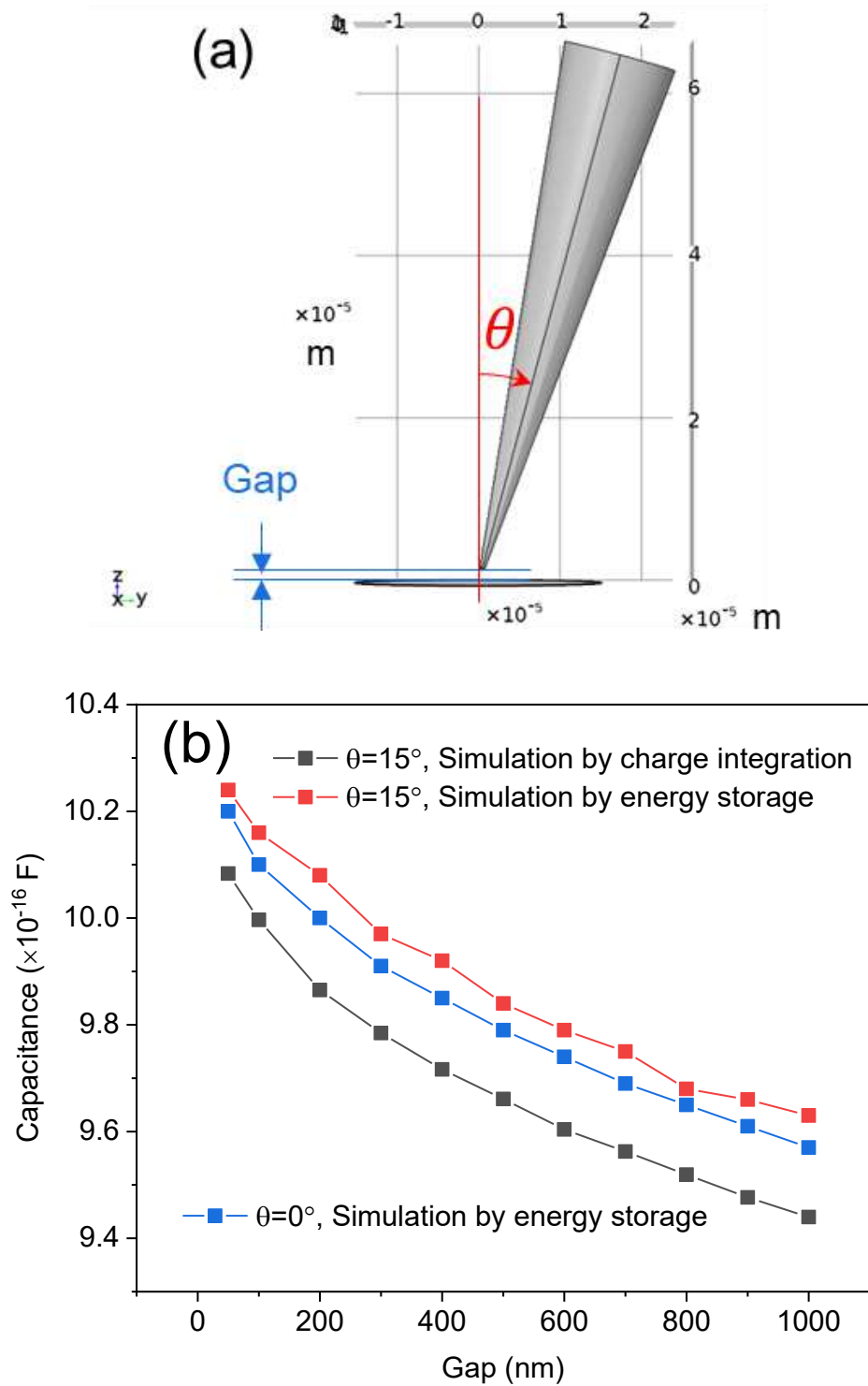


Figure 4.2.4. Simulation results of the coupling capacitance as a function of the gap between the tip and the membrane. (a) The geometry of the simulated system, the tip and the circular membrane, which is spaced by a gap distance. (b) Simulation capacitance as function of the gap distance.

Capacitance vs. the gap. While fixing the tilt angle $\theta = 15^\circ$, the studied geometry can be modelled in **Fig. 4.2.4(a)**, where the gap between the tip and the membrane surface can be varied. The capacitance simulation results are plotted in **Fig. 4.2.4(b)**. The capacitance values decrease as the gap increases. Both two simulation results generally agree with each other, with 2% differences in values. In order to compare between $\theta = 15^\circ$ and $\theta = 0^\circ$, the simulation results corresponding to $\theta = 0^\circ$ are also presented, as the values still present differences below 2%.

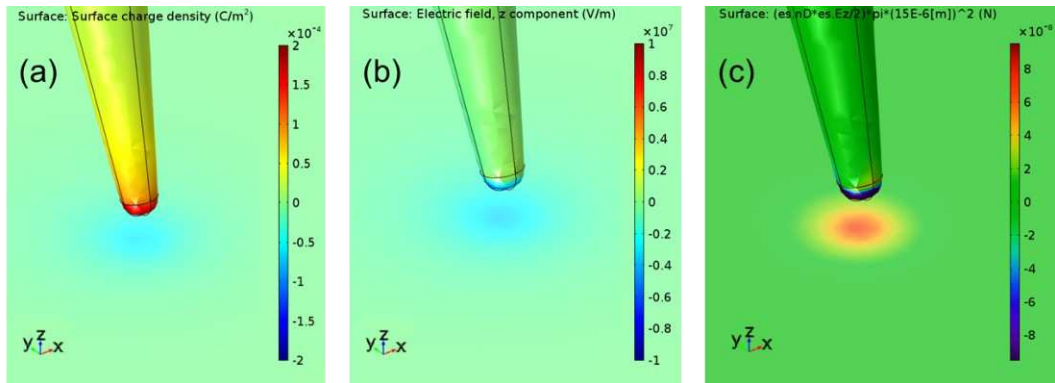


Figure 4.2.5. Simulation results of electrostatic properties. (a) Electric charge distribution. (b) Electric field distribution. (c) Electrostatic force distribution. All colour bars are the magnitude.

Electrostatic force distributions. In the experiment, the vibrations of the circular membrane are excited through its coupled tip by electrostatic forces. In order to better understand this point, the geometry is simulated for first showing the charge distribution Q_{charge} and electric field distribution $E_{electricfield}$. **Fig. 4.2.5(a)** shows electric charge distribution. The attractive electrostatic force can be observed because of the positive charge concentration on the apex of the AFM-tip and the negative charge distribution on the centre part of the membrane. **Fig.4.2.5(b)** shows electric field distribution. The electric field marked by dark blue mainly concentrates on the apex of the AFM-tip and the other marked by light blue distributes on the membrane. It is due to the electric field gradient $E_{electricfield} = -\nabla V$ definitely used in the simulation. Because the electrostatic force can be described by the expression $F = Q_{charge} \cdot E_{electricfield}$, the electrostatic force point-by-point can be re-built so as to study the electrostatic force distribution on the membrane. **Fig. 4.2.5(c)** shows the rebuilt electrostatic force distribution. It demonstrates the membrane can be resonated by the external electrostatic forces adding by the AFM-tip through biasing mixed voltage $V_{ac}+V_{dc}$.

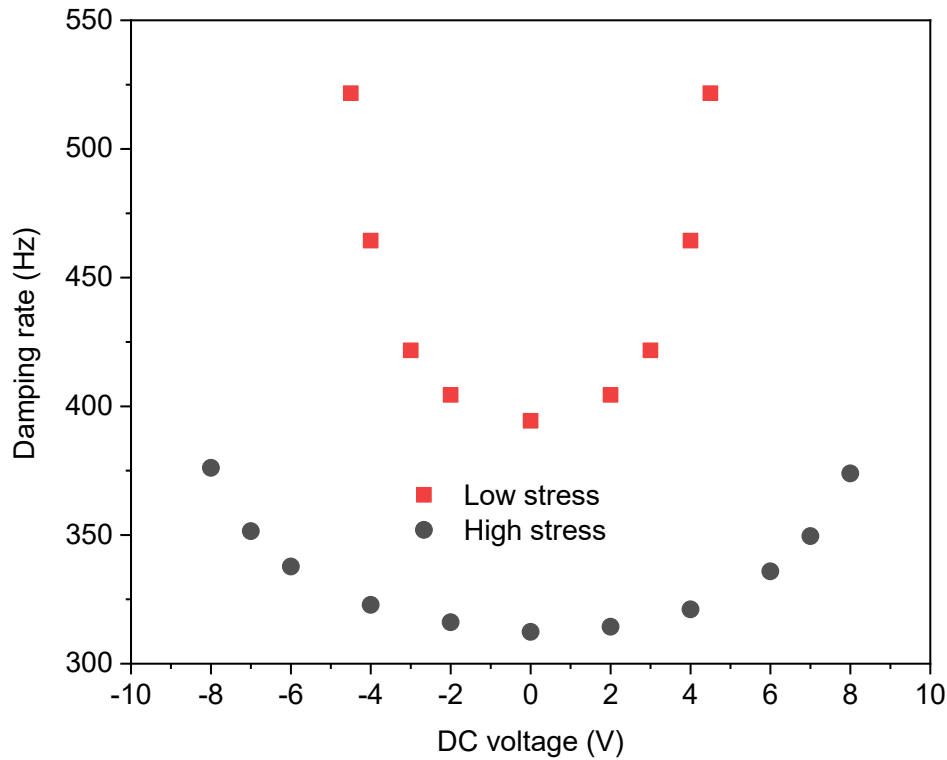


Figure 4.2.6. Simulation results of damping rate for high (black circle) and low (red square) stress SiN circular membrane.

Damping rate vs. DC voltage. Damping is an intrinsic property of the membrane. Based on the tip-circular membrane capacitive coupling scheme, we expect the damping rate of membrane can be simulated and explained by adding the electrostatic force through the tip. In our case, high (0.8 GPa) and low (0.2 GPa) stressed SiN circular membranes have been simulated and compared. Here, we simulated the membrane vibrations with real and imaginary parts of a complex matrix eigenfrequency in formalism of $f_m = Re[f_m] + i \cdot Im[f_m]$, as the vibration of membrane resonator cannot go infinite. For $Re[f_m]$ term, frequency versus DC voltages agrees with the quadratic curve (see Fig. 2.3.4(b) in section 2.3.3). For $Im[f_m]$ term, it should be damping coefficient proportional to the dissipation $1/Q$. With increasing DC voltages, the membrane is electrostatically attracted to the metallic tip, resulting in a smaller spring constant. Therefore, the dissipation is quadratically increased. This phenomena have also been observed in the doubly-clamped beam that is capacitively coupled to its side-gate [175]. **Fig.4.2.6** shows the damping rate value as a function of DC voltages, exhibiting the parabolic shapes exactly in agreement with the previous literatures [176,177]. Unfortunately, our experiment results show a different damping behaviour of the membrane, which does not agree

with the previous simulation results. In the following, the specific discussion will base on our measurement results. Besides, in the following experimental parts, all values of distance between the tip and membrane still need further efforts for better calibration.

4.2.2 Linear mechanical response of SiN membrane

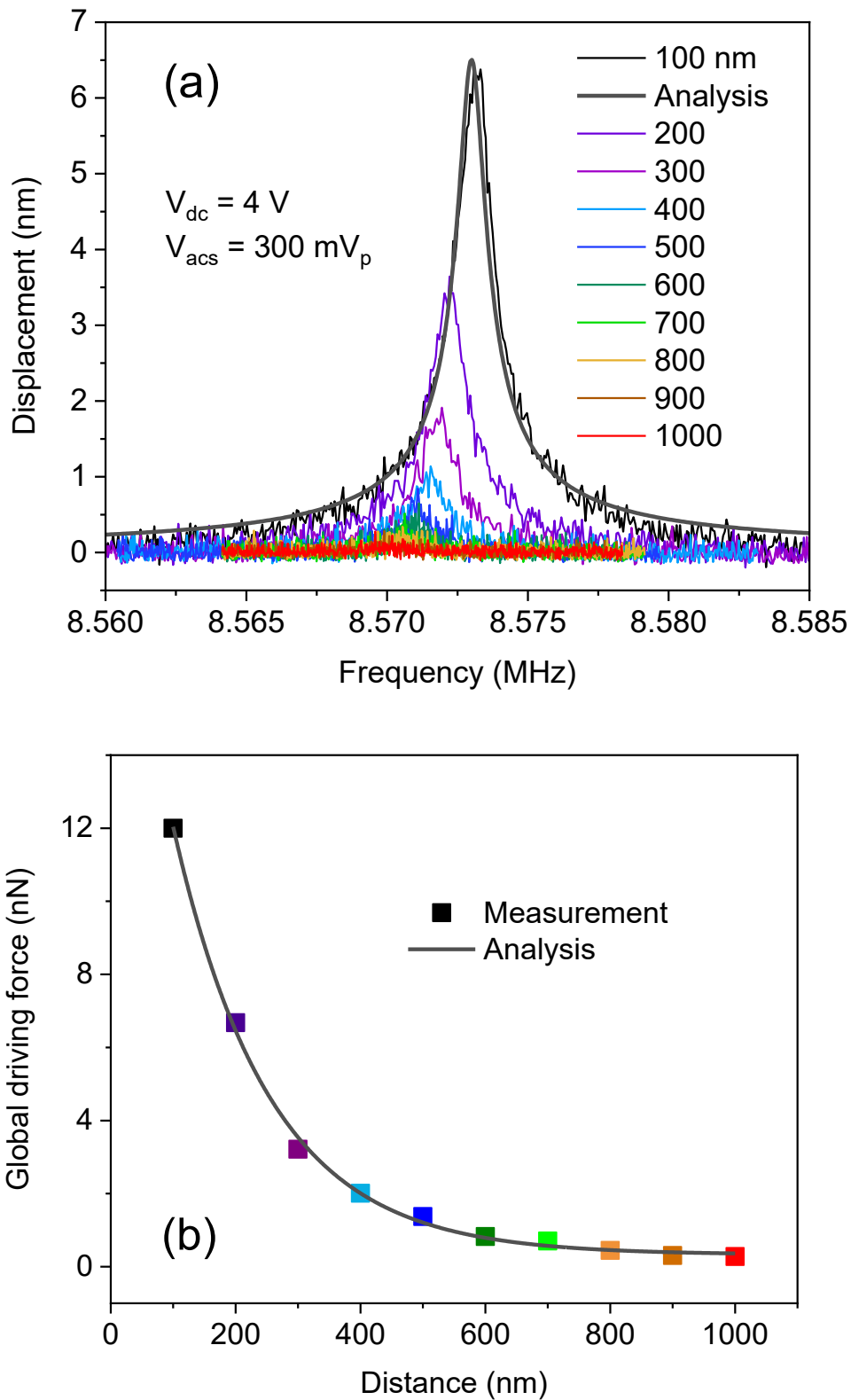


Figure 4.2.7. (a) Signal amplitude and (b) Global driving force dependence of different distances.

With the distance of the gap increasing, coupling capacitance becomes much smaller, leading to larger impedance mismatch. It further causes the microwave signal losses in the detection of mechanical vibrations. Thus, the detection signal goes smaller. In order to understand better for this driving scheme, the force on the apex of the tip and the global driving force through the tip are introduced. **Fig. 4.2.7(a)** shows signal amplitude decrease with the distance increasing, while the global driving force through the tip is set as $F_{gl}(C_{g0,sim} \approx 9.8 \times 10^{-16} F, V_{dc} = 4V, V_{acs} = 300mV_p) = \frac{C_{sim}V_{dc}V_{acs}}{d} \approx 12 nN$. By the calculation of the global force distribution, the force on the tip apex can be defined as $F_{apex}(r_{eff} \approx 0.3 \mu m) = \frac{r_{eff}^2}{R^2} \times F_{gl} \approx 4.8 pN$, which agrees well with the analysis through the function of $|\mu_x(\omega_d)| = \frac{Fd}{m_{eff} |\Omega_m^2 - \omega_d^2 - i\omega_d\gamma_m|}$, giving $F_{apex,fit}(r_{eff} \approx 0.3 \mu m) \approx 2.37 pN$ as shown in **Fig. 4.2.7(a)**. It also needs to mention that r_{eff} is an effective charge distribution radii on the centre of membrane in radii R , does not definitely equal the radii of the apex of the tip. Here, fitting parameters are the effective radii $r_{eff} \approx 0.3 \mu m$, the effective mass $m_{eff} = 4.5 \times 10^{-14} kg$ and the damping rate $\gamma_m/2\pi = 944.48 Hz$. Moreover, each amplitude curve in Fig. 4.2.7(a) can be analysed by the formula $F_{apex}(r_{eff}) \cdot Q \approx (m_{eff}\Omega_m^2) \cdot x$, where Q is the quality factor and x is the detected signal amplitude. Besides, we also see the shift of resonance frequency going larger when the distance decreases. This effect is inferred that the larger interaction area is achieved, the interaction force between the both is larger, then the tensile stress is modulated by the force, it becomes smaller, therefore, it is tough to drive the membrane, corresponding to higher driving frequency. **Fig.4.2.7(b)** shows the re-built global driving force data extracted from (a), indicating the impact of the distance on the signal amplitude. This further results in a weaker detected signal. The global force acting onto the membrane can be well fit by an analytical model $F = F_0 e^{-(d/d_0)} + F_{offset}$. This means the global driving force in the tip-membrane scheme at $d = 100 nm$ can be lost as increasing the distance. Here, fitting parameters are $F_0=22.36 nN$, $d_0 = 154.59 nm$ and $F_{offset}=0.32 nN$. This analytics helps us for understanding whether a coupling capacitance value facilitates detecting the signal magnitude.

4.2.3 Resonance frequency modulation of SiN membrane

Resonance frequency modulation through DC voltages can study mechanical properties of the resonator. Therefore, the resonance dependence of DC voltages has been measured by setting the AFM-tip on the top of the SiN membrane centre. Based on this capacitive coupled scheme, the DC and AC electrical signals are added on the tip by a coaxial cable in order to drive the

membrane through electrostatic forces. The microwave detection is also implemented for readout mechanical responses through frequency down conversion.

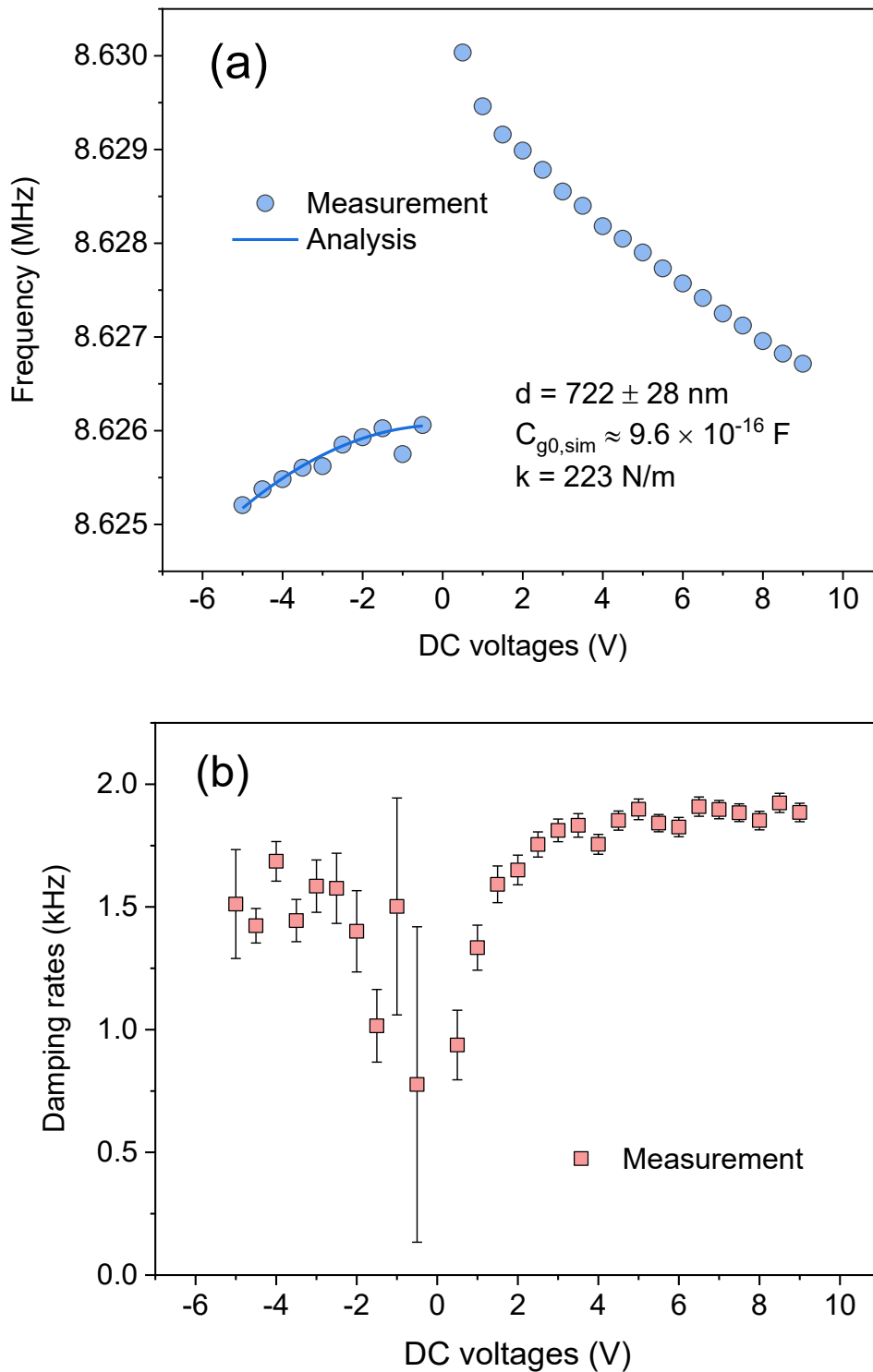


Figure 4.2.8. (a) Resonance frequency modulation and (b) Damping rate as function of DC voltages.

Fig. 4.2.8 shows the measured results and an analytical frequency modulation as function of DC voltages, namely $\Omega \approx \Omega_m \left(1 - \frac{C_{go} V_{dc}^2}{2kd^2}\right)$ that has been derived in the section 2.2 in Chapter 2. From this formula, we knew that the resonance frequency can be normally tuned by the positive and negative DC voltages. In this case, we suppose whether the damping of membrane depends on (i) the chip clamping γ_{chip} or (ii) tensile stress γ_σ . Unfortunately, **Fig.4.2.8(a)** shows the frequency modulation cannot be done in the positive voltage region. **Fig.4.2.8(b)** shows the related damping rates behaving the chip clamping dependence. We therefore suppose (i) if $\gamma_{chip} > \gamma_\sigma$, that means the measured data not dependent of the AFM-tip. The data cannot be fit through the above analytics. In the negative voltage region, **Fig.4.2.8(a)** shows the frequency can be tuned through the AFM-tip. **Fig. 4.2.8(b)** also shows the related damping dependent of the AFM-tip, due to the damping values as in a stable range. We therefore suppose (ii) if $\gamma_{chip} < \gamma_\sigma$, it is due to the modulation dependence of the tensile stress. The measurement data agree well with the analytical formula, giving the spring constant $k \approx 223 \text{ N/m}$. The DC voltage-induced frequency tuning range is about 1000 Hz. Besides, the variation of resonance frequency and damping rate is normalized by the maximum or minimum values, remaining the same trend changing. This may explain how much the resonance frequency or damping can be tuned by DC voltages. It is also worth to mention that the damping dependence of DC voltages has been studied [176], which presents quadratic fit. Unfortunately, we have no same observation.

4.2.4 Duffing nonlinear mechanical response of SiN membrane

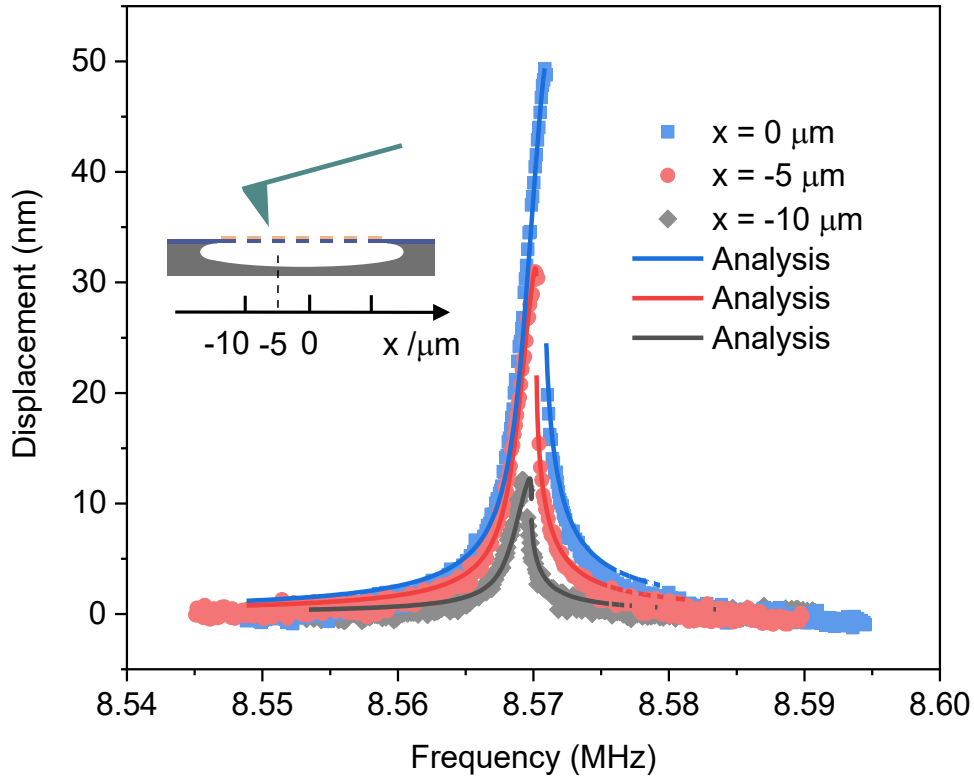


Figure 4.2.9. Duffing nonlinear responses as the AFM-tip position changing. The measurement data are taken when the AFM-tip position is $x = 0 \mu\text{m}$, $-5 \mu\text{m}$ and $-10 \mu\text{m}$ respectively. Square symbols are the measured data and solid lines are the analysis fitting. The distance is fixed at about 300 nm. Inset shows schematic of the AFM-tip position moving on the top of membrane.

To study whether nonlinearity dependence of AFM-tip position exists, three different positions on the SiN drum membrane, along its radial axis at $x = 0 \mu\text{m}$, $x = -5 \mu\text{m}$ and $x = -10 \mu\text{m}$, are characterized respectively. **Fig. 4.2.9** shows nonlinear responses as function of frequency, corresponding to different positions. These three AFM-tip positions correspond to different global driving forces, namely $F_{gl1}(x = 0 \mu\text{m}) \approx 10.45 \text{ nN}$, $F_{gl2}(x = -5 \mu\text{m}) \approx 14.37 \text{ nN}$, and $F_{gl3}(x = -10 \mu\text{m}) \approx 19.6 \text{ nN}$. Through these global driving forces, nonlinear responses can be measured and be well fit by the Duffing resonator function $|a|^2 = \frac{g^2}{(2\Omega_x + \frac{4}{3}|a|^2)^2 + 1}$, where $\Omega_x = Q(\omega_d/\Omega_m - 1)$, $a = x\sqrt{\alpha Q/\Omega_m^2}$ and $g = (F/\Omega_m^3)\sqrt{\alpha Q^3/m_{eff}^2}$. They have same fitting parameters of the effective mass $m_{eff} = 4.5 \times 10^{-14} \text{ kg}$ and the quality factor 8500, as

detailed in **Table 4.2.1**. When $x = 0 \mu m$, the fit gives Duffing parameter about $4 \times 10^{26} m^{-2}s^{-2}$, the force 760 pN. It is worth noting that this fit force basically agrees with the force on the tip apex about 418 pN as it has been analysed in the section 4.2.2. When $x = -5 \mu m$, the fit gives Duffing parameter about $7.8 \times 10^{26} m^{-2}s^{-2}$, the fit force 480 pN. The fit force agrees with the force on the tip apex about 574.8 pN. When $x = -10 \mu m$, the fit gives Duffing parameter about $4.6 \times 10^{27} m^{-2}s^{-2}$, the fit force 188 pN. This fit force seems to disagree well with the force on the tip apex about 784 pN. On one hand, the effective radii is chosen $r_{eff} \approx 3 \mu m$; on the other hand, this effect is possible due to clamping losses at the edge of the membrane. Obviously, the AFM-tip position slightly affect the nonlinear mechanical behaviour. Duffing parameter increases with the position moving toward the edge along the radial axis of the membrane. This cause may attribute to the clamping losses of the membrane near the edge.

| Table 4.2.1. Duffing nonlinear mechanical response | | |
|---|-----------------------|-----------------------|
| Parameters | Fitting results | Setting values |
| AFM-tip position at $x = 0$ | | |
| DC voltage | 4 V | 4 V |
| Drive voltage (V_{acs}) | - | $0.8 V_p$ |
| Global capacitance (F) | 9.8×10^{-16} | 9.8×10^{-16} |
| Duffing parameter ($m^{-2}s^{-2}$) | 4×10^{26} | - |
| Effective mass (kg) | 4.5×10^{-14} | - |
| Quality factor | 8500 | - |
| Global driving force (nN) | - | 10.45 |
| Force on the apex (pN) | 760 | 418 |
| AFM-tip position at $x = -5 \mu m$ | | |
| DC voltage | 4 V | 4 V |
| Drive voltage (V_{acs}) | - | $1.1 V_p$ |
| Global capacitance (F) | 9.8×10^{-16} | 9.8×10^{-16} |
| Duffing parameter ($m^{-2}s^{-2}$) | 7.8×10^{26} | - |
| Effective mass (kg) | 4.5×10^{-14} | - |
| Quality factor | 8500 | - |
| Global driving force (nN) | - | 14.37 |
| Force on the apex (pN) | 480 | 574.8 |
| AFM-tip position at $x = -10 \mu m$ | | |
| DC voltage | 4 V | 4 V |
| Drive voltage (V_{acs}) | - | $1.5 V_p$ |
| Global capacitance (F) | 9.8×10^{-16} | 9.8×10^{-16} |
| Duffing parameter ($m^{-2}s^{-2}$) | 4.6×10^{27} | - |
| Effective mass (kg) | 4.5×10^{-14} | - |
| Quality factor | 8500 | - |
| Global driving force (nN) | - | 19.6 |
| Force on the apex (pN) | 188 | 784 |

4.2.5 Mechanical modes detection of SiN membrane

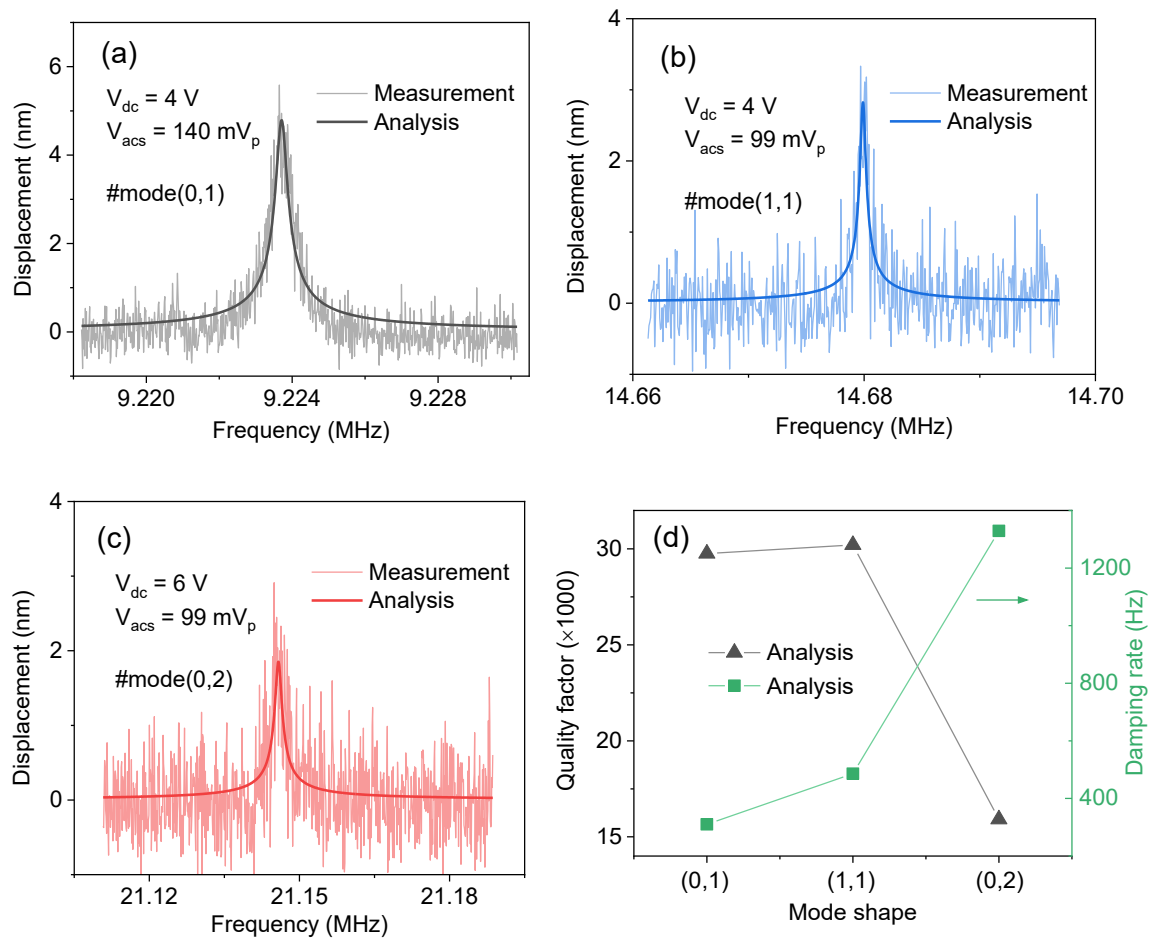


Figure 4.2.10. Mechanical modes measured at the distance of about 300 nm and detected with distinct frequencies ~ 9.223 MHz (a), ~ 14.68 MHz (b) and ~ 21.15 MHz (c), respectively. (d) The analysis of quality factor and damping rate.

Mechanical modes of nanoelectromechanical resonators can be used in investigating signal transduction [78,93,172,178] and multimode mass sensing [51]. Therefore, finding distinct mechanical modes becomes very interesting. **Fig. 4.2.10(a-c)** shows three mechanical modes (0,1), (1,1) and (0,2) that have been detected at the distinct resonance frequencies. It indicates our nanoelectromechanical resonator has potential capabilities of allowing multimode signal processing. Through the linear mechanical amplitude function $\mu_x(\omega_d) = \frac{F}{m_{eff}} \frac{1}{\Omega_m^2 - \omega_d^2 - i\omega_d\gamma_m}$, the fit results are achieved as given in the **Table 4.2.2** below. The achieved f_{mn}/f_{01} ratios including modes (0,1), (1,1) and (0,2) are in good agreement with the analytical mechanical mode theory as presented details in the section 2.1 in Chapter 2. Besides, **Fig. 4.2.10(d)** shows

the analysis of the measured data corresponding to the distinct mechanical modes. The quality factor has a increase trend for the mode (0,1) and (1,1), leading to the dissipation (Q^{-1}) decreasing. This is a good agreement with the modal dependence of the dissipation reported before [6,87]. In addition, observing that the quality factor of the higher order mode(0,2) going down, it results in the larger dissipation. Comparing with the reported results [6], we found the dissipation trend of these three modes is same. Therefore, we explain the dissipation is limited by the clamping losses corresponding to the radial modes and the higher order mode is limited by referring to the intrinsic materials. Then, we also see the damping rate increases with the mode shapes with higher frequency detecting.

| Table 4.2.2. Mechanical modes and measured frequency | | |
|---|-----------------------|-----------------------|
| Parameters | Fitting results | Setting values |
| #Mode(0,1) | | |
| DC voltage | - | 4 V |
| Drive voltage (V_{acs}) | - | 140 mV _p |
| Global capacitance (F) | 9.9×10^{-16} | 9.9×10^{-16} |
| Effective mass (kg) | 4.5×10^{-14} | - |
| Resonance frequency f_{mn} (MHz) | ~9.223 | - |
| f_{mn}/f_{01} ratio | 1 | - |
| Quality factor | 29753 | - |
| Damping rate (Hz) | 310 | - |
| Global driving force (nN) | - | 1.84 |
| Force on the apex (pN) | 0.61 | 0.74 |
| #Mode(1,1) | | |
| DC voltage | - | 4 V |
| Drive voltage (V_{acs}) | - | 99 mV _p |
| Global capacitance (F) | 9.9×10^{-16} | 9.9×10^{-16} |
| Effective mass (kg) | 4.5×10^{-14} | - |
| Resonance frequency f_{mn} (MHz) | ~14.679 | - |
| f_{mn}/f_{01} ratio | 1.5915 | - |
| Quality factor | 30203 | - |

| | | |
|---------------------------------------|-----------------------|-----------------------|
| Damping rate (Hz) | 486 | - |
| Global driving force (nN) | - | 1.31 |
| Force on the apex (pN) | 0.91 | 0.52 |
| #Mode(0,2) | | |
| DC voltage | - | 6 V |
| Drive voltage (V_{acs}) | - | 99 mV _p |
| Global capacitance (F) | 9.9×10^{-16} | 9.9×10^{-16} |
| Effective mass (kg) | 4.5×10^{-14} | - |
| Resonance frequency f_{mn} (MHz) | ~21.145 | - |
| f_{mn}/f_{01} ratio | 2.2926 | - |
| Quality factor | 15910 | - |
| Damping rate (Hz) | 1329 | - |
| Global driving force (nN) | - | 1.96 |
| Force on the apex (pN) | 2.34 | 0.78 |

So far, AFM-tip has been used to study damping losses by mechanical impedance mismatch[177] and strong coupling between two ultracoherent membrane modes [13,179]. In the following, we present the spatial mapping of the mechanical mode using this metallic AFM tip, in addition to the functions that can also be provided by a coupled aluminium gate. In the setup, the AFM-tip is fixed and the piezo-actuator positioner carrying the drum can move flexibly along X-Y-Z axes, respectively. Therefore, we can fix the distance between the tip and the membrane, and excite the mechanical modes when moving the tip in X-Y axes. The mode shape can be re-built by plotting the maximum amplitude of the detected signal at the frequency of mechanical resonance, as functions of the tip position in X-Y axes.

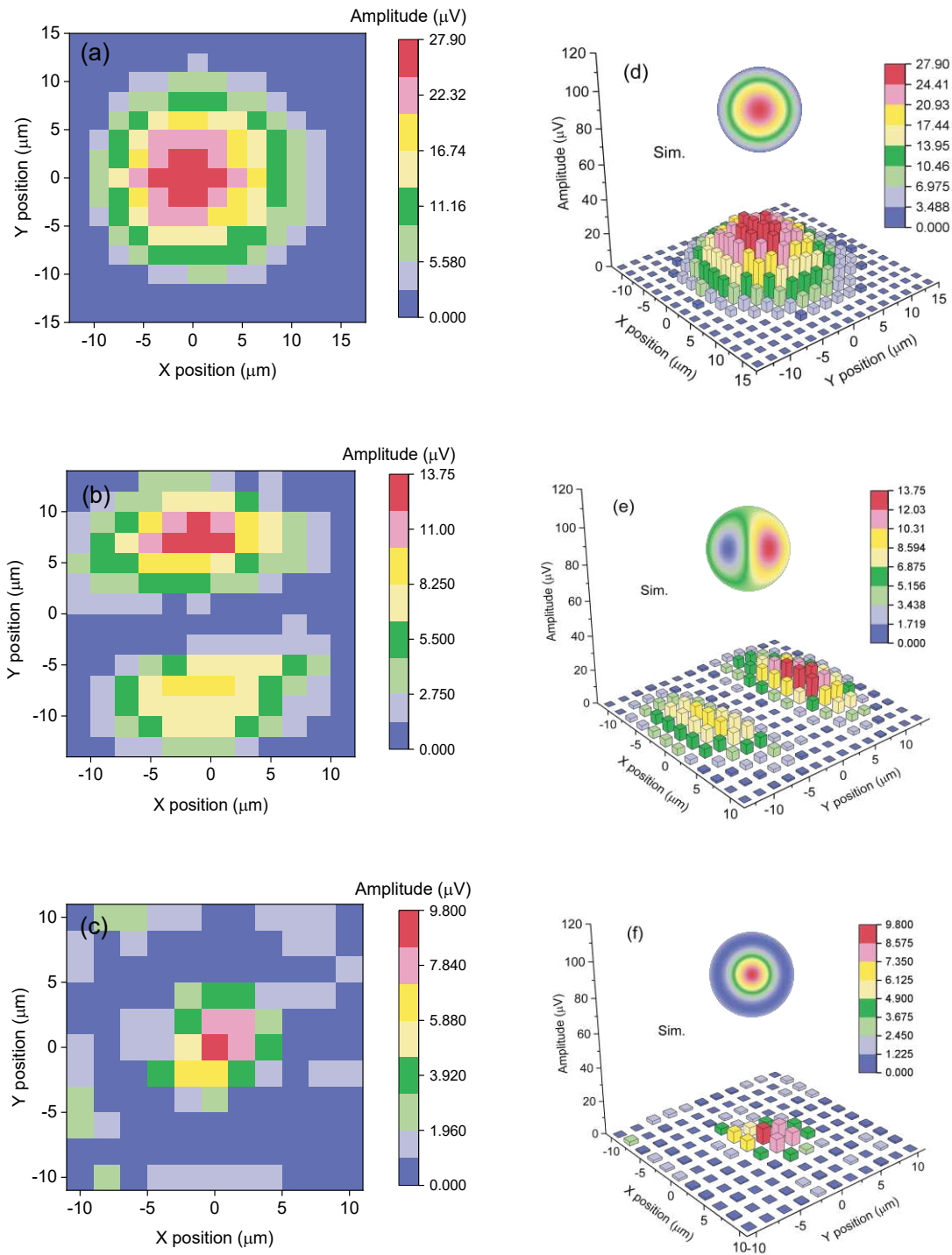


Figure 4.2.11. Mechanical modes (0,1), (1,1) and (0,2) detected by the metallic AFM-tip. (a-c) are the re-built mechanical amplitudes mapping and (d-f) are the related resultant 3D maps. The insets are the simulation results. The color bars are the detected mechanical amplitudes.

The scanning rate in the measurement is $28 \mu\text{m}$ X-axis \times $28 \mu\text{m}$ Y-axis at a fixed distance in the Z-axis. **Fig. 4.2.11(a-c)** shows the measured mechanical modes (0,1), (1,1) and (0,2) in amplitude mapping. **Fig. 4.2.11(d-f)** also shows their resultant spatial 3D maps, exhibiting a good overview of the measured mechanical modes. Obviously, the mechanical displacements approaching the edge are much smaller than that of the centre. The insets show they have a good agreement with the analytical mechanical motion function $z(r, \theta, t) = \sum_m \sum_n \cos(\Omega_{mn}t) \cos(m\theta) J_m\left(\frac{\alpha_{mn}r}{a}\right)$. It has been derived and analyzed in the section 2.1 in Chapter 2.

4.2.6 Capacitive coupling two mechanical modes in a two-tones driving scheme

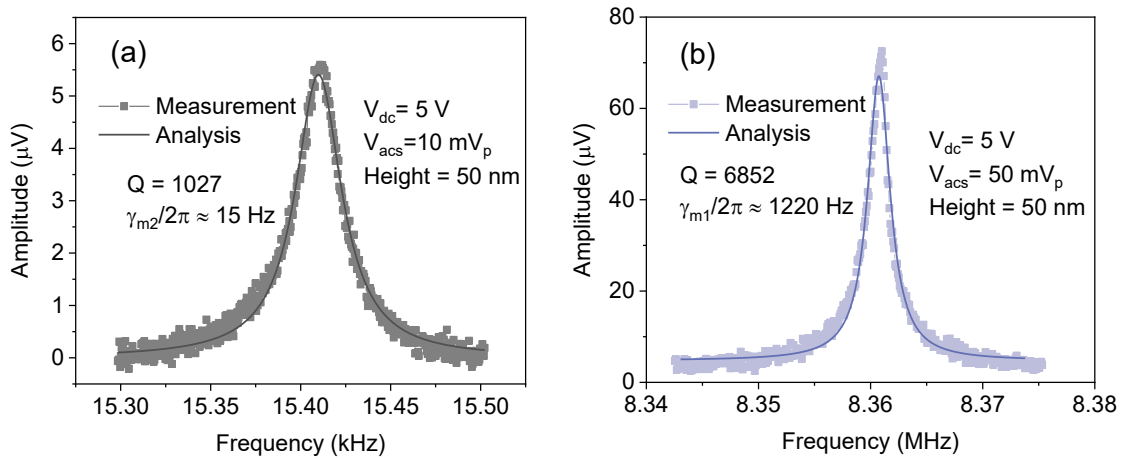


Figure 4.2.12. Linear mechanical responses of the AFM-tip (a) and SiN circular membrane (b).

As can be seen in **Fig. 4.2.12**, the AFM-tip is measured at a resonance frequency $\sim 15.4\text{ kHz}$ and the SiN membrane is measured at a resonance frequency $\sim 8.36\text{ MHz}$. The SiN membrane can be chosen as phonon-cavity in order to study the mode coupling through analogy to the optomechanical system. The basic principles of phonon-cavity electromechanics have been developed and analyzed in section 2.2.4 in Chapter 2. Following the concept of this phonon-cavity electromechanics, we pump this cavity at the frequency sum/difference $\Omega_1 \pm \Omega_2$, where $\Omega_2/2\pi \sim 15.4\text{ kHz}$ is low resonance frequency from the AFM-tip mode. Notably, “-” and “+” correspond to the red sideband and blue sideband of the phonon-cavity, respectively.

In our measurement, besides the pump tone, we also use the second tone to probe either the phonon-cavity or the coupled tip. Both two-tone operations are able to generate the destructive or constructive interference. These inherited physical interference phenomena, namely electromechanically-induced transparency [119][120] and amplification [117,120], have been introduced in previous microelectromechanical resonators. Four situations, namely when red sideband pumping the phonon-cavity, probing either SiN membrane (i) or AFM-tip (ii) and when blue sideband pumping the phonon-cavity, probing either SiN membrane (iii) or AFM-tip (iv), will be discussed in the following.

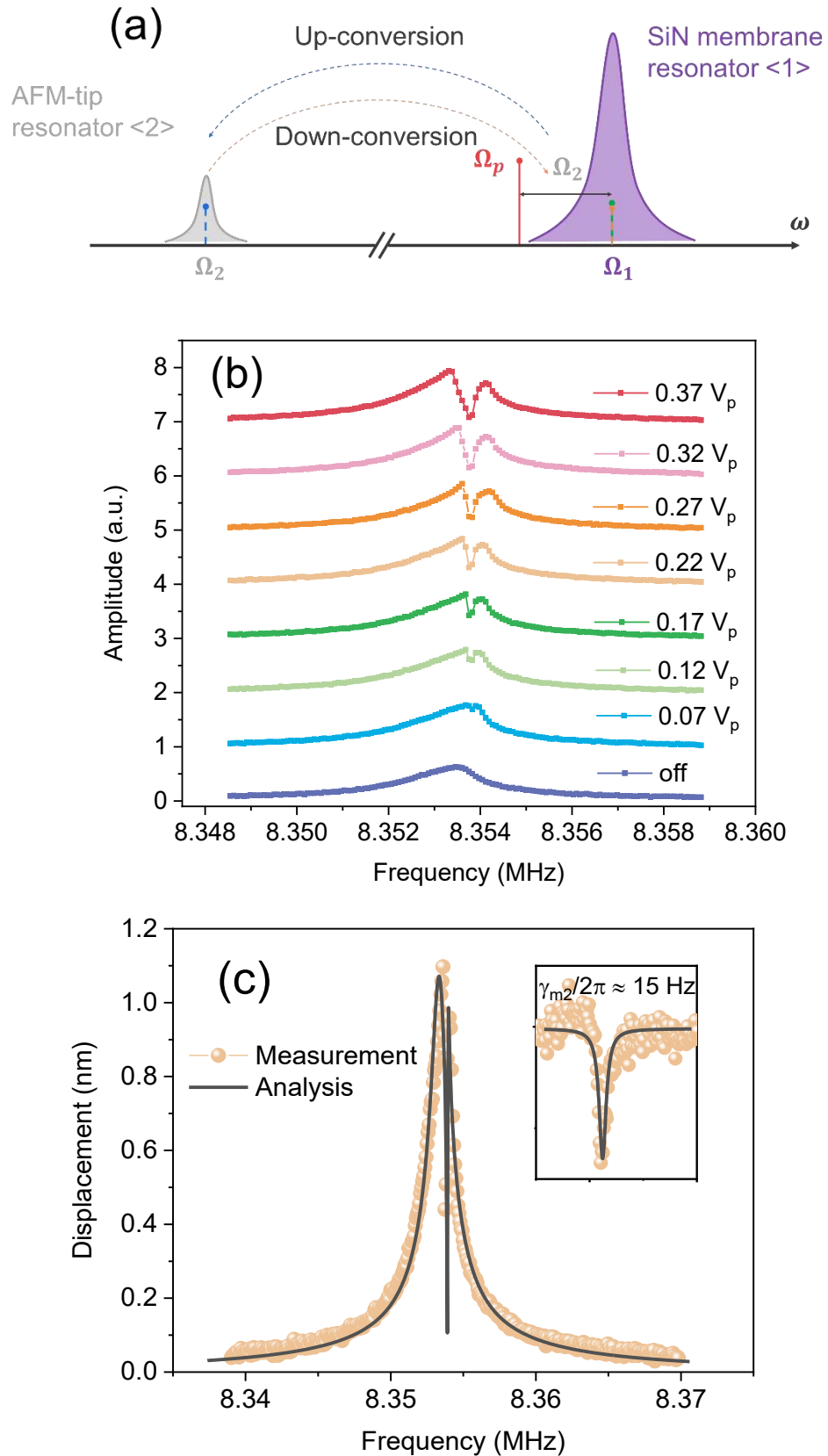


Figure 4.2.13. Red sideband pumping scheme, $\Omega_p = \Omega_1 - \Omega_2$. (a) is schematic of probing SiN membrane (Ω_1), where blue and yellow signal bars are the transduced phonons and green bar

is for the probe signal. (b) shows the detected amplitudes of the SiN membrane. (c) the measured curve ($0.22 V_p$) in (b) is well fit by using analytical calculation, where a small pump frequency detuning is defined as $\Omega_p = \Omega_1 - \Omega_2 + \Delta$. Here, the plot uses $\Delta/2\pi = 500 \text{ Hz}$.

(i) Red sideband pumping the phonon-cavity at $\Omega_p = \Omega_1 - \Omega_2$ and probing the phonon-cavity around Ω_1

Fig. 4.2.13(a) shows phonon transfer traces based on up-conversion and down-conversion, which correspond to generating phonons in the unprobed AFM-tip resonator and the generated phonons that can feed back the probed phonon-cavity. The interference between these phonons generated by the sideband pump and those phonon at Ω_1 created by the probe tone therefore can be built. **Fig. 4.2.13(b)** shows vibrating amplitudes of the SiN membrane, which have been fitted well by using analytical formula (see section 2.2.4). The fitting parameters are given in **Table 4.2.3**. Besides, a clear dip decrease of vibrating amplitudes of the SiN membrane takes place in **Fig. 4.2.13(c)**. It is because the destructive interference, namely electromechanically-induced transparency [119][120]. As the pump amplitude increasing, the observation of the dip is more clear. The further reason is that the damping rate of SiN membrane about $\gamma_{m1}/2\pi \approx 1220 \text{ Hz}$ is two orders larger than that of the AFM-tip about $\gamma_{m2}/2\pi \approx 15 \text{ Hz}$. Then, the transparency window can be defined by the un-probed AFM-tip. It is obvious that there is a dip within the linewidth of the SiN membrane.

| Table 4.2.3. Essential parameters for red sideband pumping the phonon-cavity and probing the phonon-cavity | | |
|--|------------------------|------------------------|
| Parameters | Fitting values | Setting values |
| DC voltage | - | 5 V |
| Drive voltage (V_{acs}) | - | 30 mV _p |
| Red sideband pump (V_{acp}) | - | 0.22 V _p |
| Global capacitance (F) | 10.1×10^{-16} | 10.1×10^{-16} |
| SiN damping rate (Hz) | 1220 | - |
| AFM-tip damping rate (Hz) | 15 | - |
| SiN effective mass (kg) | 4.4×10^{-14} | - |
| AFM-tip effective mass (kg) | 2.2×10^{-13} | - |
| Global driving force (nN) | - | 3.03 |
| Driving force on the apex (pN) | 9.59 | 1.21 |
| Global pumping force (nN) | - | 22.2 |
| Pumping force on the apex (pN) | 13.63 | 8.88 |

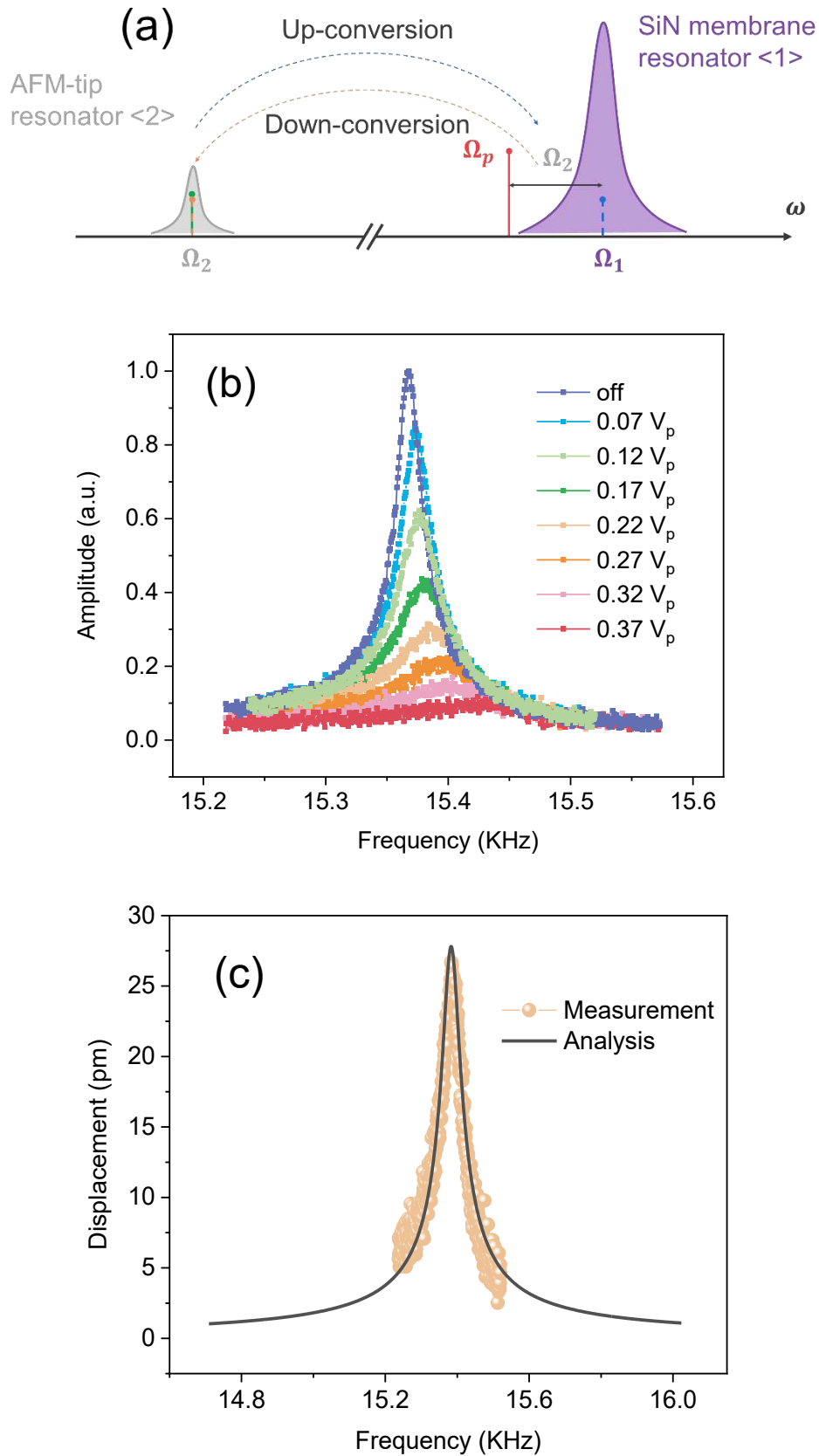


Figure 4.2.14. Red sideband pumping scheme, namely $\Omega_p = \Omega_1 - \Omega_2$. (a) is schematic of probing AFM-tip (Ω_2), where blue and yellow signal bars are the transduced phonons and green

bar is for the probe signal. (b) shows the detected amplitudes for the AFM-tip. (c) the measured curve ($0.22 V_p$) in (b) is well fit by using analytical calculation.

(ii) Red sideband pumping the phonon-cavity at $\Omega_p = \Omega_1 - \Omega_2$ and probing the AFM-tip around Ω_2

Fig. 4.2.14(a) shows phonon transfers based on up-conversion and down-conversion, which correspond to generating phonons in the unprobed phonon-cavity and the generated phonons feeding back the probed AFM-tip. Therefore, the interference between these phonons can be built. **Fig. 4.2.14(b,c)** shows vibrating amplitudes of the AFM-tip, which have been fitted well by using our analytical calculation (subsection 2.2.4). The fitting parameters can be found in **Table 4.2.4**. Besides, we note that the suppressing of vibrating amplitudes of the AFM-tip as increasing red sideband pump amplitude. It correlates to the destructive interference yielding electromechanically-induced transparency [119,120]. The mechanical responses are suppressed because of the destructive interferences. In addition, the linewidth of the tip increases with increasing the pump amplitude. It is obvious that there is the optomechanical damping effect. In other words, the pump forces modulate the mechanical susceptibility of the tip, leading to such increases of bandwidth.

| Table 4.2.4. Essential parameters for red sideband pumping the phonon-cavity and probing the AFM-tip | | |
|---|------------------------|------------------------|
| Parameters | Fitting values | Setting values |
| DC voltage | 5 V | 5 V |
| Drive voltage (V_{acs}) | - | 50 mV _p |
| Red sideband pump (V_{acp}) | - | 0.22 V _p |
| Global capacitance (F) | 10.1×10^{-16} | 10.1×10^{-16} |
| SiN damping rate (Hz) | - | - |
| AFM-tip damping rate (Hz) | 50 | - |
| SiN effective mass (kg) | 4.4×10^{-14} | - |
| AFM-tip effective mass (kg) | 2.2×10^{-9} | - |
| Global driving force (nN) | - | 5.05 |
| Driving force on the apex (pN) | 0.93 | 2.02 |
| Global pumping force (nN) | - | 22.22 |
| Pumping force on the apex (pN) | 4.04 | 8.89 |

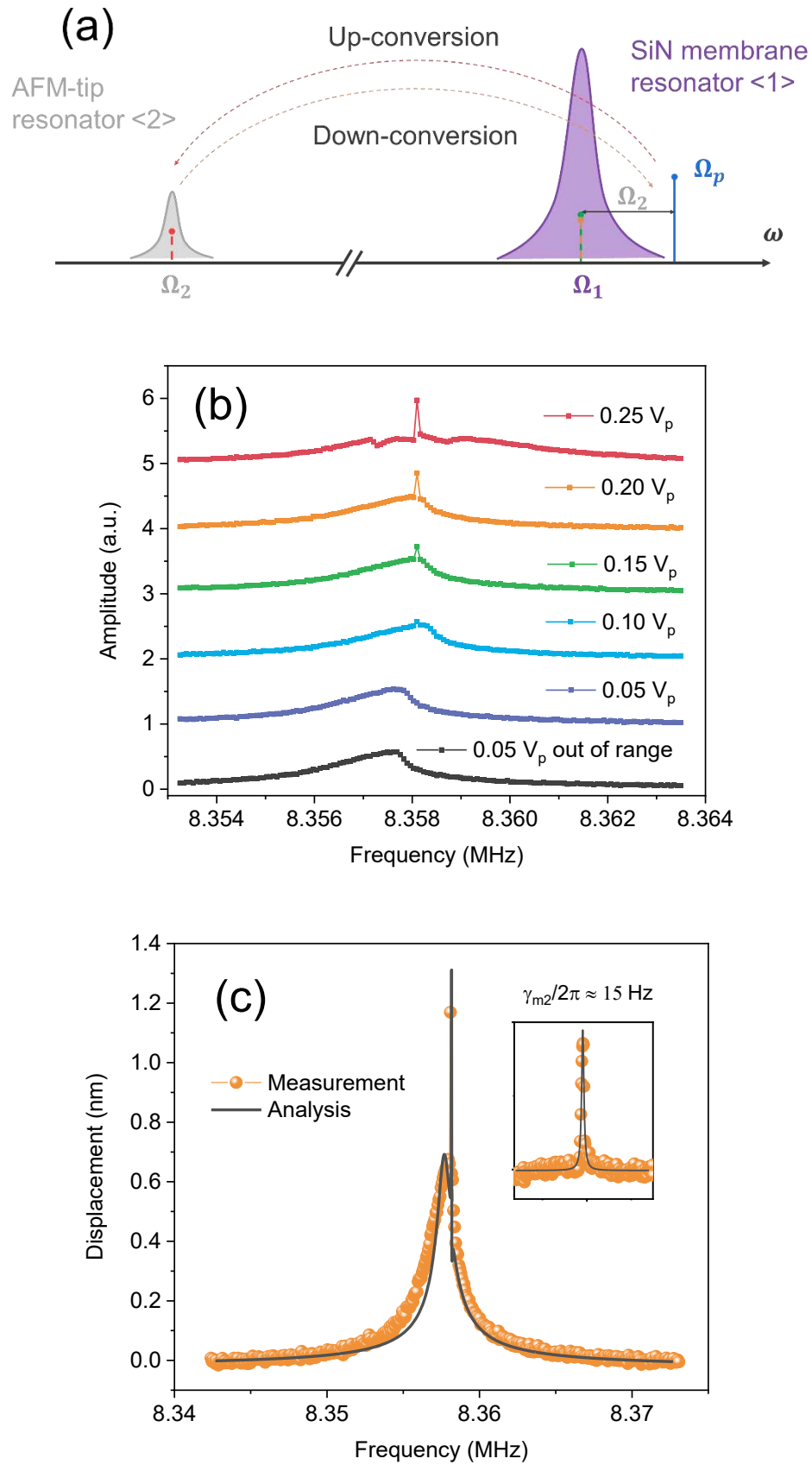


Figure 4.2.15. Blue sideband pumping scheme, namely $\Omega_p = \Omega_1 + \Omega_2$. (a) is schematic of probing SiN membrane (Ω_1), where red and yellow signal bars are the transduced phonons and

green bar is for the probe signal. (b) shows the detected amplitudes for the SiN membrane. (c) the measured curve ($0.20 V_p$) in (b) is well fit by using analytical calculation, where a small pump frequency detuning is defined as $\Omega_p = \Omega_1 + \Omega_2 + \Delta$. Here, the plot uses $\Delta/2\pi = 500 \text{ Hz}$.

(iii) Blue sideband pumping the phonon-cavity at $\Omega_p = \Omega_1 + \Omega_2$ and probing the phonon-cavity around Ω_1

Fig. 4.2.15(a) shows phonon generation based on up-conversion and down-conversion, corresponding to creating phonons in the unprobed AFM-tip resonator and the created phonons feeding back the probed phonon-cavity. Thus, these created phonons still build an interference.

Fig. 4.2.15(b) shows vibrating amplitudes of the SiN membrane, which have been well fit by using our analytical calculation (see section 2.2.4). The fitting parameters have been detailed in **Table 4.2.5**. Besides, a clear peak increase of vibrating amplitudes of the SiN membrane has been observed in **Fig. 4.2.15(b,c)** with increasing the pump amplitude. It demonstrates the constructive interference, namely electromechanically-induced amplification [117,120]. In particular, the narrow peak is because the damping rate of the SiN membrane is two orders larger than that of the AFM-tip as have been mentioned above. The amplifications of tip vibrations are projected onto the resonance of the drum, forming a small peak with a bandwidth $\gamma_{m2}/2\pi \approx 15\text{Hz}$ as the inset shows.

| Table 4.2.5. Essential parameters for blue sideband pumping the phonon-cavity and probing the phonon-cavity | | |
|---|------------------------|------------------------|
| Parameters | Fitting values | Setting values |
| DC voltage | 5V | 5 V |
| Drive voltage (V_{acs}) | - | 40 mV _p |
| Red sideband pump (V_{acp}) | - | 0.20 V _p |
| Global capacitance (F) | 10.1×10^{-16} | 10.1×10^{-16} |
| SiN damping rate (Hz) | 1750 | - |
| AFM-tip damping rate (Hz) | 15 | - |
| SiN effective mass (kg) | 4.4×10^{-14} | - |
| AFM-tip effective mass (kg) | 2.2×10^{-13} | - |
| Global driving force (nN) | - | 4.04 |
| Driving force on the apex (pN) | 4.54 | 1.61 |
| Global pumping force (nN) | - | 20.2 |
| Pumping force on the apex (pN) | 5.56 | 8.08 |

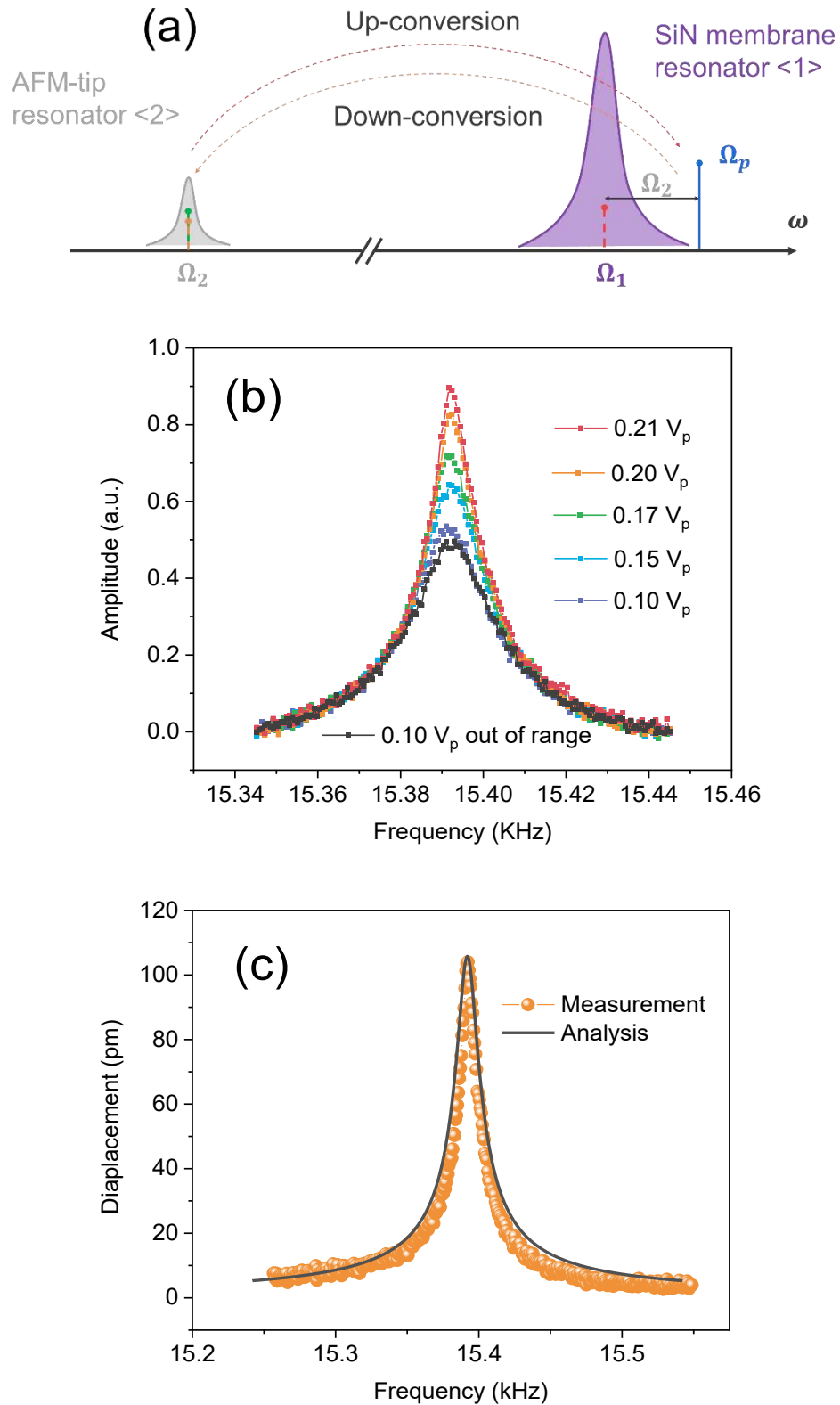


Figure 4.2.16. Blue sideband pumping scheme, namely $\Omega_p = \Omega_1 + \Omega_2$. (a) is schematic of probing AFM-tip (Ω_2), where red and yellow signal bars are the transduced phonons and green

signal bar is for the probe signal. (b) shows the detected amplitudes for the AFM-tip. (c) the measured curve ($0.20 V_p$) in (b) is well fit by using analytical calculation.

(iv) Blue sideband pumping the phonon-cavity at $\Omega_p = \Omega_1 + \Omega_2$ and probing the AFM-tip around Ω_2

Fig. 4.2.16(a) shows phonon generation for up-conversion and down-conversion processes, corresponding to creating phonons in the unprobed phonon-cavity and the generated phonons feeding back the probed AFM-tip. These creating phonons can generate an interference. **Fig.4.2.16(b,c)** shows vibrating amplitudes of the AFM-tip, which have been well fit by using our analytical calculation (see section 2.2.4). The fitting parameter details have been given by **Table 4.2.6**. Besides, an increase of vibrating amplitudes of the AFM-tip has been observed with increasing pump amplitude. It reveals the constructive interference, namely electromechanically-induced amplification [117,120]. In the blue sideband pumping scheme, the bandwidth of the tip decreases with increasing pump amplitude, in agreement with our calculation for the effective damping rate as analyzed in the section 2.2.4 In Chapter 2.

| Table 4.2.6. Essential parameters for blue sideband pumping the phonon-cavity and probing the AFM-tip | | |
|---|------------------------|------------------------|
| Parameters | Fitting values | Setting values |
| DC voltage | 5 V | 5 V |
| Drive voltage (V_{acs}) | - | 50 mV _p |
| Red sideband pump (V_{acp}) | - | 0.20 V _p |
| Global capacitance (F) | 10.1×10^{-16} | 10.1×10^{-16} |
| SiN damping rate (Hz) | - | - |
| AFM-tip damping rate (Hz) | 15 | - |
| SiN effective mass (kg) | 4.4×10^{-14} | - |
| AFM-tip effective mass (kg) | 2.2×10^{-9} | - |
| Global driving force (nN) | - | 5.05 |
| Driving force on the apex (pN) | 1.06 | 2.02 |
| Global pumping force (nN) | - | 20.2 |
| Driving force on the apex (pN) | 3.03 | 8.08 |

As the four situations discussed above, the phonon interferences have been carefully analysed and explained in our nanoelectromechanical resonators by using the developed models, namely electromechanically-induced transparency[119,120] and amplification[117,120], analog to the optomechanical system.

4.2.7 White noise drive of SiN membrane

In order to verify whether SiN membrane resonator can be driven by white noise, the SiN membrane is actuated by setting $V_{dc} = 4, 2, 1V$ and the input noise amplitude is increased so that the SiN membrane can be artificially heat up by these stochastic forces and its thermal Brownian motions can be observed. From previous measurements, as shown in Chapter 2, the spring constant of the SiN drum membrane is around 100. Comparing with these mechanical resonator, having the low spring constant, exciting thermal Brownian motion of the SiN membrane requires larger amplitude of driving forces. In this thesis, the SMM technique is used with a metallic AFM-tip to measure the thermomechanical motion due to Brownian motion of

the SiN membrane resonator, and it is flexible and feasible to achieve a desirable gap distance, namely the distance between the tip and the membrane. To date, ~ 50 nm gap has reached.

Fortunately, white noise spectral density is observed without a microwave cavity in the tip-membrane coupling scheme. When the gap distance is 50 nm, a larger capacitive coupling allows enough microwave photons to reach the drum membrane. Their reflection signals can carry the thermomechanical motion of the SiN membrane driven by stochastic forces.

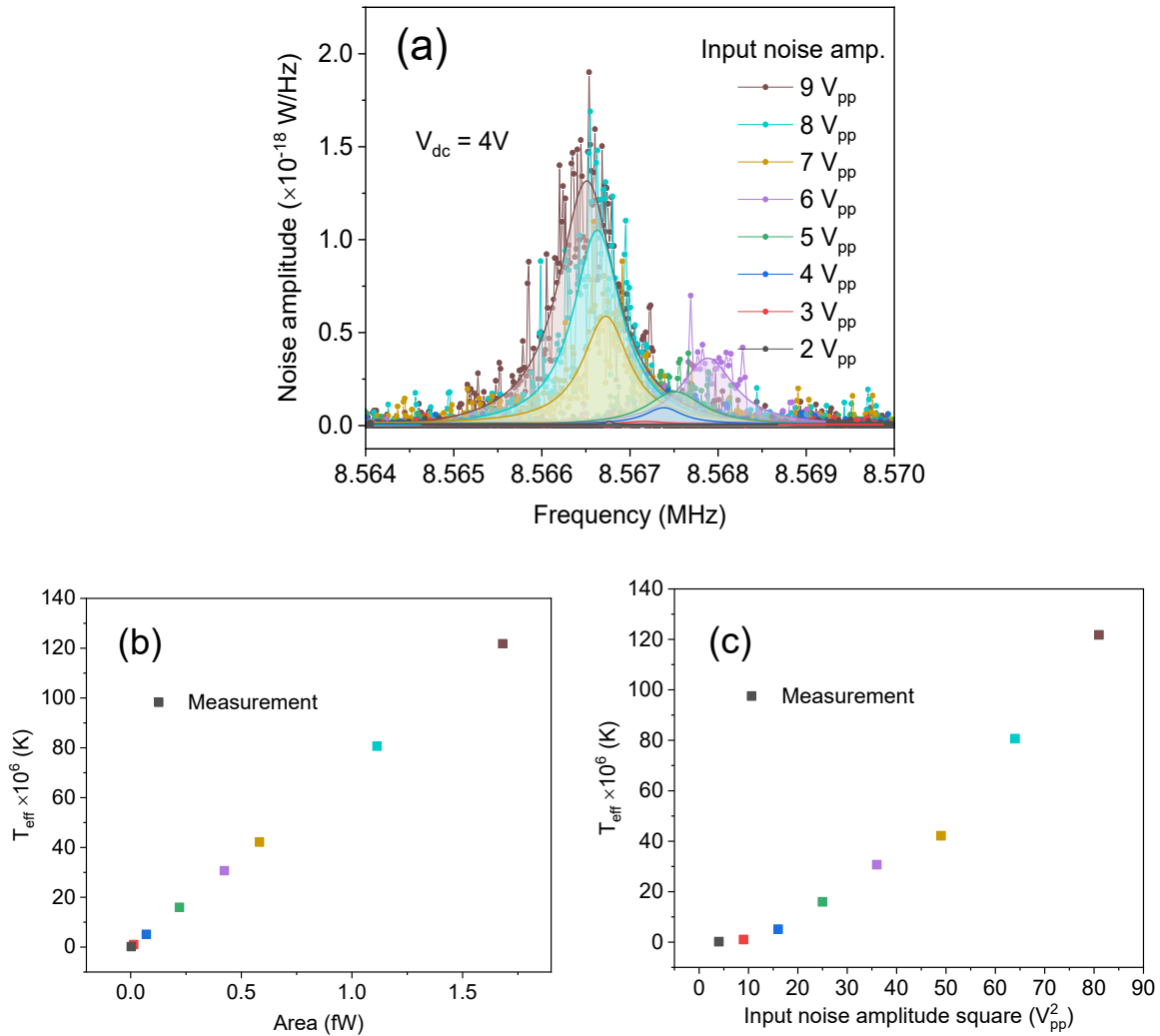


Figure 4.2.17. White noise power spectral density when $V_{dc} = 4$ V. (a) Power spectral density of the SiN membrane. (b) Effective temperatures are calculated from the areas under PSD. (c) Effective temperatures as function of the input noise amplitudes V_{pp}^2 .

The power spectral density (PSD) data of SiN membrane can be used for calculating the effective temperature. **Fig. 4.2.17(a)** shows PSD of the membrane, driven by different noise

amplitudes at a fixed DC voltage $V_{dc} = 4$ V. **Fig. 4.2.17(a)** also shows the areas corresponding to $S_x[\omega_d]$ that have been integrated across the frequency around its resonance frequency. The effective temperature (T_{eff}) calculation is given by [180]

$$S_x[\omega_d] \left(\frac{m^2}{rad/s} \right) = \frac{4k_B T_{eff}}{m_{eff} \Omega_m^2} \frac{\gamma_m}{\gamma_m^2 + 4(\omega_d - \Omega_m)^2} \quad Eq. 4.2$$

This formula is the single-sided noise spectral density. The useful transform of Eq.4.2 also reads below in order to know the temperature origin in physics

$$4k_B T_{eff} = m_{eff} \Omega_m^2 S_x[\omega_d] \cdot \gamma_{eff} \quad Eq. 4.3$$

where the effective damping rate is defined by $\frac{1}{\gamma_{eff}} = \frac{\gamma_m}{\gamma_m^2 + 4(\omega_d - \Omega_m)^2}$ when $\omega_d \sim \Omega_m$, and the right side member relates to the one-side noise power spectral density.

Obviously, we see that the effective temperature corresponds to the noise power spectral density. The noise amplitude spectral density at two sidebands also associates to the measuring areas surrounded by the measured curves, revealing how much physical temperature is occupied by the mechanical resonator. The more details related to the physical temperature will be presented in section 5.1.2 in chapter 5.

Fig. 4.2.17(b) shows the effective temperature is proportional to the areas under PSD. **Fig.4.2.17(c)** shows the effective temperature increasing with the input noise amplitudes V_{pp}^2 increasing, because of the Langevin force spectral density $S_{FF} \propto V_{pp}^2$ [110].

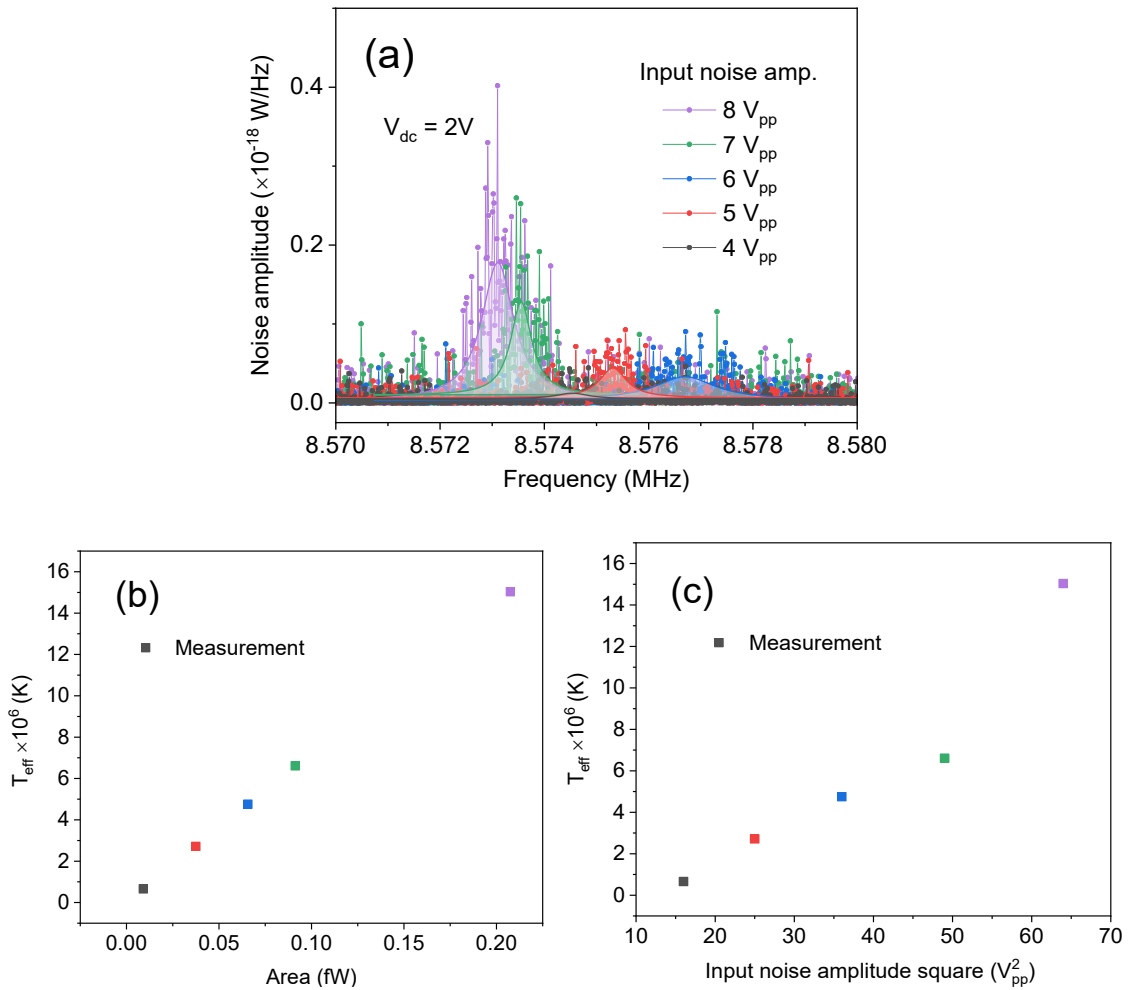


Figure 4.2.18. White noise power spectral density when $V_{dc} = 2$ V. (a) Squared noise amplitudes of the SiN membrane. (b) Effective temperature is calculated from the area under PSD. (c) Effective temperature as function of the input noise amplitude V_{pp}^2 .

In the presence of $V_{dc} = 2$ V, **Fig. 4.2.18(a)** shows the SiN membrane can sense smaller noise amplitudes, as the measured signals have been weaker than that of using $V_{dc}=4$ V. **Fig. 4.2.18(b)** shows the effective temperature proportional to the areas under PSD. **Fig. 4.2.18(c)** shows the effective temperature increasing with the input noise amplitude V_{pp}^2 increasing.

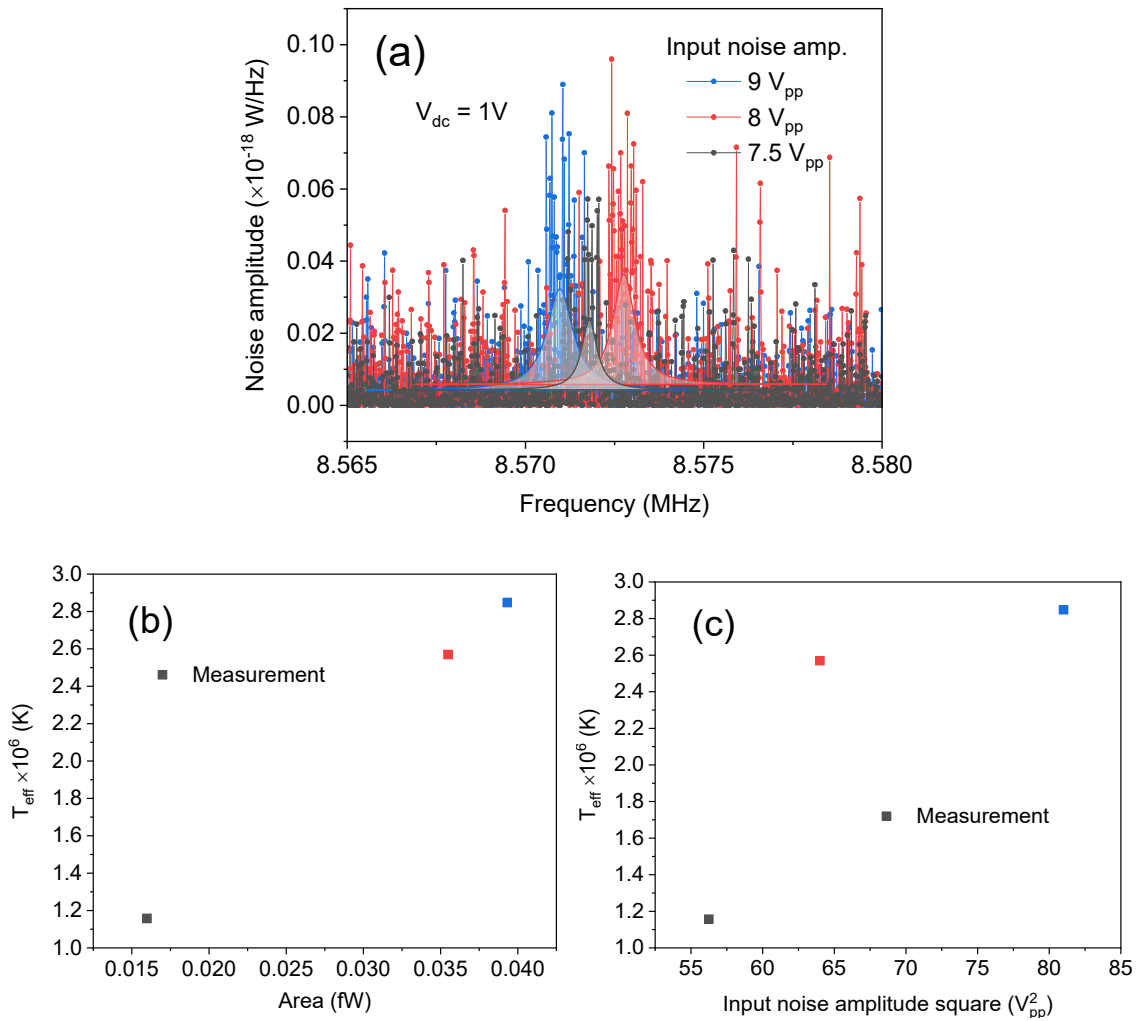


Figure 4.2.19. White noise power spectral density when $V_{dc} = 1$ V. (a) Squared noise amplitudes of the SiN membrane. (b) Effective temperature is calculated from the area under PSD. (c) Effective temperature as function of the input noise amplitudes.

When setting $V_{dc} = 1$ V, the spring constant modulation of the SiN membrane goes fluctuations. This specific discussion has been done in section 2.3.3 in Chapter 2. The DC voltage goes to be small, leading to a small electrostatic force, which can be affected by the noise floor. In fact, if DC voltage near 0, the data cannot well be detected. Fortunately, although this small voltage

$V_{dc} = 1$ V, the weak signals were still observed in our experiments. It shows the high sensitivity of the SiN membrane used to potentially measure the thermal Brownian motion.

4.3 Summary

In this chapter, the state-of-the-art of SMM tool is overviewed, normally containing AFM-in-SEM and VNA. Based on the coupling capacitance scheme, the AFM-tip-sample interactions and principles are importantly introduced and analysed. We have demonstrated that SMM can be used to in-situ characterize mechanical vibrations through a capacitive coupling scheme. Then, SiN membrane is able to be measured with the AFM-tip *via* either VNA or microwave interferometry measurement. The setup brings simplicities as both signals for the drive and detection are set through a single tip. In order to study the membrane, one COMSOL simulation part for the tip-membrane scheme and then six characterization parts of the membrane have been performed. First of all, the multiphysics simulation for simulating the tip-membrane scheme is to help us for understanding the electrostatic behaviours. Then, the six experiment characterizations are summarized below:

(i) drive and detect linear mechanical responses. It can verify whether the SiN membrane is fabricated well or not. Besides, the linear responses are investigated for evaluating key parameters, such as quality factor, damping rate and resonance frequency. SMM tool can be used to carry on MEMS test, especially the vibration element that is embedded in complex circuits. (ii) the resonance frequency modulation through DC voltages. Although the capacitive coupling is small, the tip can still be used to tune the spring constant of SiN membrane, and further achieve frequency tuning by adding DC voltages. (iii) Duffing nonlinear mechanical responses. It can be measured as the tip position changes along the radial axis of the membrane and used flexibly to characterize whether nonlinearity depends on the tip position. (iv) mechanical modes detection. It helps us to understand the spatial mapping of vibrating amplitudes of the SiN membrane and is useful to guide us for choosing mechanical modes used in mode-mode coupling experiments. (v) double-tone driving scheme, an analogy to the optomechanical system. Double-tone driving scheme, consisting of SiN membrane capacitively coupled to a metallic AFM-tip, can be utilized for electromechanically-induced transparency and amplification, which exhibits its capabilities of signal amplification and de-amplification. Especially, for the blue sideband pumping, the motion of the tip can be amplified. Its bandwidth becomes narrowing which could be extended for applications of sensing improvement for the

AFM-tip. (vi) white noise drive of the SiN membrane. Our setup exhibits enough sensibilities to detect the thermal Brownian motion of the SiN membrane when it is artificially heated up by external white noise.

In addition, the spatial mapping of the mechanical damping and the effect of DC voltages on the mechanical damping still need further efforts to understand. In particular, the experiment data as shown in Fig. 4.2.8, the damping rates seem to be saturated at the positive DC voltages. However, in previous works [176,181], mechanical damping exhibits quadratic dependence on the DC voltages, which are quite different with our fully clamped membrane. Some microscopic damping model should be developed in order to understand this observation.

Chapter 5 Microwave optomechanical thermometry

In this chapter, we first present the thermometry principles and discussions, including cavity optomechanical scheme and cavity optomechanical readout of thermal Brownian motion. Then, we show the experiment expectations of this thesis.

5.1 The thermometry principles

As mentioned in Chapter 4, SiN drum membrane serving as NEMS has been tested and demonstrated, being able to measure the white noise amplitude. It indicates this drum resonator can be a promising NEMS candidate for detecting thermal Brownian motion.

So far, the cavity-enhanced sensitivity to the readout has been studied by using RLC circuit fabricated on printed circuit board (PCB) and coupled with doubly clamped beam structures at RT [46,61]. Meanwhile, sideband pump technique enhancing readout sensitivity has also been detected. Besides, an optomechanical architecture, containing a three-dimensional optomechanical cavity coupling with a prestressed SiN membrane, has been made working down to sub-millikelvin, which points the research direction to new optomechanical experiments with a high optomechanical cooperativity [47]. Recently, an on-chip thermometry was also built by using superconducting microwave circuit cavity to couple with a doubly clamped suspended SiN beam [79], which works at millikelvin. So as to focus on the wide working temperature range, building an on-chip thermometry needs efforts. In this thesis, SiN drum membrane resonator has been developed and tested. On one hand, this drum resonator in principle can work not only at RT but also at millikelvin. On the other hand, the large coupling capacitance between the drum and the coupled external circuit allows its thermal Brownian motion to be read out with relatively lower power operations.

Using cavity optomechanical scheme, the phonon numbers (n_m) of the NEMS oscillator can be readout through the photon population (n_c) in a microwave cavity through the coupling strength. Moreover, the optomechanical sideband pumping method provides an optomechanical gain that can help the readout of photons to get rid of thermal noise floor in the detection chain in the measurement.

5.1.1 Cavity optomechanical scheme

The cavity optomechanical system studies the interaction between the light and the mechanical displacement. It consists of two systems, the cavity and the movable object, in which the cavity is used to confine electromagnetic fields, in forms of optical/microwave photons. It allows mechanical motions to be detected and manipulated by photons. For instance, mechanical oscillator has been cooled down into quantum ground states through red sideband cooling technique [9]. This technique pumped out the initial thermal phonons carried by the mechanical oscillator. Besides, microwave mechanical amplification can also be realized by pumping a microwave cavity at its blue sideband [182], through increasing the number of mechanical phonons.

(i) Coupling strength

In both optomechanical pumping schemes, one of the key important parameters is the coupling strength, G , which defines the energy exchanges between photons and mechanical displacements in the form of phonons, $G = -d\omega_c/dx = -d\omega_c/dC_m \times dC_m/dx$. It is also written as a function of the photon number n_c ,

$$g = Gx_{ZPF}\sqrt{n_c} \quad \text{Eq. 5.1}$$

where n_c is generated by the pump tone, which replies to the pumping scheme. And, x_{ZPF} is the zero-point fluctuations, $x_{ZPF} = \sqrt{\hbar/2m_{eff}\Omega_m}$.

$$n_c = \frac{2\kappa_{ex} \left(\frac{C_t \omega_c^2 |\mu_p|^2}{2} \right)}{\hbar\omega_c(\kappa^2 + 4\Delta^2)} \quad \text{Eq. 5.2}$$

Here, C_t is total static capacitance, μ_p is the pump amplitude, and κ_{ex} is the coupling rate to the outside, κ is the decay rate of the microwave mode [110]. From the coupling strength expression, we know that the C_m plays a key role in increasing the value of the coupling strength, allowing the mechanical motions to be more easily detected/manipulated with the relatively lower pump amplitude. From Eq.5.2, it is also easy to see that the pump becomes more efficient in generating microwave photons, n_c , at the sideband resolved condition, $\Omega_m \gg \kappa$. Therefore, our nanoelectromechanical membrane resonator is expected to provide the higher coupling strength in microwave optomechanical circuits, comparing with those doubly-clamped suspended beams.

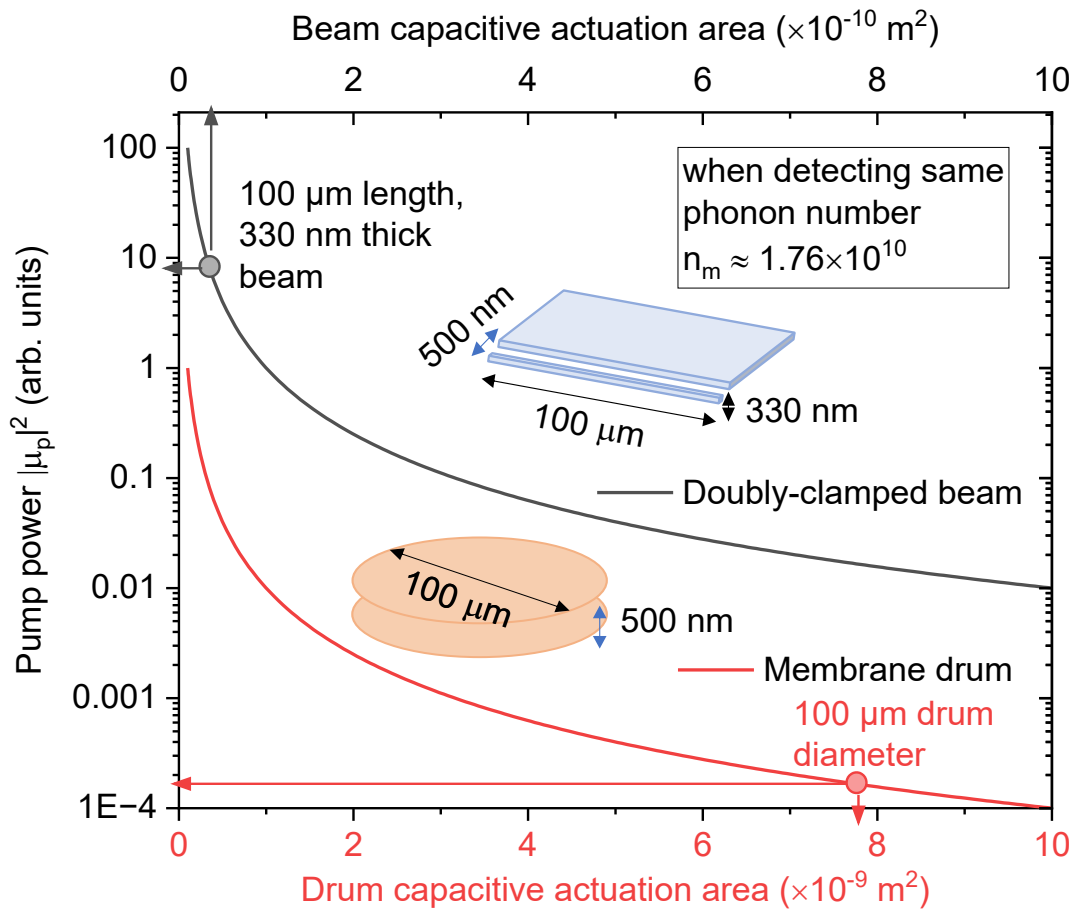


Figure 5.1.1. Pump power as function of drum (red) and beam (black) capacitive actuation area. The capacitive distance is fixed at 500 nm. The insets show schematics for doubly clamped beam and membrane drum in capacitive coupling scheme, respectively.

When fixing the capacitive distance at 500 nm, the coupling strength G , depending on the capacitive actuation area, affects the pump power amount. **Fig. 5.1.1** shows if requiring the same cavity photon number, the membrane drum, having area about 100-times larger than the beam, can reach the photon number with highly efficient pump power.

For instance, when fixing the phonon number n_m , related to T_m , we are able to discuss whether the pump power is reduced and optimized by the device capacitive actuation area. Then, we can choose membrane drum (diameter: $100 \mu\text{m}$) comparing with the doubly-clamped beam (dimension: $100 \mu\text{m}$ length \times 330 nm thickness). Thus, the device actuation area is estimated about $3.3 \times 10^{-11} \text{ m}^2$ for the doubly-clamped beam and about $7.85 \times 10^{-9} \text{ m}^2$ for the membrane drum. Obviously, the capacitive actuation area of the membrane drum is about 100 times larger than the doubly-clamped beam. It means the coupling strength G of the membrane

drum is also larger 100 times than the beam. If requiring to detect same phonon number $n_m \approx 1.76 \times 10^{10}$, according to Eq.5.2, corresponding photon numbers to beam and drum are calculated to be $n_{c,beam} \approx 3.05 \times 10^{19}$ and $n_{c,drum} \approx 7.27 \times 10^{21}$. It is obvious that drum devices having larger capacitive coupling area generate much photons in the cavity with high pumping efficiency. Calculation parameters are the detection frequency of cavity $\omega_c/2\pi \approx 4.8 \text{ GHz}$, the resonance frequency of resonator $\Omega_m/2\pi \approx 11.8 \text{ MHz}$, decay rate of cavity $\kappa/2\pi \approx 61 \text{ MHz}$, coupling efficiency $\kappa_{ex}/\kappa = 0.044$.

(ii) Optical damping effect

This optical damping effect plays a role in studying whether a sideband pump contributes pump photons to a microwave cavity. Its further explanation is described below:

Cavity-dependent optical damping rate Γ_{opt} is given by [110]

$$\Gamma_{opt} = G^2 \frac{1}{\omega_c(2m_{eff}\Omega_m)} \left(\frac{C_t \omega_c^2 |\mu_p|^2}{2} \right) \times \left(\frac{\kappa}{(\Delta + \Omega_m)^2 + \frac{\kappa^2}{4}} - \frac{\kappa}{(\Delta - \Omega_m)^2 + \frac{\kappa^2}{4}} \right) \quad Eq. 5.3$$

In order to describe the red and blue sideband pumping, schematic of spectrum operation is shown in **Fig. 5.1.2**.

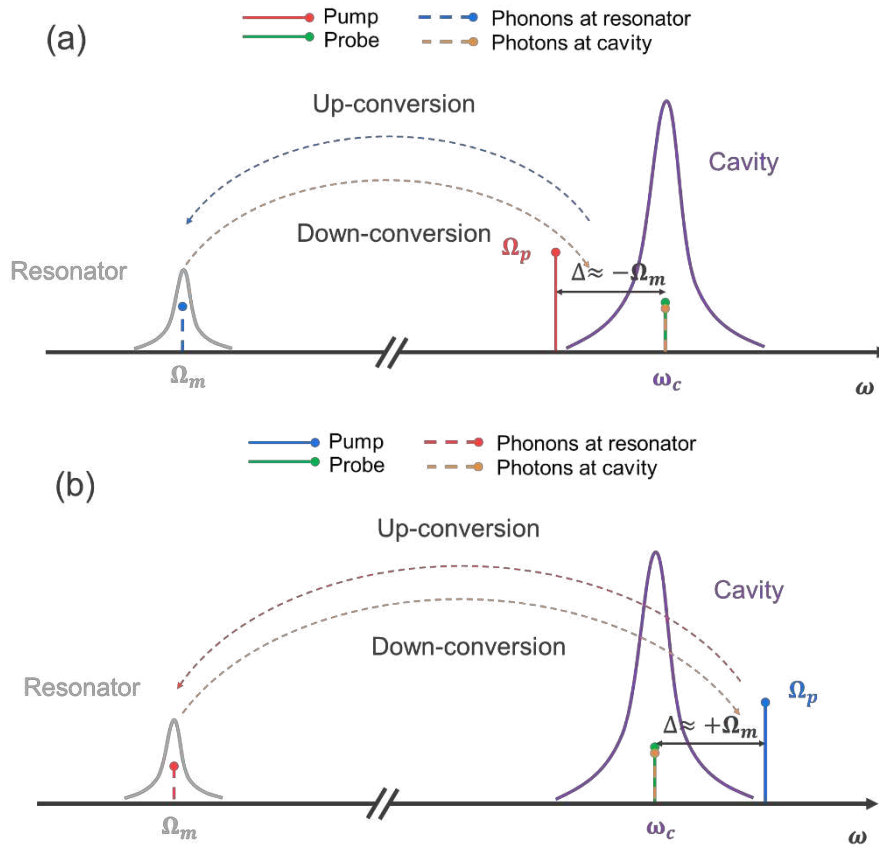


Figure 5.1.2. (a) Red sideband pumping, namely $\Omega_p = \omega_c - \Omega_m$, where red sideband pumps the cavity and another signal probes the cavity around ω_c . (b) Blue sideband pumping, namely $\Omega_p = \omega_c + \Omega_m$, where a blue sideband pumps the cavity and another signal probes the cavity around ω_c .

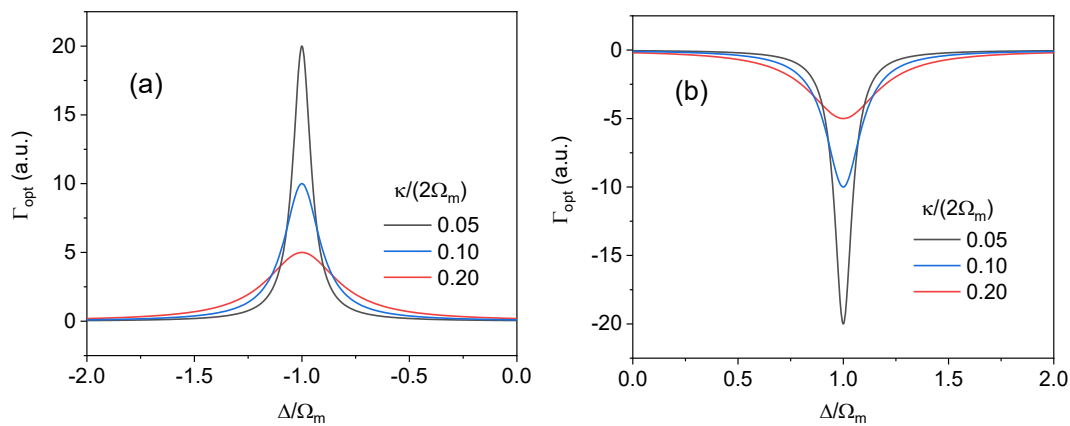


Figure 5.1.3. Optical damping effects at red (a) and blue sideband (b), due to the ratio $\kappa/(2\Omega_m) < 1$, in sideband-resolved condition.

In red sideband, the first term in Eq.5.3 dominates the transduction behaviour. Approximation is given to be $\Gamma_{opt} \approx g^2 4/\kappa$. **Fig. 5.1.3(a)** shows $\Gamma_{opt} > 0$. As $\kappa/(2\Omega_m)$ decreasing, this

results in $\Gamma_{eff} = \Gamma_m + \Gamma_{opt}$ increase. It demonstrates the mechanical response of the resonator is de-amplified, leading to the reduction of quality factor. Moreover, this observation also indicates the system energy pumped out of the mechanical mode. Then, this red sideband pumping is sideband cooling technique, usually used in quantum engineering [9].

In blue sideband, the second term in Eq.5.3 dominates the transduction behaviour. Approximately, $\Gamma_{opt} \approx -g^2/4\kappa$ is deduced. **Fig. 5.1.3(b)** shows $\Gamma_{opt} < 0$. As $\kappa/(2\Omega_m)$ decreasing, it leads to $\Gamma_{eff} = \Gamma_m + \Gamma_{opt}$ decrease. This indicates the mechanical amplitude of the resonator is amplified, increasing the quality factor of the resonator. This explains pumping energy transduced to the mechanical system.

5.1.2 Cavity optomechanical readout of thermal Brownian motion

The basic principle of phonon thermometry is to readout the thermal Brownian motion of the mechanical resonators, which is generated by Langevin force. The integration of the measured spectrum density of S_x^\pm gives the half variance of the thermal motion $\langle \delta x^2 \rangle$, further giving the detected temperature T_m . In optomechanical scheme, the sideband pumping readout method will change the mechanical damping rate, as mentioned above. The relationships between the T_m and spectrum density of thermal Brownian motion are described as [110]:

$$\frac{1}{2\pi} \int S_x^\pm d\omega = \sigma_x^{\pm 2} = \sigma_x^2 \quad Eq. 5.4$$

where S_x^+ and S_x^- are symmetric.

Then, σ_x^2 related to $\langle \delta x^2 \rangle$ is given by

$$\sigma_x^2 = \langle \delta x^2 \rangle \frac{\Gamma_m}{\Gamma_{eff}} \quad Eq. 5.5$$

where Γ_m is the damping rate, Γ_{eff} is the effective damping rate at blue sideband pumping scheme. Moreover, $\langle \delta x^2 \rangle$, a half variance of the thermal motion, is given by

$$\langle \delta x^2 \rangle = \frac{k_B T_m}{2m_{eff}\Omega_m^2} = x_{ZPF}^2 n_m \quad Eq. 5.6$$

In terms of the thermometry principle, Eq.5.6, 5.5, 5.3 and 5.2 and 5.1 are all reinjected to Eq.5.4. The detected physical temperature by the nanoelectromechanical resonator, at blue sideband, arrived at

$$T_m = \frac{\frac{1}{2\pi} \int S_x^\pm d\omega (2m_{eff}\Omega_m^2)}{k_B} \left(1 - \frac{|\Gamma_{opt}(\Delta, C_m, n_c)|}{\Gamma_m} \right) \quad Eq. 5.7$$

Therefore, this optomechanical thermometer is needed to calibrate, in order to remove the effects from sideband pump. One of the methods is to calibrate the variations of the measured temperature δT_m as function of pump power.

$$\begin{aligned} \delta T_m &= \frac{\frac{1}{2\pi} \int S_x^\pm d\omega (2m_{eff}\Omega_m^2)}{k_B} \cdot \frac{|\Gamma_{opt}(\Delta, C_m, n_c)|}{\Gamma_m} \\ &= \frac{\frac{1}{2\pi} \int S_x^\pm d\omega (2m_{eff}\Omega_m^2)}{k_B} \\ &\quad \cdot G^2 \frac{1}{\omega_c (2m_{eff}\Omega_m)\Gamma_m} \left(\frac{C_t \omega_c^2 |\mu_p|^2}{2} \right) \times \left(\frac{\kappa}{(\Delta - \Omega_m)^2 + \frac{\kappa^2}{4}} \right) \\ &= \frac{\frac{1}{2\pi} \int S_x^\pm d\omega (2m_{eff}\Omega_m^2)}{k_B} \\ &\quad \cdot g_0^2 n_c \times \left(\frac{\frac{\kappa}{2\Omega_m}}{\left(\frac{\Delta}{\Omega_m} - 1 \right)^2 + \left(\frac{\kappa}{2\Omega_m} \right)^2} \right) \times \frac{2}{\Omega_m} \quad Eq. 5.8 \end{aligned}$$

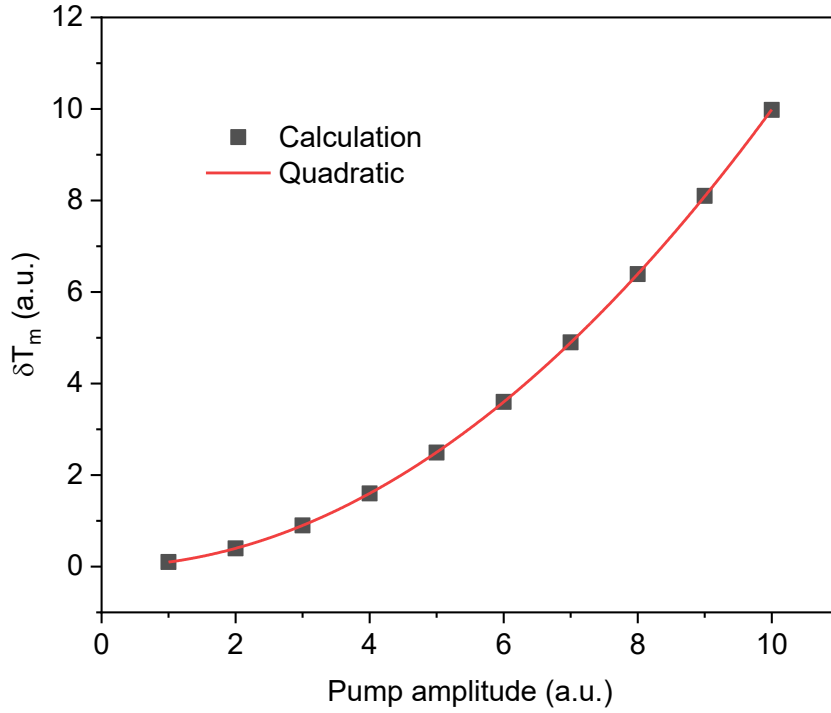


Figure 5.1.4. Physical temperature variation as function of pump amplitude, where $\frac{\kappa}{2\Omega_m} = 0.01 \ll 1$, in the sideband-resolved condition, is chosen.

When fixing the coupling strength, $G = -\frac{d\omega_c}{dx} = \frac{\omega_c}{2C_t} \frac{dC_m(x)}{dx}$, **Fig. 5.1.4** shows the δT_m increasing as the pump amplitude increasing. Because more phonons are added to the resonator due to the pump power from μ_p . The real temperature, detected by the resonator, can be obtained by extending this curve to $\mu_p=0$. Besides, Eq.5.8 can also be used from calibration of the coupling strength, G . In addition, we could also see that blue sideband pumping helps to readout small values of n_m , as it brings optomechanical gain.

Besides, it is also interesting to make comparisons between the microwave optomechanical system [36] and the phonon cavity system [93]. The phonon cavity system consists of two coupled mechanical resonators. It can be used to exploit as a model system to study classic features of optomechanics. For instance, “optical damping” effects have also been demonstrated in the phonon-cavity system, consisting of a SiN membrane resonator capacitively coupled to an aluminium membrane resonator. This effect is in the phonon cavity scheme given by [93]. Its optical damping effect is given by

$$\begin{aligned}\Gamma_{opt,phonon-cavity} &= \frac{|f_p|^2}{4m_1m_2d^2\Omega_1\Omega_2} \left[\frac{\gamma_1}{(\Omega_2 + \Delta)^2 + \frac{\gamma_1^2}{4}} - \frac{\gamma_1}{(\Omega_2 - \Delta)^2 + \frac{\gamma_1^2}{4}} \right] \\ &= n_p g_0^2 \left[\frac{\gamma_1}{(\Omega_2 + \Delta)^2 + \frac{\gamma_1^2}{4}} - \frac{\gamma_1}{(\Omega_2 - \Delta)^2 + \frac{\gamma_1^2}{4}} \right] \quad Eq. 5.9\end{aligned}$$

where γ_1 is the damping rate of SiN membrane resonator, Ω_2 is the angular frequency of aluminium membrane resonator, f_p is the pump force.

| Cavity design | Cavity decay rate or damping rate | NEMS Al drum | Capacitive coupling strength (G) when distance at 500 nm |
|---------------------------|--|--|---|
| RLC microwave cavity [36] | $\kappa_{cavity,RLC}/2\pi \approx 61 \text{ MHz}$ | $\Omega_{m,Al}/2\pi \approx 3 \text{ MHz}$ | $G_{RLC} \approx \frac{\omega_c}{4\pi d} \approx 4.8 \text{ MHz/nm}$ |
| Phonon-cavity [93] | $\gamma_{cavity,SiN}/2\pi \approx 333 \text{ Hz}$ high stress SiN drum | $\Omega_{m,Al}/2\pi \approx 3 \text{ MHz}$ | $G_{phonon-cavity} \approx \frac{\Omega_1}{4\pi d} \approx 11.8 \text{ kHz/nm}$ |

This expression Eq.5.9 is in the similar form of the Eq. 5.3. Now, we can put some experimental parameters in both two expressions, in order to make a comparison. To do so, we choose capacitive coupling strengths in optomechanical system and phonon-cavity scheme to be the same, in order to compare the optomechanical damping effect between them. Fixing the capacitive coupling distance at 500 nm in both system, we take RLC microwave cavity with frequency of 4.8 GHz reported in [36] and phonon cavity (SiN drum) with frequency of 11.8 MHz reported in [93]. Therefore, optomechanical coupling strengths in optomechanical system is $G_{RLC} \approx 4.8 \text{ MHz/nm}$ and it is in phonon-cavity system is $G_{phonon-cavity} \approx 11.8 \text{ kHz/nm}$, whose values are far from each other. If getting the same optomechanical damping effect, we can compare the pump amplitude between in this cavity optomechanical system and this phonon cavity scheme. According to Eq.5.3, we take $\Gamma_{opt,RLC} \approx -n_c g_0^2 \cdot 4/\kappa$. Similarly, in phonon cavity scheme, we know $\Gamma_{opt,phonon-cavity} \approx -n_p g_0^2 \cdot 4/\gamma_1$. In addition, we suppose in both

system, the “cavity” is coupled to an aluminium drum resonator, with an effective mass of $4.41 \times 10^{-13} \text{ kg}$, resonance frequency of 3 MHz, damping rate of 333 Hz, coupling capacitance is $1.25 \times 10^{-14} \text{ F}$. If we want to reduce 5Hz from the mechanical damping rate in optomechanical system and phonon-cavity system respectively, $\Gamma_{opt}/2\pi = 5\text{Hz}$, it requires a pump amplitude to be $|\mu_{p,RLC}| \approx 3.816 \times 10^{-13}$ and $|\mu_{p,phonon-cavity}| \approx 7.315 \times 10^{-12}$, respectively. Different from the evaluated values of G , the required pump amplitudes are not far from each other. From this comparison, we could see that it is not reasonable to directly compare with values of coupling strength G between both systems, because both cavities are working in different frequency ranges and definitions of G rely on the resonance frequency of the cavity.

5.2 Experiment expectations

This thesis work has future expectations of experiments for building a phonon thermometer, which consists of a microwave cavity and a nanoelectromechanical oscillator. The basic principle of this phonon thermometer is to detect the thermal Brownian motion of the oscillator. The displacement driven by stochastic forces (Langevin forces), $\delta x = \frac{F \cdot Q}{k}$, depends on high quality factor (Q) and the mechanical spring constant (k) of the device. We suppose the mechanical resonator, having the small values of k and the large values of Q , will be perfect candidates.

Unfortunately, it is difficult to reach both ideal conditions. Our SiN membrane nanoelectromechanical resonators only bring advantages in the high Q. On the other hand, a microwave cavity is also important for the readout of the thermometer. First, a sideband resolved condition ($\kappa/(2\Omega_m) \ll 1$) is ideal for building optomechanical thermometer, as discussed above. Second, one must consider the coupling strength ($g = Gx_{ZPF}\sqrt{n_c}$), which indicates the sensitivity of the mechanical displacement in readout external circuits. The coupling capacitance between the movable element and the couple external circuit plays important role. The larger values of C_m requires the lower pump power for readout the same amount of the phonon occupation number, n_m . But, at the same time, the optomechanical back-action effects, optomechanical damping effects will not be negligible and have to be calibrated in order to readout the initial values of n_m , which is related to the real detected temperature.

5.3 Summary

In this chapter, a basic principle of such a kind of phonon thermometry, namely $\frac{1}{2\pi} \int S_x^\pm d\omega = k_B T_m = \hbar\Omega_m \cdot n_m$, is introduced, where k is the spring constant of the device and k_B is the Boltzmann constant. Besides, we also introduced the important optomechanical features, including optomechanical coupling strength, the optical damping effect. For the coupling strength, we made comparisons between two kinds of mechanical resonator design, the doubly-clamped beam and the drum. The capacitance actuation areas are discussed. Membrane drum has 100 times larger the capacitance than the doubly-clamped beam, allowing its thermal Brownian motion to be readout by relatively lower pump power. Besides, we also make comparisons between the optomechanical system and the phonon-cavity system, regarding to the optical damping effect, which helps us better understand the classic features of the optomechanics. In the final part, we also discussed the expectations of experimental design for building the optomechanical phonon-thermometer.

Chapter 6 Conclusion and outlook

In this Ph.D. thesis, main tasks are focused on the theory analysis of the SiN circular membrane in Chapter 2, critical nanofabrication processes of the SiN circular membrane in Chapter 3, the characterization and simulation of the SiN membrane resonator using SMM techniques in Chapter 4, and the discussions of microwave optomechanical thermometry in Chapter 5.

6.1 Conclusion

In this thesis work, we have studied membrane nanoelectromechanical resonators, consisting of a SiN membrane capacitively coupled to a suspended aluminium top gate. The device exhibits good mechanical properties at room temperature, high resonance frequency (MHz) and quality factor ($> 10^4$) under vacuum. It also offers large coupling capacitance, compared with conventional SiN doubly clamped nanobeam.

The design of the membrane nanomechanical resonator is special and can be modelled as an electrical component, a parallel plate capacitor. It gives an access to perform parametric amplifications in this device. Based on this unique device design, we demonstrated electromechanically induced transparency and amplification in a two-tone scheme, which allows to make an analogy to optomechanical system.

Before the nanofabrication, we use the finite element simulation method to optimize the device design, making reasonable trade-off between achieving low clamping losses and feasible fabrication process. Two critical nanofabrication steps, including the XeF_2 etch for releasing of the SiN membrane from silicon substrate and the reflow process for fabricating an aluminium top gate, have been elaborated. These discussions helped us for further developing/optimizing robust fabrication process to achieve SiN membrane resonators.

Besides using the aluminium top gate, SMM techniques, containing AFM-in-SEM equipment, have also been exploited to characterize mechanical properties of the membrane. This AFM-tip is able to be manipulated in X-Y-Z axes (about step Min. 1 nm and step Max. 10 μm) in a high vacuum chamber. In this part, the tip-membrane interaction has been simulated through finite element method, so as to help us for understanding the capacitance and electrostatic force behaviours. Then, the AFM-tip capacitively coupling with the SiN membrane resonator covered with a thin aluminium has been studied well. In particular, a double-tones driving scheme, one

sideband tone and the other probe tone, has also been used for experimentally demonstrating amplification and de-amplification in a mode coupling scheme. It is very promising for improving the readout sensitivity of signal from the AFM-tip, as the signal is amplified by using sideband pumping method. In addition, SMM techniques have the potential for extending to measuring other MEMS devices through adding electrostatic forces.

Considering the future work in developing optomechanical phonon thermometer, we have discussed the basic principle of the phonon thermometer based on our drum membrane nanoelectromechanical resonator, in optomechanical circuits. Both coupling strength and optical damping effects have also been analysed. The SiN membrane drum, comparing with the doubly clamped beam structures, has a 100-times larger capacitance, contributing to decrease 100-times the amount of pump power to the thermometry while reaching the same signal detecting gain, in optomechanical readout circuit. Besides, we also made comparisons between optomechanical system and the phonon-cavity system, which helps us to understand the classical features in optomechanics.

6.2 Outlook

This thesis work builds essential blocks for developing optomechanical phonon thermometer based on SiN membrane resonator in the future. So far, most of microwave cavities, used to couple with mechanical resonator, are fabricated with superconducting materials. They are therefore limited for the working temperature due to the transition temperature of superconducting materials. In the future work, we could expect to develop optomechanical thermometer through exploiting 3D cavity to couple with nanoelectromechanical resonator. As previous reports, 3D cavity can work well at both RT [61,180] and low temperatures [47]. It will allow to have a wide range of working temperature. Besides, it is interesting to study several kinds of issues by using this 3D cavity optomechanical system through benefiting from large coupling strength, such as exploring nonlinear coupling in optomechanical circuits [183] and two-level systems [184]. The specific issues to be solved for building such a thermometer can be either theoretical analysis or experimental measurement. For instance, we can propose the following problems, including (i) device design and fabrication process, and (ii) characterization. To make a reliable thermometer, some future tips can be focused on:

(i) device design and fabrication process. The large capacitance between the top gate and the membrane may be reduced when the number and size of holes are increased. But, these holes

are necessary to be etched successfully the underneath silicon and release SiN membrane. A compromise between feasible holes pattern and successful releasing of SiN membrane must also be determined. The capacitive distance between the membrane and top gate can be decreased in order to increase the coupling capacitance. However, decreasing below 500 nm needs efforts to investigate the fine control of the distance, avoiding the sticking between both objects.

In order to have proper releasing of SiN membrane, the XeF_2 etch process should be optimized continuously. In our fabrication process, a triangle pattern has been designed for estimating whether a membrane is released well or not. Nevertheless, the XeF_2 etching rate highly depends on the exposure area of the pattern. Further optimization for etching needs to be deeply understood. So as to optimize the XeF_2 etching, a future work has been considered that it contains several holes on the membrane with different diameters for observing the effect of XeF_2 etching. In this case, the etch time can be evaluated for proper releasing of SiN membrane in order to achieve a proper etching process. Furthermore, the distance between neighbouring holes can also be changed for estimating the XeF_2 etch procedure. This etch optimization can also be used in other topological pattern applications, such as heat conduction research with ordered or disordered holes pattern [185,186].

(ii) characterization. The measurement of temperature for such a device requires to determine the parameters that impact the measurement accuracy. Careful characterization needed for the NEMS may be performed to better understand the relationship between the device properties and the temperature measurement. Moreover, the measured temperature is related to the SiN membrane as it has high quality factor. Investigating how the SiN membrane may be thermally connected to the detection of the number of phonon carried by the membrane is critical so as to usefully measure its physical temperature.

Besides, when characterizing the membrane through the metallic AFM-tip, we considered whether the coupling capacitance between the tip and membrane could be analytically calculated. We tried to find the calculation method of the coupling capacitance. We found several papers [187,188] that show adjustable capacitors with coaxial cone electrodes. The old ideas motivated us for calculating the adjustable capacitor between the tip and membrane, as the tip can be seen as a simple cone. There are three steps to be proposed for calculating the coupling capacitance, including (I) setup design and calculation, (II) comsol simulation, and (III) characterization. To tackle the problem, some future tips may be focused on:

(I) setup design and calculation. The sketch of the coupling capacitance between the tip and membrane shall be proposed based on the interactions between the both. According to prior reports [187,188], they use the coaxial cone electrodes to calculate the capacitance, as the active surfaces between the two coaxial cone electrodes are parallel in the geometry structure. However, in our case, we have no parallel electrodes, containing a metallic tip suspended on the top of a circular conductive membrane. It is obvious that the electric field lines between the two electrodes are not uniform along the electrode. This points out a future research direction that requires much efforts to solve. In addition, the calculation of the capacitance may be conducted once the distribution of electric field lines determined in physics. Based on active actuation areas (S_f) estimated in the formalism of effective distribution of electric fields, Gauss's law, $\int \mathbf{D}d\mathbf{S} = \varepsilon E_{electricfield} S_f = Q_{charge}$, can be applied in order to deduce the relationship between electric field ($E_{electricfield}$) and charge (Q_{charge}). Using the electric field relationship, we can deduce the potential difference (ΔV), because the integral of the potential difference is directly related to the electric field ($E_{electricfield}$). Thus, using the definition of the capacitance, namely $C = \frac{Q_{charge}}{\Delta V}$, we can derive the final capacitance value. In this part, there still exists several problems that limit the current calculation of the capacitance: first, the tilt angle θ of the tip (see section 4.2.1); second, the consideration of apex of the tip [189]; third, the boundary condition.

(II) comsol simulation. Based on the setup design and calculation, we can use the simulation process (see section 4.2.1) to obtain the capacitance value. In order to approximate the real capacitance value, we have to take same parameters from the setup design and calculation into account.

(III) characterization. After carrying out steps (I) and (II), it may be applied to the practical characterization. For instance, in future applications, such as imaging af/fF capacitance [153,157], the calibration of the capacitance is very important, because of impedance from parasitic capacitance possibly affecting the measurement precision [161]. It is feasible for our calculation of the tip-membrane modelling to help to precisely calibrate the capacitance used for the applications.

List of publications

Peer-reviewed journals:

Hao Xu, Srisaran Venkatachalam, Christophe Boyaval, Pascal Tilmant, Francois Vaurette, Yves Deblock, Didier Theron, Xin Zhou. “Fabrication of silicon nitride membrane nanoelectromechanical resonator”, *Microelectronic Engineering*, 280, 112064 (2023)

Alok Pokharel, Hao Xu, Srisaran Venkatachalam, Eddy Collin, and Xin Zhou. “Coupling Capacitively Distinct Mechanical Resonators for Room-Temperature Phonon-Cavity Electromechanics”, *Nano Letters*, 22(18), 7351-7357 (2022)

Xin Zhou, Srisaran Venkatachalam, Ronghua Zhou, Hao Xu, Alok Pokharel, Andrew Fefferman, Mohammed Zaknونة, and Eddy Collin. “High-Q silicon nitride drum resonators strongly coupled to gates”, *Nano Letters*, 21(13), 5738-5744 (2021)

International/national conferences:

Xin Zhou, Hao Xu, Didier Theron, Sophie Eliet, Christophe Boyaval, Pascal Tilmant, Francois Vaurette, Dmitri Yarekha, Jeanmarcel Houpin. “Scanning microwave microscopy for investigations of mechanical vibrations and mode coupling”, *Frontiers of Nanomechanical Systems (FNS) workshop*, Delft, The Netherlands, June (2023) (poster)

Hao Xu, Didier Theron, Sophie Eliet, and Xin Zhou. “Scanning microwave microscopy for detecting mechanical vibrations of silicon nitride membranes”, *7th Annual Meeting of the GDR MecaQ quantum optomechanics & nanomechanics*, Bordeaux, France, October (2022) (poster)

Bibliography

- [1] S.R.A. Ruth, V.R. Feig, H. Tran, Z. Bao, Microengineering Pressure Sensor Active Layers for Improved Performance, *Adv. Funct. Mater.* 30 (2020) 2003491.
- [2] A. Koh, D. Kang, Y. Xue, S. Lee, R.M. Pielak, J. Kim, T. Hwang, S. Min, A. Banks, P. Bastien, A soft, wearable microfluidic device for the capture, storage, and colorimetric sensing of sweat, *Science Translational Medicine.* 8 (2016) 366ra165-366ra165.
- [3] R. Kononchuk, J. Cai, F. Ellis, R. Thevamaran, T. Kottos, Exceptional-point-based accelerometers with enhanced signal-to-noise ratio, *Nature.* 607 (2022) 697–702.
- [4] J.C. Howell, M. Kahn, E. Grynszpan, Z.R. Cohen, S. Residori, U. Bortolozzo, Doppler Gyroscopes: Frequency vs Phase Estimation, *Phys. Rev. Lett.* 129 (2022) 113901.
- [5] A. Sharaf, A. Nasr, A. Elshurafa, M. Serry, Design analysis and simulation of a digital RF MEMS varactor with high capacitive ratio, *Microsystem Technologies.* 28 (2022) 1831–1844.
- [6] V.P. Adiga, B. Ilic, R.A. Barton, I. Wilson-Rae, H.G. Craighead, J.M. Parpia, Modal dependence of dissipation in silicon nitride drum resonators, *Appl. Phys. Lett.* 99 (2011) 253103.
- [7] Y. Tsururyan, A. Barg, E.S. Polzik, A. Schliesser, Ultracoherent nanomechanical resonators via soft clamping and dissipation dilution, *Nature Nanotech.* 12 (2017) 776–783.
- [8] E. Romero, V.M. Valenzuela, A.R. Kermany, L. Sementilli, F. Iacopi, W.P. Bowen, Engineering the Dissipation of Crystalline Micromechanical Resonators, *Phys. Rev. Applied.* 13 (2020) 044007.
- [9] J.D. Teufel, T. Donner, D. Li, J.W. Harlow, M.S. Allman, K. Cicak, A.J. Sirois, J.D. Whittaker, K.W. Lehnert, R.W. Simmonds, Sideband cooling of micromechanical motion to the quantum ground state, *Nature.* 475 (2011) 359–363.
- [10] S. Kotler, G.A. Peterson, F. Lecocq, K. Cicak, A. Kwiatkowski, S. Geller, S. Glancy, E. Knill, R.W. Simmonds, J. Aumentado, J.D. Teufel, Direct observation of deterministic macroscopic entanglement, *Science.* 372 (2021) 622–625.
- [11] O. Arcizet, P.-F. Cohadon, T. Briant, M. Pinard, A. Heidmann, J.-M. Mackowski, C. Michel, L. Pinard, O. François, L. Rousseau, High-Sensitivity Optical Monitoring of a Micromechanical Resonator with a Quantum-Limited Optomechanical Sensor, *Phys. Rev. Lett.* 97 (2006) 133601.

- [12] A. Beccari, D.A. Visani, S.A. Fedorov, M.J. Berekhi, V. Boureau, N.J. Engelsen, T.J. Kippenberg, Strained crystalline nanomechanical resonators with quality factors above 10 billion, *Nat. Phys.* 18 (2022) 436–441.
- [13] D. Hälg, T. Gisler, E.C. Langman, S. Misra, O. Zilberberg, A. Schliesser, C.L. Degen, A. Eichler, Strong Parametric Coupling between Two Ultracoherent Membrane Modes, *Phys. Rev. Lett.* 128 (2022) 094301.
- [14] J. Guo, S. Gröblacher, Integrated optical-readout of a high-Q mechanical out-of-plane mode, *Light Sci Appl.* 11 (2022) 282.
- [15] X. Lu, J.Y. Lee, Q. Lin, Silicon carbide zipper photonic crystal optomechanical cavities, *Appl. Phys. Lett.* 116 (2020) 221104.
- [16] D.M. Lukin, C. Dory, M.A. Guidry, K.Y. Yang, S.D. Mishra, R. Trivedi, M. Radulaski, S. Sun, D. Vercruyse, G.H. Ahn, J. Vučković, 4H-silicon-carbide-on-insulator for integrated quantum and nonlinear photonics, *Nat. Photonics.* 14 (2020) 330–334.
- [17] P. Weber, J. Güttinger, A. Noury, J. Vergara-Cruz, A. Bachtold, Force sensitivity of multilayer graphene optomechanical devices, *Nat Commun.* 7 (2016) 12496.
- [18] J. Güttinger, A. Noury, P. Weber, A.M. Eriksson, C. Lagoin, J. Moser, C. Eichler, A. Wallraff, A. Isacsson, A. Bachtold, Energy-dependent path of dissipation in nanomechanical resonators, *Nature Nanotech.* 12 (2017) 631–636.
- [19] A.W. Barnard, M. Zhang, G.S. Wiederhecker, M. Lipson, P.L. McEuen, Real-time vibrations of a carbon nanotube, *Nature.* 566 (2019) 89–93.
- [20] V. Sazonova, Y. Yaish, H. Üstünel, D. Roundy, T.A. Arias, P.L. McEuen, A tunable carbon nanotube electromechanical oscillator, *Nature.* 431 (2004) 284–287.
- [21] K. Cao, S. Feng, Y. Han, L. Gao, T. Hue Ly, Z. Xu, Y. Lu, Elastic straining of free-standing monolayer graphene, *Nat Commun.* 11 (2020) 284.
- [22] A. Falin, Q. Cai, E.J.G. Santos, D. Scullion, D. Qian, R. Zhang, Z. Yang, S. Huang, K. Watanabe, T. Taniguchi, M.R. Barnett, Y. Chen, R.S. Ruoff, L.H. Li, Mechanical properties of atomically thin boron nitride and the role of interlayer interactions, *Nat Commun.* 8 (2017) 15815.
- [23] J.-F. Faure, Aluminium based alloy with a high Young's modulus and high mechanical strength, US patent no. 5047092 (1991).
- [24] A. Khan, J. Philip, P. Hess, Young's modulus of silicon nitride used in scanning force microscope cantilevers, *Journal of Applied Physics.* 95 (2004) 1667–1672.
- [25] J. Kim, D. Cho, R.S. Muller, Why is (111) silicon a better mechanical material for MEMS?, in: Springer, 2001: pp. 662–665.

- [26] O. Pabst, M. Schiffer, E. Obermeier, T. Tekin, K.D. Lang, H.-D. Ngo, Measurement of Young's modulus and residual stress of thin SiC layers for MEMS high temperature applications, *Microsystem Technologies*. 18 (2012) 945–953.
- [27] H. Ehrenreich, H.R. Philipp, B. Segall, Optical Properties of Aluminum, *Phys. Rev.* 132 (1963) 1918–1928.
- [28] N. Tavakoli, R. Spalding, A. Lambertz, P. Koppejan, G. Gkantzounis, C. Wan, R. Röhrich, E. Kontoleta, A.F. Koenderink, R. Sapienza, M. Florescu, E. Alarcon-Llado, Over 65% Sunlight Absorption in a 1 μm Si Slab with Hyperuniform Texture, *ACS Photonics*. 9 (2022) 1206–1217.
- [29] J. Steinlechner, C. Krüger, I.W. Martin, A. Bell, J. Hough, H. Kaufer, S. Rowan, R. Schnabel, S. Steinlechner, Optical absorption of silicon nitride membranes at 1064 nm and at 1550 nm, *Phys. Rev. D*. 96 (2017) 022007.
- [30] G. Colston, M. Myronov, Controlling the optical properties of monocrystalline 3C-SiC heteroepitaxially grown on silicon at low temperatures, *Semicond. Sci. Technol.* 32 (2017) 114005.
- [31] S.-E. Zhu, S. Yuan, G.C.A.M. Janssen, Optical transmittance of multilayer graphene, *Europhysics Letters*. 108 (2014) 17007.
- [32] A. Soltani, P. Thévenin, A. Bath, Optical properties of boron nitride thin films deposited by microwave PECVD, *Materials Science and Engineering: B*. 82 (2001) 170–172.
- [33] D. Golla, K. Chattrakun, K. Watanabe, T. Taniguchi, B.J. LeRoy, A. Sandhu, Optical thickness determination of hexagonal boron nitride flakes, *Applied Physics Letters*. 102 (2013) 161906.
- [34] X. Song, M. Oksanen, J. Li, P.J. Hakonen, M.A. Sillanpää, Graphene Optomechanics Realized at Microwave Frequencies, *Phys. Rev. Lett.* (2014) 5.
- [35] X. Song, M. Oksanen, M.A. Sillanpää, H.G. Craighead, J.M. Parpia, P.J. Hakonen, Stamp Transferred Suspended Graphene Mechanical Resonators for Radio Frequency Electrical Readout, *Nano Lett.* 12 (2012) 198–202.
- [36] X. Zhou, S. Venkatachalam, R. Zhou, H. Xu, A. Pokharel, A. Fefferman, M. Zaknune, E. Collin, High- Q Silicon Nitride Drum Resonators Strongly Coupled to Gates, *Nano Lett.* 21 (2021) 5738–5744.
- [37] B.M. Zwickl, W.E. Shanks, A.M. Jayich, C. Yang, A.C. Bleszynski Jayich, J.D. Thompson, J.G.E. Harris, High quality mechanical and optical properties of commercial silicon nitride membranes, *Appl. Phys. Lett.* 92 (2008) 103125.

- [38] H. Miura, H. Ohta, N. Okamoto, T. Kaga, Crystallization-induced stress in silicon thin films, *Applied Physics Letters*. 60 (1992) 2746–2748.
- [39] L. Tong, M. Mehregany, L.G. Matus, Mechanical properties of 3C silicon carbide, *Applied Physics Letters*. 60 (1992) 2992–2994.
- [40] C. Lee, X. Wei, J.W. Kysar, J. Hone, Measurement of the elastic properties and intrinsic strength of monolayer graphene, *Science*. 321 (2008) 385–388.
- [41] V.-T. Pham, T.-H. Fang, Mechanical and thermal characterizations of nanoporous two-dimensional boron nitride membranes, *Sci Rep*. 12 (2022) 6306.
- [42] R. De Alba, F. Massel, I.R. Storch, T.S. Abhilash, A. Hui, P.L. McEuen, H.G. Craighead, J.M. Parpia, Tunable phonon-cavity coupling in graphene membranes, *Nature Nanotech*. 11 (2016) 741–746.
- [43] I. Sánchez Arribas, T. Taniguchi, K. Watanabe, E.M. Weig, Radiation Pressure Backaction on a Hexagonal Boron Nitride Nanomechanical Resonator, *Nano Lett*. 23 (2023) 6301–6307.
- [44] L.Y. Beliaev, E. Shkondin, A.V. Lavrinenko, O. Takayama, Optical, structural and composition properties of silicon nitride films deposited by reactive radio-frequency sputtering, low pressure and plasma-enhanced chemical vapor deposition, *Thin Solid Films*. 763 (2022) 139568.
- [45] E. Cianci, F. Pirola, V. Foglietti, Analysis of stress and composition of silicon nitride thin films deposited by electron cyclotron resonance plasma-enhanced chemical vapor deposition for microfabrication processes, *Journal of Vacuum Science & Technology B: Microelectronics and Nanometer Structures Processing, Measurement, and Phenomena*. 23 (2005) 168–172.
- [46] T. Faust, P. Krenn, S. Manus, J.P. Kotthaus, E.M. Weig, Microwave cavity-enhanced transduction for plug and play nanomechanics at room temperature, *Nat Commun*. 3 (2012) 728.
- [47] M. Yuan, V. Singh, Y.M. Blanter, G.A. Steele, Large cooperativity and microkelvin cooling with a three-dimensional optomechanical cavity, *Nat Commun*. 6 (2015) 8491.
- [48] L. Hilico, J. Courty, C. Fabre, E. Giacobino, I. Abram, J. Oudar, Squeezing with χ (3) materials, *Applied Physics B*. 55 (1992) 202–209.
- [49] D. Vitali, S. Gigan, A. Ferreira, H. Böhm, P. Tombesi, A. Guerreiro, V. Vedral, A. Zeilinger, M. Aspelmeyer, Optomechanical entanglement between a movable mirror and a cavity field, *Phys. Rev. Lett*. 98 (2007) 030405.

- [50] M. Yuksel, E. Orhan, C. Yanik, A.B. Ari, A. Demir, M.S. Hanay, Nonlinear Nanomechanical Mass Spectrometry at the Single-Nanoparticle Level, *Nano Lett.* 19 (2019) 3583–3589.
- [51] S. Sbarra, L. Waquier, S. Suffit, A. Lemaître, I. Favero, Multimode Optomechanical Weighting of a Single Nanoparticle, *Nano Lett.* 22 (2022) 710–715.
- [52] Y.-T. Yang, C. Callegari, X. Feng, K.L. Ekinici, M.L. Roukes, Zeptogram-scale nanomechanical mass sensing, *Nano Letters.* 6 (2006) 583–586.
- [53] H.J. Mamin, D. Rugar, Sub-attoNewton force detection at millikelvin temperatures, *Appl. Phys. Lett.* 79 (2001) 3358–3360.
- [54] S.S. Verbridge, D.F. Shapiro, H.G. Craighead, J.M. Parpia, Macroscopic Tuning of Nanomechanics: Substrate Bending for Reversible Control of Frequency and Quality Factor of Nanostring Resonators, *Nano Lett.* 7 (2007) 1728–1735.
- [55] J.D. Teufel, J.W. Harlow, C.A. Regal, K.W. Lehnert, Dynamical Backaction of Microwave Fields on a Nanomechanical Oscillator, *Phys. Rev. Lett.* 101 (2008) 197203.
- [56] D. Hoch, X. Yao, M. Poot, Geometric Tuning of Stress in Predisplaced Silicon Nitride Resonators, *Nano Lett.* 22 (2022) 4013–4019.
- [57] T. Gisler, M. Helal, D. Sabonis, U. Grob, M. Héritier, C.L. Degen, A.H. Ghadimi, A. Eichler, Soft-Clamped Silicon Nitride String Resonators at Millikelvin Temperatures, *Phys. Rev. Lett.* 129 (2022) 104301.
- [58] Y. Seis, T. Capelle, E. Langman, S. Saarinen, E. Planz, A. Schliesser, Ground state cooling of an ultracoherent electromechanical system, *Nat Commun.* 13 (2022) 1507.
- [59] M.J. Beryhi, A. Beccari, R. Groth, S.A. Fedorov, A. Arabmoheghi, T.J. Kippenberg, N.J. Engelsen, Hierarchical tensile structures with ultralow mechanical dissipation, *Nat Commun.* 13 (2022) 3097.
- [60] M.J. Beryhi, A. Arabmoheghi, A. Beccari, S.A. Fedorov, G. Huang, T.J. Kippenberg, N.J. Engelsen, Perimeter Modes of Nanomechanical Resonators Exhibit Quality Factors Exceeding 10^9 at Room Temperature, *Phys. Rev. X.* 12 (2022) 021036.
- [61] A.T. Le, A. Brioussel, E.M. Weig, Room temperature cavity electromechanics in the sideband-resolved regime, *Journal of Applied Physics.* 130 (2021) 014301.
- [62] F. Yang, M. Fu, B. Bosnjak, R.H. Blick, Y. Jiang, E. Scheer, Mechanically Modulated Sideband and Squeezing Effects of Membrane Resonators, *Phys. Rev. Lett.* 127 (2021) 184301.
- [63] D. Høj, F. Wang, W. Gao, U.B. Hoff, O. Sigmund, U.L. Andersen, Ultra-coherent nanomechanical resonators based on inverse design, *Nat Commun.* 12 (2021) 5766.

- [64] E. Ivanov, T. Capelle, M. Rosticher, J. Palomo, T. Briant, P.-F. Cohadon, A. Heidmann, T. Jacqmin, S. Deléglise, Edge mode engineering for optimal ultracoherent silicon nitride membranes, *Appl. Phys. Lett.* 117 (2020) 254102.
- [65] J.M. Fink, M. Kalaei, R. Norte, A. Pitanti, O. Painter, Efficient microwave frequency conversion mediated by a photonics compatible silicon nitride nanobeam oscillator, *Quantum Sci. Technol.* 5 (2020) 034011.
- [66] P. Sadeghi, A. Demir, L.G. Villanueva, H. Kähler, S. Schmid, Frequency fluctuations in nanomechanical silicon nitride string resonators, *Phys. Rev. B.* 102 (2020) 214106.
- [67] P. Sadeghi, M. Tanzer, S.L. Christensen, S. Schmid, Influence of clamp-widening on the quality factor of nanomechanical silicon nitride resonators, *Journal of Applied Physics.* 126 (2019) 165108.
- [68] R. St-Gelais, S. Bernard, C. Reinhardt, J.C. Sankey, Swept-Frequency Drumhead Optomechanical Resonators, *ACS Photonics.* 6 (2019) 525–530.
- [69] F. Yang, F. Rochau, J.S. Huber, A. Briussel, G. Rastelli, E.M. Weig, E. Scheer, Spatial Modulation of Nonlinear Flexural Vibrations of Membrane Resonators, *Phys. Rev. Lett.* 122 (2019) 154301.
- [70] S.A. Fedorov, V. Sudhir, R. Schilling, H. Schütz, D.J. Wilson, T.J. Kippenberg, Evidence for structural damping in a high-stress silicon nitride nanobeam and its implications for quantum optomechanics, *Physics Letters A.* 382 (2018) 2251–2255.
- [71] M. Pernpeintner, P. Schmidt, D. Schwienbacher, R. Gross, H. Huebl, Frequency Control and Coherent Excitation Transfer in a Nanostring-resonator Network, *Phys. Rev. Applied.* 10 (2018) 034007.
- [72] A.H. Ghadimi, S.A. Fedorov, N.J. Engelsen, M.J. Breyhi, R. Schilling, D.J. Wilson, T.J. Kippenberg, Elastic strain engineering for ultralow mechanical dissipation, *Science.* 360 (2018) 764–768.
- [73] A.H. Ghadimi, D.J. Wilson, T.J. Kippenberg, Radiation and Internal Loss Engineering of High-Stress Silicon Nitride Nanobeams, *Nano Lett.* 17 (2017) 3501–3505.
- [74] O. Maillet, F. Vavrek, A.D. Fefferman, O. Bourgeois, E. Collin, Classical decoherence in a nanomechanical resonator, *New J. Phys.* 18 (2016) 073022.
- [75] J.M. Fink, M. Kalaei, A. Pitanti, R. Norte, L. Heinzle, M. Davanço, K. Srinivasan, O. Painter, Quantum electromechanics on silicon nitride nanomembranes, *Nat Commun.* 7 (2016) 12396.
- [76] R.A. Norte, J.P. Moura, S. Gröblacher, Mechanical Resonators for Quantum Optomechanics Experiments at Room Temperature, *Phys. Rev. Lett.* 116 (2016) 147202.

- [77] M. Yuan, M.A. Cohen, G.A. Steele, Silicon nitride membrane resonators at millikelvin temperatures with quality factors exceeding 10^8 , *Appl. Phys. Lett.* 107 (2015) 263501.
- [78] Y.S. Patil, S. Chakram, L. Chang, M. Vengalattore, Thermomechanical Two-Mode Squeezing in an Ultrahigh- Q Membrane Resonator, *Phys. Rev. Lett.* 115 (2015) 017202.
- [79] X. Zhou, D. Cattiaux, R.R. Gazizulin, A. Luck, O. Maillet, T. Crozes, J.-F. Motte, O. Bourgeois, A. Fefferman, E. Collin, On-chip Thermometry for Microwave Optomechanics Implemented in a Nuclear Demagnetization Cryostat, *Phys. Rev. Applied.* 12 (2019) 044066.
- [80] A. Barg, Optomechanics with Soft-clamped Silicon Nitride Membranes and Carrier-mediated Forces in Coupled Quantum Wells, Ph.D. dissertation, University of Copenhagen, Faculty of Science, Niels Bohr Institute, Danish Center for Quantum Optics (2018).
- [81] H. Xu, S. Venkatachalam, C. Boyaval, P. Tilmant, F. Vaurette, Y. Deblock, D. Theron, X. Zhou, Fabrication of silicon nitride membrane nanoelectromechanical resonator, *Microelectronic Engineering.* 280 (2023) 112064.
- [82] G. Nicollini, D. Devecchi, MEMS capacitive microphones: Acoustical, electrical, and hidden thermal-related issues, *IEEE Sensors Journal.* 18 (2018) 5386–5394.
- [83] B.-H. Kim, H.-S. Lee, Acoustical-Thermal Noise in a Capacitive MEMS Microphone, *IEEE Sensors J.* 15 (2015) 6853–6860.
- [84] K.B. Balavalad, B. Sheeparamatti, A critical review of MEMS capacitive pressure sensors, *Sensors & Transducers.* 187 (2015) 120.
- [85] J.B. Clark, F. Lecocq, R.W. Simmonds, J. Aumentado, J.D. Teufel, Observation of strong radiation pressure forces from squeezed light on a mechanical oscillator, *Nature Phys.* 12 (2016) 683–687.
- [86] J.D. Teufel, D. Li, M.S. Allman, K. Cicak, A.J. Sirois, J.D. Whittaker, R.W. Simmonds, Circuit cavity electromechanics in the strong-coupling regime, *Nature.* 471 (2011) 204–208.
- [87] V.P. Adiga, B. Ilic, R.A. Barton, I. Wilson-Rae, H.G. Craighead, J.M. Parpia, Approaching intrinsic performance in ultra-thin silicon nitride drum resonators, *Journal of Applied Physics.* 112 (2012) 064323.
- [88] L.D. Tóth, N.R. Bernier, A. Nunnenkamp, A.K. Feofanov, T.J. Kippenberg, A dissipative quantum reservoir for microwave light using a mechanical oscillator, *Nature Phys.* 13 (2017) 787–793.

- [89] N.R. Bernier, L.D. Tóth, A. Koottandavida, M.A. Ioannou, D. Malz, A. Nunnenkamp, A.K. Feofanov, T.J. Kippenberg, Nonreciprocal reconfigurable microwave optomechanical circuit, *Nat Commun.* 8 (2017) 604.
- [90] A. Youssefi, S. Kono, A. Bancora, M. Chegnizadeh, J. Pan, T. Vovk, T.J. Kippenberg, Topological lattices realized in superconducting circuit optomechanics, *Nature.* 612 (2022) 666–672.
- [91] X. Ji, S. Roberts, M. Corato-Zanarella, M. Lipson, Methods to achieve ultra-high quality factor silicon nitride resonators, *APL Photonics.* 6 (2021) 071101.
- [92] A. Eichler, Ultra-high-Q nanomechanical resonators for force sensing, *Mater. Quantum. Technol.* 2 (2022) 043001.
- [93] A. Pokharel, H. Xu, S. Venkatachalam, E. Collin, X. Zhou, Coupling Capacitively Distinct Mechanical Resonators for Room-Temperature Phonon-Cavity Electromechanics, *Nano Letters.* 22 (2022) 7351–7357.
- [94] B. Legrand, D. Ducatteau, D. Théron, B. Walter, H. Tanbakuchi, Detecting response of microelectromechanical resonators by microwave reflectometry, *Applied Physics Letters.* 103 (2013) 053124.
- [95] B. Legrand, J.-P. Salvetat, B. Walter, M. Faucher, D. Théron, J.-P. Aimé, Multi-MHz micro-electro-mechanical sensors for atomic force microscopy, *Ultramicroscopy.* 175 (2017) 46–57.
- [96] T. Dinh, H.-P. Phan, A. Qamar, P. Woodfield, N.-T. Nguyen, D.V. Dao, Thermoresistive effect for advanced thermal sensors: Fundamentals, design considerations, and applications, *Journal of Microelectromechanical Systems.* 26 (2017) 966–986.
- [97] T. Dinh, H.-P. Phan, D.V. Dao, P. Woodfield, A. Qamar, N.-T. Nguyen, Graphite on paper as material for sensitive thermoresistive sensors, *Journal of Materials Chemistry C.* 3 (2015) 8776–8779.
- [98] N. Kawamoto, M.-S. Wang, X. Wei, D.-M. Tang, Y. Murakami, D. Shindo, M. Mitome, D. Golberg, Local temperature measurements on nanoscale materials using a movable nanothermocouple assembled in a transmission electron microscope, *Nanotechnology.* 22 (2011) 485707.
- [99] S. Elyamny, E. Dimaggio, S. Magagna, D. Narducci, G. Pennelli, High power thermoelectric generator based on vertical silicon nanowires, *Nano Letters.* 20 (2020) 4748–4753.
- [100] C.D. Brites, P.P. Lima, N.J. Silva, A. Millán, V.S. Amaral, F. Palacio, L.D. Carlos, Thermometry at the nanoscale, *Nanoscale.* 4 (2012) 4799–4829.

- [101] W.-S. Chang, S. Link, Enhancing the sensitivity of single-particle photothermal imaging with thermotropic liquid crystals, *The Journal of Physical Chemistry Letters*. 3 (2012) 1393–1399.
- [102] J. Li, S. Gauzia, S.-T. Wu, High temperature-gradient refractive index liquid crystals, *Optics Express*. 12 (2004) 2002–2010.
- [103] P.M. Morse, CHAPTER V: MEMBRANES AND PLATES, 19. the circular membrane. Acoustical Society of America, American Institute of Physics, Vibration and sound, McGraw-Hill New York (1936).
- [104] M. Bao, Analysis and design principles of MEMS devices, Chapter 2: mechanics of beam and diaphragm structures, Elsevier (2005).
- [105] B.D. Hauer, C. Doolin, K.S.D. Beach, J.P. Davis, A general procedure for thermomechanical calibration of nano/micro-mechanical resonators, *Annals of Physics*. 339 (2013) 181–207.
- [106] P. Moon, D.E. Spencer, *Field theory handbook: including coordinate systems, differential equations and their solutions*, Springer (2012).
- [107] G. Anetsberger, O. Arcizet, Q.P. Unterreithmeier, R. Rivière, A. Schliesser, E.M. Weig, J.P. Kotthaus, T.J. Kippenberg, Near-field cavity optomechanics with nanomechanical oscillators, *Nature Physics*. 5 (2009) 909–914.
- [108] A.K. Naik, M. Hanay, W. Hiebert, X. Feng, M.L. Roukes, Towards single-molecule nanomechanical mass spectrometry, *Nature Nanotechnology*. 4 (2009) 445–450.
- [109] S. Gigan, H. Böhm, M. Paternostro, F. Blaser, G. Langer, J. Hertzberg, K.C. Schwab, D. Bäuerle, M. Aspelmeyer, A. Zeilinger, Self-cooling of a micromirror by radiation pressure, *Nature*. 444 (2006) 67–70.
- [110] X. Zhou, D. Cattiaux, D. Theron, E. Collin, Electric circuit model of microwave optomechanics, *Journal of Applied Physics*. 129 (2021) 114502.
- [111] D. Bothner, S. Yanai, A. Iniguez-Rabago, M. Yuan, Ya.M. Blanter, G.A. Steele, Cavity electromechanics with parametric mechanical driving, *Nat Commun*. 11 (2020) 1589.
- [112] D. Rugar, P. Grütter, Mechanical parametric amplification and thermomechanical noise squeezing, *Physical Review Letters*. 67 (1991) 699.
- [113] X. Zhou, V. Schmitt, P. Bertet, D. Vion, W. Wustmann, V. Shumeiko, D. Esteve, High-gain weakly nonlinear flux-modulated Josephson parametric amplifier using a SQUID array, *Physical Review B*. 89 (2014) 214517.

- [114] R.J. Dolleman, P. Belardinelli, S. Hourii, H.S.J. van der Zant, F. Alijani, P.G. Steeneken, High-Frequency Stochastic Switching of Graphene Resonators Near Room Temperature, *Nano Lett.* 19 (2019) 1282–1288.
- [115] S. Venkatachalam, X. Zhou, Effects of stochastic forces on the nonlinear behaviour of a silicon nitride membrane nanoelectromechanical resonator, *Nanotechnology.* 34 (2023) 215202.
- [116] M. Aspelmeyer, T.J. Kippenberg, F. Marquardt, Cavity optomechanics, *Rev. Mod. Phys.* 86 (2014) 1391–1452.
- [117] F. Hocke, X. Zhou, A. Schliesser, T.J. Kippenberg, H. Huebl, R. Gross, Electromechanically induced absorption in a circuit nano-electromechanical system, *New J. Phys.* 14 (2012) 123037.
- [118] I. Mahboob, K. Nishiguchi, H. Okamoto, H. Yamaguchi, Phonon-cavity electromechanics, *Nature Phys.* 8 (2012) 387–392.
- [119] S. Weis, R. Rivière, S. Deléglise, E. Gavartin, O. Arcizet, A. Schliesser, T.J. Kippenberg, Optomechanically induced transparency, *Science.* 330 (2010) 1520–1523.
- [120] S. Kumar, D. Cattiaux, E. Collin, A. Fefferman, X. Zhou, Microwave optomechanically induced transparency and absorption between 250 and 450 mK, *Journal of Low Temperature Physics.* 210 (2023) 562–572.
- [121] H.B. Chan, M.I. Dykman, C. Stambaugh, Paths of Fluctuation Induced Switching, *Phys. Rev. Lett.* 100 (2008) 130602.
- [122] J.S. Ochs, G. Rastelli, M. Seitner, M.I. Dykman, E.M. Weig, Resonant nonlinear response of a nanomechanical system with broken symmetry, *Phys. Rev. B.* 104 (2021) 155434.
- [123] D.N. Guerra, A.R. Bulsara, W.L. Ditto, S. Sinha, K. Murali, P. Mohanty, A Noise-Assisted Reprogrammable Nanomechanical Logic Gate, *Nano Lett.* 10 (2010) 1168–1171.
- [124] G. Dion, S. Mejaouri, J. Sylvestre, Reservoir computing with a single delay-coupled non-linear mechanical oscillator, *Journal of Applied Physics.* 124 (2018).
- [125] S. Cho, S.U. Cho, M. Jo, J. Suh, H.C. Park, S.G. Kim, S.-B. Shim, Y.D. Park, Strong Two-Mode Parametric Interaction and Amplification in a Nanomechanical Resonator, *Phys. Rev. Applied.* 9 (2018) 064023.
- [126] M. Altissimo, E-beam lithography for micro-/nanofabrication, *Biomicrofluidics.* 4 (2010) 026503.
- [127] M.M. Greve, B. Holst, Optimization of an electron beam lithography instrument for fast, large area writing at 10 kV acceleration voltage, *Journal of Vacuum Science &*

- Technology B, Nanotechnology and Microelectronics: Materials, Processing, Measurement, and Phenomena. 31 (2013) 043202.
- [128] I. Haller, M. Hatzakis, R. Srinivasan, High-resolution Positive Resists for Electron-beam Exposure, *IBM Journal of Research and Development*. 12 (1968) 251–256.
- [129] M. Hatzakis, Electron Resists for Microcircuit and Mask Production, *J. Electrochem. Soc.* 116 (1969) 1033.
- [130] Y. Nakamura, S. Takechi, Y. Tsurunaga, K. Fujino, Y. Ban, Resist characteristics of α -methylstyrene-methyl α -chloroacrylate copolymers. *Polym. Preprints* 36(7): 2078–2080 (1987).
- [131] T. Nishida, M. Notomi, R.I. Ryuzo Iga, T.T. Toshiaki Tamamura, Quantum Wire Fabrication by E-Beam Elithography Using High-Resolution and High-Sensitivity E-Beam Resist ZEP-520, *Jpn. J. Appl. Phys.* 31 (1992) 4508.
- [132] M. Schirmer, B. Büttner, F. Syrowatka, G. Schmidt, T. Köpnick, C. Kaiser, Chemical Semi-Amplified positive E-beam Resist (CSAR 62) for highest resolution, in: U.F.W. Behringer, W. Maurer (Eds.), Dresden, Germany, 2013: p. 88860D.
- [133] S. Thoms, D.S. Macintyre, Investigation of CSAR 62, a new resist for electron beam lithography, *Journal of Vacuum Science & Technology B, Nanotechnology and Microelectronics: Materials, Processing, Measurement, and Phenomena*. 32 (2014) 06FJ01.
- [134] M.M. Plakhotnyuk, M. Gaudig, R.S. Davidsen, J.M. Lindhard, J. Hirsch, D. Lausch, M.S. Schmidt, E. Stamate, O. Hansen, Low surface damage dry etched black silicon, *Journal of Applied Physics*. 122 (2017) 143101.
- [135] S.Q. Xiao, S. Xu, K. Ostrikov, Low-temperature plasma processing for Si photovoltaics, *Materials Science and Engineering: R: Reports*. 78 (2014) 1–29.
- [136] B. Gorowitz, R.J. Saia, Reactive ion etching, in: *VLSI Electronics Microstructure Science*, Elsevier, 1984: pp. 297–339.
- [137] B. Keville, Y. Zhang, C. Gaman, A.M. Holohan, S. Daniels, M.M. Turner, Real-time control of electron density in a capacitively coupled plasma, *Journal of Vacuum Science & Technology A: Vacuum, Surfaces, and Films*. 31 (2013) 031302.
- [138] F.I. Chang, R. Yeh, G. Lin, P.B. Chu, E.G. Hoffman, E.J. Kruglick, K.S. Pister, M.H. Hecht, Gas-phase silicon micromachining with xenon difluoride, in: *SPIE*, 1995: pp. 117–128.

- [139] C. Chernick, H. Claassen, P. Fields, H. Hyman, J. Malm, W. Manning, M. Matheson, L. Quarterman, F. Schreiner, H. Selig, Fluorine compounds of xenon and radon, *Science*. 138 (1962) 136–138.
- [140] H.F. Winters, J.W. Coburn, The etching of silicon with XeF₂ vapor, *Appl. Phys. Lett.* 34 (1979) 70–73.
- [141] E. Hoffman, B. Warneke, E. Kruglick, J. Weigold, K.S.J. Pister, 3D structures with piezoresistive sensors in standard CMOS, in: *Proceedings IEEE Micro Electro Mechanical Systems*. 1995, IEEE, Amsterdam, Netherlands, 1995: p. 288.
- [142] J. Vähänissi, Xenon difluoride etching of sacrificial layers for fabrication of microelectromechanical devices, Master thesis, Aalto University, School of Electrical Engineering, Major: advanced materials and photonics (2019).
- [143] M. Ronde, A.J. Walton, J.G. Terry, Manipulating Etch Selectivities in XeF₂ Vapour Etching, *J. Microelectromech. Syst.* 30 (2021) 156–164.
- [144] S.S. Verbridge, J.M. Parpia, R.B. Reichenbach, L.M. Bellan, H.G. Craighead, High quality factor resonance at room temperature with nanostrings under high tensile stress, *Journal of Applied Physics*. 99 (2006) 124304.
- [145] M. Abuwasib, P. Krantz, P. Delsing, Fabrication of large dimension aluminum air-bridges for superconducting quantum circuits, *Journal of Vacuum Science & Technology B, Nanotechnology and Microelectronics: Materials, Processing, Measurement, and Phenomena*. 31 (2013) 031601.
- [146] K. Haddadi, O.C. Haenssler, C. Boyaval, D. Theron, G. Dambrine, Near-field scanning millimeter-wave microscope combined with a scanning electron microscope, in: *2017 IEEE MTT-S International Microwave Symposium (IMS)*, IEEE, Honolulu, HI, USA, 2017: pp. 1656–1659.
- [147] O.C. Haenssler, S. Fatikow, D. Theron, Multimodal imaging technology by integrated scanning electron, force, and microwave microscopy and its application to study microscaled capacitors, *Journal of Vacuum Science & Technology B, Nanotechnology and Microelectronics: Materials, Processing, Measurement, and Phenomena*. 36 (2018) 022901.
- [148] A. Buchter, J. Hoffmann, A. Delvallée, E. Brinciotti, D. Hapiuk, C. Licitra, K. Louarn, A. Arnoult, G. Almuneau, F. Piquemal, M. Zeier, F. Kienberger, Scanning microwave microscopy applied to semiconducting GaAs structures, *Review of Scientific Instruments*. 89 (2018) 023704.

- [149] M. Horibe, S. Kon, I. Hirano, Measurement Capability of Scanning Microwave Microscopy: Measurement Sensitivity Versus Accuracy, *IEEE Trans. Instrum. Meas.* 68 (2019) 1774–1780.
- [150] Y. Shi, J. Kahn, B. Niu, Z. Fei, B. Sun, X. Cai, B.A. Francisco, D. Wu, Z.-X. Shen, X. Xu, D.H. Cobden, Y.-T. Cui, Imaging quantum spin Hall edges in monolayer WTe₂, *Sci. Adv.* 5 (2019) eaat8799.
- [151] K. Lee, M.I.B. Utama, S. Kahn, A. Samudrala, N. Leconte, B. Yang, S. Wang, K. Watanabe, T. Taniguchi, M.V.P. Altoé, G. Zhang, A. Weber-Bargioni, M. Crommie, P.D. Ashby, J. Jung, F. Wang, A. Zettl, Ultrahigh-resolution scanning microwave impedance microscopy of moiré lattices and superstructures, *Sci. Adv.* 6 (2020) eabd1919.
- [152] J.A. Morán-Meza, A. Delvallée, D. Allal, F. Piquemal, A substitution method for nanoscale capacitance calibration using scanning microwave microscopy, *Meas. Sci. Technol.* 31 (2020) 074009.
- [153] T. Le Quang, A.C. Gungor, D. Vasyukov, J. Hoffmann, J. Smajic, M. Zeier, Advanced calibration kit for scanning microwave microscope: Design, fabrication, and measurement, *Review of Scientific Instruments.* 92 (2021) 023705.
- [154] D.A.A. Ohlberg, D. Tami, A.C. Gadelha, E.G.S. Neto, F.C. Santana, D. Miranda, W. Avelino, K. Watanabe, T. Taniguchi, L.C. Campos, J.C. Ramirez, C.G. do Rego, A. Jorio, G. Medeiros-Ribeiro, The limits of near field immersion microwave microscopy evaluated by imaging bilayer graphene moiré patterns, *Nat Commun.* 12 (2021) 2980.
- [155] S.N.A. Azman, G. Fabi, E. Pavoni, C.H. Joseph, N. Pini, T. Pietrangelo, L. Pierantoni, A. Morini, D. Mencarelli, A. Di Donato, J.C.M. Hwang, M. Farina, Inverted Scanning Microwave Microscopy of a Vital Mitochondrion in Liquid, *IEEE Microw. Wireless Compon. Lett.* 32 (2022) 804–806.
- [156] W. Lin, Y. Feng, Y. Wang, J. Zhu, Z. Lian, H. Zhang, H. Li, Y. Wu, C. Liu, Y. Wang, J. Zhang, Y. Wang, C.-Z. Chen, X. Zhou, J. Shen, Direct visualization of edge state in even-layer MnBi₂Te₄ at zero magnetic field, *Nat Commun.* 13 (2022) 7714.
- [157] G. Gramse, M. Kasper, L. Fumagalli, G. Gomila, P. Hinterdorfer, F. Kienberger, Calibrated complex impedance and permittivity measurements with scanning microwave microscopy, *Nanotechnology.* 25 (2014) 145703.
- [158] S. Gu, X. Zhou, T. Lin, H. Happy, T. Lasri, Broadband non-contact characterization of epitaxial graphene by near-field microwave microscopy, *Nanotechnology.* 28 (2017) 335702.

- [159] G. Gramse, A. Kölker, T. Lim, T.J.Z. Stock, H. Solanki, S.R. Schofield, E. Brinciotti, G. Aeppli, F. Kienberger, N.J. Curson, Nondestructive imaging of atomically thin nanostructures buried in silicon, *Sci. Adv.* 3 (2017) e1602586.
- [160] A. Tselev, J. Velmurugan, A.V. Ievlev, S.V. Kalinin, A. Kolmakov, Seeing through Walls at the Nanoscale: Microwave Microscopy of Enclosed Objects and Processes in Liquids, *ACS Nano.* 10 (2016) 3562–3570.
- [161] C. Balocco, A.M. Song, M. Åberg, A. Forchel, T. González, J. Mateos, I. Maximov, M. Missous, A.A. Rezazadeh, J. Saijets, L. Samuelson, D. Wallin, K. Williams, L. Worschech, H.Q. Xu, Microwave Detection at 110 GHz by Nanowires with Broken Symmetry, *Nano Lett.* 5 (2005) 1423–1427.
- [162] K. Haddadi, O.C. Haenssler, K. Daffe, S. Eliet, C. Boyaval, D. Theron, G. Dambrine, Combined scanning microwave and electron microscopy: A novel toolbox for hybrid nanoscale material analysis, in: 2017 IEEE MTT-S International Microwave Workshop Series on Advanced Materials and Processes for RF and THz Applications (IMWS-AMP), IEEE, Pavia, 2017: pp. 1–3.
- [163] R. Schoelkopf, P. Wahlgren, A. Kozhevnikov, P. Delsing, D. Prober, The radio-frequency single-electron transistor (RF-SET): A fast and ultrasensitive electrometer, *Science.* 280 (1998) 1238–1242.
- [164] S. Li, Z. Yu, S.-F. Yen, W. Tang, P.J. Burke, Carbon nanotube transistor operation at 2.6 GHz, *Nano Letters.* 4 (2004) 753–756.
- [165] J.B. Camp, T.W. Darling, R.E. Brown, Macroscopic variations of surface potentials of conductors, *Journal of Applied Physics.* 69 (1991) 7126–7129.
- [166] N.A. Burnham, R.J. Colton, H.M. Pollock, Work-function anisotropies as an origin of long-range surface forces, *Phys. Rev. Lett.* 69 (1992) 144–147.
- [167] J.N. Israelachvili, *Intermolecular and surface forces*, Academic press, 2011.
- [168] C.C. Speake, C. Trenkel, Forces between Conducting Surfaces due to Spatial Variations of Surface Potential, *Phys. Rev. Lett.* 90 (2003) 160403.
- [169] M. Héritier, R. Pachlatko, Y. Tao, J.M. Abendroth, C.L. Degen, A. Eichler, Spatial Correlation between Fluctuating and Static Fields over Metal and Dielectric Substrates, *Phys. Rev. Lett.* 127 (2021) 216101.
- [170] H. Ibach, H. Lüth, *Solid-state physics: an introduction to principles of materials science*, Springer Science & Business Media, (2009) 370-403.

- [171] O.C. Haenssler, *Multimodal Sensing and Imaging Technology by Integrated Scanning Electron, Force, and Near-field Microwave Microscopy and its Application to Submicrometer Studies*, Ph.D. dissertation, Universite de Lille IEMN (2018).
- [172] F. Mubarak, R. Romano, M. Spirito, Evaluation and modeling of measurement resolution of a vector network analyzer for extreme impedance measurements, in: 2015 86th ARFTG Microwave Measurement Conference, IEEE, Atlanta, GA, USA, 2015: pp. 1–3.
- [173] M. Ding, Z. Jin, J. Chen, G. Wu, Wideband Vector Network Analyzer Based on Direct Microwave Photonic Digitization, *J. Lightwave Technol.* 40 (2022) 4581–4588.
- [174] D.M. Pozar, *Microwave engineering*, John wiley & sons, Chapter 2: transmission line theory (2011).
- [175] I. Kozinsky, H.W.Ch. Postma, I. Bargatin, M.L. Roukes, Tuning nonlinearity, dynamic range, and frequency of nanomechanical resonators, *Appl. Phys. Lett.* 88 (2006) 253101.
- [176] J. Rieger, T. Faust, M.J. Seitner, J.P. Kotthaus, E.M. Weig, Frequency and Q factor control of nanomechanical resonators, *Appl. Phys. Lett.* 101 (2012) 103110.
- [177] J. Rieger, A. Isacson, M.J. Seitner, J.P. Kotthaus, E.M. Weig, Energy losses of nanomechanical resonators induced by atomic force microscopy-controlled mechanical impedance mismatching, *Nat Commun.* 5 (2014) 3345.
- [178] S. Rechnitz, T. Tabachnik, M. Shlafman, S. Shlafman, Y.E. Yaish, Mode coupling bistability and spectral broadening in buckled carbon nanotube mechanical resonators, *Nat Commun.* 13 (2022) 5900.
- [179] D. Hälg, T. Gisler, Y. Tsaturyan, L. Catalini, U. Grob, M.-D. Krass, M. Héritier, H. Mattiat, A.-K. Thamm, R. Schirhagl, E.C. Langman, A. Schliesser, C.L. Degen, A. Eichler, Membrane-Based Scanning Force Microscopy, *Phys. Rev. Applied.* 15 (2021) L021001.
- [180] S. Kumar, S. Spence, S. Perrett, Z. Tahir, A. Singh, C. Qi, S. Perez Vizan, X. Rojas, A novel architecture for room temperature microwave optomechanical experiments, *Journal of Applied Physics.* 133 (2023) 094501.
- [181] T. Barois, A. Ayari, A. Siria, S. Perisanu, P. Vincent, P. Poncharal, S.T. Purcell, Ohmic electromechanical dissipation in nanomechanical cantilevers, *Phys. Rev. B.* 85 (2012) 075407.
- [182] F. Massel, T.T. Heikkilä, J.-M. Pirkkalainen, S.U. Cho, H. Saloniemi, P.J. Hakonen, M.A. Sillanpää, Microwave amplification with nanomechanical resonators, *Nature.* 480 (2011) 351–354.

- [183] D. Cattiaux, X. Zhou, S. Kumar, I. Golokolenov, R. Gazizulin, A. Luck, L.M. de Lépinay, M. Sillanpää, A. Armour, A. Fefferman, Beyond linear coupling in microwave optomechanics, *Physical Review Research*. 2 (2020) 033480.
- [184] O. Maillet, D. Cattiaux, X. Zhou, R.R. Gazizulin, O. Bourgeois, A.D. Fefferman, E. Collin, Nanomechanical damping via electron-assisted relaxation of two-level systems, *Physical Review B*. 107 (2023) 064104.
- [185] R. Anufriev, A. Ramiere, J. Maire, M. Nomura, Heat guiding and focusing using ballistic phonon transport in phononic nanostructures, *Nat Commun*. 8 (2017) 15505.
- [186] J. Maire, R. Anufriev, R. Yanagisawa, A. Ramiere, S. Volz, M. Nomura, Heat conduction tuning by wave nature of phonons, *Sci. Adv*. 3 (2017) e1700027.
- [187] M. Selby, Conical coaxial capacitors and their advantages, *Journal of Research*. 63 (1959) 87–89.
- [188] M.C. Selby, Analysis of coaxial two-terminal conical capacitor, US Department of Commerce, National Bureau of Standards, full version (1962).
- [189] S. Hudlet, M. Saint Jean, C. Guthmann, J. Berger, Evaluation of the capacitive force between an atomic force microscopy tip and a metallic surface, *The European Physical Journal B-Condensed Matter and Complex Systems*. 2 (1998) 5–10.